Influence of surface treatments on corrosion resistance properties of ultrafine grained Titanium alloys for implant applications

Diego Godoy

▶ **To cite this version:**

Diego Godoy. Influence of surface treatments on corrosion resistance properties of ultrafine grained Titanium alloys for implant applications. Material chemistry. Université Grenoble Alpes; Universidade federal de São Carlos, 2019. English. NNT : 2019GREAI040 . tel-02935735

HAL Id: tel-02935735

https://theses.hal.science/tel-02935735v1

Submitted on 10 Sep 2020

HAL is a multi-disciplinary open access archive for the deposit and dissemination of scientific research documents, whether they are published or not. The documents may come from teaching and research institutions in France or abroad, or from public or private research centers.

L'archive ouverte pluridisciplinaire **HAL**, est destinée au dépôt et à la diffusion de documents scientifiques de niveau recherche, publiés ou non, émanant des établissements d'enseignement et de recherche français ou étrangers, des laboratoires publics ou privés.

THÈSE

Pour obtenir le grade de

DOCTEUR DE L'UNIVERSITÉ GRENOBLE ALPES
et
DOUTOR EM ENGENHARIA DE MATERIAIS, UNIVERSIDADE FEDERAL DE SÃO CARLOS

préparée dans le cadre d'une cotutelle entre **l'Université Grenoble Alpes et Université Federal de São Carlos**

Spécialité : **Matériaux, Mécanique, Génie civil, Electrochimie**

Arrêté ministériel : le 6 janvier 2005 – 25 mai 2016

Présentée par

Diego GODOY

Thèse dirigée par **Jean Claude LEPETRE (France)** et **Walter BOTTA (Brésil)** et codirigée par **Virginie ROCHE (France)** et **Alberto MOREIRA (Brésil)**

préparée au sein des

- Laboratoire d'Electrochimie et de Physicochimie des Matériaux et des Interfaces (LEPMI), France
- Structural Characterization Laboratory (LCE), Brésil

dans **l'École Doctorale Ingénierie - Matériaux, Mécanique, Environnement, Energétique, Procédés, Production (IMEP2)**

Influence de traitements de surface sur les propriétés de résistance à la corrosion d'alliages de Titane à grains ultrafins pour des applications biomédicales

Thèse soutenue publiquement le **9 août 2019**,
devant le jury composé de :

M. Jean-Claude LEPRETRE
Professeur, Université Grenoble Alpes, Directeur de thèse
M. Walter JOSE BOTTA FILHO
Professeur, Université Fédérale de São Carlos, Brésil, Directeur de thèse
Mme. Virginie ROCHE
Maître de conférences, Université Grenoble Alpes, Co-encadrante de thèse
M. Alberto MOREIRA JORGE JUNIOR
Professeur, Université Fédérale de São Carlos, Brésil, Co-encadrante de thèse
M. Ricardo NOGUEIRA
Professeur, The Petroleum Institute, Emirats arabe unis, Rapporteur et Président
M. Claudemiro BOLFARINI
Professeur, Université Fédérale de São Carlos, Brésil, Examinateur
M. Dilermando TRAVESSA NAGLE
Professeur, Université Fédérale de São Paulo, Brésil, Rapporteur
Mme. Katia REGINA CARDOSO
Professeur, Université Fédérale de São Paulo, Brésil, Examinateur

INFLUENCE OF SURFACE TREATMENTS ON CORROSION RESISTANCE PROPERTIES OF ULTRAFINE GRAINED TITANIUM ALLOYS FOR IMPLANT APPLICATIONS

Diego Alfonso Godoy Pérez

UNIVERSITÉ GRENOBLE ALPES

Laboratoire d'Electrochimie et de Physicochimie des Matériaux et des Interfaces (LEPMI), F-38000 Grenoble, France.

UNIVERSIDADE FEDERAL DE SÃO CARLOS

Department of Materials Engineering, Rod. Washington Luiz, São Carlos - SP, 13565-905

2019

Abstract

Titanium and its alloys are used as biomaterials because their excellent combination of high corrosion resistance, low modulus of elasticity and biocompatibility. However, titanium and its alloys cannot meet all the clinical requirements. In this sense, in order to improve the electrochemical and bioactive properties, this thesis aims to evaluate the effect of the severe plastic deformation as well as the surface modification treatments on the corrosion resistance and bioactivity of titanium alloys (α' + β) and (β).

The titanium alloys, Ti13Nb13Zr (α' + β) and Ti35Nb7Zr5Ta (β), were deformed by the high-pressure torsion (HPT) method. Afterward, surface modification treatments, such as the anodization and chemical treatments, were carried out both in samples non-deformed and deformed by HPT. Finally, corrosion and bioactivity tests were performed in simulated body fluid (SBF). The tests were performed on samples with treated surfaces compared with non-treated surfaces in the deformed and undeformed conditions.

The samples' microstructures were analyzed by confocal laser microscopy (CLM), scanning electron microscopy (SEM) and X-ray diffraction (XRD). Hardness tests were also performed after the HPT process. On the other hand, surface modification treatments, and the formation of apatite in bioactivity assays were evaluated by scanning electron microscopy (SEM), with chemical analyzes carried out by dispersive energy spectroscopy (EDS) and phase identification by X-ray diffraction (XRD).

In general, the corrosion resistance of the titanium alloys improved with the anodization treatment. Apatite deposits were observed on Ti13Nb13Zr alloy samples, in the conditions non-deformed and deformed by HPT. The Ti35Nb7Zr5Ta appears to have a lower apatite-formation ability compared to Ti13Nb13Zr.

Keywords: Titanium alloys, Ti13Nb13Zr alloy, Ti35Nb7Zr5Ta alloy, Severe plastic deformation, TiO_2 nanotubes, Apatite, Corrosion resistance, Bioactivity.

Résumé

Le titane et ses alliages sont utilisés comme biomatériaux en raison de leur excellente combinaison de résistance élevée à la corrosion, de faibles modules d'élasticité et de biocompatibilité. Cependant, le titane et ses alliages ne peuvent pas répondre à toutes les exigences cliniques. En ce sens, afin d'améliorer les propriétés électrochimiques et bioactives, cette thèse vise à évaluer l'effet de la déformation plastique sévère ainsi que des traitements de modification de surface sur la résistance à la corrosion et la bioactivité des alliages de titane (α '+ β) et (β).

Les alliages Ti13Nb13Zr (α' + β) et Ti35Nb7Zr5Ta (β) ont été déformés par la méthode de torsion à haute pression (HPT-High Pressure torsion). Ensuite, des traitements de modification de surface, tels que l'anodisation et les traitements chimiques, ont été effectués dans des échantillons non déformés et déformés par HPT. Enfin, des tests de corrosion et de bioactivité ont été réalisés dans un fluide corporel simulé (SBF). Les tests ont été effectués sur des échantillons de surfaces traitées par rapport à des surfaces non traitées de conditions déformées et non déformées.

La microstructure des échantillons a été analysée par microscope confocal à balayage laser (CLM), microscopie électronique à balayage (SEM) et diffraction des rayons X (XRD). Des tests de dureté sont également effectués après le processus HPT. D'autre part, les traitements de modification de surface et la formation d'apatite dans les tests de bioactivité sont évalués par SEM, analyses chimiques par spectroscopie d'énergie dispersive (EDS) et DRX.

En général, la résistance à la corrosion des alliages de titane évaluées, améliorée avec le traitement d'anodisation. Des dépôts d'apatite ont été observés sur des échantillons d'alliage Ti13Nb13Zr, non déformés et déformés par HPT, pour les traitements de modification de surface proposés. Le Ti35Nb7Zr5Ta semble avoir une capacité de formation d'apatite inférieure à celle du Ti13Nb13Zr.

Mots-clés : Alliage de titane, Alliage Ti13Nb13Zr, Alliage Ti35Nb7Zr5Ta, Déformation plastique sévère, Nanotubes de TiO_2, Apatite, Résistance à la corrosion, Bioactivité.

Resumo

Titânio e suas ligas são utilizados como biomateriais devido à sua excelente combinação de alta resistência à corrosão, baixo módulo de elasticidade e biocompatibilidade. No entanto, o titânio e suas ligas não podem atender a todos os requisitos clínicos. Neste sentido, a fim de melhorar as propriedades eletroquímicas e bioativas, esta tese tem como objetivo avaliar o efeito da deformação plástica severa e os tratamentos de modificação de superfície na resistência à corrosão e bioatividade de ligas de titânio (α '+ β) e (β).

As ligas de titânio, (α' + β) Ti13Nb13Zr e a liga (β) Ti35Nb7Zr5Ta foram deformadas pelo método de deformação plástica severa de torção sob alta pressão (HPT, High Pressure Torsion). Além disso, tratamentos de modificação de superfície são propostos, como anodização e tratamentos químicos em amostras deformadas por HPT e em amostras não deformadas. Finalmente, os testes de corrosão e bioatividade foram realizados em fluido corporal simulado (SBF). Os testes foram realizados em amostras de superfícies tratadas em comparação com superfícies não tratadas de condições deformadas e não deformadas.

A microestrutura das amostras foi analisada por microscopia confocal laser (MCL), microscopia eletrônica de varredura (MEV) e difração de raios X (DRX). Testes de dureza também são realizados após o processo HPT. Por outro lado, tratamentos de modificação de superfície e a formação de apatita em ensaios de bioatividade são avaliados por MEV, análises químicas por espectroscopia de energia dispersiva (EDS) e DRX.

Em geral, a resistência à corrosão das ligas de titânio avaliadas melhorou com o tratamento de anodização. Depósitos de apatita foram observados em amostras da liga Ti13Nb13Zr, não deformadas e deformadas por HPT, para todos os tratamentos de modificação de superfície propostos A liga Ti35Nb7Zr5Ta parece ter uma menor capacidade de formação de apatita que a liga de Ti13Nb13Zr.

Palavras-chave: Liga de titânio, Liga Ti13Nb13Zr, Liga Ti35Nb7Zr5Ta, Deformação plástica severa, Nanotubos de TiO_2, Apatita, Resistência à corrosão, Bioatividade.

Acknowledgments

Acknowledging everyone who helped me, in one way or another, during my thesis work in two different laboratories.

I would like to start by expressing my gratitude to the National Commission on Scientific and Technological Research of Chile (CONICYT), for the partial Ph.D. fellowship. I would also like to thank the French Committee for the Evaluation of Academic and Scientific Cooperation with Brazil (COFECUB), the Brazilian CAPES (Process number #88887.137755/2017-00- Finance Code 001) for funding the bilateral cooperation, and also FAPESP under the grant number FAPESP Thematic # 2013/05987-8, for the partial funding.

Thank you, my main supervisors, Walter Jose Botta Filho, and Alberto Moreira Jorge Júnior, for the patience, scientific insight, and suggestions during the planning and development of this research work. My grateful thanks are also extended to my co-supervisors in Grenoble, Virginie Roche, and Jean Claude Lepretre, for their advice and supervision in the corrosion laboratory.

I would like to acknowledge the people who made key inputs to this work: Claudemiro Bolfarini for having provided the alloys studied in this work and also for his valuable and constructive suggestions. Fanny Hilario for helping me when I arrived to Grenoble as well as for her support in the electrochemical measurements; Verónica Müller for her help with Raman spectroscopy; and Gabriel Hitoshi Asato and Murillo Romero for helping me with the deformation by HPT of some samples. A special thank you to the technicians of both the Laboratory of Structural Characterization (LCE/DEMa/UFSCar) in São Carlos and the Consortium des Moyens Technologiques Communs (CMTC) within the INP in Grenoble. I particularly acknowledge to Diego Coimbrão, Manoel Denari, Ana Vieira, Frederic Charlot, and Thierry Encinas.

My thanks to all the people who made me feel welcome to the labs in São Carlos and Grenoble. To my colleagues, thank you for the help in the experiments, for the coffee and lunch sessions.

To my Family and Margarita, for the unlimited support and for encouraging me to pursue my dreams, thank you very much. This thesis is dedicated to you.

LIST OF FIGURES

LIST OF TABLES

TABLE OF CONTENTS

LIST OF ABBREVIATIONS

at % Atomic percent

CPE Constant-Phase-Element

ξ Interfacial impedance of the transmission line (Ω·cm)

E_{corr} Corrosion potential

EDS Energy dispersive spectroscopy

EIS Electrochemical impedance spectroscopy

H_3PO_4 Phosphoric acid

HCl Hydrochloric acid

HPT High-pressure torsion

HV Hardness Vickers

I_{pass} Passivation current density

ISO International organization for standardization

NaOH Sodium hydroxide

ND Non-deformed

OCP Open circuit potential

Q_3 Interfacial pseudo-capacitance

r1 Distributed resistance along with the liquid phase ($\Omega \cdot cm^{-1}$)

r2 Distributed resistance along with the solid phase ($\Omega \cdot cm^{-1}$)

Rs Electrolyte resistance ($\Omega \cdot cm^{-2}$)

SBF Solution body fluid

SCE Saturated calomel electrode

SHE Standard hydrogen electrode

SEM Scanning electron microscopy

SPD Severe plastic deformation

TEM Transmission electron microscopy

χ_1 Impedance distributed in the liquid phase of the transmission line ($\Omega \cdot cm^{-1}$)

χ_2 Impedance distributed in the solid phase of the transmission line ($\Omega \cdot cm^{-1}$)

XRD X-ray diffraction

Z_A Boundary impedance at the interface electrolyte | top of the pores (Ω)

Z_B Boundary impedance at the interface electrolyte | substrate (Ω)

1 INTRODUCTION

The application of materials in the substitution of human tissues to restore bodily functions is not a new fact. Scientists of materials science and implantology have been looking for advances in device designs that can be valuable for the replacement of body parts. It is not surprising that from the Roman period, there are reports of the use of metals for dental prostheses [1]. With the development at the scientific level of biomedical devices at the beginning of the 20th century, the increase of the prosthetic market was favored. The biomedical devices currently in use (prostheses, implants) have satisfactory performance in many cases. However, sometimes the body reacts to the insertion of a device, which can lead to the rapid replacement of this device.

In this context, titanium (Ti) and its alloys are today the most relevant and sought materials for several designed implants in orthopedics and dentistry due to their excellent biocompatibility and corrosion resistance [2]. Some of the most common uses for titanium implants are in hip and knee replacement surgeries [3]. They are also used to replace shoulder and elbow joints and to protect the vertebrae following complicated and invasive back surgery. Titanium pegs are used to attach false eyes and ears, and titanium heart valves are even competing with conventional tissue valves [4].

On the other hand, the mechanical properties of titanium and its alloys must be near the bone tissue as a prerequisite for the success of orthopedic implants [5]. α + β and β type are the most appropriate titanium alloys for orthopedic implants because their mechanical properties are similar to the bone tissue [6]. α + β titanium alloys are the easiest found and have already been used as a biomaterial for at least three decades [7]. For example, the Ti6Al4V alloy (α + β type) was initially developed to be applied in the aerospace industry. However, due to its high availability is widely used in orthopedic implants [8]. Nevertheless, biocompatibility studies have indicated that the release of Al and V ions can cause harm to patients [9]. The formation of unstable oxides of V is associated with

disorders of the respiratory system, while Al is associated with Alzheimer's disease [10].

On the other hand, β alloys have attracted considerable interest as they can be obtained from metal elements considered biocompatible such as Nb, Ta, Zr, Mo, and Sn [11]. Moreover, the most interesting biomechanical characteristic is the low modulus of elasticity, which results in better interaction between the implant and the bone [12].

The recent interest in reducing the modulus of elasticity has resulted in the development of a new generation of titanium alloys for orthopedic applications, such as Ti29Nb13Ta4.6Zr [13], Ti12Mo6Zr2Fe (TMZF) [14], Ti35Nb7Zr5Ta (TNZT) [15] and Ti13Nb13Zr [16].

As well as the modulus of elasticity, other mechanical properties of titanium alloys such as hardness, strength, and ductility can be significantly improved using severe plastic deformation (SPD) [17]. It is due to ultrafine-grained (UFG) microstructure obtained by this process [18]. The most commonly applied SPD techniques are Equal-channel Angular Pressing (ECAP) and High-Pressure Torsion (HPT) [19].

In a previous work [20], we have confirmed the above mentioned. In this work, it was observed that the processing by high-pressure torsion technique leads to an increase of microhardness of the Ti13Nb13Zr alloy. The microhardness value increased significantly from 220 HV to 402 HV for the applied pressure of 4.5 GPa. Moreover, grain size refining was also observed (from 200 μm at the initial state to 130 nm) [20].

On the other hand, previous works concerning titanium and titanium alloys processed by SPD have been focused on evaluating the relationship between the microstructure obtained by SPD and the mechanical properties [21–23]. However, few studies relate the microstructure obtained by SPD and the corrosion resistance of titanium alloys [24]. Corrosion resistance (prevention of ion release) and

mechanical resistance (prevention of debris formation) are key factors that could affect the biocompatibility of titanium alloys [25].

Corrosion is a major problem for the implantation of metallic materials because it can cause loss of both the structural integrity and surface properties of the implants. Moreover, it can also alter the mechanical properties of the implant and accelerate its fatigue and wear, which will further intensify corrosion itself. Corrosion process of a metallic material can also alter the physiological environment (pH change) or release of the debris that can cause allergic reactions [25].

The corrosion behavior of titanium alloy is mainly dependent on the passive film that it forms on its surface and its properties (composition and thickness) and the microstructure of the substrate (grain size and dislocation density) [26]. The passivation phenomenon contributes to improving the corrosion resistance and makes titanium alloys suitable for use as implants, for instance, dental and orthopedic implants without promoting adverse reactions locally or systemically [27].

The low rate of dissolution and chemical inertness of titanium oxide passive layer (TiO_2) dissolution products allow the bone to thrive and osseointegrate with titanium alloy [28]. Moreover, it has been reported that TiO_2 with high dielectric constants, inhibits the movement of cells to implant surfaces and might play an essential role in facilitating osseointegration [29].

The osseointegration refers to the adjacent neighborhood between the implant and bone tissue [30]. Brhnemark (1985) suggested the following definition of osseointegration: "*A direct structural and functional connection between ordered, living bone and the surface of a load-carrying implant"* [31]. In this way, the biological response of an implant depends on the physicochemical properties of the surface [32]. Recently, surface modification methods for titanium implant materials such as calcium phosphate ($Ca_3(PO_4)_2$) coatings [33], the alkali- and heat-treatments [34], plasma coatings [35] and TiO_2 nanotubes [36] have been

studied as a means of improving implant integration. These methods of surface preparation can be based on clean and well-characterized surfaces for general biological evaluation as well as for understanding the role of specific surface contaminants [28].

Therefore, aiming to advance the understanding of the mechanical and corrosion properties of titanium alloys for biomedical applications, in this work two titanium alloys, (α'+ β) Ti13Nb13Zr and β Ti35Nb7Zr5Ta alloys deformed by the HPT method at conditions already defined in previous work [20], were studied. Also, two different surface modification treatments, the anodization and chemical treatments in the samples deformed by HPT as well as in samples non-deformed were carried out. Finally, the effects of severe plastic deformation and surface modification treatments were established through corrosion and bioactivity assays.

2 OBJECTIVES

This doctoral project aims to evaluate the effect of the severe plastic deformation as well as the surface modification treatments on the corrosion resistance and bioactivity of the alloys Ti13Nb13Zr and Ti35Nb7Zr5Ta. The specific objectives of this study are:

- Study of surface modification such as anodization, chemical treatment by both HCl and H_3PO_4 etching and NaOH activation in the alloys Ti13Nb13Zr and Ti35Nb7Zr5Ta with different levels of severe plastic deformation by high-pressure torsion (HPT) methodology.
- Electrochemical characterization in a simulated body fluid (SBF), regarding the corrosion resistance of surfaces (modified and not) of the alloys Ti13Nb13Zr and Ti35Nb7Zr5Ta, processed with different levels of severe plastic deformation by HPT.
- Evaluate the effect of different levels of severe plastic deformation and surface modification treatments on the bioactivity of the alloys Ti13Nb13Zr and Ti35Nb7Zr5Ta.

3 THEORETICAL BACKGROUND

3.1 Titanium: Physical Metallurgy

The physical metallurgy of titanium is both complex and exciting. Table 1 presents the physical properties of pure titanium [37].

Table 1: Physical properties of titanium (at room temperature). Adapted from Froes (2015) [37].

Physical properties of pure titanium:	Elastic moduli, polycrystalline:
Atomic number: 22	Young's: 109 GPa
Atomic weight: 47.90 g/mol	Shear: 37 GPa
Crystal structure:	Bulk: 123 GPa
α: to 885 °C hexagonal close-packed	Poisson's ratio: 0.34
c = 4.6832 Å, *a* = 2.9504 Å, *c*/*a* = 1.5873	Melting temperature: 1670 °C
β: 885 °C up to the melting point: body-centered cubic	Boiling temperature: 3260 °C
a = 3.3065 Å, closest atom distance, 2.860 Å	X-ray spectra:
Density:	Kα: 2.750 Å
α: 4.505 g/cm^3	Kβ: 2.514 Å
β: 4.32 g/cm^3	K absorption edge: 2.496 Å

Pure titanium exhibits the phenomenon of allotropy. At low temperatures, it exists as a hexagonal close-packed (HCP) crystalline structure, designated as alpha phase (α), as shown in Figure 1. At high temperatures, above 882.5 °C, its stable crystalline structure is the body-centered cubic (BCC) [37], designated as beta phase (β), as also shown in Figure 1. For pure titanium, the temperature which the transformation from alpha (HCP) to beta (BCC) occurs is called the beta transus temperature. The addition of alloying elements changes this temperature.

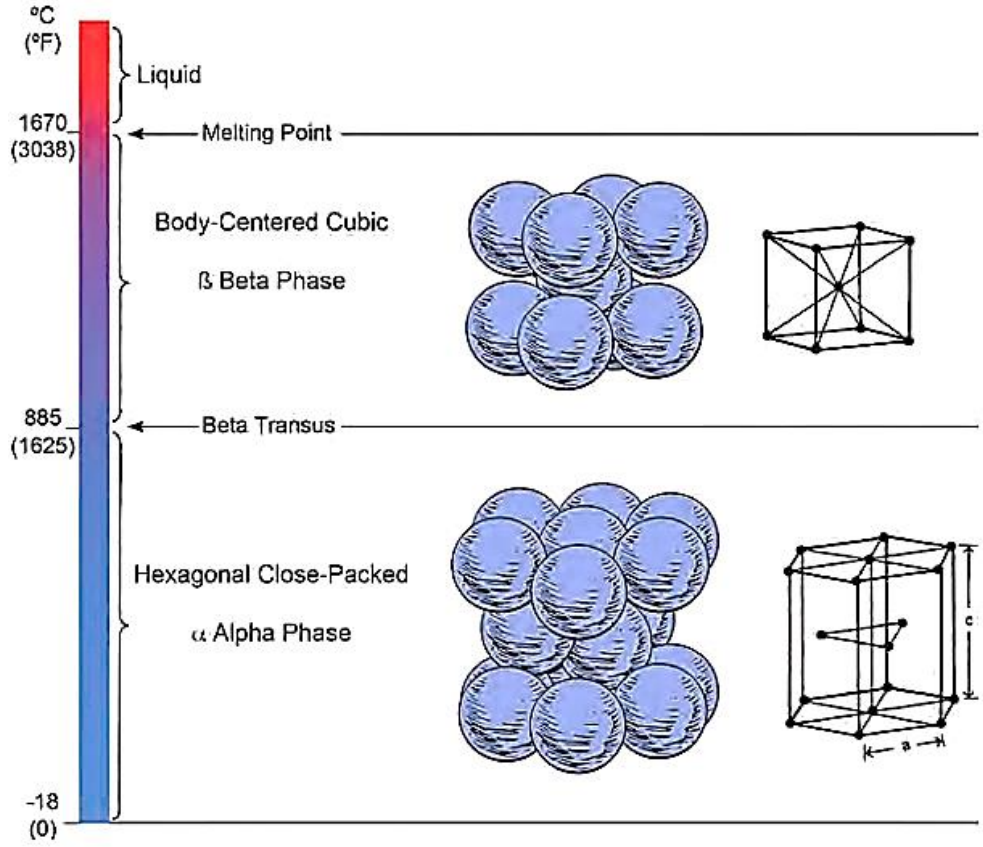

Figure 1: Crystal structure of titanium. Adapted from Froes (2015) [37].

Titanium alloys are classified into three main groups: α alloys, β alloys, α + β alloys, and two other secondary ones: near-α and near-β, referring to alloys with compositions which place them near to α/(α + β) or β/(α + β) phase boundaries, respectively [38]. These groups are characterized by the phases that exist in the alloy near ambient temperature. The temperatures at which the alpha and beta phases may exist are altered with alloying elements which are added to pure titanium. Based on their influence on the proportions of the alpha and beta phases below the beta transus, the alloying elements are divided into three groups: α stabilizers, β stabilizers, and neutral elements. The beta stabilizers are subdivided into two groups: β isomorphic and β eutectoid. The β isomorphic group contains alloying elements whose titanium solubility is unlimited, such as vanadium, molybdenum, and niobium. The elements of the eutectoid β group, which have eutectoid reactions with titanium, include magnesium, iron, chromium, and copper.

Figure 2 shows the influence of the elements on the phase diagrams in titanium alloys [39].

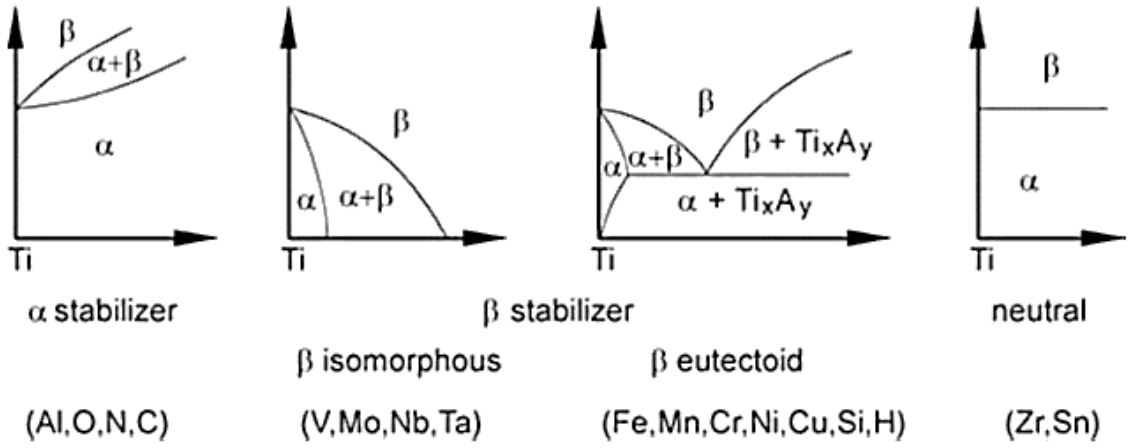

Figure 2: Effect of alloying elements on phase diagrams of titanium alloys (schematically). Adapted from Lütjering et al., (2003) [39].

The α structure mainly composes α and near α titanium alloys. Depending on processing conditions, such alloys may have different grain morphologies, ranging from equiaxial to acicular (martensitic). These kinds of titanium alloys are preferred for high-temperature applications. β titanium alloys contain a balance of beta stabilizers to α-stabilizers which is enough to ensure that a fully β-phase microstructure can be maintained in fast cooling conditions (slow cooling in the furnace, for example, causes β phase decomposition). In this condition, the metastable β alloys are generally thermodynamically unstable. Such behavior can be used as an advantage (for cold deformation before aging, for example), by allowing some decomposition reaction (α-precipitation) during an aging treatment in order to provide secondary strengthening. As a result, the metastable β-titanium alloys generally have higher strength and improved formability at room temperature as compared to the α and α + β titanium alloys [40].

3.2 Ti13Nb13Zr alloy

The Ti13Nb13Zr alloy (in some articles named as TNZ) was developed in 1990 [41] by Davidson and Kovacs. Nowadays, it is part of a new class of biomedical alloys used in medical implants [42].

It is an (α'+ β) alloy in water-quenched condition [43]. With subsequent aging, the alloy consists of HCP martensite (α') and a retained BCC β phase. The dispersed beta phase strengthens and hardens the material. Aging treatment usually results in the conversion of the martensite into an α+ β mixture [44]. In the water-quenched condition, this alloy has an elasticity modulus around 65 GPa [45]. As the modulus of this alloy is much closer to that of bone (30 GPa), it is considered to be a better alternative when compared to the conventional alloys like AISI Type 316L Stainless Steel with a modulus of 220 GPa and Co–Cr–Ni alloy with a modulus of 240 GPa [46].

Khan et al., (1999) [47] called the attention to the fact that the Ti13Nb13Zr alloy, made of non-toxic elements, had been proposed as more favorable for orthopedic implants than the Ti6Al4V alloy because of its superior corrosion resistance and biocompatibility. Reasons for this superiority have included the fact that less metal ion release is likely to occur during spontaneous passivation of Ti13Nb13Zr alloy because the corrosion products of the minor alloying elements, niobium, and zirconium, are less soluble than those of aluminum and vanadium [48]. Also, the passive oxide layer on the surface of the alloy is more inert consisting of a dense rutile structure providing more excellent protection to the underlying alloy.

Furthermore, the corrosion resistance of Ti13Nb13Zr in phosphate-buffered saline (PBS) solution has also been evaluated, concluding that this alloy had better corrosion resistance properties than pure titanium and Ti15Mo alloy, due to formation of a very dense and stable passive layer [49].

On the other hand, this alloy exhibits good mechanical [27,43,50,51] and excellent tissue compatibility properties [42,52–54], which make it well suited for biomedical applications where a bone anchorage is required, particularly for implant applications. Standard specification for wrought Ti13Nb13Zr alloy for medical implant application was settled in the ASTMF 1713-96 [55].

3.3 Ti35Nb7Zr5Ta alloy

The β type titanium alloy, Ti35Nb7Zr5Ta, (in some articles named as TNZT) was developed by Dr. Henry Rack at Clemson University [56]. This alloy also is a new metallic biomaterial that was designed to have outstanding osseointegration ability, good mechanical strength, improved ductility, very low elastic modulus, and excellent hot and cold workability [57].

The Ti35Nb7Zr5Ta alloy stood out as a prospective alloy mainly because it had one of the lowest moduli to date (55 GPa) [56,58], almost 20-25% lower than other available alloys [59], which is very close to the modulus of the bone [15].

Atapour et al., (2011) [60] reported that the corrosion resistance of Ti35Nb7Zr5Ta alloy in 0.9 wt.% NaCl solution at 37 °C, is higher than for Ti6Al4V and Ti13Mo7Zr3Fe alloys in these conditions. This observation reveals an improvement in the corrosion protection characteristics of the alloys rich in niobium [61].

On the other hand, Sonia et al., (2010) [62] reported that the Ti35Nb7Zr5Ta alloy deposited with laser exhibits excellent corrosion resistance in both 0.1 N HCl as well as in Ringer's solution, comparable to, and in some cases even better than, currently used Ti6Al4V ELI and CP Ti (Grade 2) alloys. Also, in-vitro studies conducted on laser-deposited Ti35Nb7Zr5Ta alloy is encouraging and indicate that these alloys are biocompatible aiding in both cell proliferation as well as in cell differentiation [62].

Concerning the standard specification for Ti35Nb7Zr5Ta alloy for medical implant application was settled in the Task Force F-04.12.23 [63].

3.4 Severe Plastic Deformation (SPD)

The severe plastic deformation (SPD) is defined as a process in which ultra-large plastic strains are introduced into a bulk material in order to achieve significant grain refinement. The metallic materials obtained by SPD are ultrafine-grained (UFG) (grain size in the range of 100–1000 nm) or nanostructured (NS) (grain size below 100 nm) [64]. A large number of different SPD methods, such as high-pressure torsion (HPT), equal channel angular pressing (ECAP) and accumulative roll-bonding (ARB), have been developed [65]. The SPD by HPT has shown a greater refinement of microstructure [18]. The principle of current HPT process is described schematically in Figure 3 [66].

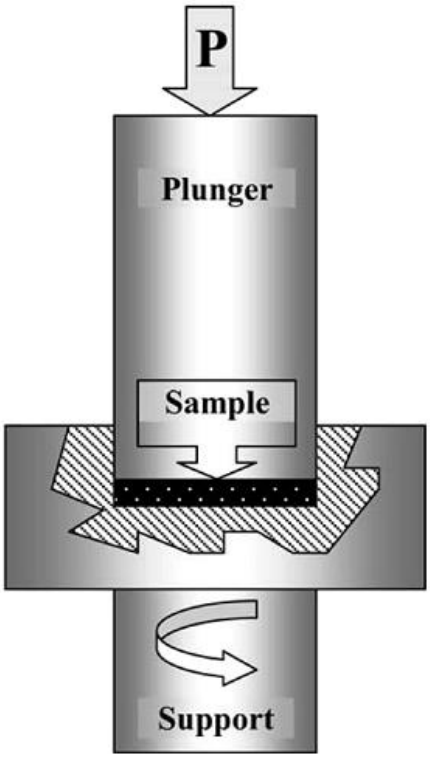

Figure 3: Schematic illustration of the HPT process. Adapted from Zhilyaev et al., (2008) [66].

The sample in a disk form is located between two anvils under compressive pressure, P, of several GPa at room or elevated temperature and simultaneously it is subjected to a torsional strain which is imposed through rotation of the lower

anvil. Surface frictional forces, therefore, deform the disk by shear so that deformation proceeds under a quasi-hydrostatic pressure.

Pure Ti displays the highest biocompatibility with living organisms. Nonetheless, it has limited use in medicine due to its low strength [67]. Recently it has been shown that high-strength nanostructured pure Ti processed via SPD can provide a new and promising alternative in medical device technology [23]. This approach has the advantages of improved biocompatibility and reduces the size of the implants significantly, decreasing the level of surgical intervention in the human body [43,44].

The mechanical properties of the nanostructured Ti are even higher compared to those of conventional high-strength Ti alloys (such as Ti6Al4V) used in biomedical engineering [69]. Nanostructuring of Ti also positively affects its biomedical properties. The company 'Timplant' (Ostrava, Czech Republic) manufactures nanostructured Ti dental implants under the trademark Nanoimplant® since 2006 [www.timplant.cz]. To date, these dental implants have been certified according to the European standard EN ISO 13485:2003. The new generation implants have a smaller diameter (2.0 mm) compared to the standard ones (3.5 mm) [69]. Therefore, they can be successfully inserted into thin jawbones where larger implants cannot be used. Another advantage of smaller dental implants is less damage induced into the jawbone during surgical intervention. For example, Figure 4(a) illustrates the Nanoimplant®. It is installed into the body of an 18-year-old patient with thin jawbones between teeth 11 and 13 [69]. Another implant with a diameter of 2.4 mm was inserted to the right-side position 12 (Figures. 4(b) and (c)). The patient left the dental office with two nano implants and with two temporary crowns made on the same day as implants were inserted. After six weeks, final metal-ceramic crowns were fixed on the implants.

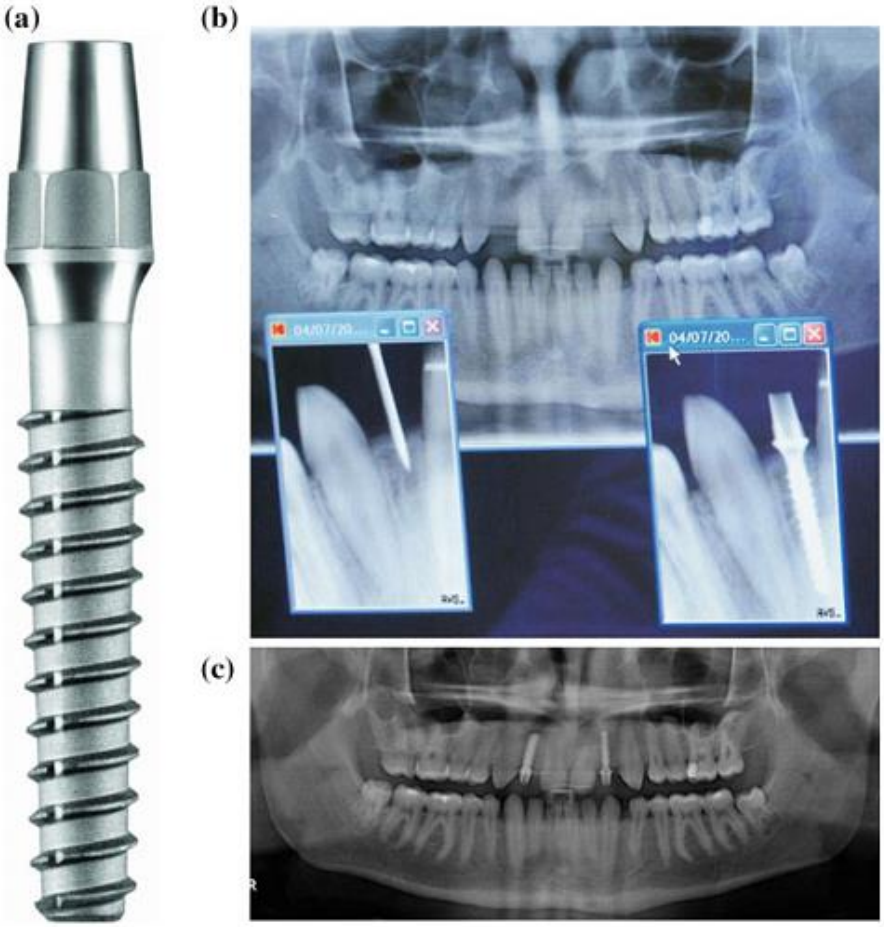

Figure 4: a) Dental implant from nanostructured Ti; b), c) X-ray photographs after surgery and control photograph after incorporation of dental implants into the human jaw. Adapted from Sabirov et al., (2015) [67].

3.5 Surface modification treatments.

Titanium and titanium alloys are widely used in biomedical devices and components, especially as hard tissue replacements as well as in cardiac and cardiovascular applications, because of their desirable properties, such as relatively low elastic modulus, good fatigue strength, formability, machinability, corrosion resistance, and biocompatibility. However, titanium and its alloys cannot meet all of the clinical requirements because of its poor tribological properties [70]. Therefore, in order to improve the biological, chemical, and mechanical properties of titanium and titanium alloys, surface modification treatments are often

performed. Two surface modification treatments related to titanium and titanium alloys will be reviewed hereafter.

3.5.1 The growth of TiO_2 nanostructures by electrochemical anodization

The discovery of carbon nanotubes reported by Iijima in 1991 opened a new area of research in materials science [71]. The one-dimensional (1D) nanostructures provide unique electronic properties such as electron mobility and a very high specific surface area [72]. Although carbon is still the most explored nanotube material, a considerable range of other materials have been studied, which are mainly transition metal oxides and sulfides, which have also shown fascinating new properties and features [72].

Among the transition metal oxides, the titanium dioxide (TiO_2) is one of the most studied because of its exceptional properties: non-toxicity, high electrical conduction, corrosion resistance, and biocompatibility (use in medicine) [72]. The TiO_2 is frequently used in paint, white pigments, sun-blockers, solar panels, for photocatalytic reactions and biomedical coatings [73,74]. For most of these applications, it is necessary to increase the specific surface area of the material to achieve maximum overall efficiency and therefore nanoparticulated forms of TiO_2 are widely used [75].

As mentioned previously, titanium is widely used in the replacement of hard tissue and cardiovascular tissue. Since the surface of the implant is responsible for the osseointegration process, it is essential to modify this surface to obtain better biocompatibility. The adhesion of a nanostructured surface increases the biocompatibility when compared usual metal surfaces, showing that nanotubes improve osseointegration. Surfaces that contain TiO_2 nanotubes increase cell growth and increase hydroxyapatite (HAp) deposition [76]. The HAp ($Ca_{10}(PO_4)_6(OH)_2$) presents chemical and structural similarities with the inorganic component of the bone matrix. It adapts to the rate of resorption and growth of bone, turning the nanostructured material the right choice for use in prostheses.

TiO_2 nanotubes are obtained by electrochemical anodization in aqueous or organic electrolytes with fluoride ions (e.g., aqueous electrolyte either with acids- H_2SO_4, or H_3PO_4 [9], or salts $(NH_4)_2SO_4$, or Na_2SO_4 or glycerol or ethylene glycol, and so forth) [22].

The critical processes involved in TiO_2 nanotubes formation are (1) the oxide growth at the metal surface due to the interaction of the metal with O^{2-} or OH^- ions [77]. After the formation of a first oxide layer, these anions migrate through the oxide layer reaching the metal/oxide interface where they react with the metal. (2) Metal ion (Ti^{4+}) migration from the metal at the metal/oxide interface; Ti^{4+} cations will be ejected from the metal/oxide interface under application of an electric field that move toward the oxide/electrolyte interface [78]. (3) Field-assisted dissolution of the oxide at the oxide/electrolyte interface. Due to the applied electric field, the Ti–O bond undergoes polarization and is weakened, promoting dissolution of the metal cations. Ti^{4+} cations dissolve into the electrolyte, and the free O^{2-} anions migrate toward the metal/oxide interface, process (1), to interact with the metal [78]. Finally, (4) chemical dissolution of the metal, or oxide, by the acidic electrolyte. Chemical dissolution of TiO_2 in the HF electrolyte plays a crucial role in the formation of nanotubes rather than simple nanoporous structures [78].

3.5.1.1 Chemistry of the process

The process of formation of anodic oxide appears rather complicated, yet a general and simplified model of the chemistry involved is required to understand the process. The outer anodic layer (partly exposed to the electrolyte) has an excess of hydroxyl ions compared to the inner layer and is considered to be $Ti(OH)_4$ [79]. The inner layer, where the dehydroxylation of the film (water releasing) has occurred, is represented as TiO_2. In reality, there is likely to be a concentration gradient across the film, which can be written as $TiO_2.xH_2O$, to represent the inner (dry) and outer (hydrated) anodic oxide.

The reactions which occur at the anode are (i) oxidation of the metal which releases Ti^{4+} ions and electrons, see Eq. (1) [79]:

$$2\mathrm{Ti} \rightarrow 2\mathrm{Ti}^{4+} + 8\mathrm{e}^{-} \quad \textbf{(1)}$$

(ii) combination of Ti^{4+} ions with OH^{-} and O^{2-} species provided by the water.

The following equations (2) and (3) explain the hydrated anodic layer and the oxide layer. The further oxide is produced when the hydrated anodic layer releases water by a condensation reaction, Eq. (4) [79]:

$$\mathrm{Ti}^{4+} + 4\mathrm{OH}^{-} \rightarrow \mathrm{Ti(OH)}_4 \quad \textbf{(2)}$$

$$\mathrm{Ti}^{4+} + 2\mathrm{O}^{2-} \rightarrow \mathrm{TiO}_2 \quad \textbf{(3)}$$

$$\mathrm{Ti(OH)}_4 \rightarrow \mathrm{TiO}_2 + 2\mathrm{H}_2\mathrm{O} \quad \textbf{(4)}$$

At the cathode, hydrogen evolution occurs, according to Eq. (5):

$$2\mathrm{H}^{+} + 2\mathrm{e}^{-} \rightarrow \mathrm{H}_2 \quad \textbf{(5)}$$

The overall process of oxide formation is given by Eq. (6):

$$\mathrm{Ti} + 2\mathrm{H}_2\mathrm{O} \rightarrow \mathrm{TiO}_2 + 4\mathrm{H}^{+} + 4\mathrm{e}^{-} \quad \textbf{(6)}$$

Fluorine ions can attack the oxide and hydrated layer; or, the ions being mobile in the anodic layer under the applied electric field as described by Eq. (7) [80]:

$$\mathrm{TiO}_2 + 6\mathrm{F}^{-} \rightarrow \mathrm{TiF}_6^{2-} + 2\mathrm{O}^{2-} \quad \textbf{(7)}$$

In the initial stages of the anodization process, field-assisted dissolution dominates chemical dissolution due to the relatively large electric field across the thin oxide layer [81]. Small pits formed due to the localized dissolution of the oxide; represented by the (Eq 7), act as pore-forming centers, after which these pits

convert into pores with increasing pore density, uniformly, over the surface. The pore growth occurs due to the inward movement of the oxide layer at the pore bottom (barrier layer) [78]. The Ti^{4+} ions migrating from the metal to the oxide/electrolyte interface dissolve in the HF electrolyte. The rate of oxide growth at the metal/oxide interface and the rate of oxide dissolution at the pore-bottom/electrolyte interface ultimately become equal, after that the thickness of the barrier layer remains unchanged although it moves further into the metal increasing the pore depth [78].

Usually, anodization experiments are carried out in a two-electrode or three-electrode electrochemical cell with titanium or a titanium alloy as the anode, platinum foil as the cathode and in the case of a three-electrode cell with an Ag/AgCl electrode as the reference electrode [22]. A constant potential is applied using a DC power supply, as shown in Figure 5.

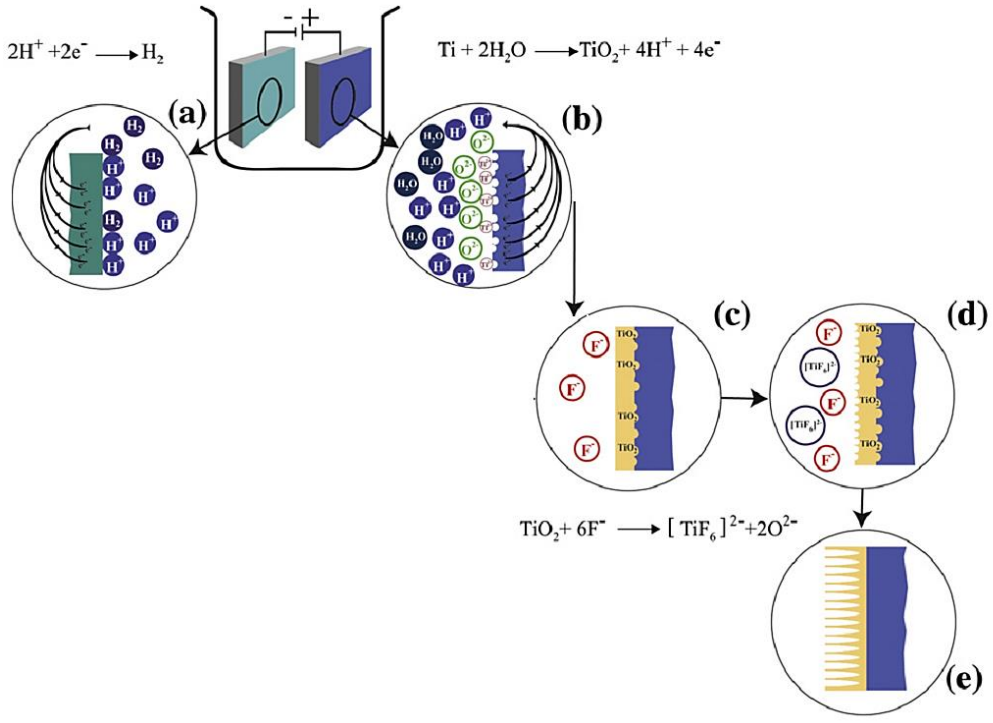

Figure 5: Growth of regular TiO_2 nanotubes: (a) cathodic reaction, (b) anodic reaction, (c) transition state of TiO_2 layer, (d) starting of nanotube formation and (e) titania nanotubes. Adapted from Minagar et al., (2012) [80].

3.5.1.2 Structure and properties of TiO_2 nanotubes

TiO_2 is a semiconductor present in different crystalline forms. The most stable is the rutile and anatase structures. The brookite is much rarer than the first two. Figure 6 shows the crystal structures of TiO_2

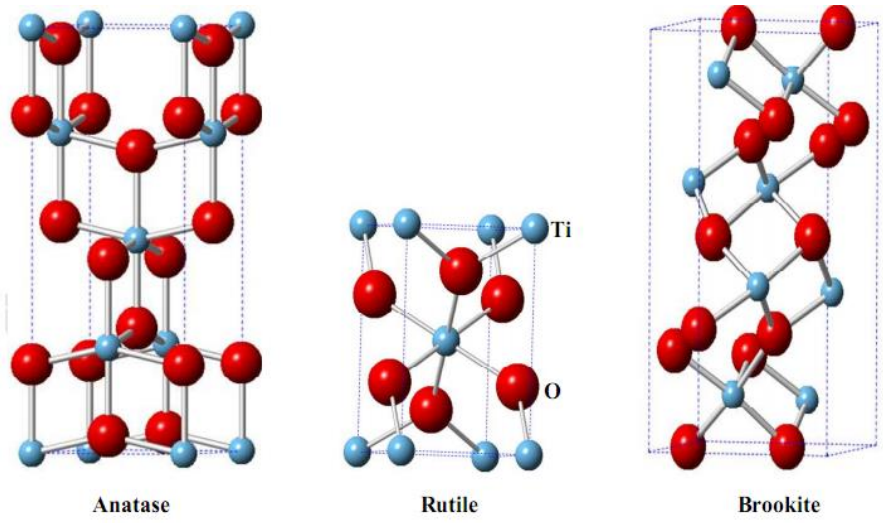

Figure 6: Crystal structure of anatase, rutile, and brookite. Gray sphere: Ti, Red sphere: O. Adapted from Etacheri et al., (2015) [82].

The anatase has a tetragonal structure of theoretical density of 3.893 $g.cm^{-3}$. Beyond 700°C, this structure turns into rutile. Furthermore, anatase has many technological applications due to its high refractive index and its non-absorbance in the visible light. On the other hand, the rutile phase is a quadratic (or tetragonal) mineral with a density of 4.230 $g.cm^{-3}$. The Ti^{4+} cations are surrounded by six O^{2-} anions in octahedral coordination. The length of the Ti-O bond is 1.955 Å on average.

Thus, heat treatments are necessary for the formation of these two phases from the amorphous phase obtained after electrochemical anodization. For the anatase phase, heat treatment should be carried out around 450 °C and to form a mixed phase (80% anatase-20% rutile) the heat treatment should be performed at 550 °C. Above 600 °C, the rutile phase is obtained in the vast majority [83].

3.5.1.3 Nanotube arrays on titanium alloys

Nanotubes had been synthesized using Ti alloys as substrate material. For example, Macak et al., (2007) reported the synthesis of oxide nanotube layers grown on Ti6Al7Nb alloy and TiNb alloy, as is shown in Figure 7 [84].

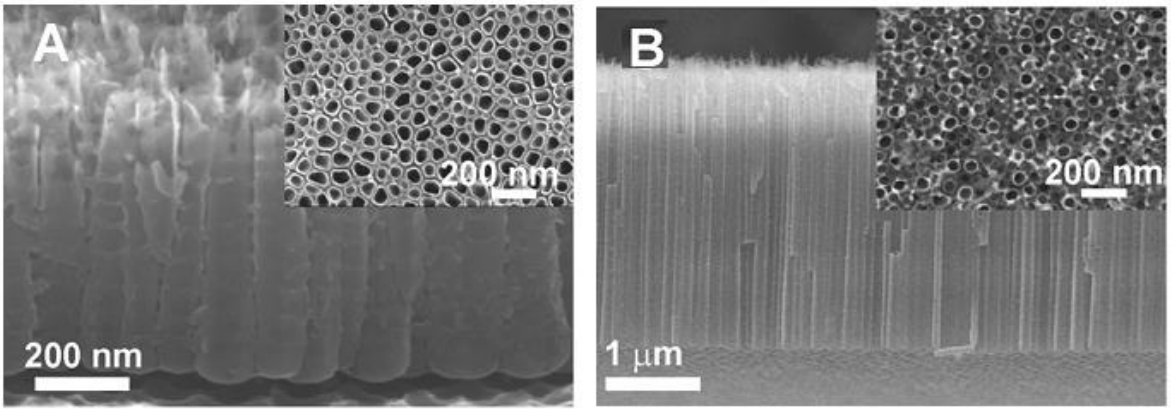

Figure 7: SEM images showing self-organized oxide nanotube layers grown on Ti6Al7Nb alloy (A) and (B), TiNb alloy. The insets show top-views of the nanotube layers. Adapted from Macak et al., (2007) [84].

Most of the Ti alloys used in engineering/biomedical applications show a dual-phase that is α + β microstructure [85]. Therefore, the formation of a uniform nanotubular oxide layer on these Ti alloys cannot be achieved due to the difference in chemistries of these phases [85].

3.5.2 Chemical treatment by acid etching and alkali activation

3.5.2.1 Acid etching

Acid treatment is often used to remove oxide and contamination to obtain clean and uniform surface finishes. Takeuchi et al., 2003 investigated the decontamination efficiency of three acids, $Na_2S_2O_8$, H_2SO_4, and HCl, on the titanium surface and found that HCl was the best decontamination agent because it could easily dissolve the titanium salts and not weaken Ti surface [28].

Acid-etching has been shown to enhance osseointegration greatly [86]. For example, the immersion of titanium implants for several minutes in a mixture of concentrated HCl and H_2SO_4 heated above 100°C (dual acid-etching) was employed to produce a micro-rough surface (see Figure 8). This type of surface promoted rapid osseointegration and maintained long-term success over three years [87]. Similarly, it has been found that dual acid-etched surfaces enhance the osteoconductive process through the attachment of fibrin and osteogenic cells, resulting in bone formation directly on the surface of the implant [88].

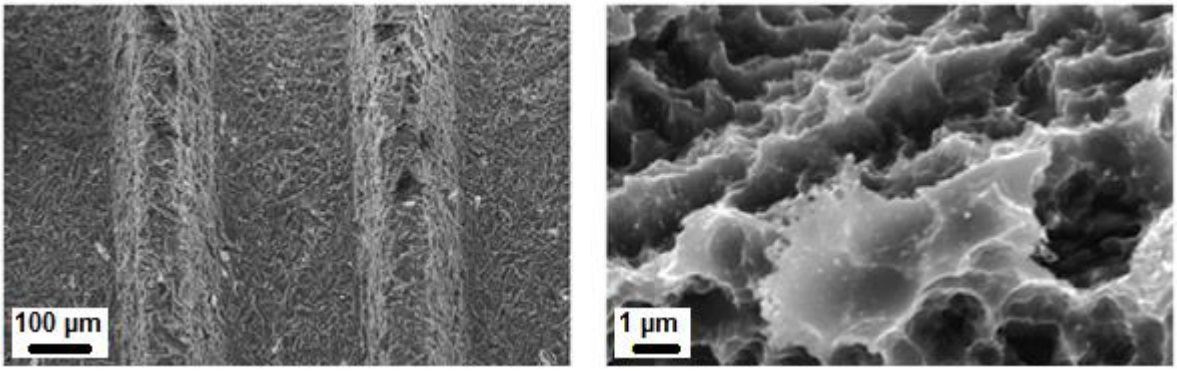

Figure 8: SEM micrographs of an SLA surface on a titanium dental implant (Courtesy of Straumann AG, Switzerland).Adapted from Le Guéhennec et al., (2007) [86].

3.5.2.2 Alkali activation

A simple chemical method was established to induce bioactivity of titanium and its alloys. When Ti alloys were treated with NaOH solution (10 M) and subsequently heat-treated at 60 °C, a thin sodium titanate layer was formed on their surfaces [89]. Thus, the treated samples, immersed in simulated body fluid (SBF), formed a dense and uniform bonelike apatite layer on their surfaces with ion concentrations nearly equal to those of human blood plasma [89].

The structural change on the titanium surface during alkali and heat treatments and the mechanism of apatite formation on the treated surface, of samples immersed in SBF, are described as follows [70].

$$TiO_2 + NaOH \rightarrow HTiO_3^- + Na^+ \quad \textbf{(8)}$$

During the alkali treatment, the TiO_2 layer partially dissolves in the alkaline solution because of the attack by hydroxyl groups. This reaction is assumed to proceed simultaneously with the hydration of titanium [70].

$$Ti + 3OH^- \rightarrow HTiO_3^- + 4e^- \quad \textbf{(9)}$$

$$Ti(OH)_3^+ + e^- \rightarrow TiO_2.H_2O + {}^1/_2\, H_2 \uparrow \quad \textbf{(10)}$$

$$Ti(OH)_3^+ + OH^- \leftrightarrow Ti(OH)_4 \quad \textbf{(11)}$$

A further hydroxyl attack on the hydrated TiO_2 produces negatively charged hydrates on the surfaces of the substrates as follows [70]:

$$TiO_2.H_2O + OH^- \leftrightarrow HTiO_3^-.nH_2O \quad \textbf{(12)}$$

These negatively charged species combine with the alkali ions in the aqueous solution to produce an alkaline titanate hydrogel layer. During the heat treatment, the hydrogel layer is dehydrated and densified to form a stable amorphous or crystalline alkali titanate layer [70].

The process of apatite formation can be interpreted regarding the electrostatic interaction between the functional groups and ions in the fluid. The Ti-OH groups formed on the surface of sodium titanate, after soaking in SBF, are negatively charged and hence, selectively combine with the positively charged Ca^{2+} ions in the fluid to form calcium titanate, as shown in Figure 9 [90].

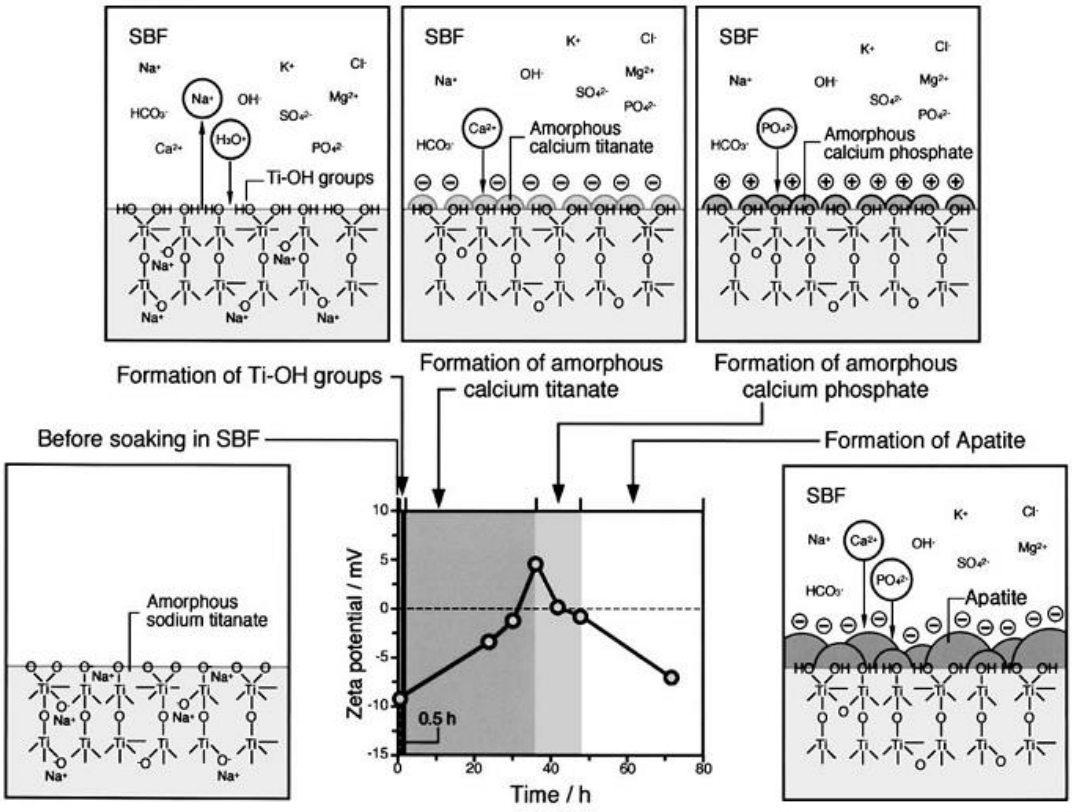

Figure 9: Schematic representation of the relationship between changes in surface structure and the potential of amorphous sodium titanate in the apatite formation process on its surface, in an SBF solution. Adapted from Kokubo et al., (2003) [90].

As the calcium ions accumulate on the surface, it gradually gains an overall positive charge. Then, the positively charged surface combined with negatively charged phosphate ions forms amorphous calcium phosphate which spontaneously is transformed into apatite. The apatite is a stable phase in the body environment [90].

3.6 Electrochemical characterization

Electrochemical characterization is a powerful technique used to understand the relevant reaction mechanisms involved in charge transfer, mass transport, electrolyte transport, electron transport, and so on [91].

Several methods of electrochemical characterization are used in this study: open circuit potential measurement, polarization curve graph (and Tafel extrapolation) and electrochemical impedance spectroscopy (EIS). Therefore, they will be explained below.

3.6.1 Measurements of open circuit potential (OCP)

Measurements of the electrochemical potential are one of the most basic measurements in electrochemistry. The potential of a metal in an aqueous solution is a function of the inherent reactivity of the metal and the oxidizing power of the solution [92]. The goal of potential measurements is to measure the potential of the specimen without affecting, in any way, electrochemistry reactions on the specimen surface. It is necessary to make the potential measurements relative to a stable reference electrode so that any changes in the measured potential can be attributed to changes at the specimen/solution interface [93]. A reference electrode requires that its potential is reproducible and stable. When a suitable reference electrode is used, the potential of the specimen or working electrode can be controlled reproducibly, and any changes in the measured potential during the test can be related with confidence to changes in working electrode potential [93]. An unstable or contaminated reference electrode is unacceptable and will result in incorrect results.

3.6.2 The principle of potentiodynamic polarization and extrapolation of Tafel

Potentiodynamic polarization is a destructive technique where the potential of the electrode is varied at a selected rate, and the resulting current is measured. In this test, the potential is varied from slightly cathodic (or anodic) to anodic (or cathodic) region to know the reactivity of the system close to its corrosion potential or OCP. Also to other potential values which the interface could take during modification of the medium (for example, the conditions of use of the material or the formation of corrosion zones).

The plot of the current vs. voltage curve of a system is called the polarization curve. The representation usually used in the context of the study of corrosion consists in plotting the absolute value of the current density (i) in logarithmic scale (obtained by dividing the current measured by the exposed surface) as a function of the applied voltage. This type of curve gives us information as the passive and active region of the system, as well as the corrosion potential (E_{corr}), and corrosion current density (i_{corr}).

When recording a polarization curve, the corrosion potential is marked by a sharp drop in current on both anodic (right part) and cathodic (left part) branches, thus forming a “peak” directed down.

Moreover, it is possible to plot Tafel lines (linearity zone of current or current density in a defined range of potentials) as presented in Figure 10. This method is strictly applicable only if the linear part covers at least one decade of current. In this case, the intersection of these lines at the corrosion potential gives the value of the corrosion current density, which is directly proportional to the corrosion rate — the lower the icorr, the better corrosion resistance of the material in the medium under study.

The most basic procedure for experimentally evaluating corrosion current (I_{corr}) is by Tafel extrapolation [94]. It is possible to plot Tafel lines, as presented in Figure 10. The intersection of these lines at the corrosion potential gives the value of the corrosion current density, which is directly proportional to the corrosion rate — the lower the i_{corr}, the better corrosion resistance of the material in the medium under study.

This method requires the presence of a linear or Tafel section in the polarization curve (Figure 10). A potential scan of approximately ±30 mV around corrosion voltage (E_{corr}) is required to determine if a linear region of at least one decade of current is present, such that a reasonably accurate extrapolation can be made to the E_{corr} [95].

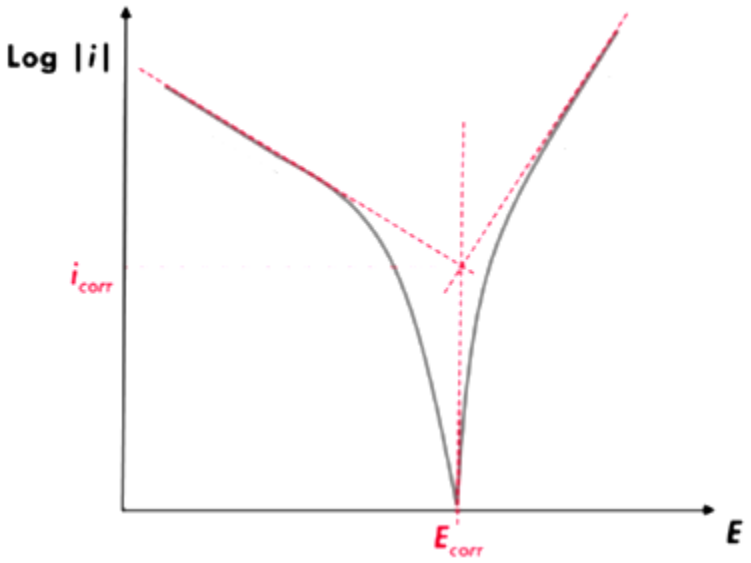

Figure 10: Schematic representation of the Tafel extrapolation method.

In many cases, a linear region may not be observed even in the cathodic branch. This behavior can be a result of corrosion under diffusion control or, on decreasing the potential, entering into the diffusion control region, or even that the nature of the interface changes with changing potential.

3.6.3 Electrochemical Impedance Spectroscopy (EIS)

While potentiodynamic polarization provides a very informative approach for the corrosion behavior of metals, it is nevertheless, destructive and only informs about the global electrochemical processes taking place at the interface, the weight of the slowest processes is preponderant.

On the other hand, the EIS is a technique non-destructive, and it is based on the excitation of the working electrode by a low amplitude alternating current (AC) voltage (typically 10 - 20 mVrms) at several discrete frequencies logarithmically distributed along several decades. This principle is illustrated in Figure 11.

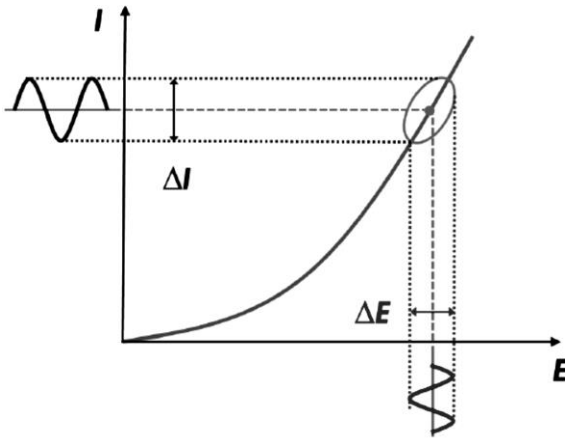

Figure 11: Schematic representation of the principle of measurements by EIS.

The alternating current (AC) voltage, applied to an electrochemical cell, and the current response are shown by equations 13 and 14.

$$E(t) = E_0 \sin(\omega t) \quad \textbf{(13)}$$

$$I(t) = I_0 \sin(\omega t + \phi) \quad \textbf{(14)}$$

Where E_0 is the signal amplitude, ω is the radial frequency such as ω= 2πf, f the frequency (in Hz), ϕ is the phase shift relative to the potential input and, I_0 is the amplitude of the current.

Following this and using Ohm's law, the impedance is determined according to equation 15. Thus, the impedance can be defined as the measure of an electrochemical system's tendency to resist (or impede) the flow of the alternating electrical current [96].

$$Z(\omega) = \frac{E_0}{I_0} \exp(j\Phi) = |Z| \exp(j\Phi) \quad \textbf{(15)}$$

Where |Z| is the impedance modulus of a complex number and can be represented as a sum of real and imaginary parts of the impedance.

$$Z(\omega) = |Z|(\cos\Phi + j\sin\Phi) = Z_r(\omega) + jZ_i(\omega) \quad \textbf{(16)}$$

As the various elementary processes evolve at different speeds, the response of the system dissects the overall electrochemical process. Thus, as a general appreciation of the method, high frequencies most often correspond to capacitive phenomena (non-faradic), medium frequencies to charge transfers (faradic) and low frequencies to diffusion phenomena.

Two types of complementary graphic representations are used to analyze the impedance measurements. The impedance modulus (|Z|), the phase (ϕ), and the frequency (ω) are plotted on what is known as a Bode plot, such as in Figure 12(b) (Bode magnitude plot) and Figure 12(c) (Bode phase plot). The |Z| and ϕ information can also be displayed in a complex plane plot called the Nyquist plot, such as that in Figure 12(a). It is a plot of the imaginary part of the impedance (Z´´ or Zim) versus the real part of the impedance (Z´ or Zre) and where the frequency never explicitly appears; it must be obtained from the raw data point [97].

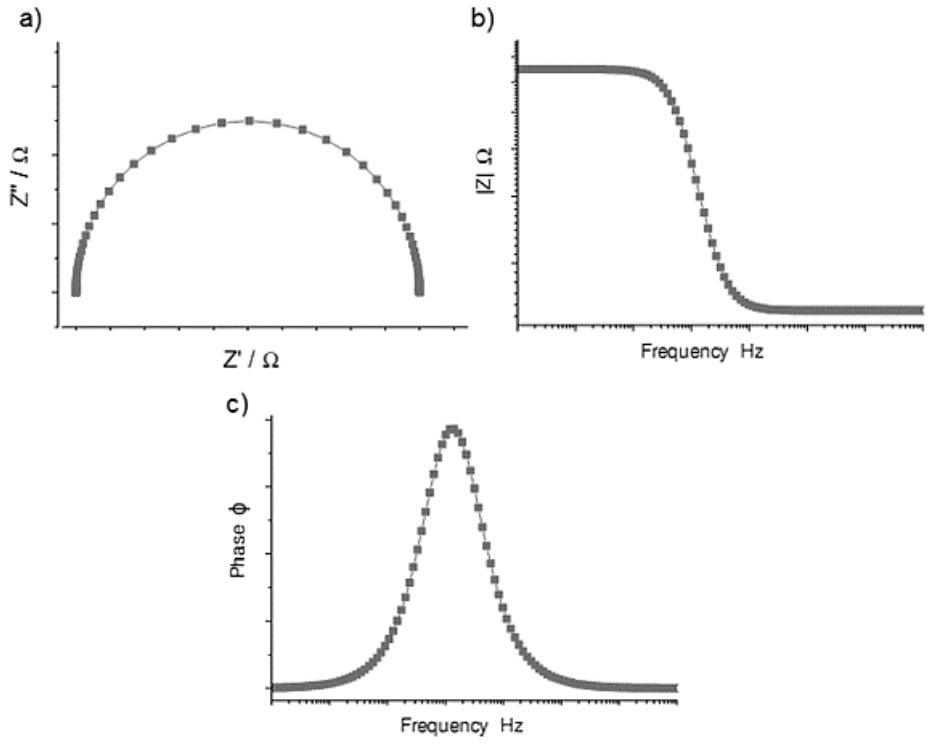

Figure 12: Nyquist plot (a), Bode magnitude (b) and Bode phase angle (c).

Both plots show precisely the same data but plotted in a different format. The Bode plot shows the frequency directly, and the whole frequency range is identifiable. However, impedances at low frequencies may be difficult to identify from the Nyquist plot [98].

As electrochemical systems often behave like simple electrical circuits, it is possible to identify them by the EIS data analysis. For example, in a simple resistor, the current sine wave is exactly in phase with the voltage sine wave. Thus, the phase angle of a resistor's impedance is 0°. For an ideal resistor, this is true at all frequencies. Therefore, the Bode magnitude plot is just a horizontal straight line, and the Bode phase angle is always zero [98]. In the Nyquist plot, the imaginary part of the impedance will also be zero, and the resistor's impedance lies on the real axis.

The capacitor is another simple electrical circuit element. For a pure capacitor, the current is 90° out of phase with the voltage. The Bode magnitude

plot for a capacitor is a straight line with a slope of –1 with high impedance at low frequency. Because the phase shift of a capacitor is always 90°, the Bode phase plot is a horizontal line at –90° throughout the entire frequency range [99]. The Nyquist plot for an ideal capacitor lacks essential information. The intercept on the real axis at high frequencies is the resistance of the electrolyte between the working electrode and the reference electrode, which is indistinguishable on this plot. As well, the real component of the impedance is zero, and the total impedance is equal to the imaginary impedance.

In electrochemical systems, examples of the resistor are the resistance of the electrolyte in the electrochemical cell, the resistance of a porous layer and the polarization resistance. On the other hand, examples of a capacitor are a metal coated with a passive film, immersed in an electrolyte and the metal-electrolyte interface knows as the “double layer”.

3.6.3.1 Equivalent Circuit Models and Analysis of Electrochemical Impedance

EIS data commonly can be modeled by an equivalent electrical circuit (EEC). Most of the circuit elements in the model are constructed by combining electrical elements in series and/or in parallel, such as resistors (R), capacitors (C), and inductors (L).

The interpretation of the impedance results requires an appropriate model and knowledge about chemical-physical processes that occur in the metal/electrolyte interface [100]. The typical circuit elements, the equation for their current versus voltage relationship, and their impedance are listed in Table 2.

Table 2: Common electrical elements.

Component	Current vs. Voltage	Impedance
Resistor	$E = IR$	$Z = R$
Inductor	$E = L\, di / dt$	$Z = j\omega L$
Capacitor	$I = C\, dE / dt$	$Z = 1 / j\omega C$

When modeling an electrochemical system as an electrochemical circuit, a potential waveform is applied across the circuit, and a current response to the frequency signal generates impedance data. Thus, the impedance data is related to a phase shift angle and a variation in potential and current amplitudes. This technique is a straightforward approach for analyzing the corrosion behavior of a metal [101].

For instance, Figure 13 shows two schematic electrical circuit models can be used to represent electrochemical systems. For a bare, corroding metal in an electrolyte solution (Fig. 13(a)), only the solution resistance (R_s), polarization resistance (R_p) and the capacitor (C), associated with the double layer capacitance (Cdl) of the metal/electrolyte interface, are needed in a simple circuit [101].

On the other hand, if the electrochemical system is diffusion control (Fig. 13(b)), a diffusion impedance (ZD) is incorporated in the circuit [101].

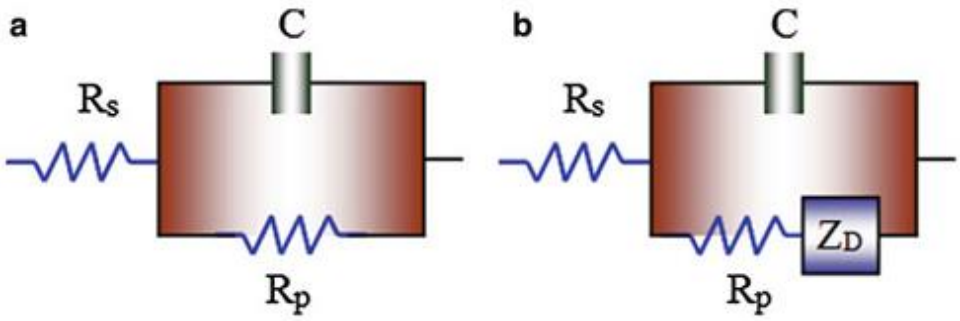

Figure 13: Schematic electrochemical impedance circuits. (a) Charge control. (b) Diffusion control, adapted from Perez (2016) [101].

When the electrochemical responses are not ideal and cannot be represented by a connection of simple R-C-L elements, the Constant Phase Element (CPE) is used. CPE is a parameter usually used in fitting EEC in electrochemical impedance spectroscopy. The impedance of a constant-phase element is defined as [102]:

$$Z = [Q(j\omega)^{\alpha}]^{-1} \quad \textbf{(17)}$$

The CPE parameters α and Q are independent of frequency. When the electrode shows a capacitive behavior, α is equal to 1, Q has units of a capacitance (μF/cm^2). When α< 1, the system shows behavior that has been attributed to surface heterogeneity [103] or to continuously distributed time constants for charge-transfer reactions. When α is 0.5, it indicates an infinite Warburg impedance.

The CPE parameters α and Q can be obtained from graphical methods [104]. The parameter α is calculated from the slope of the log |Zi | vs. log f curve [104]:

$$\alpha(f) = \left|\frac{d\ log|Z_i(f)|}{d \log f}\right| \quad \textbf{(18)}$$

and Q is obtained from:

$$Q = -\frac{1}{Z_i(f)x(2\pi f)^{\alpha}} x\ sin\left(\frac{\alpha\pi}{2}\right) \quad \textbf{(19)}$$

The parameters α and Q obtained by graphical evaluation of equations (18) and (19) are the same as would be obtained by regression analysis [104].

On the other hand, two different equations were developed for estimating effective capacitance from Constant-Phase-Element (CPE) parameters [103]. If the CPE behavior is assumed to be associated with surface distributed time constants for charge-transfer reactions (time-constant distribution along the electrode surface), then it is possible to apply the equation derived by Brug et al. to calculate the effective capacitance associated with the CPE [104]:

$$C_{eff}(Brug) = Q^{\frac{1}{\alpha}}(R_e^{-1} + R_t^{-1})^{\frac{\alpha-1}{\alpha}} \quad \textbf{(20)}$$

where R_e is the electrolyte resistance and R_t the charge transfer resistance.

The second equation (normal distribution of time constants) is described by the relation of Hsu-Mansfeld [25,103]:

$$C_{eff}(H-M) = Q^{\frac{1}{\alpha}}(R_t)^{\frac{1-\alpha}{\alpha}} \quad \textbf{(21)}$$

thus, CPE impedance response can be associated with an effective capacitance, the dielectric constant or the film thickness may be obtained from [105]:

$$C_{eff} = \frac{\epsilon \cdot \epsilon_0}{\delta} \quad \textbf{(22)}$$

where δ is the film thickness, ϵ is the dielectric constant, and ϵ_0 is the permittivity of vacuum with a value of $\epsilon_0 = 8.8542 \times 10^{-14}$ F/cm [105].

3.6.4 Corrosion of ultrafine-grained materials obtained by severe plastic deformation

Development of corrosion-resistant metallic materials for advanced applications is a current task for modern materials science with attention to both effectiveness and security of the cutting-edge technologies and environmental security taking into consideration risks of global warming and industrial disasters. The problem of utmost importance is the development of new functional materials with reasonable corrosion resistance to be used in new-generation applications.

Grain refinement by SPD processing accompanies other microstructural changes in a complicated way. These changes include phase transformation [20], redistribution of impurity and solute elements [106], the morphology change of

precipitation by partial dissolution and physical fragmentation [107], residual dislocation density [108], texture [109], and so on. Effect of these changes is superimposed on grain size effect on corrosion.

Titanium alloys have high corrosion resistance. Several factors influence the corrosion resistance in titanium alloys processed by SPD. Particularly, basal planes of CP Ti offer higher corrosion resistance independently of grain size. On the other hand, corrosion studies for titanium alloys after severe plastic deformation have been minimal [24].

Deformation processing imparts significant physical and chemical changes to the material in addition to the grain refinement that, in turn, considerably affects the demonstrated functional properties, including corrosion behavior. Thus, systematic investigations of corrosion stability of SPD nanostructured materials and revealing its dependence on nanostructural parameters remain as one of the most challenging tasks in modern materials science [67].

3.7 Osseointegration

Osseointegration, defined as a direct structural and functional connection between ordered, living bone and the surface of a load-carrying implant, is critical for implant stability and is considered a prerequisite for implant loading and long-term clinical success of endosseous implants [110]. Otherwise, the formation of fibrous tissue around the implant could lead to rejection of the prosthesis.

The osseointegration must be linked to bioactivity. A material with proper osseointegration is a bioactive material. When this material is immersed in a physiological fluid, it spontaneously forms on its surface an apatite layer, or specifically hydroxyapatite [70].

Hydroxyapatite (HAp) is an inorganic compound made of calcium phosphate and hydroxyl groups, with a stoichiometry of ($Ca_{10}(PO_4)_6(OH)_2$) and a hexagonal crystal structure. Natural HAp is the primary mineral constituent of hard human tissues such as bones and teeth. It has the same crystal structure, but a

stoichiometry slightly different from the synthetic one since some calcium ions can be exchanged by other metallic ions, such as magnesium or sodium [111]. The production of synthetic HAp has acquired a great significance in recent years due to its excellent properties of biocompatibility, bioactivity, osteoconductivity, and osteoinductivity [47, 48].

In this context, some experiments that will be carried out as part of this project have as a particular objective the study of bioactivity specifically by the growth of HAp.

4 MATERIALS AND METHODS

Figure 14 shows a schematic representation with the most important experimental methodologies used in this work. These experimental methodologies will be better explained below.

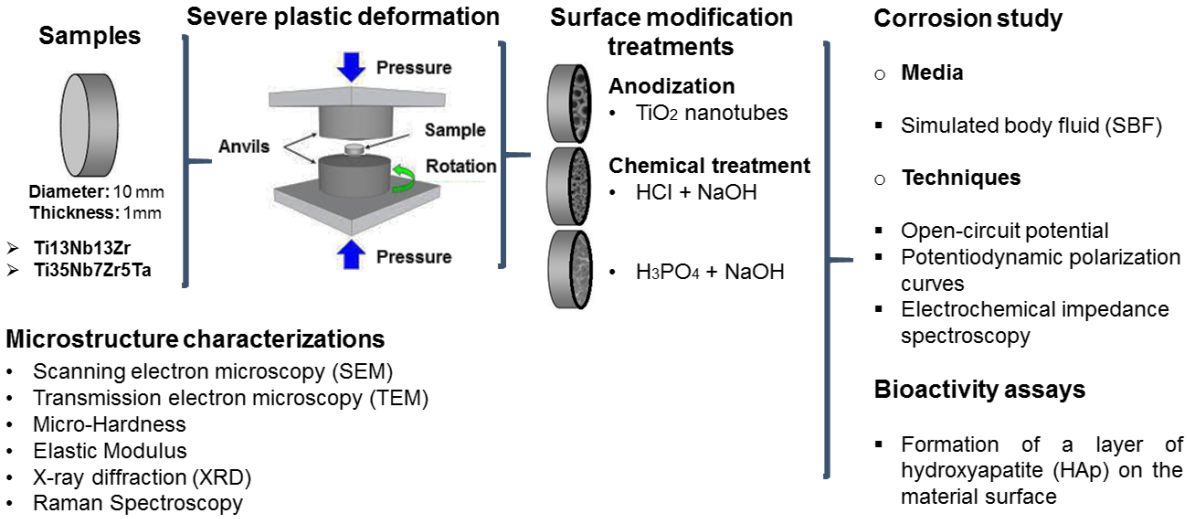

Figure 14: Flow diagram of the experimental procedures used in this doctoral project (read from left to right).

4.1 Preparation of samples

The titanium alloys used in this study, Ti13Nb13Zr (α+β) and Ti35Nb7Zr5Ta (β), were purchased from ERCATA GmbH, Development Co., Ltd., Germany. Bars of the alloys were cut in disks of 10 mm of diameter and 1 mm of thickness. In order to reduce the modulus of elasticity [113] and homogenize microstructure [114], the specimens were vacuum-sealed in a quartz tube and then heat-treated above the β transus temperature for one hour and then fast cooled in water according to the procedure used by Majumdar et al. (2011) [115]. The β transus temperatures for Ti13Nb13Zr and Ti35Nb7Zr5Ta are 735 °C and 750 °C, respectively [78, 79].

In this work, all the samples of each alloy were initially thermally treated. The phases present in the samples after thermal treatment were identified by confocal laser microscopy (CLM), scanning electron microscopy (SEM), transmission electron microscopy (TEM) and X-ray diffraction (XRD). Moreover, the thermally treated samples were also characterized by micro-hardness studies and elastic modulus.

4.2 High-Pressure Torsion (HPT) deformation

The deformation by HPT of the samples of Ti13Nb13Zr and Ti35Nb7Zr5Ta was performed at room temperature. The disks were processed under pressures of 1.0 and 4.5 GPa. Three turns were applied using a rotation speed of 3 rpm. Figure 15 shows the Universal Testing Machine (EMIC®) and the HPT accessory used for the HPT assays.

Figure 15: Universal Testing Machine EMIC and HPT accessory.

The phases present in the samples after deformation by HPT were identified by confocal laser microscopy (CLM), scanning electron microscopy (SEM), transmission electron microscopy (TEM) and X-ray diffraction (XRD). Moreover,

the samples deformed were also characterized by micro-hardness studies and elastic modulus.

4.3 Surface modification treatments

The surface modification treatments that will be described below were applied to the titanium alloys (Ti13Nb13Zr and Ti35Nb7Zr5Ta) deformed by HPT (see section 3.5) as well as to non-deformed samples (ND). The microstructure of the samples, with surface modifications, was evaluated by SEM, analyzed chemically by energy dispersive spectroscopy (EDS) and by Raman's spectroscopy. Phase identification was performed by XRD.

4.3.1 Electrochemical anodization

The conditions used in the electrochemical anodization were selected according to the best results reported for pure titanium by Hilario et al. (2017) [118].

4.3.1.1 Surface preparation

Initially, the surface of samples was polished successively with SiC abrasive paper of P320 (grain size 46 μm), P600 (26 μm), P1200 (15 μm) and P2400 (10 μm) grades. Then, the samples were also polished with a colloidal silica suspension of 0.03 μm, dispersed on a polishing cloth tender, and cleaned ultrasonically in distilled water, ethanol, and acetone for 10 minutes in each case. Finally, the samples were rinsed with distilled water and acetone and dried with compressed air. This surface preparation was carried out just before anodization assays, and in order to ensure orderly growth of the nanotubes on the sample surface [25].

4.3.1.2 Anodization

The TiO_2 nanostructures were obtained by anodization of the polished and cleaned samples. The anodization was then carried out in an electrochemical cell with a conventional two-electrode arrangement. The cell used during this work

allowed the simultaneous anodization of four samples. The disks of the samples embedded in a Teflon holder were employed as the working electrodes (each sample exposed a superficial area of 0.283 cm^2 to the electrolyte), the counter electrode was a cylindrical platinum grid (placed 3 cm from the working electrodes surface). The samples were connected to the positive terminal (+) of the power supply (TCR - Electronic Measures Inc.), and the counter electrode was connected to an amperemeter which was connected to the negative terminal (-) of the power supply. The diagrammatic representation of the experimental assembly is shown in Figure 16(a). Figure 16(b) shows a photograph of the electrochemical cell used in this work.

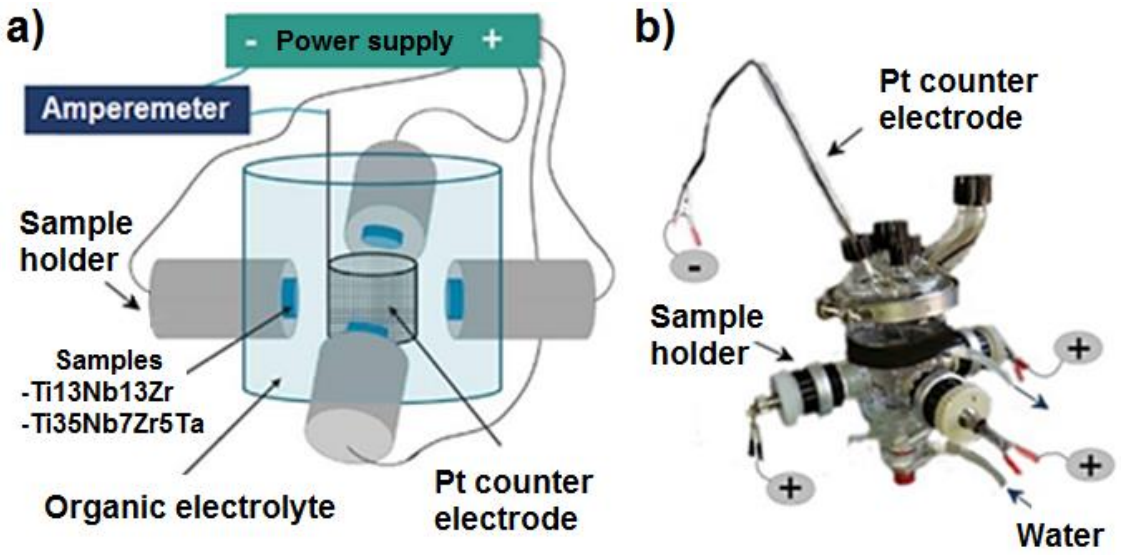

Figure 16: (a) Diagrammatic representation of the assembly with four working electrodes and one counter-cylindrical electrode of Pt connected to a power supply. (b) Photograph of the electrochemical cell used in this work for anodization experiments. Adapted from Hilario (2017) [25].

The anodization experiments were performed at 25 °C for one hour, in an organic electrolyte consisting of glycerol, containing 25 vol% of water and 0.25M of NH_4F. A constant voltage of 20 V was applied during the experiments.

After anodization, samples were first rinsed with distilled water, then with acetone, and finally dried with compressed air.

Finally, the samples were annealed in air at 550 ºC for 2 h to crystallize TiO_2 nanotubes into a mix of anatase and rutile phases.

4.3.2 Chemical treatment by acid etching and alkali activation

The chemical treatment consisted of an acid etching followed by the alkaline activation. The acid attack was carried out with 37% hydrochloric acid (HCl) or 85% phosphoric acid (H_3PO_4) in order to define which acid favors more the growth of hydroxyapatite.

Initially, 150 ml of concentrated acid were transferred to a 300 ml beaker. The solution was then maintained, with the help of a heating plate, at 60 °C or 80 ºC, during the attacks with HCl or H_3PO_4, respectively. When the temperature stabilized, the samples were immersed in the solution for 30 minutes. Finally, the samples previously attacked with acid were immersed in a NaOH solution (10 M) and then kept at 60 °C into an incubator, Memmert UF55, for 24 h. Finally, the samples were left in a desiccator to dry.

4.4 Electrochemical characterization

Samples non-deformed and deformed by HPT in the as-polished condition and those with surface modifications were characterized electrochemically. All experiments were performed in triplicate. Simad® software developed at the Laboratory of Interfaces and Electrochemical Systems (LISE) was used for the analysis of EIS data.

4.4.1 Experimental assembly

An experimental assembly of four electrodes and a potentiostat (GAMRY Instruments, Reference 600 +) were used to perform the electrochemical characterizations. The sample disk embedded in a Teflon holder was employed as the working electrode (a surface of 0.283 cm^2 was exposed to the electrolyte), the reference electrode was a saturated calomel electrode (SCE, 0.242 V vs. SHE at 25 ºC), which was connected in parallel to a platinum wire exceeded by a capacity

of 1 μF. The platinum wire is used in order to avoid capacitive and inductive artifacts, originated in stray capacities that can be present in the impedance measurements [119]. The counter electrode was a flat platinum mesh placed about 3 cm from the working electrode surface. A schematic representation of the experimental configuration just described is shown in Figure 17.

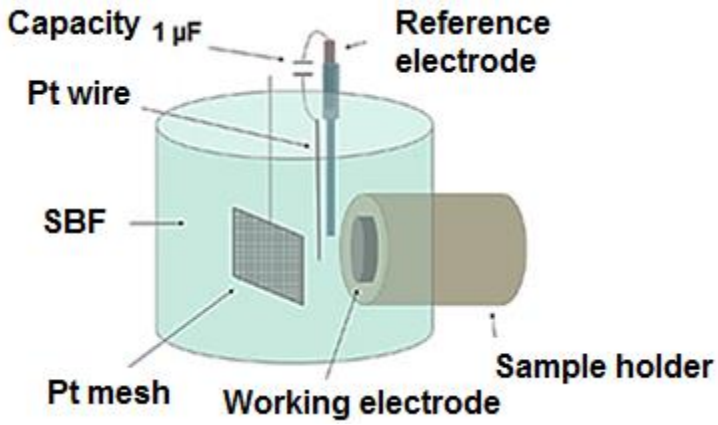

Figure 17: Schematic representation of the experimental assembly for the electrochemical characterization of the alloys Ti13Nb13Zr and Ti35Nb7Zr5Ta. Adapted from Hilario (2017) [25].

The electrolyte solution of simulated body fluid (SBF) was prepared according to the detailed protocol proposed by Kokubo et al.,2006 [120] and the ISO 23317: 2014 standard. The pH of the solution was adjusted to 7.40. The final composition of the SBF is shown in Table 3.

The experimental assembly was placed inside a Faraday cage (steel box) connected to earth ground. It reduces current noise picked up by the working electrode and voltage noise picked up by the reference electrode. Additionally, the electrochemical characterizations were performed in dark ambient, thus reproducing physiological conditions.

Table 3: Ion concentrations of simulated body fluid (SBF). Adapted from Kamalian et al. (2012) [121].

Ion	SBF (mmol/l)
Na^{+}	142.0
K^{+}	5.0
Mg^{+2}	1.5
Ca^{+2}	2.5
Cl^{-}	147.8
HCO_3^{-}	4.2
HPO_4^{-2}	1.0
SO_4^{-2}	0.5

4.4.2 Protocol and measurement sequence

For each sample, the Open Circuit Potential (OCP) was recorded during 1 h of immersion in the electrolyte. Next, the impedance spectroscopy measurements were recorded on steady-state OCP with a frequency range of 20 kHz to 20 mHz. The amplitude of the disturbing sinusoidal signal was 10 mVrms (amplitude large enough for the output signal to be easily measured, but also to satisfy the criterion of linearity). Finally, the corrosion resistance was assessed through potentiodynamic polarization curves recorded in a potential range of -30 mV to +1.50 V relative to the OCP, with a scanning speed of 0.20 mV s^{-1}.

4.5 Bioactivity assays

The bioactivity assays were performed on the samples deformed by HPT in the as-polished condition and on those with surface modifications, as well as on samples non-deformed. All experiments were performed in triplicate.

In order to characterize the bioactivity of the titanium alloy used in this work, the amount of hydroxyapatite (HAp) spontaneously deposited on the surface of the

samples, when they were immersed in SBF, was measured according to the protocol reported by Kokubo et al., 2006 [120]. The in vitro formation of HAp is an indicator of the in vivo bioactivity of a material surface.

The samples were immersed in 30 mL of simulated body fluid (SBF) at 37 °C for different times (1, 7 or 14 days) into an incubator, Memmert UF55. The pH of the solution was adjusted to 7.40. To avoid precipitation problems of Ca/P compounds, the active surface of the sample tested was placed perpendicular to the bottom of the container, as shown in Figure 18.

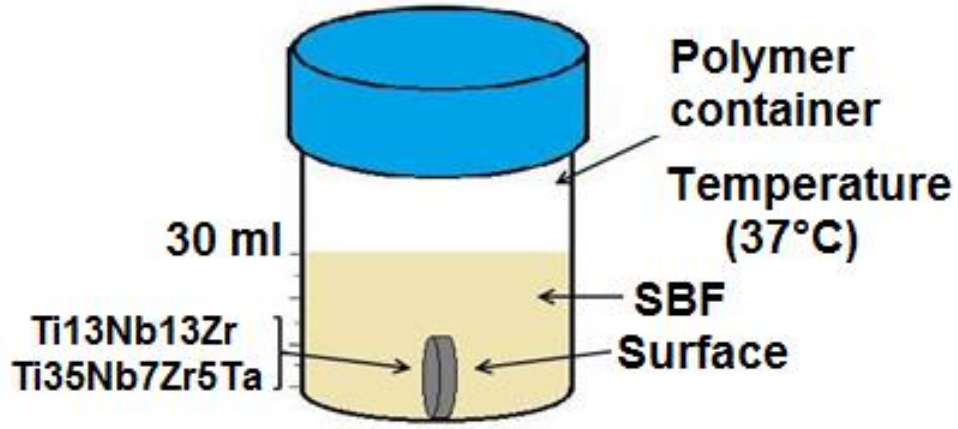

Figure 18: Schematic representation of the experimental assembly used to bioactivity assays.

After the immersion time, the samples were removed from the solution, rinsed with distilled water and dried in a desiccator. The apatite formation was then evaluated by Scanning electron microscopy SEM-FEG observations, chemical analysis by energy dispersive spectroscopy (EDS), X-ray diffraction (XRD), Raman spectroscopy and also weighing the samples before and after the immersion.

4.6 Methods of characterization of samples

The methods used to the mechanical and microstructural characterization of samples will be mentioned below. Samples polished and those with surface

modifications, as well as non-deformed and deformed by HPT, were mechanical and microstructural characterized.

4.6.1 Mechanical characterization

4.6.1.1 Micro-Hardness studies

The hardness of samples deformed by HPT and those non-deformed was determined by the Vickers microhardness tests (HV) using the microdurometer Stiefelmayer shown in Figure 19(a). Vickers microhardness tests were performed at a load of 300 g for 15 s on the polished cross-sections of samples. Microhardness mappings were constructed from hardness measurements along over several samples' radii. The measurements were made in a straight line from center to edge of specimens at 1 mm intervals. They were also made in the other quadrants of the sample surface, as is shown in Figure 19(b).

The results showed in mapping are expressed as the mean of the hardness values obtained at each interval.

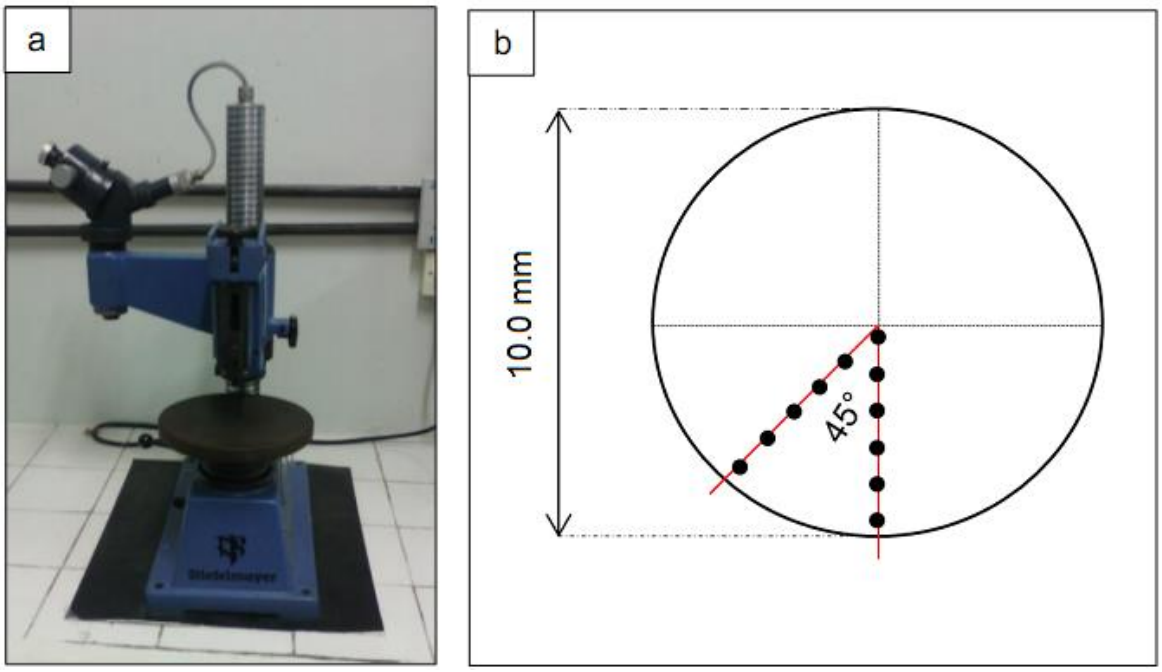

Figure 19: (a) Vickers hardness tester; (b) Scheme of the positions of the hardness measurements.

4.6.1.2 Elastic Modulus

The elastic modulus of deformed and not deformed samples (disks of 10 mm of diameter and 1 mm of thickness) was measured according to the Pulse excitation technique (ASTM E1876) [122]. This technique consists of determining the elastic modulus of a material according to the natural frequency of a sample of regular geometry. These frequencies are excited by a short mechanical impulse, followed by the acquisition of the acoustic response using a microphone [123]. Figure 20 shows the system used in the measurements of elastic modulus.

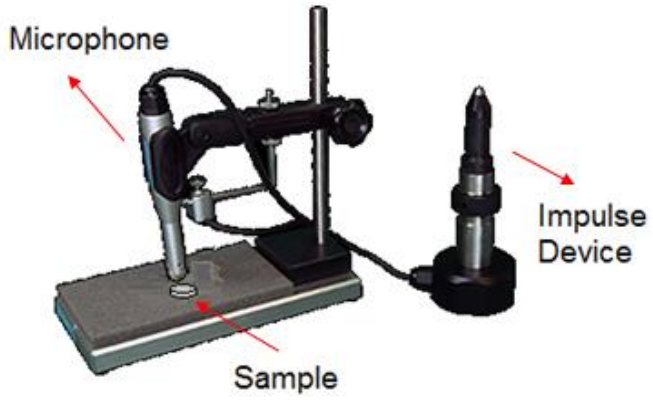

Figure 20: Equipment used for the measurements of the elastic modulus.

The experiments were performed in triplicate, and the results are expressed as mean of triplicates ± standard deviation.

4.6.1.3 Confocal laser microscopy

Confocal laser microscopy (CLM), is a powerful technique that allows enhanced optical resolution and the reduction of background information away from the focal plane (that leads to image degradation) [124]. A microscope LEXT OLS4000 by Olympus was used during the experiments in order to characterize polished samples.

Samples of Ti13Nb13Zr analyzed by CLM were ground in a multistep process using SiC abrasive paper (320, 400, 600, 800, 1200, and 2000 grit). After

grinding, Keller's reagent (or Kroll's reagent for samples of Ti35Nb7Zr5Ta) was used to etch the samples [20,125].

4.6.1.4 Scanning electron microscopy

The microstructural characterization of the samples was examined by scanning electron microscopy (SEM), in a Philips XL30 FEG equipped with energy-dispersive spectroscopy (EDS) (OXFORD – LINK ISIS 300). The morphology of the anodized TiO_2 nanotubes was determined using a FEG-SEM Zeiss Ultra 55, equipped with a Gemini column.

4.6.1.5 Transmission electron microscopy

Conventional transmission electron microscopy and Orientation-phase mapping were accomplished by transmission electron microscopy (TEM) using an FEI TECNAI G2 operated at 200 kV. This microscope is equipped with an orientation and phase mapping precession unit NanoMEGAS (model ASTAR) and with a Digistar P1000 unit. The recently developed technique based on transmission electron microscopy, called ASTAR, makes use of electron-beam (in precession mode or not) together with spot diffraction pattern recognition, allowing to perform Automated Crystal Orientation Mapping (ACOM) in micro- or nanoprobe mode. ACOM-TEM opens the opportunity of acquiring reliable orientation/phase maps with a spatial resolution that can go down to the nm range. In short, the ACOM-TEM consists in scanning the electron beam (in precession or not) in the nanoprobe mode on a specimen area, thus collecting, by a CCD cam, thousands of electron diffraction spot patterns to be subsequently indexed automatically through a template matching. In fact, and very important, ACOM-TEM closes the gap between EBSD in SEM and bright field (BF)/dark field (DF) in TEM by providing full orientation maps with nanometer resolution and even materials severely plastic deformed (SPD), e.g., by ECAP or HPT, can be reliably analyzed. When SPD is performed, problems can arise when observations by EBSD are carried out, because of the Kikuchi lines, used by any EBSD system or in the TEM,

are very sensitive to the crystal orientation, and they rapidly disappear if the diffracting volume suffers distortions induced by high dislocation densities [20].

The samples analyzed by TEM were thinned down to 10 µm by a Gatan Dimple Grinder (model 656) using diamond polishing paste and alumina suspension. The final stage of sample preparation was ion milling using a Gatan Precision Ion Polishing System (model 691) under conditions in which damage is avoided in the structure during thinning (2.5 keV at the initial stage of polishing and 1.6 keV at the final stage) [20].

4.6.1.6 X-ray diffraction

Within this study, X-ray diffraction (XRD) were used to characterize crystalline phases in the deformed surfaces and the phases in TiO_2 nanotubes. Two different diffractometers were used in this investigation. The first X-ray diffractometer is a Rigaku ME210GF2 with a diffracted beam monochromator that uses CuKα radiation (λ = 1.5406 Å) and operates at 40 kV and 30 mA. Diffraction was recorded for angles of 2θ between 30° and 90°, with a step from 0.033° to 0.067°.

The second XRD measurements were made on a PANalytical X'Pert Pro MPD diffractometer/goniometer with Bragg-Brentano geometry, equipped with a diffracted beam monochromator using CuKα radiation (λ = 1.5418 Å) and operating at 45 kV and 40 mA. Diffraction was recorded for angles of 2θ between 10° and 90°, with a step from 0.033° to 0.067°.

4.6.1.7 Raman Spectroscopy

Raman spectroscopy, a vibrationally spectroscopic technique, it is excellent for chemical analysis on both the macroscopic and microscopic scale. The technique can provide information about concentration, structure, and interaction between chemical components of a material. Raman spectroscopic techniques were used for this study in order to characterize the formation of sodium titanate layer after the chemical treatment. Raman Spectroscopy was performed on

samples' surfaces using the RENISHAW InVia Raman Microscope employing an Argon Ion laser of 20 mW with a wavelength of 514 nm.

5 EXPERIMENTAL RESULTS: Ti13Nb13Zr ALLOY

In this section, the results regarding the Ti13Nb13Zr alloy in the conditions of non-deformed, deformed by HPT, and with different surface conditions will be presented. The results will be presented in the following sequence: microstructural and mechanical characterization, electrochemical characterization, and finally, bioactivity.

5.1 Microstructural and mechanical characterizations

In this section, the microstructural and mechanical characterization of samples of Ti13Nb13Zr alloy in the conditions non-deformed and deformed by HPT will be presented. These samples without surface treatment are named “Polished samples”.

5.1.1 Polished samples

Figure 21 shows XRD patterns of Ti13Nb13Zr alloy non-deformed (ND) and deformed by HPT at 1 GPa and 4.5 GPa. The indexation of the XRD patterns indicates the presence of the HCP α' (ICSD # 253841) and the BCC β (ISCD # 645545) phases before and after the deformation by HPT. The peak broadening observed after deformation, at both pressure conditions, points to very high grain refinement in the Ti13Nb13Zr alloy.

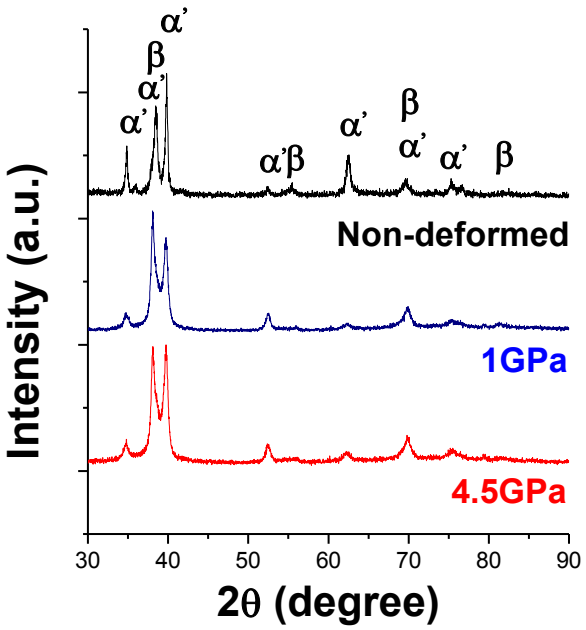

Figure 21: XRD patterns of Ti13Nb13Zr alloy at the non-deformed condition and deformed by HPT at 1 GPa and 4.5 GPa and three turns.

The microstructures of Ti13Nb13Zr alloy at (a) non-deformed condition and deformed by HPT at (b) 1 GPa and (c) 4.5 GPa and three turns are shown in Figure 22.

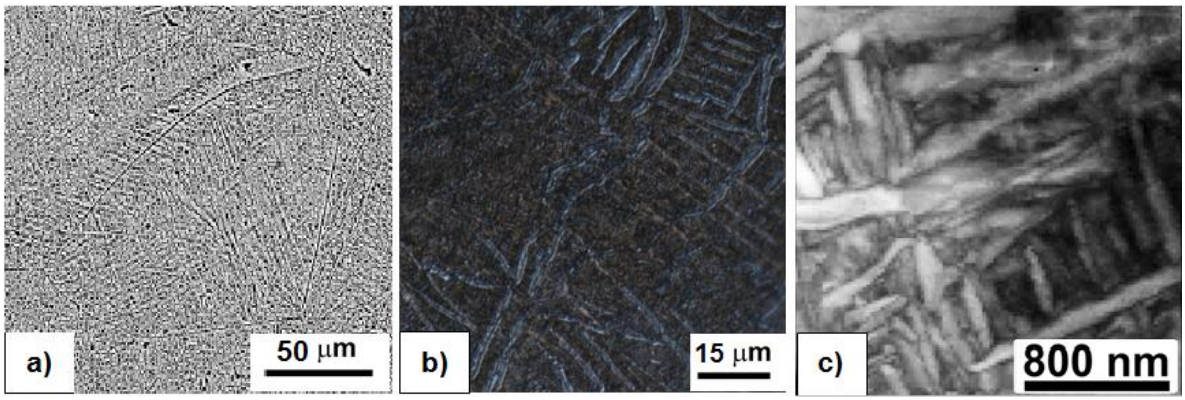

Figure 22: Microstructures of Ti13Nb13Zr alloy at (a) non-deformed condition and deformed by HPT at (b) 1 GPa and (c) 4.5 GPa and three turns.

Figure 22(a) is an SEM picture that shows details of the microstructure of Ti13Nb13Zr alloy at the non-deformed condition. It reveals the existence of a

retained BCC β phase as well as a coarse non-equilibrium metastable martensite (HCP α') phase, precipitated after heating and quenching. The XRD results presented in Figure 21 confirm such observation. Measurements of grain size were conducted by using the commercial TSL OIM Analysis software and gave a mean initial size of about 250 μm for the β phase, and α' laths presented an average length of ~20 μm with thickness ranging from 1 to 2 μm.

Figure 22(b) is an image obtained by confocal laser microscopy. This image corresponds to Ti13Nb13Zr alloy deformed by HPT at 1 GPa and three turns. The average grain size measured was ~ 22 μm.

Figure 22(c) presents the equivalent bright field image from the surface of the sample received by conventional TEM. This image corresponds to Ti13Nb13Zr alloy deformed by HPT at 4.5 GPa and three turns. This image shows a remarkable grain refinement in Ti13Nb13Zr alloy after deformation by HPT since the average grain size measured was ~ 203 nm. Moreover, it is possible to observe a non-homogeneous distribution of grains/subgrains sizes and comparing with Figure 22(a), a redistribution of the α' after mechanical processing.

Figure 23 presents hardness mappings for Ti13Nb13Zr alloy non-deformed and deformed by HPT at 1 GPa and 4.5 GPa.

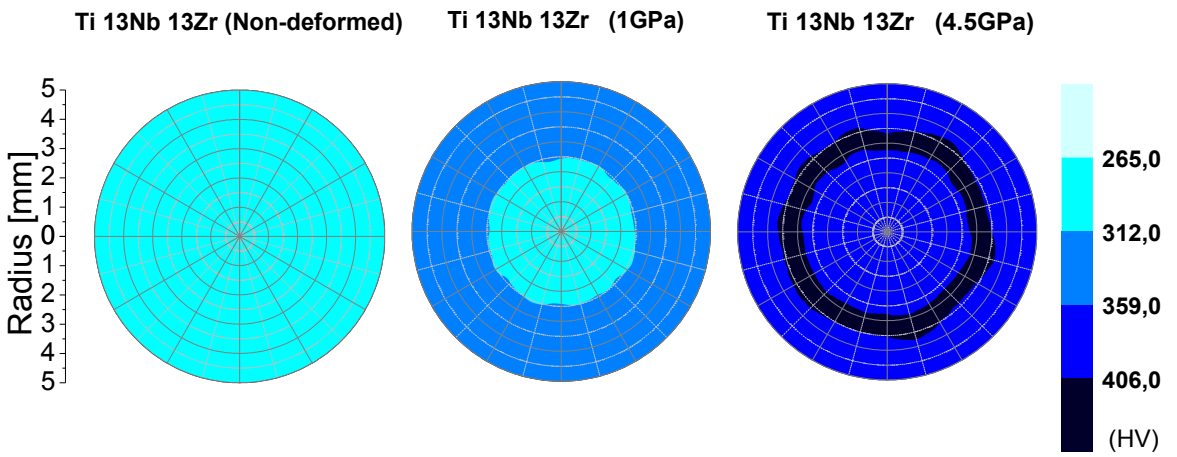

Figure 23: Hardness mappings for Ti13Nb13Zr alloy at the non-deformed condition and deformed by HPT 1 GPa and 4.5 GPa and three turns.

As shown in Figure 23, when samples of Ti13Nb13Zr alloy were deformed by HPT, the hardness significantly increased, from a mean value of 265 HV at the non-deformed condition to values between 359 and 406 HV at 4.5 GPa. This result can be related to the grain refinement shown in Figure 22. Moreover, the deformed samples show a radial increase in hardness, from the center to the edge. This may be because the HPT deformation is a torsional process. On the other hand, since the increase in hardness is related to the decrease in grain size, it is possible to assume that deformed samples display smaller grains in the edge than in the center [20].

Figure 24 shows the elastic modulus measured for samples of Ti13Nb13Zr alloy at ND, HPT1GPa, and HPT4.5GPa conditions. The elastic modulus of the samples in the non-deformed condition, deformed at 1 GPa, and deformed at 4.5 GPa were 63 GPa, 58 GPa, and 60 GPa, respectively. The values showed in Figure 24 are the result of a statistical analysis of 3 measurements (mean and standard deviation).

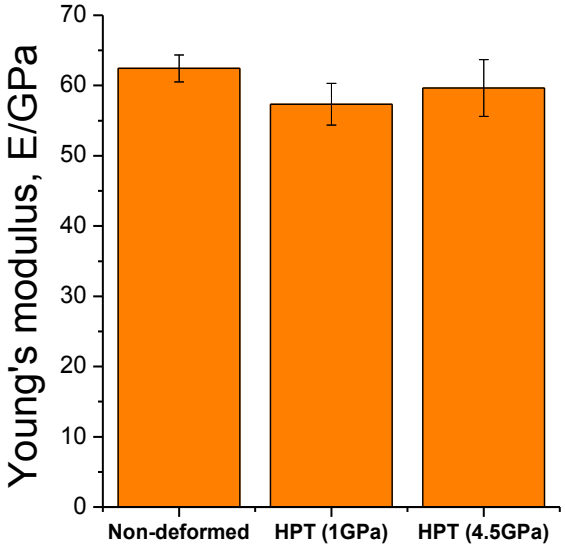

Figure 24: Graph comparing elastic modulus values for the Ti13Nb13Zr alloy at the non-deformed condition and deformed by HPT at 1 GPa and 4.5 GPa.

5.1.2 Anodized samples

Figure 25 shows the XRD patterns of anodized samples of Ti13Nb13Zr alloy in the conditions ND, HPT1GPa, and HPT4.5GPa.

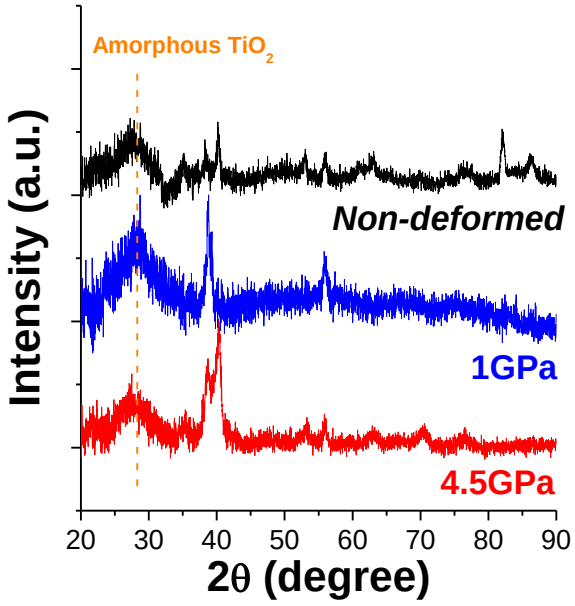

Figure 25: XRD patterns of anodized samples of Ti13Nb13Zr alloy in the ND, HPT1GPa, and HPT4.5GPa conditions.

These XRD patterns indicate that TiO_2 nanotubes and nanopores obtained during anodization are amorphous. However, when TiO_2 nanotubes and nanopores were heat-treated at 550 °C for two hours, an anatase-rutile mixture was obtained (Figure 26). The indexing of the Bragg peaks indicates the presence of the anatase TiO_2 phases (2θ = 25.4 °, 38.3 °, 48.1 °, and 55.2 °) [126] and TiO_2 -rutile phases (2θ = 27.4 ° and 36.0 °)[127].

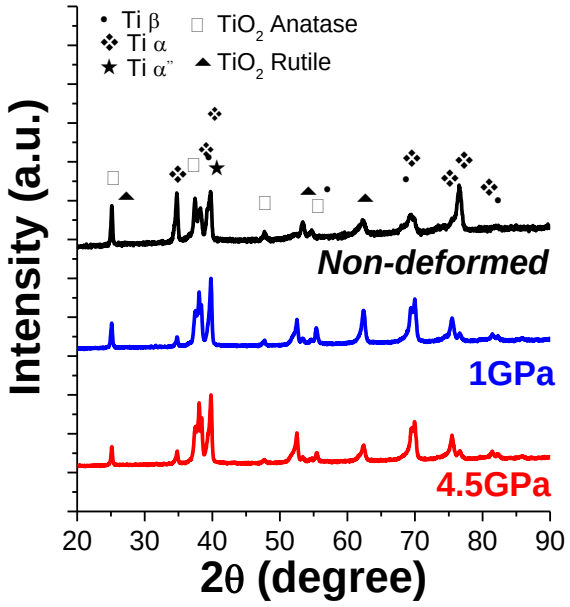

Figure 26: XRD pattern of anodized and annealed samples of Ti13Nb13Zr alloy in the ND, HPT1GPa, and HPT4.5GPa conditions. TiO_2 nanostructures were annealed at 550 °C in air.

TiO_2 nanotubes morphologies were investigated by SEM. Figure 27 shows the top and lateral views of anodized and annealed samples of Ti13Nb13Zr alloy (a and b) ND; and HPT1GPa in (c and d) and HPT4.5GPa in (e and f).

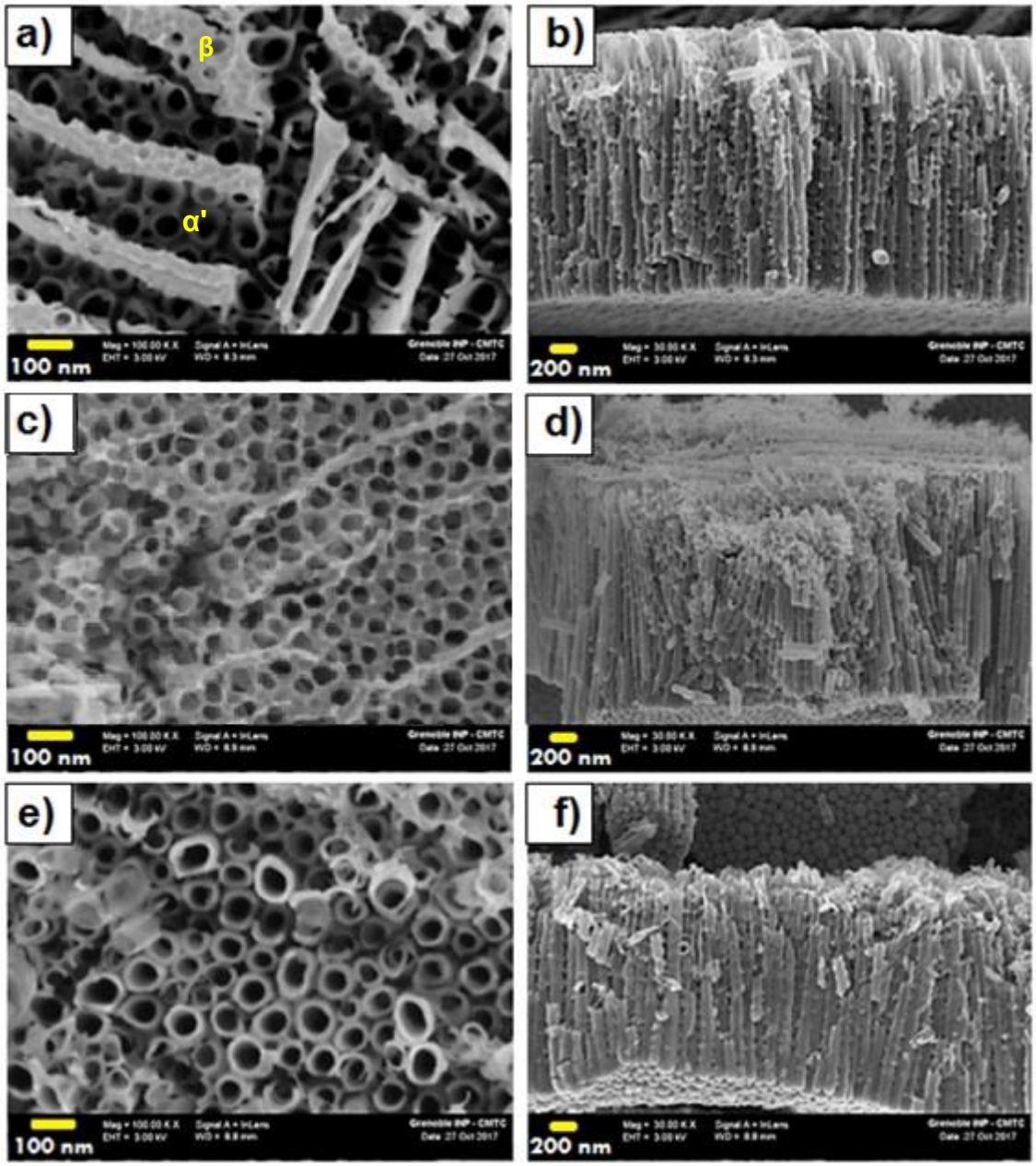

Figure 27: SEM micrographs of anodized and annealed samples of Ti13Nb13Zr alloy at non-deformed condition, (a) Top and (b) Lateral views, deformed by HPT at 1 GPa, (c) Top and (d) Lateral views and deformed at 4.5 GPa, (e) Top and (f) Lateral views.

Figure 27(a) shows self-organized TiO_2 nanotubes formed in the α' phase and TiO_2 nanoporous in the β phase of Ti13Nb13Zr alloy non-deformed. The different nanostructures observed may be explained by the fact that there is a competition between the dissolution and the formation of oxides depending on the

chemical composition of both phases. The lateral view of these nanostructures (Figure 27(b)) shows self-organized arrays of nanotubes whose dimensions are described in Table 4.

Table 4: Summary of observed morphologies and dimensions of the formed nanostructures observed in Figure 27 for samples of Ti13Nb13Zr alloy at different conditions.

Ti13Nb13Zr alloy				
Condition	**Morphology**	**Diameter (nm)**		**Length (nm)**
		Internal	**External**	
Non-deformed	Nanotubes and nanopores	58 ± 7	96 ± 20	1839 ± 72
1 GPa	Nanotubes and nanopores	44 ± 7	67 ± 11	1557 ± 158
4.5 GPa	Nanotubes and nanopores	47 ± 10	94 ± 11	1492 ± 73

In the same way, the samples deformed by HPT, Figures 27(c) and (e), presented different nanostructures. However, since processing by HPT caused a refinement and spatial redistribution of the α' and β phases, the deformed samples presented a more homogenous distribution of the nanostructures.

5.1.3 Samples chemically treated by HCl etching and NaOH activation

The surface morphology of samples of Ti13Nb13Zr alloy, chemically treated by HCl etching and NaOH activation, was examined by scanning electron microscopy (SEM). The secondary electron (SE) detection mode with an acceleration voltage of 25 kV was selected for SEM analysis. Figure 28 shows SEM images of Ti13Nb13Zr alloy, chemically treated, at the conditions ND, HPT1GPa, and HPT4.5GPa. Figures 28(b), (d) and (f) are SEM images of higher magnification to show more details of surface morphology.

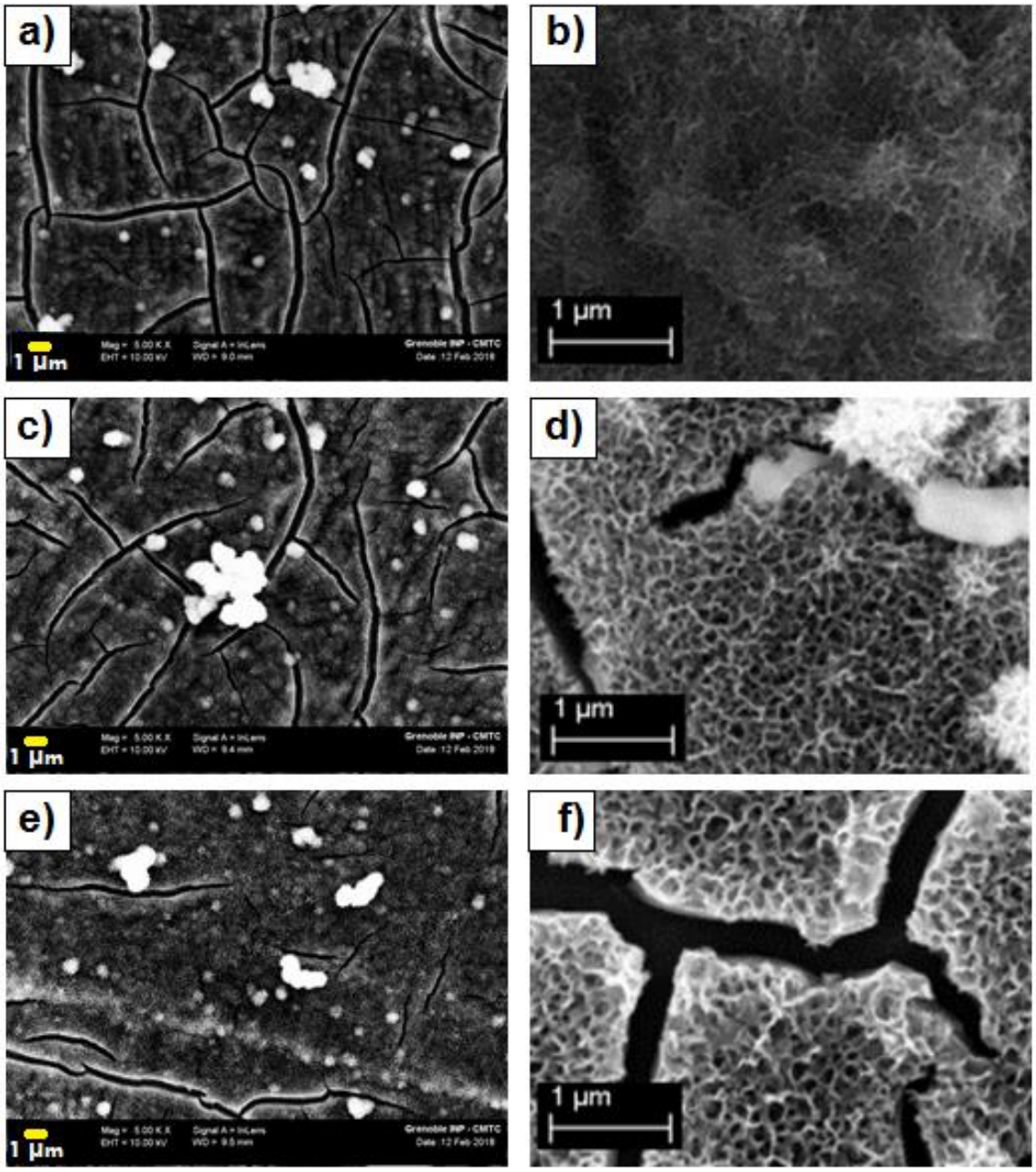

Figure 28: SEM images of Ti13Nb13Zr alloy, chemically treated by HCl etching and NaOH activation, (a and b) non-deformed, deformed by HPT at (c and d) 1 GPa and deformed by HPT at (e and f) 4.5 GPa.

As shown in the micrographs of Figure 28, the chemically treated by HCl and NaOH, induced the formation of a nano topographic sponge-like morphology on the samples' surface. Also observed in Figure 28 is that the surface is completely cracked. This behavior has previously been described. For example,

Jonášová et al., (2004) reported, that HCl etching of commercially pure Ti leads to the formation of a micro-roughened surface, which after subsequent alkali treatment in NaOH is maintained [128]. Yi et al., (2006) reported, for commercially pure grade 2 Ti treated with H_2SO_4/H_2O_2 mixture, a texture characterized by a three-dimensional sponge-like porosity on chemically treated cp Ti surface [129].

On the other hand, in order to obtain an analysis of the surface composition, EDS analysis was performed. The results are shown in Table 5.

Table 5: Quantitative chemical EDS analysis of samples chemically treated by HCl etching and NaOH activation.

	Ti13Nb13Zr (at %)		
Chemical element	**Non-deformed**	**1 GPa**	**4.5 GPa**
O	61.79	54.4	63.37
Na	2.01	3.53	2.11
Zr	2.24	1.51	1.13
Nb	2.41	2.80	2.97
Ti	28.68	33.58	28.33
Cl	2.87	4.18	2.09

Raman spectroscopy was used to identify the crystalline phases present on the surface of samples of Ti13Nb13Zr alloy chemically treated. The results shown in Figure 29 indicate that sodium titanate, anatase, and rutile are the main phases present in all the samples.

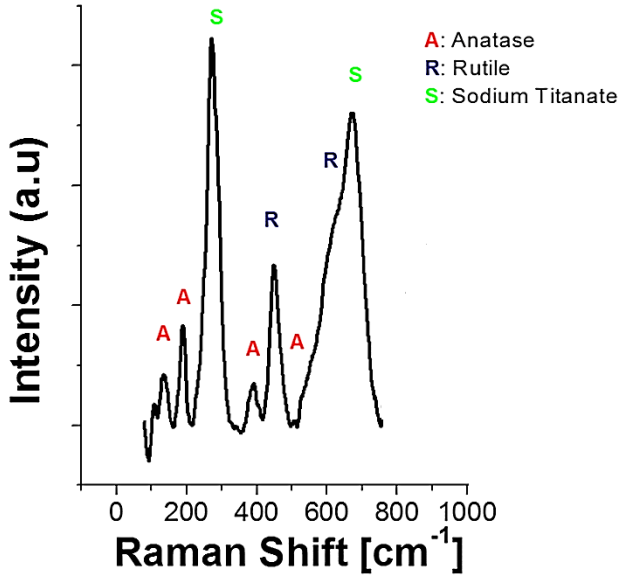

Figure 29: Raman spectra of the surface of Ti13Nb13Zr alloy chemically treated by HCl etching and NaOH activation.

5.1.4 Samples chemically treated by H_3PO_4 etching and NaOH activation

The surface morphology of Ti13Nb13Zr alloy samples, which were chemically treated by H_3PO_4 etching and NaOH activation, was examined by scanning electron microscopy (SEM). Figure 30 shows SEM images of chemically modified surfaces of Ti13Nb13Zr alloy in the conditions ND, HPT1GPa, and HPT4.5GPa. Figures 30(b), (d) and (f) are SEM images of higher magnification to show more details about the surface morphology.

As observed in the samples treated with HCl, the chemically treated by H_3PO_4 and NaOH also induced the formation of a nano topographic sponge-like morphology on the samples' surface, and a surface full of cracks. The etched in different acids, such as HCl, H_3PO_4 or a mixture of $HF+HNO_3$, and subsequently pretreated in NaOH, were reported for sintered Ti13Nb13Zr alloy by Müller et al., (2008) [130]. The authors also reported a micro-roughened surface as well as microcracks.

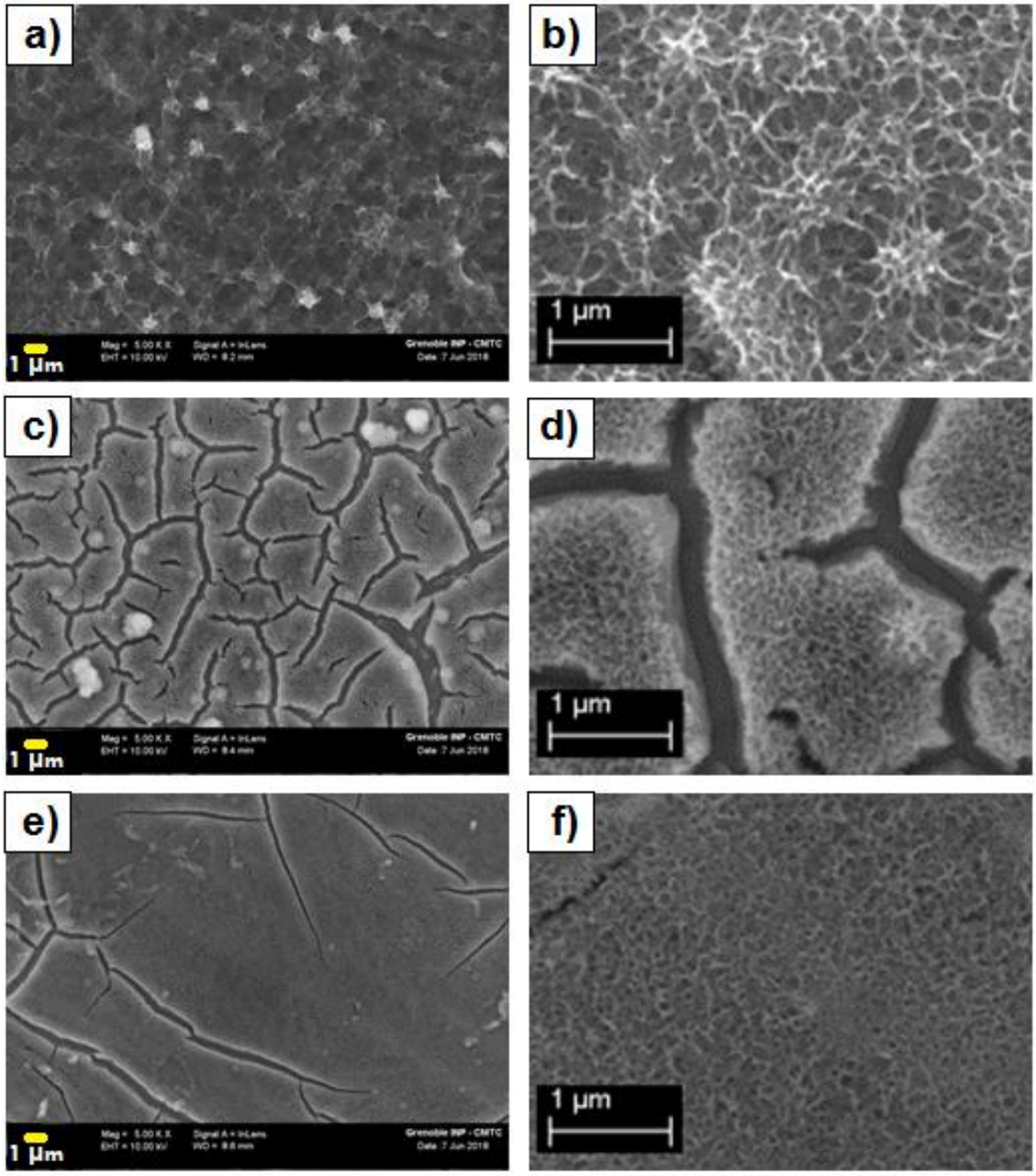

Figure 30: SEM images of Ti13Nb13Zr alloy, chemically treated by H_3PO_4 and NaOH, (a and b) ND sample, (c and d) HPT1GPa sample (e and f) HPT4.5GPa sample.

Moreover, Raman results also indicate sodium titanate, anatase, and rutile phases in the samples, see Figure 31. Table 6 presents the quantitative EDS chemical analysis of samples chemically treated by H_3PO_4 and NaOH.

Table 6: Quantitative chemical EDS analysis of chemically treated samples by H_3PO_4 etching and NaOH activation.

	Ti13Nb13Zr (at %)		
Chemical element	**Non-deformed**	**1 GPa**	**4.5 GPa**
O	66.38	65.38	66.47
Na	1.35	1.3	1.08
Zr	1.89	1.91	1.10
Nb	2.49	2.15	2.03
Ti	27.89	29.26	29.32

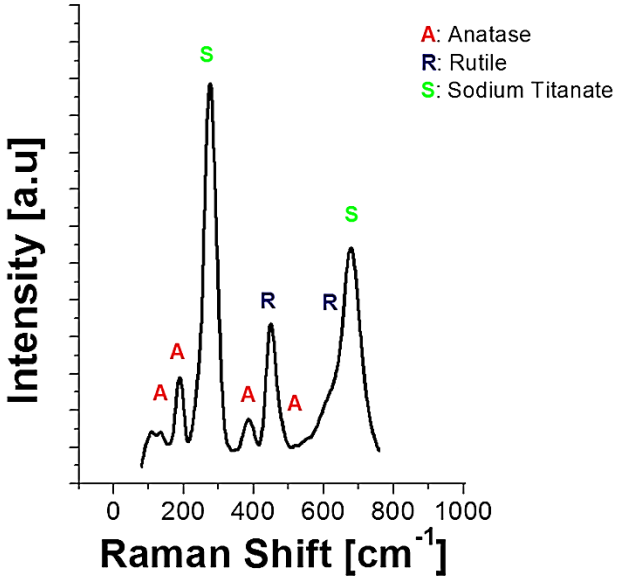

Figure 31: Raman spectra of the surface of Ti13Nb13Zr alloy chemically treated by H_3PO_4 and NaOH.

5.2 Electrochemistry characterization

5.2.1 Polished samples

5.2.1.1 Open circuit potential (OCP) measurements

Table 7 summarizes the values of open circuit potential (or corrosion potential, E_{corr}) recorded after one hour of immersion in simulated body fluid (SBF)

for Ti13Nb13Zr alloy, in the conditions ND, HPT1GPa and HPT4.5GPa. The values are the result of a statistical analysis of 3 measurements (mean and standard deviation).

Table 7: OCP measurements after 1-hour immersion in SBF at 37 °C of the polished surfaces of Ti13Nb13Zr alloy in the conditions ND, HPT1GPa, and HPT4.5GPa samples.

Condition	OCP or E_{corr} (mV vs. SCE)
Non-deformed	-530 ± 54
1 GPa	-466 ± 56
4.5 GPa	-513 ± 62

The OCP is used as a criterion for the corrosion behavior, the higher the potential, the nobler, and the more stable the surface in the medium.

A slight variation of the open circuit potential is observed for deformed conditions. The OCP of Ti13Nb13Zr alloy, at ND condition, was - 530 mV vs. SCE, while samples with HPT1Gpa and HPT4.5GPa showed a slight increase, - 466 mV vs. SCE and - 513 mV vs. SCE, respectively. Therefore, regardless of the crystal structure, it appears that severe plastic deformation causes a slight increase in the corrosion potential compared to the ND samples.

5.2.1.2 Potentiodynamic polarization curves

Figure 32 shows the anodic polarization curves, recorded in SBF at 37 ºC, for the polished samples at ND, HPT1GPa, and HPT4.5GPa conditions. The polarization curve for each sample represents a single measure, arbitrarily chosen from a series of three measurements carried out under the same conditions.

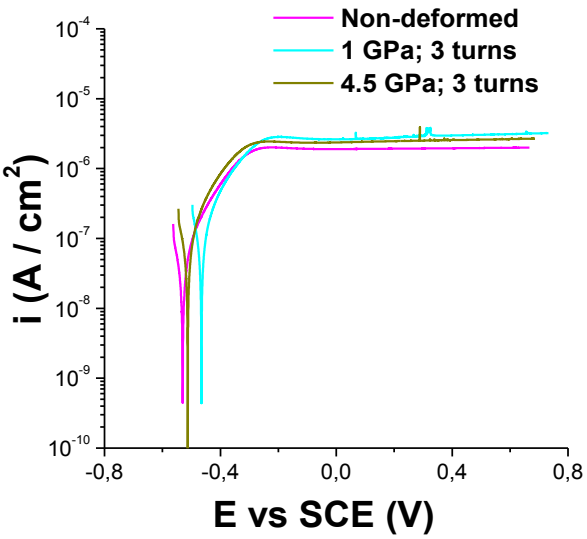

Figure 32: Anodic polarization curves, recorded in SBF at 37 °C of the polished surfaces of Ti13Nb13Zr alloy in the conditions ND, HPT1GPa, and HPT4.5GPa samples.

The current density (i), represented on the ordinate axis of Figure 32, was calculated by dividing the current measured by the geometric area (0.283 cm^2). It is considered that the current measured in the anode region is mainly due to the oxidation reaction of the substrates to form TiO_2, which contributes to the thickening of the passive layer. This reaction takes place in the metal/oxide interface. Therefore, the area in which it is produced is equal to the geometric area.

On the other hand, the Ecorr values obtained by extrapolation on the polarization curves shown in Figure 32 were comparable with the values measured in the OCP measurements (see Table 7). Moreover, as shown in Figure 32, a current plateau was quickly established due to spontaneously formation of a protective oxide layer on the surface of the sample. Thus, in this passive state, the corrosion current density (icorr) could be considered equivalent to the current density of the passive plateau (ipass).

The passivation current density (i_{pass}) values, for the ND, HPT1GPa, and HPT4.5GPa Ti13Nb13Zr samples were graphically established and summed up in

Table 8. It shows the mean current density values of three points at the current plateau in the polarization curves and their standard deviations.

Table 8: Passivation current density of the polished samples of Ti13Nb13Zr alloy in the conditions ND, HPT1GPa, and HPT4.5GPa.

Conditions	i_{pass} (μA/cm^2)
Non-deformed	2.00 ± 0.10
1 GPa	2.95 ± 0.15
4.5 GPa	2.45 ± 0.32

The passivation current density of the non-deformed Ti13Nb13Zr alloy was 2.00 μA/cm^2, while samples HPT1GPa and HPT4.5GPa showed a slight increase, 2.95 μA/cm^{2,} and 2.45 μA/cm^2, respectively. Therefore, it appears that the increase in the pressure from 1 GPa to 4.5 GPa does not affect the passivation current density in the Ti13Nb13Zr alloy.

5.2.1.3 Electrochemical impedance measurements (EIS)

To conclude the electrochemical characterization of the samples without surface treatments (polished samples), the samples were subjected to electrochemical impedance spectroscopy measurements. The EIS was also performed in SBF at 37 °C and in the dark. Figure 33 shows the EIS graphs in the (a) Nyquist and (b) Bode representation of the Ti13Nb13Zr alloy in the conditions ND, HPT1GPa, and HPT4.5GPa.

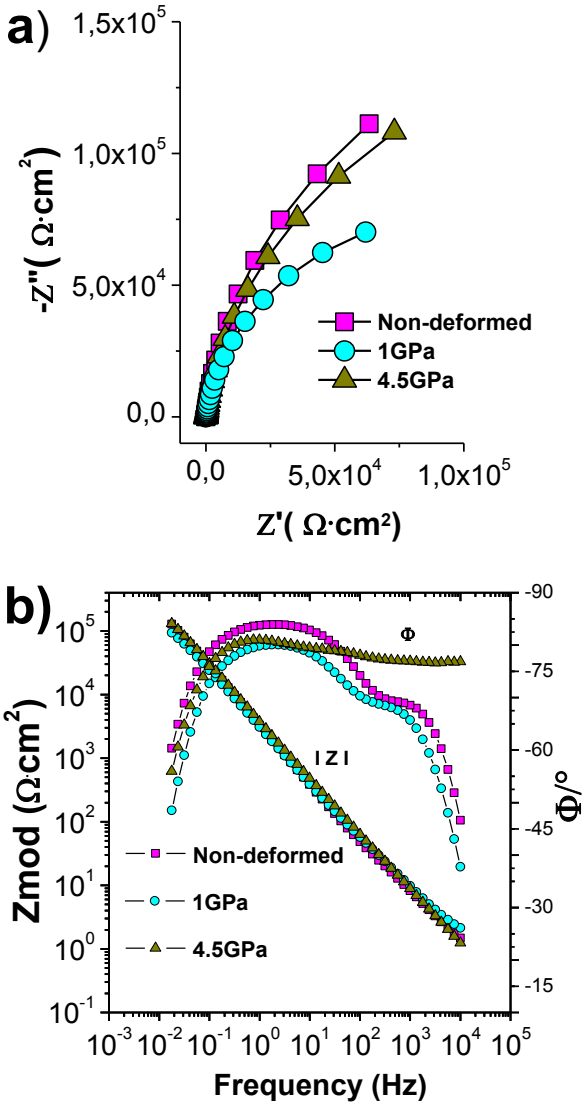

Figure 33: EIS graphs in the Nyquist diagrams (a) and Bode diagrams (b) of the polished samples of Ti13Nb13Zr alloy in the conditions ND, HPT1GPa, and HPT4.5GPa.

Note that the diagrams for each sample present a single measurement, chosen arbitrarily from a series of three experiments carried out under the same conditions. It should also be taken into account that the influence of electrolyte resistance confounds the use of Bode phase angle plots, to estimate the nature of the impedance response [131]. Therefore, all Bode diagrams in this work were corrected from the electrolyte resistance. A modified Bode representation is possible following

$$\Phi_{adj} = \tan^{-1}\left(\frac{Z''}{Z' - R_e}\right) \quad \textbf{(23)}$$

$$Zmod_{adj} = \sqrt{(Z' - R_e)^2 + (Z'')^2} \quad \textbf{(24)}$$

The impedance spectra in Nyquist diagrams of Figure 33(a) show the typical shape (arc) for a capacitive-resistive system (associations of capacitive phenomena, accumulation of charges, and resistive phenomena, load transfers or resistance of a layer). Additionally, it can be seen from Figure 33(a) that the spectrum of ND samples has a higher amplitude, which indicates that SPD process displays a slight effect on the formation of the protective layer in Ti13Nb13Zr alloy. It can be related to the increasing surface energy of the alloy induced by dislocations [132]. Thus, the tendency to loss of electrons and releasing atoms into electrolyte is accelerated [133].

On the other hand, the effect of the dislocations caused by SPD was higher for samples deformed at 1GPa (spectrum with the lowest amplitude). This may be explained by the fact that, in the samples deformed at low pressure, the density of dislocations was not enough to initiate the recrystallization of the material [20,134]. Instead of this, in the samples deformed at 4.5GPa, the greater amount of dislocations generated probably induced certain recrystallization of the material [20], which involves nucleation, growth of new dislocation free grains from the deformed structure [135], and then decreasing surface energy.

The Bode diagrams, in Figure 33(b), show a capacitive behavior, from medium to low frequencies, with phase angles approaching – 90° and straight lines in Bode magnitude plot. It is typical of passive materials [136]. From the Bode phase angle plot for all samples, two plateaus can be identified, where the phase angle is independent of frequency.

Moreover, high values of Zmod (or |Z|) at low frequencies, above 10^5 Ω·cm^2, suggest that the passive film formed offers high corrosion resistance. This behavior is consistent with the low passivation current determined in the polarization tests.

5.2.2 Anodized samples

In this section, the effect of the SPD by HPT as well as the presence of TiO_2 nanostructures on the electrochemical properties of Ti13Nb13Zr alloy is presented. The anodized samples were annealed according to section 4.3.1.2.

5.2.2.1 Open circuit potential measures

Table 9 summarizes the values of E_{corr} recorded after 1 hour of immersion in SBF for anodized Ti13Nb13Zr alloy in the conditions ND, HPT 1GPa and HPT4.5GPa. The values are the result of a statistical analysis of 3 measurements (mean and standard deviation).

Table 9: OCP measurements, after 1-hour immersion in SBF at 37° C for the anodized samples of Ti13Nb13Zr alloy in the conditions ND, HPT1GPa, and HPT4.5GPa.

Condition	OCP or E_{corr} (mV vs. SCE)
Non-deformed	-3.9 ± 9.3
1 GPa	-49 ± 18
4.5 GPa	-71 ± 29

The OCP of anodized Ti13Nb13Zr alloy, at the non-deformed condition, was - 3.9 mV vs. SCE, while the anodized samples HPT1GPa and HPT4.5GPa showed a decrease in their corrosion potential, - 49 mV vs. SCE and - 71 mV vs. SCE, respectively. Therefore, the anodized ND Ti13Nb13Zr alloy showed the noblest corrosion potential (the nobler and more stable surface in SBF).

On the other hand, the E_{corr} of the anodized samples showed a drastic increase compared to samples without TiO_2 nanostructures (Table 7), meaning

that electrochemical anodization of the Ti13Nb13Zr alloy in both ND and HPT deformed conditions, ennobled its surface.

5.2.2.2 Potentiodynamic polarization curves

Figure 34 shows the anodic polarization curves, recorded in SBF at 37 ºC, of anodized samples of Ti13Nb13Zr alloy in the conditions ND, HPT1GPa, and HPT4.5GPa. From Figure 34, it can also be seen a current plateau in a wide range of potentials which is formed faster than in non-anodized samples (see Figure 32). However, for anodized samples, the passive current density is not absolutely constant but increases slowly between Ecorr and 1 V vs. SCE. This evolution of the current reflects poorer stability of the passive layer when it is subjected to anode potentials.

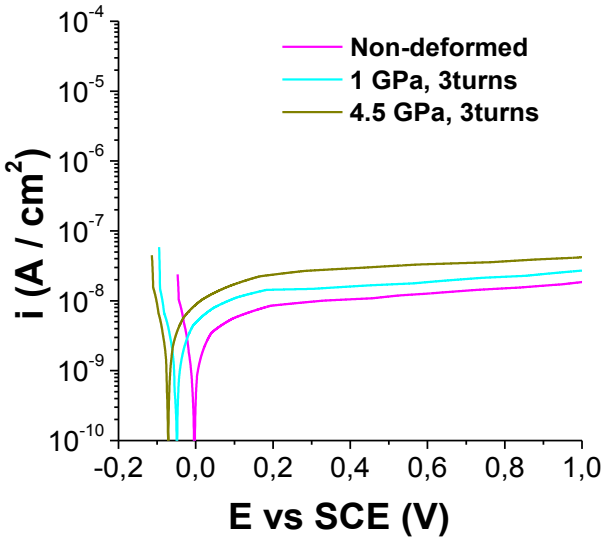

Figure 34: Anodic polarization curves, recorded in SBF at 37 °C for the anodized Ti13Nb13Zr samples in the conditions ND, HPT1GPa, and HPT4.5GPa.

The ipass values, of anodized Ti13Nb13Zr alloy samples in the conditions ND, HPT1GPa, and HPT4.5GPa, were graphically established and summed up in Table 10. It shows the mean current density values of three points at the current plateau in the polarization curves and their standard deviations.

Table 10: Passivation current density for the anodized Ti13Nb13Zr samples in the conditions ND, HPT1GPa, and HPT4.5GPa.

Condition	i_{pass} (μA/cm^2)
Non-deformed	0.012 ± 0.004
1 GPa	0.017 ± 0.004
4.5 GPa	0.033 ± 0.006

The passivation current density of anodized ND Ti13Nb13Zr alloy, was 0.012 μA/cm^2, while the HPT1GPa and HPT4.5GPa samples showed a slight increase, 0.017 μA/cm^2 and 0.033 μA/cm^2, respectively. Therefore, it appears that severe plastic deformation causes a slight increase in the passivation current of anodized Ti13Nb13Zr alloy. On the other hand, the i_{pass} of the samples anodized also showed a drastic change compared to samples without TiO_2 nanostructures (Table 8). This result is also in agreement with earlier observations, which showed that electrochemical anodization of Ti13Nb13Zr alloy, non-deformed or deformed by HPT, ennobled its surface.

5.2.2.3 Electrochemical impedance measurements

Figure 35 shows the EIS graphs in the (a) Nyquist and (b) Bode representation of anodized Ti13Nb13Zr alloy in the ND, HPT1GPa, and HPT4.5GPa conditions.

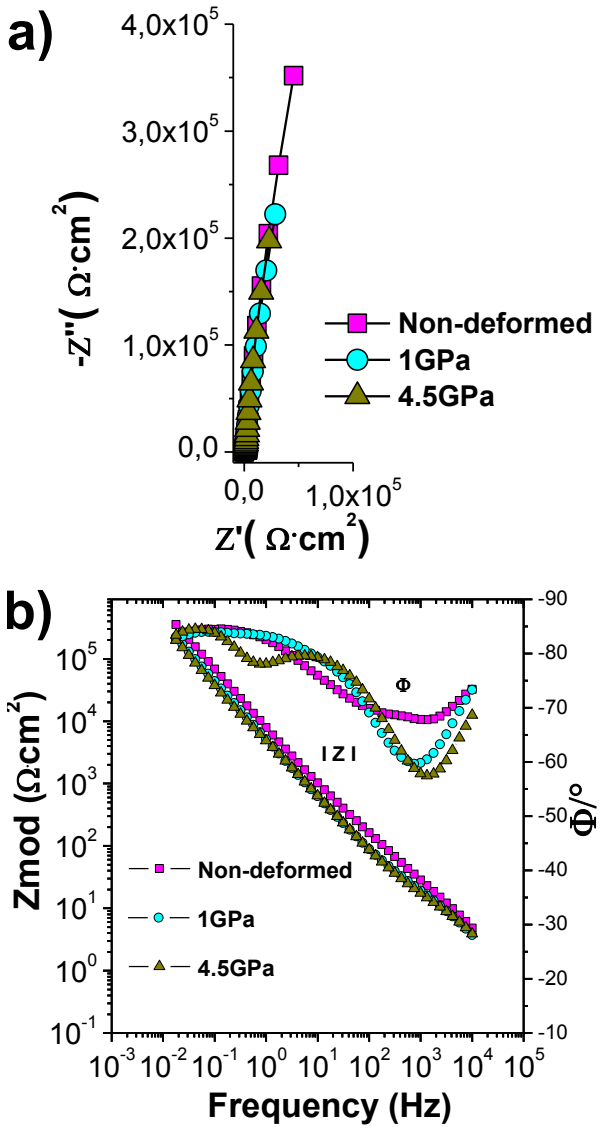

Figure 35: Nyquist diagrams (a) and Bode diagrams (b) for the anodized Ti13Nb13Zr samples in the conditions ND, HPT1GPa, and HPT4.5GPa.

The impedance spectra in Nyquist diagrams of Figure 35(a) show a pseudocapacitive shape (tilted straight line). This behavior suggests that the electron exchanges, and therefore, the reactions, are minimal or that the oxide layer is very resistive [137]. Additionally, it can be seen from Figure 35(a) that the amplitude of spectra is much higher than in non-anodized samples (Figure 33(a)). It suggests that the nanostructure arrays on the samples improved the protection of the surface in Ti13Nb13Zr alloy.

On the other hand, deformed samples showed a spectrum with a lower amplitude. Hence, the SPD process also affected the formation of nanostructures on Ti13Nb13Zr alloy.

In contrast, comparing with the result obtained for polished samples, the effect of the dislocations caused by SPD was lower for samples deformed at 1 GPa. This may be explained by the fact that the heat treatment carried out on anodized samples possibly allowed the relief of residual stresses developed during the deformation by HPT [138].

The Bode diagrams, in Figure 35(b), show a capacitive behavior with the maximum phase angles close to −90° and high values of |Z| above 10^5 Ω·cm^2 in the low frequencies region, suggesting that the formed passive film offers high corrosion resistance. This fact is consistent with the low passivation current determined in polarization tests. From Bode phase angle plots, three plateaus can be identified, which is more noticeable for samples deformed at 4.5 GPa.

5.2.3 Samples chemically treated by HCl etching and NaOH activation

In this section, the effect of the SPD by HPT as well as, surface modification treatment by HCl etching and subsequent NaOH activation, on the electrochemical properties of Ti13Nb13Zr alloy will be studied.

5.2.3.1 Open circuit potential measures

Table 11 summarizes the values of E_{corr} for samples ND and deformed by HPT as well as chemically treated by HCl and NaOH. The values are the result of a statistical analysis of 3 measurements (mean and standard deviation).

Table 11: OCP measurements, after 1-hour immersion in SBF at 37° C of samples of Ti13Nb13Zr alloy chemically treated by HCl and NaOH in the conditions ND, HPT1GPa and HPT4.5GPa.

Condition	Corrosion potential (mV vs SCE)
Non-deformed	-132 ± 26
1 GPa	-144 ± 37
4.5 GPa	-147 ± 38

The OCP of Ti13Nb13Zr alloy chemically treated by HCl and NaOH, non-deformed, was -132 mV vs. SCE, while the corrosion potentials for samples deformed at 1 GPa and 4.5 GPa did not show a significant variation being -144 mV vs. SCE and -147 mV vs. SCE, respectively.

On the other hand, the E_{corr} of chemically treated samples also showed an increase compared to polished samples (Table 7), meaning that the chemically treated by HCl and NaOH turns nobler and more stable the surface of Ti13Nb13Zr alloy.

5.2.3.2 Potentiodynamic polarization curves

Figure 36 shows the anodic polarization curves for samples ND and deformed as well as chemically treated by HCl and NaOH.

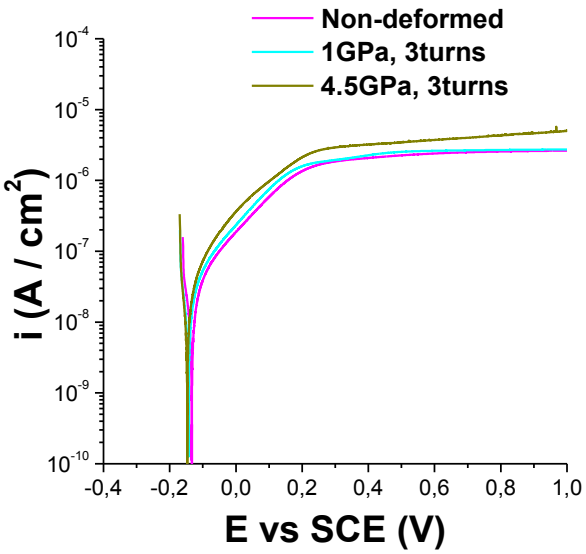

Figure 36: Anodic polarization curves, recorded in SBF at 37 °C for samples of Ti13Nb13Zr alloy chemically treated by HCl and NaOH in the conditions ND, HPT1GPa, and HPT4.5GPa.

From Figure 36, it can be seen that the behavior of the samples chemically treated by HCl and NaOH, in a physiological environment is characteristic of a passive state. However, these samples show, for potentials higher than Ecorr, a large active region of at least 300 mV. These results suggest that the chemical treatment, by HCl etching and NaOH activation, has a deleterious effect on the passivation of the Ti13Nb13Zr alloy. It may be related to the crack on samples surface (see Figure 28), as well as the degradation of the passive layer by acid etching [139].

The i_{pass} values of samples chemically treated by HCl and NaOH were graphically established and summed up in Table 12. It shows the mean current density values of three points at the current plateau in the polarization curves and their standard deviations.

Table 12: Passivation current density of samples of Ti13Nb13Zr alloy chemically treated by HCl and NaOH in the conditions ND, HPT1GPa, and HPT4.5GPa.

Condition	i_{pass} (μA/cm²)
Non-deformed	2.30 ± 0.19
1 GPa	2.51 ± 0.11
4.5 GPa	3.40 ± 0.59

The passivation current of samples chemically treated by HCl and NaOH, ND Ti13Nb13Zr alloy, was 2.30 μA/cm^2, while the HPT1GPa and HPT4.5GPa samples showed a slight increase, 2.51 μA/cm^2 and 3.40 μA/cm^2, respectively. Therefore, it appears that severe plastic deformation causes a slight increase in the passivation current of the chemically treated Ti13Nb13Zr samples.

5.2.3.3 Electrochemical impedance measurements

Figure 37 shows the EIS graphs in the (a) Nyquist and (b) Bode representation for the Ti13Nb13Zr samples chemically treated by HCl and NaOH.

The impedance spectra in Nyquist diagrams of Figure 37(a) show a typical behavior of a capacitive-resistive system that indicates corrosion protection. Comparing Nyquist diagrams in Figure 37 with those shown in Figure 33(a), for polished samples, the amplitude of ND sample chemically treated was lower. Therefore, the chemical treatment with HCl and NaOH affected the formation of the protective layer on Ti13Nb13Zr alloy.

The SPD also affected the formation of passive layers on samples chemically treated. In this case, the sample deformed at 4.5 GPa showed a spectrum with the lowest amplitude for the lowest frequency, unlike the polished samples. These results are likely to be related to a more active dissolution of the passive film at the surface near the grain boundaries [140]. Therefore, the resistance of the passive film is more affected in samples with more grain boundaries such as those deformed at 4.5 GPa.

On the other hand, the Bode diagrams, in Figure 37(b), show a capacitive behavior with the maximum phase angles close to −90° and straight lines in the Bode magnitude plot. The high values of |Z|, above 10^5 Ω·cm^2 at low frequencies region, suggest that the passive film formed offers high corrosion resistance. From the Bode phase angle plot for all samples, three plateaus can be identified.

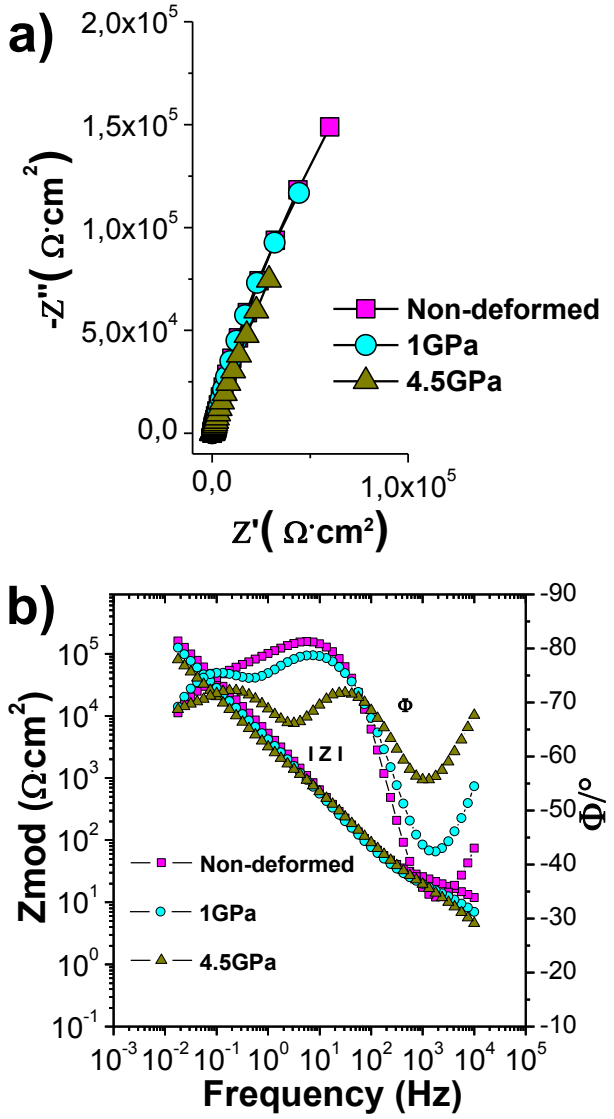

Figure 37: Nyquist diagrams (a) and Bode diagrams (b) for samples of Ti13Nb13Zr alloy chemically treated by HCl and NaOH in the conditions ND, HPT1GPa, and HPT4.5GPa.

5.2.4 Samples chemically treated by H_3PO_4 etching and NaOH activation

In this section, the effect of the SPD by HPT as well as, surface modification treatment by H_3PO_4 etching and subsequent NaOH activation, on the electrochemical properties of Ti13Nb13Zr alloy will be studied.

5.2.4.1 Open circuit potential measures

Table 13 summarizes the values of E_{corr} for samples non-deformed and deformed by HPT as well as chemically treated by H_3PO_4 etching and NaOH activation. The values are the result of a statistical analysis of 3 measurements (mean and standard deviation).

Table 13: OCP measurements, after 1-hour immersion in SBF at 37° C of samples of Ti13Nb13Zr alloy chemically treated by H_3PO_4 and NaOH in the conditions ND, HPT1GPa and HPT4.5GPa.

Condition	Corrosion potential (mV vs SCE)
Non-deformed	-724 ± 57
1 GPa	-501 ± 60
4.5 GPa	-321 ± 49

Significant changes have been observed on the recorded corrosion potential depending on the processing condition. The OCP for the ND Ti13Nb13Zr alloy chemically treated by H_3PO_4 and NaOH was - 724 mV vs. SCE, while the corrosion potentials for samples deformed at 1 GPa and 4.5 GPa were -501 mV vs. SCE and -321 mV vs. SCE, respectively. Therefore, it appears that the corrosion potential is nobler for substrates chemically treated, by H_3PO_4 etching and NaOH activation, when they were previously deformed (for high pressures).

5.2.4.2 Potentiodynamic polarization curves

Figure 38 shows the anodic polarization curves for samples non-deformed and deformed as well as chemically treated by H_3PO_4 and NaOH.

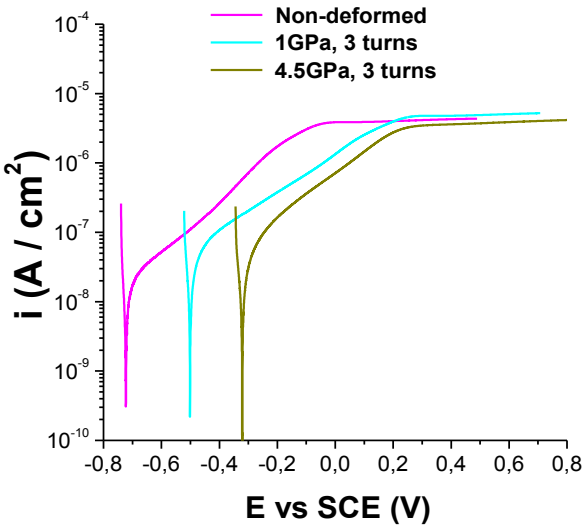

Figure 38: Anodic polarization curves, recorded in SBF at 37 °C for samples of Ti13Nb13Zr alloy chemically treated by H_3PO_4 and NaOH in the conditions ND, HPT1GPa, and HPT4.5GPa.

The polarization curves show, for potentials higher than Ecorr, a large active region of at least 400 mV. These results suggest that the chemical treatment, by H_3PO_4 and NaOH, has a deleterious effect on the passivation of the Ti13Nb13Zr alloy. This result could be explained by the high formation rate of an oxide layer which could lead to an increase of structural defects within the resultant oxide film that increases its dissolution rate [141].

The i_{pass} values of samples chemically treated by H_3PO_4 and NaOH were graphically established and summed up in Table 14. It shows the mean current density values of three points at the current plateau in the polarization curves and their standard deviations.

Table 14: Passivation current density of samples of Ti13Nb13Zr alloy chemically treated by H_3PO_4 and NaOH in the conditions ND, HPT1GPa, and HPT4.5GPa.

Condition	i_{pass} (μA/cm^2)
Non-deformed	4.05 ± 0.12
1 GPa	5.13 ± 0.21
4.5 GPa	4.21 ± 0.22

The passivation current of samples chemically treated by H_3PO_4 and NaOH, non-deformed, was 4.05 μA/cm^2, while samples deformed by HPT at 1 GPa and 4.5 GPa showed a slight increase, 5.13 μA/cm^{2,} and 4.21 μA/cm^2, respectively. Therefore, it appears that severe plastic deformation causes a slight increase in the passivation current of the chemically treated by H_3PO_4 and NaOH Ti13Nb13Zr samples.

On the other hand, the i_{pass} of the samples chemically treated by H_3PO_4 and NaOH showed an increase of i_{pass} compared with samples without chemical treatment (Table 8).

5.2.4.3 Electrochemical impedance measurements

Figure 39 shows the EIS graphs in the (a) Nyquist and (b) Bode representation of samples of Ti13Nb13Zr alloy chemically treated by H_3PO_4 and NaOH.

The impedance spectra in Nyquist diagrams of Figure 39(a) show a capacitive-like behavior. Contrary to results obtained for samples treated by HCl and NaOH, ND sample showed a spectrum with the lowest amplitude. Thus, the treatment with H_3PO_4 and NaOH affected more the formation of the protective layer on Ti13Nb13Zr alloy. In this case, deformed samples showed a layer more protective than in non-deformed samples. These results seem to be consistent with the polarization curves shown in Figure 38.

The Bode diagrams, in Figure 39(b), also show a capacitive behavior and high values of |Z| at low frequencies, suggesting that the passive film formed also offers high corrosion resistance. Likewise, three plateaus can be identified.

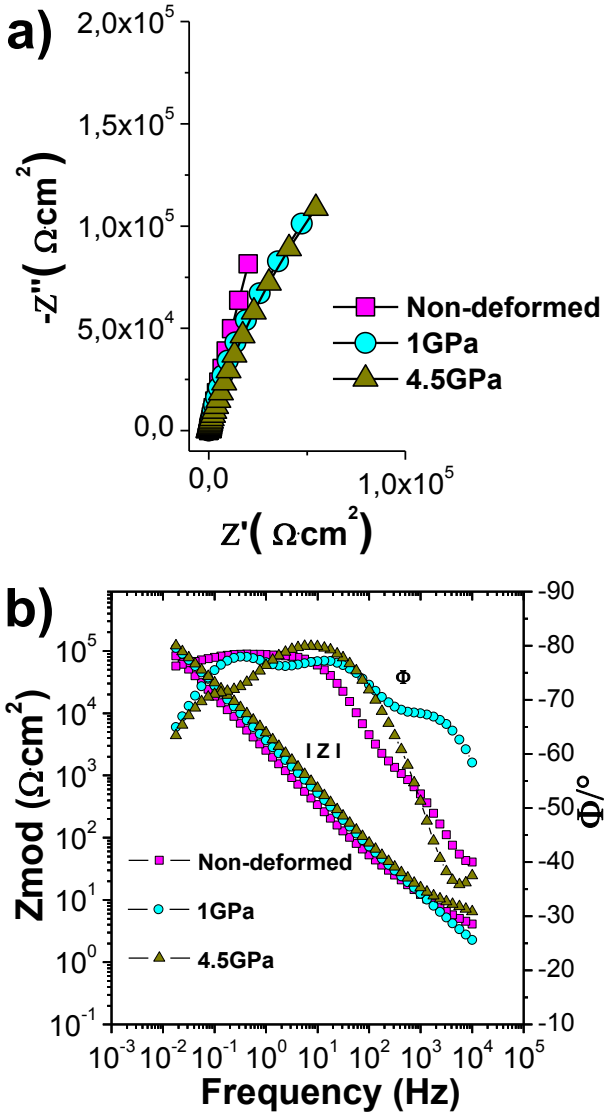

Figure 39: Nyquist diagrams (a) and Bode diagrams (b) for samples of Ti13Nb13Zr alloy chemically treated by H_3PO_4 and NaOH in the conditions ND, HPT1GPa, and HPT4.5GPa.

5.3 Modeling of impedance spectra for samples of Ti13Nb13Zr alloy

This section is focused on modeling the electrochemical impedance spectrums by equivalent electrical circuits (EEC). Different equivalent circuits

proposed in the literature will be reviewed. On the other hand, a transmission line model was proposed for modeling EIS data of samples with TiO_2 nanotubes.

The surface of the samples polished, chemically treated and with TiO_2 nanostructures are complex, and the interpretation of their impedance response is not trivial.

5.3.1 EEC proposed for polished samples

The results of EIS tests for polished samples of Ti13Nb13Zr alloy immersed in SBF were presented through Nyquist and Bode diagrams in section 5.2.1.3, Figure 33. From Bode phase angle plots (Figure 33(b)) were identified two plateaus, where the phase angle is independent of frequency. This behavior can be associated with the presence of two CPEs in the EEC applied to polished samples.

Therefore, the EIS data were simulated using the physical model and equivalent electrical circuit shown in Figure 40.

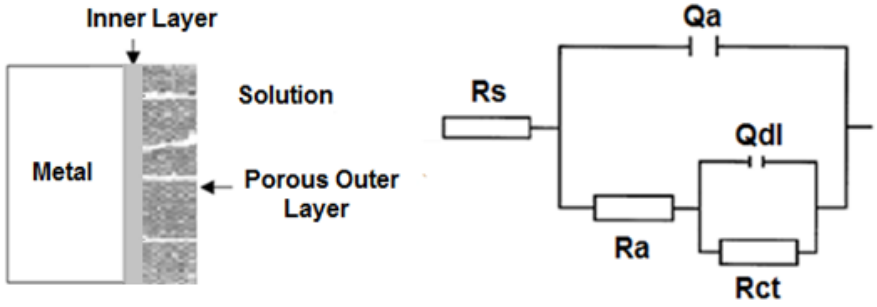

Figure 40: Model used to fit the EIS data for polished samples of Ti13Nb13Zr alloy, non-deformed, and deformed by HPT at 1 GPa and 4.5 GPa and three turns. Adapted from Valereto et al., (2004) [142].

This physical model represents a two-layer structure composed of a dense inner layer and a porous outer layer on the surface Ti13Nb13Zr alloy. It can be represented by the following EEC [142],

$$R_s + Q_a / (R_a + (Q_{dl} / R_{ct}))$$

where R_s is the electrolyte resistance, R_a is the resistance of the porous outer layer, Q_a is the constant-phase element for the porous layer, R_{ct} represents the resistance of charge-transfer and Q_{dl} is the constant-phase element for the double layer at the dense inner layer-electrolyte interface. The model and EEC illustrated in Figure 40 have been proposed by several authors to describe the bi-layer oxide film formed on Ti and its alloys [142–146].

In this work, the analysis of EIS data by regression of EEC was performed using Simad® software. Figure 41 shows the fitting of EIS data as Nyquist representations.

The errors measured for the experimental and simulated data were 0.32% for the non-deformed sample and 0.62 % for the 4.5 GPa deformed sample, indicating that the data adjusted well to the proposed EEC.

The equivalent electrical circuit parameters obtained when fitting EIS data (see section 5.2.1.3, Figure 33), of polished samples of Ti13Nb13Zr alloy at the ND, HPT1GPA and HPT4.5GPa conditions, are shown in Table 15. Additionally, the equation derived by Brug et al. (Eq. (20)) was used to calculate the effective capacitance associated with each CPE ($C_{eff(a)}$ and $C_{eff(dl)}$). The effective capacitance values also are shown in Table 15.

It can be seen from the data in Table 15, high R_{ct} values, as well as low Q_a and Q_{dl} values. These results indicate that a highly stable film was formed on the surface of the polished samples of Ti13Nb13Zr alloy. The R_{ct} is much higher than $R_{a,}$ which suggests that the protection provided by the passive layer is predominantly due to the dense inner layer. Moreover, the α values were close to 0.9, which suggest that the passive film formed displays a near capacitive behavior.

On the other hand, the R_{ct} of ND samples is higher than that of deformed samples. These results confirm that the dislocation induced by the SPD process affected the formation of the protective layer on Ti13Nb13Zr alloy.

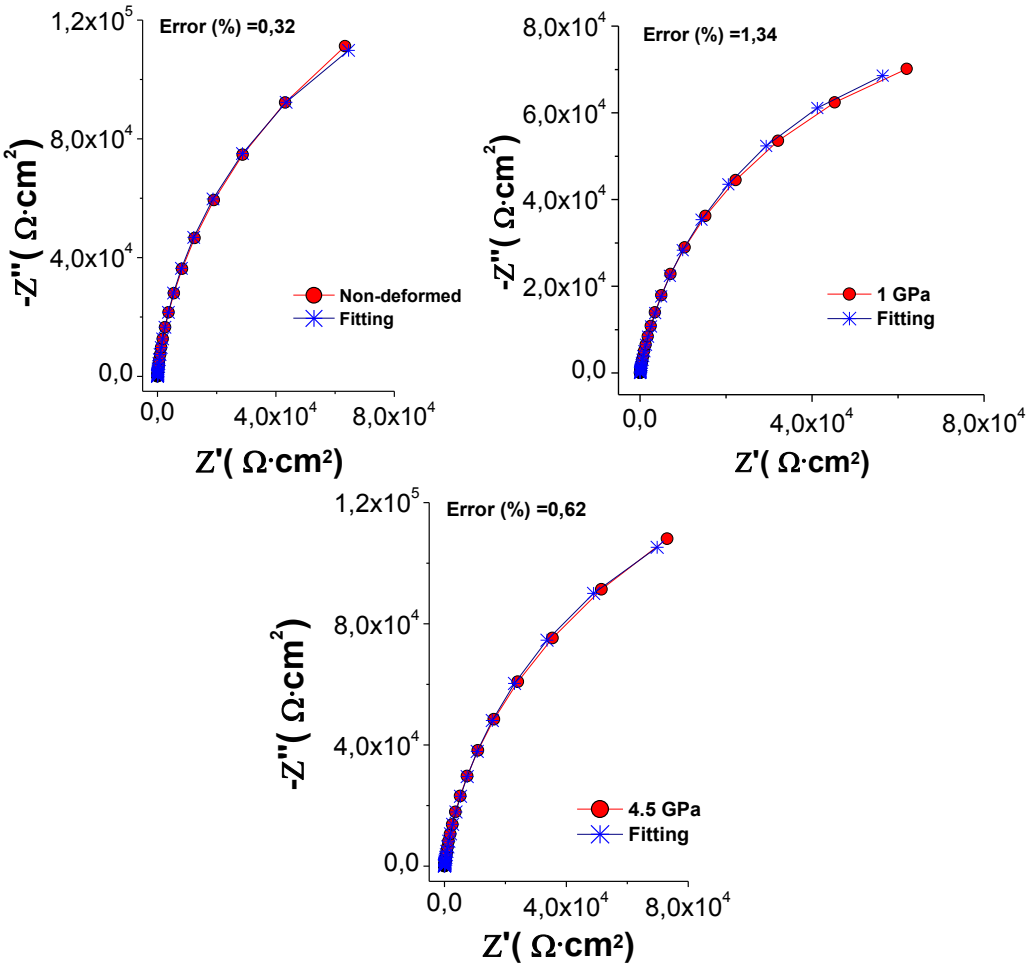

Figure 41: Nyquist diagrams of experimental data and simulated curves obtained by the Simad software for the polished surfaces of Ti13Nb13Zr alloy at ND, HPT1GPa, and HPT4.5GPa conditions.

Table 15: Equivalent electrical circuit parameters and effective capacitance associated with the CPEs obtained when fitting EIS data of polished samples of Ti13Nb13Zr alloy according to the model in Figure 40.

Condition	Rs $\Omega \cdot cm^2$	Qa $\mu F \cdot s^{(\alpha a-1)}$	α_a	Ra $\Omega \cdot cm^2$	$C_{eff(a)}$ $\mu F/cm^2$	Qdl $\mu F \cdot s^{(\alpha dl-1)}$	α_{dl}	Rct $\Omega \cdot cm^2$	$C_{eff(dl)}$ $\mu F/cm^2$
Non-deformed	22	7	0.94	57	16	9	0.94	3.0E+05	20
1 GPa	19	5	0.90	111	7	12	0.88	1.3E+05	17
4.5 GPa	21	6	0.90	124	9	11	0.91	1.7E+05	20

On the other hand, the capacitance values for the double layer ($C_{eff(dl)}$) were between 17 to 20 $\mu F \cdot cm^{-2}$ (see Table 15). These values are in the typical range,

10–40 μF/cm^2 [147]. The capacitance values for the porous layer ($C_{eff(a)}$) were lower than $C_{eff(dl)}$.

Considering the layer as a planar capacitor, the thickness of the protective film δ (in nm) can be obtained from Equation 22 (see section 3.6.3.1):

$$\delta = \frac{\epsilon \cdot \epsilon_0}{C_{eff}}$$

where ϵ_0 is the vacuum permittivity (8.8542×10^{-14} F/cm) and ϵ the dielectric constant of the material. The value of the dielectric constant of TiO_2 is in the range of 18.2 to 173 [148] and an average value of the dielectric constant, ϵ = 100, has been selected by other authors [149–151], Then, Eq. (22) gives the protective film thickness of 3.75, 4.53 and 3.80 nm for Ti13Nb13Zr alloy, at ND, HPT1GPa and HPT4.5GPa conditions, respectively. These results show that the deformation by HPT of Ti13Nb13Zr alloy contributes to increasing the tendency to loss of electrons and releasing atoms into electrolyte is accelerated [133].

The results obtained by fitting EIS data indicate that the Ti13Nb13Zr alloy, non-deformed, and deformed by HPT, behaved in a very similar way. The differences are rather small, and this can be explained by the fact that the passive film formed on these conditions are basically of the same nature.

5.3.2 EEC proposed for anodized samples

It is common in the literature to analyze impedance results for TiO_2 nanotubes by a physical model [27,151,152], this model is expressed by a mathematical equation and by a “classical equivalent circuit”. Table 15 shows EEC most frequently proposed in the literature to model EIS data of TiO_2 nanotubes.

Table 15: Equivalent electrical circuits most frequently proposed in the literature to model EIS data of TiO_2 nanotubes.

Equivalent electrical circuit	Explanation
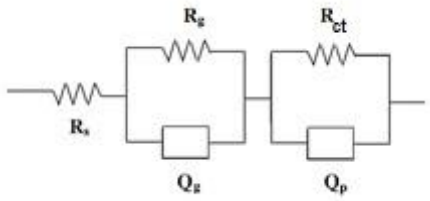	**Rs:** The solution resistance. **Qg** and **Rg**: The dielectric properties and resistivity of the film. **Qp** and **Rct**: The double-layer capacitance and interfacial charge-transfer resistance. *References:* [153–157].
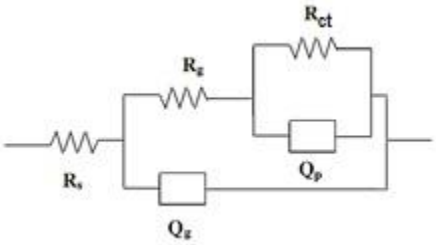	**Rs:** The solution resistance. **Qg** and **Rg**: The resistance and capacitance of the outer porous tube layer. **Qp** and **Rct**: The resistance and capacitance of the inner barrier layer. *References:* [149,158,159]
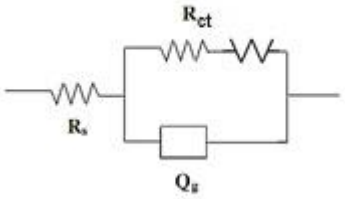	**Rs:** The solution resistance. **Rct:** Charge-transfer resistance. **Qg:** Constant phase element (CPE) used in place of double-layer capacitance. **W:** Warburg arising from a diffusion-controlled process at low frequency. *References:* [27,160]
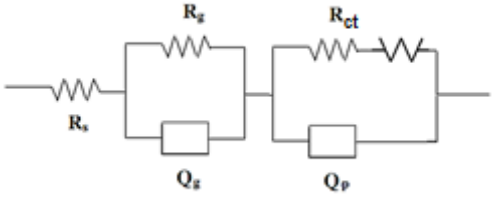	**Rs:** The solution resistance. **Qg** and **Rg**: The resistance and capacitance of the outer porous tube layer. **Qp** and **Rct**: The resistance and capacitance of the inner barrier layer. **W:** Warburg impedance. *References:* [161–163]
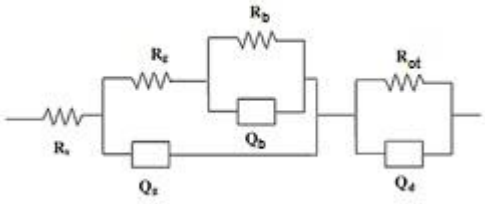	**Rs:** The solution resistance. **Qd** and **Rct**: Related to the dielectric properties and the resistivity of the film. **Qg** and **Rg**: The resistance and capacitance of the inner barrier layer. **Qb** and **Rb**: The resistance and capacitance of the outer porous tube layer. *References* [164,165]

Sometimes the experimental impedance is not a semicircle, and a certain dispersion in the frequency is usually found. Therefore, it does not seem relevant to model the impedance results of the anodized samples in this work with "classical equivalent circuits" mentioned above. However, the EEC 1, 4, and 5 shown in Table 15 were tested to fitting EIS data of the anodized samples (data not shown). The results were not satisfactory due to high fitting errors, and the values of the obtained parameters were outliers.

De Levie [166–168] proposed a model to describe the behavior of porous electrodes that can be conveniently described using a transmission line model (TL). On the other hand, Bisquert et al. developed a complete series of TL models for organic [169] and inorganic nanostructured systems [170,171]. These models will be presented below.

The remainder of this section will be dedicated to the study of the porous electrode model, and more precisely of the transmission line model.

5.3.2.1 Model of De Levie for the characterization of porous electrodes

De Levie considered that the impedance of a porous electrode could be described by a parallel schema of identical cylindrical pores of length L, as is shown in Figure 42 [172], ideally filled by the electrolyte and along which the resistivity of the solution is independent of the position x [173].

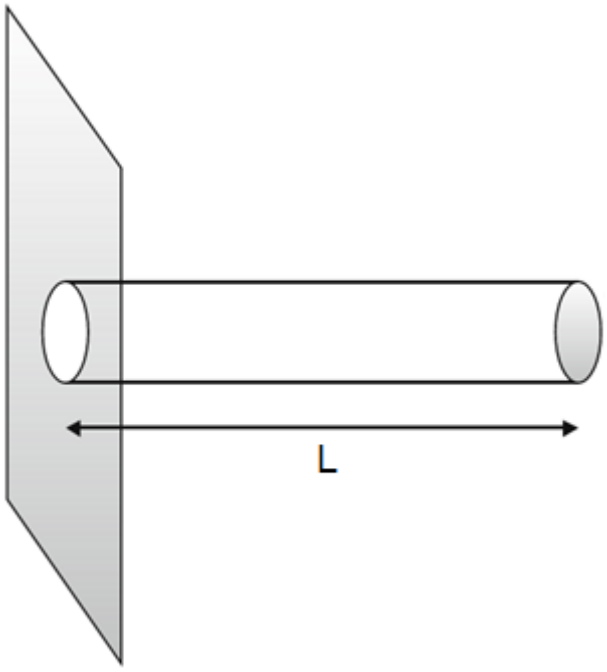

Figure 42: Model of a cylindrical porous electrode. The gray area is nonconductive. Adapted from Lasia et al., (2008) [172].

The conductivity of the solid phase is assumed to be infinite (metallic electrode behavior), and the local impedance is independent of x (thus no axial concentration gradient is considered, and the ohmic drop is neglected) [173]. The analytical expression of the impedance of a pore "$\mathbf{Z_{De\ Levie}}$" is given by Eq 18 [173]:

$$Z_{\text{De Levie}} = (R_0 Z_0)^{1/2} \coth\left(L\sqrt{\frac{R_0}{Z_0}}\right) \quad \textbf{(25)}$$

Where R_0 ($\Omega \cdot cm^{-1}$) and Z_0 ($\Omega \cdot cm^{-1}$) are, respectively, the resistance of the electrolyte in the pore and the interfacial impedance, for a unit of pore length.

5.3.2.2 Transmission lines model

To explain the impedance behavior of non-ideal porous electrodes, Bisquert et al., (2000) [169] developed an improved and generalized model involving the concept of the transmission line. The starting point is the same as for the De Levie model, i.e., the pores are considered cylindrical, of finite length L, deposited on a

conductive substrate, and immersed in an electrolyte [25]. This structure is represented in Figure 43. It is assumed that the ionic species in the pores flooded with electrolyte can be exchanged freely with the bulk solution at the pore´s mouth (x = 0 in the Figure 43) , and also that the electronic charge carrier in the solid phase can be withdrawn or injected freely at the contact with the substrate (x = L in Figure 43) [174].

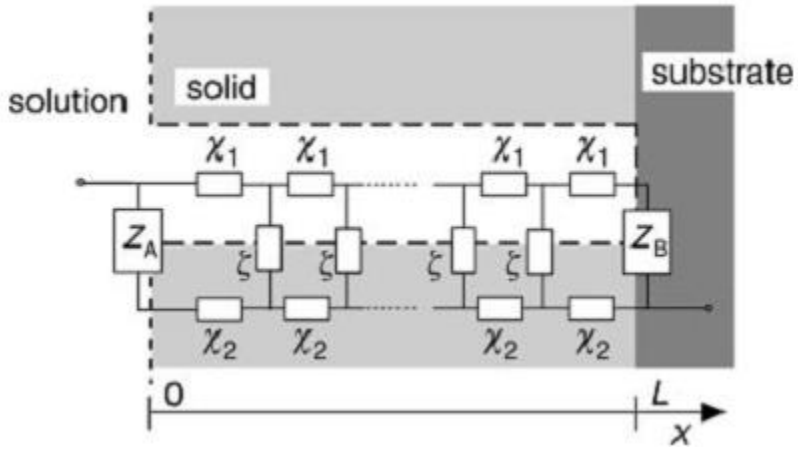

Figure 43: Scheme of a porous electrode. Adapted from Bisquert et al., (2000) [174].

The subscripts 1 and 2 denote the liquid (channel 1) and solid phase (channel 2), respectively. χ1 is the impedance of the electrolyte within the pore, and χ2 is the impedance of the porous electrode's solid phase; these also describe a local ohmic drop at each point of the transport channels. The element ξ represents the interfacial impedance and describes an exchange of electrical charge at the interface (solution/porous solid) owing to faradaic currents and polarization at the pore surface. Z_A is an impedance describing the specific conditions of polarization of electronic carriers at the film/electrolyte boundary, and similarly for Z_B ionic and/or electronic polarization at the bottom of the pore.

The complete analytic expression of such a transmission line is the following expression:

$$Z = \frac{1}{x_1 + x_2}\left[\lambda(x_1 + x_2)S_\lambda + (Z_A + Z_B)C_\lambda + \frac{1}{\lambda(x_1 + x_2)}Z_A Z_B S_\lambda\right]^{-1} \times \left(L\lambda x_1 x_2 (x_1 + x_2)S_\lambda + x_1[\lambda x_1 S_\lambda + L x_2 C_\lambda]Z_A + x_2[\lambda x_2 S_\lambda + L x_1 C_\lambda]Z_B + \frac{1}{x_1 + x_2} \times \left[2x_1 x_2 + ({x_1}^2 + {x_2}^2)C_\lambda + \frac{L}{\lambda}x_1 x_2 S_\lambda\right] Z_A Z_B\right) \quad \textbf{(26)}$$

Where the notations $C_\lambda = cosh\left(\frac{L}{\lambda}\right)$, $S_\lambda = sinh\left(\frac{L}{\lambda}\right)$, and $\lambda = [\xi/(x_1 + x_2)]^{1/2}$ have been used.

In this manner, the general transmission line shown in Figure 43 gives rise to several models of transmission lines [148,174,175] depending on the different types of assumptions concerning the geometry and microstructure leading to the TL model.

5.3.2.3 Transmission line model applied to EIS data of anodized samples.

To obtain quantitative and meaningful numerical results when a transmission line model is applied, the choice of appropriate physical models and boundary conditions with the corresponding, accurately determined, kinetic, and transport parameters are key issues.

The first hypothesis proposed in this study is for channel 1 (the liquid) and consist of admitting that a Warburg impedance is observed, which may be due to the diffusion of oxygen into channel 1. Oxygen transport takes place in the electrolyte towards pore surfaces [176]. Therefore, channel 1 can be represented by $\chi_1 = r_1 + Z_W$.

For traditional electrodes with large particle sizes, the Warburg-type diffusion impedance, which draws a 45° line in the complex plane representation (Nyquist plot), has been widely reported at low frequencies [177–179]. However,

impedance spectra of modern thin film and nanoparticle battery electrodes show deviations in the spectra away from the conventional Warburg model [178,180].

On the other hand, the second hypothesis assumes that channel 2 is a resistive channel and is modeled by a distributed resistance.

$$\chi_2 = r_2$$

Thus, the total resistance (Ω) distributed in the resistive channel is given by

$$R_2 = L \cdot r_2$$

The third hypothesis assumes that the effect of an interfacial reaction in the pore surface can be modeled by a dispersive capacitance given by a CPE with a parallel charge transfer resistance to the interfacial impedance. That is:

$$\xi = \frac{r_3}{1 + r_3 q_3 (j\omega)^{\beta}}$$

Where q_3 is a constant and β is $0 < \beta < 1$.

The total pseudo-capacitance describing the interface is defined by

$$Q_3 = L \cdot q_3 \text{ (in F s}^{\beta-1}\text{)}$$

Where L is the length of the pores (in cm).

The fourth hypothesis is concerning the boundary impedances. The electrolyte | top of the pores is modeled by an impedance consisting of a resistance (R_A). The electrolyte | substrate interface is modeled by an impedance consisting of a CPE element $(Q_B(j\omega)^n)^{-1}$.

To strictly justify these assumptions, preliminary fittings have been made, in a first approach, considering the expression of the impedance of such a transmission line as:

$$Z = R_s + \frac{1}{x_1 + x_2}\left[\lambda(x_1 + x_2)S_\lambda + (Z_A + Z_B)C_\lambda + \frac{1}{\lambda(x_1 + x_2)}Z_A Z_B S_\lambda\right]^{-1}$$
$$\times \left(L\lambda x_1 x_2 (x_1 + x_2)S_\lambda + x_1[\lambda x_1 S_\lambda + L x_2 C_\lambda]Z_A + x_2[\lambda x_2 S_\lambda + L x_1 C_\lambda]Z_B\right.$$
$$\left. + \frac{1}{x_1 + x_2} \times \left[2x_1 x_2 + ({x_1}^2 + {x_2}^2)C_\lambda + \frac{L}{\lambda}x_1 x_2 S_\lambda\right] Z_A Z_B\right)$$

Where the notations $x_1 = r_1 + Z_w$, $x_2 = r_2$, $C_\lambda = cosh\left(\frac{L}{\lambda}\right)$, $S_\lambda = sinh\left(\frac{L}{\lambda}\right)$, $Z_A = R_A$, $Z_B = \frac{1}{Q_B}(i\omega)^{-n}$, $\xi = \frac{r_3}{1 + r_3 q_3 (i\omega)^\beta}$, and $\lambda = [\xi/(x_1 + x_2)]^{1/2}$ have been used.

Figure 44 outlines the transmission line used in the present work.

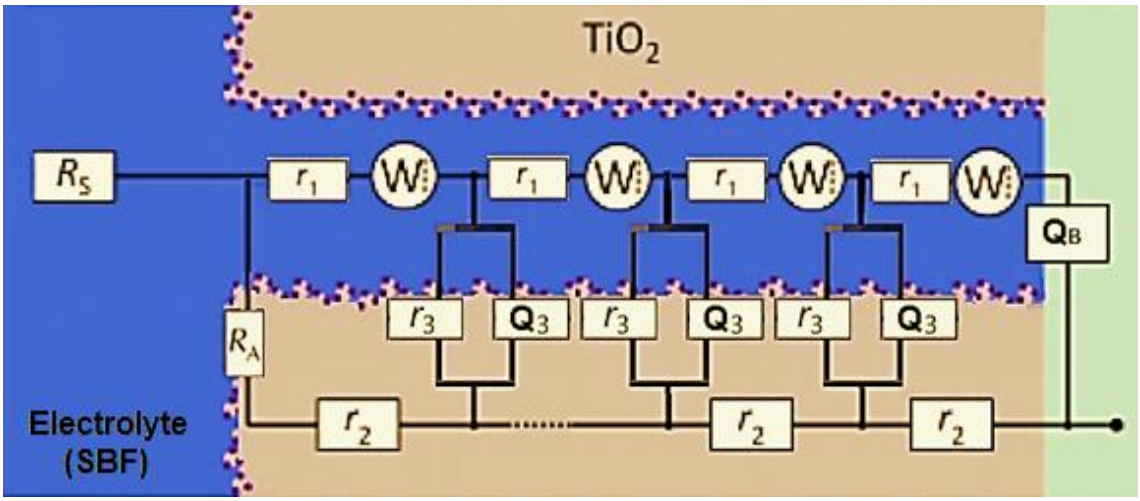

Figure 44: Transmission line used for modeling of EIS data of anodized samples of Ti13Nb13Zr alloy, non-deformed and deformed by HPT, immersed in SBF at 37 °C.

The fitting of EIS data as Nyquist representations is shown in Figure 45. The errors measured for the experimental and simulated data were 1.11% for the non-deformed sample and 2.90% for the 4.5 GPa deformed sample, which is quite reasonable.

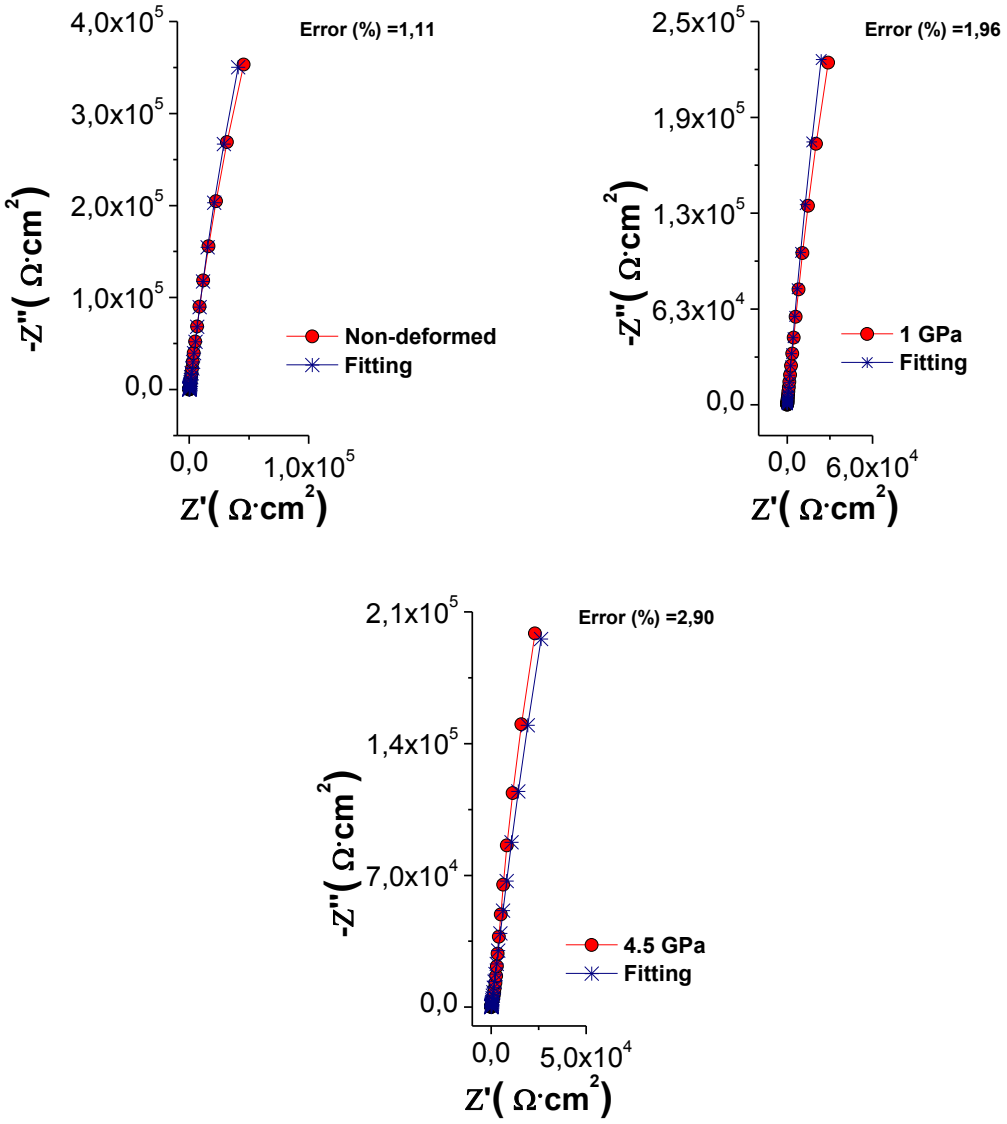

Figure 45: Nyquist diagrams of experimental data and simulated curves obtained by the Simad software for the anodized samples of Ti13Nb13Zr alloy at ND, HPT1GPa, and HPT4.5GPa conditions.

The equivalent circuit parameters obtained when fitting EIS data of anodized samples of Ti13Nb13Zr alloy (see section 5.2.2.3, Figure 35) at the ND, HPT1GPA, and HPT4.5GPa conditions, are shown in Table 16. Additionally, CPE behavior corresponding to systems for which a variation of properties is expected in the direction normal to the electrode, then it is possible to apply the equation

derived by Hsu-Mansfeld et al. Eq. (21) to calculate the effective capacitance associated with the CPE. These capacitance values are also shown in Table 16.

Table 16: Equivalent circuit parameters and effective capacitance associated with the CPEs obtained when fitting EIS data of anodized samples of Ti13Nb13Zr alloy according to the model in Figure 44.

Condition	$\chi 1$	$\chi 2$	ξ				Z_A	Z_B			R_s
	R_1 (Ω)	R_2 (Ω)	R_3 (Ω)	Q_3 ($F^{\beta-1}$)	β	C_β μF/cm^2	R_A (Ω)	Q_B (F^{n-1})	n	C_n μF/cm^2	R_s (Ω)
Non-deformed	1	241	2.3E+15	1.4E-06	0.96	14	3.0E+07	1.4E-06	0.96	3	70.0
1 GPa	6	736	1.8E+15	1.2E-06	0.97	19	3.0E+07	1.0E-06	0.96	2	70.0
4.5 GPa	1	100	1.8E+15	2.4E-06	0.94	42	2.3E+07	2.0E-06	0.96	5	70.0

It can be seen from the data in Table 16, high R_A values, as well as low Q_3 and Q_B values. These results indicate that a highly stable film was formed on the surface of the anodized samples of Ti13Nb13Zr alloy, non-deformed and deformed by HPT, immersed in SBF. Moreover, the n values were close to 0.95, which suggest that the TiO_2 nanostructures formed displays a near capacitive behavior.

On the other hand, it can be seen that internal resistance (R_2) of the solid channel is higher for the samples non-deformed and deformed by HPT at 1 GPa. This result may be explained by the fact that the nanotubular layer is thicker in these samples than in sample deformed at 4.5 GPa (see Table 4). Therefore, it seems that there is a proportional relationship between TiO_2 nanotube length and corrosion resistance.

Regarding the effective interfacial capacitance (C_β) associated to the ξ element, for all conditions, they are of the order of several tens of $\mu F \cdot cm^{-2}$ (Table 16), which are typical values for double layer capacitances. Further, the effective capacitance associated with the boundary CPE were 3, 2 and 5 $\mu F \cdot cm^{-2}$ for Ti13Nb13Zr alloy, at ND, HPT1GPa and HPT4.5GPa conditions, respectively. These values are of the order of magnitude of a passive film capacitance.

The passive film thickness was calculated from the effective capacitance (Eq (22)). The thickness values were of 25.5, 39.6 and 17.6 nm for Ti13Nb13Zr alloy at ND, HPT1GPa and HPT4.5GPa conditions, respectively. These results show that the anodization of Ti13Nb13Zr alloy contributes to increasing the passive film thickness. The passive film thicknesses, as well as the length of the nanostructures, are affected by the deformation by HPT.

Finally, the experimental EIS data obtained for the anodized Ti13Nb13Zr alloy were satisfactorily fitting by the model proposed in Figure 44. Therefore, the physical behavior of the system was well described by this transmission line model.

5.3.3 EEC proposed to samples chemically treatment by HCl etching and NaOH activation

Several reports have shown that during acid etching, the thin passive titanium oxide layer dissolves to form TiH_2 [181]. In contact with air moisture, a new titanium oxide layer is formed. This layer is thinner than the original one. In alkali solution, however, even this thin passive layer dissolves to form a layer containing Na^+ ions, as is shown in Figure 46 [128,139,182,183].

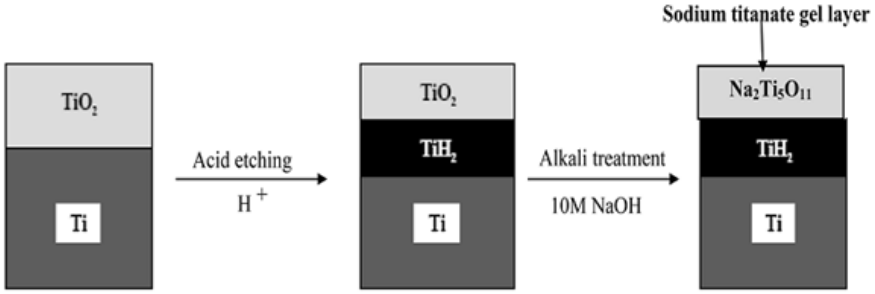

Figure 46: Schematic representation of surface structural change on titanium metal in the presence of acid etching and alkali treatment. Adapted from Sasikumar et al., (2017) [139]**.**

However, the microstructural characterization, of the chemically treated samples, indicated the presence of anatase, rutile, and sodium titanate, as was mentioned in section 5.1.3. The presence of anatase and rutile could be explained because TiH_2 is very easy to dissolve in alkaline solution, and a porous layer of

TiO_2 can be obtained [184]. On the other hand, the impedance spectrum of the samples with chemical treatment showed three-time constants that could be associated with three different layers (see Figure 37). Therefore, in this work, it is proposed an EEC for an electrode with three different layers: a compact inner layer of titanium dioxide (TiO_2), an intermediate TiO_2 layer and an outer layer of sodium titanate ($Na_2Ti_5O_{11}$).

The proposed EEC for chemically treated samples is shown in Figure 47.

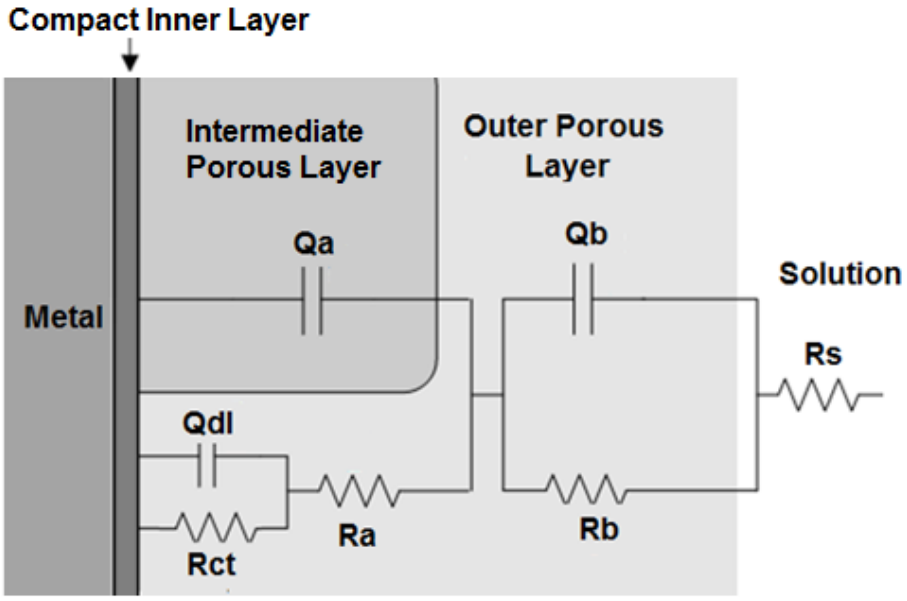

Figure 47: Equivalent circuit for samples of Ti13Nb13Zr alloy chemically treated by HCl and NaOH at ND, HPT1GPa, and HPT4.5GPa conditions. Adapted from Orazem et al., (2017)[185].

Thus, the EIS data were fitted using the following EEC:

$$R_s + (Q_b / R_b) + Q_a / (R_a + (Q_{dl} / R_{ct})),$$

where R_s represents the electrolyte resistance, R_b represents the resistance of the outer layer, Q_b is the constant-phase element for the outer layer, R_a is the resistance of the intermediate layer, Q_a is the constant-phase element for the intermediate layer, R_{ct} represents the resistance of charge-transfer, Q_{dl} is the

constant-phase element for the double layer at the dense inner layer-electrolyte interface.

The fitting of EIS data as Nyquist representation is shown in Figure 48. The errors measured for the experimental and simulated data were 0.72% for the non-deformed sample and 3.27% for the 4.5 GPa deformed sample, which is quite reasonable.

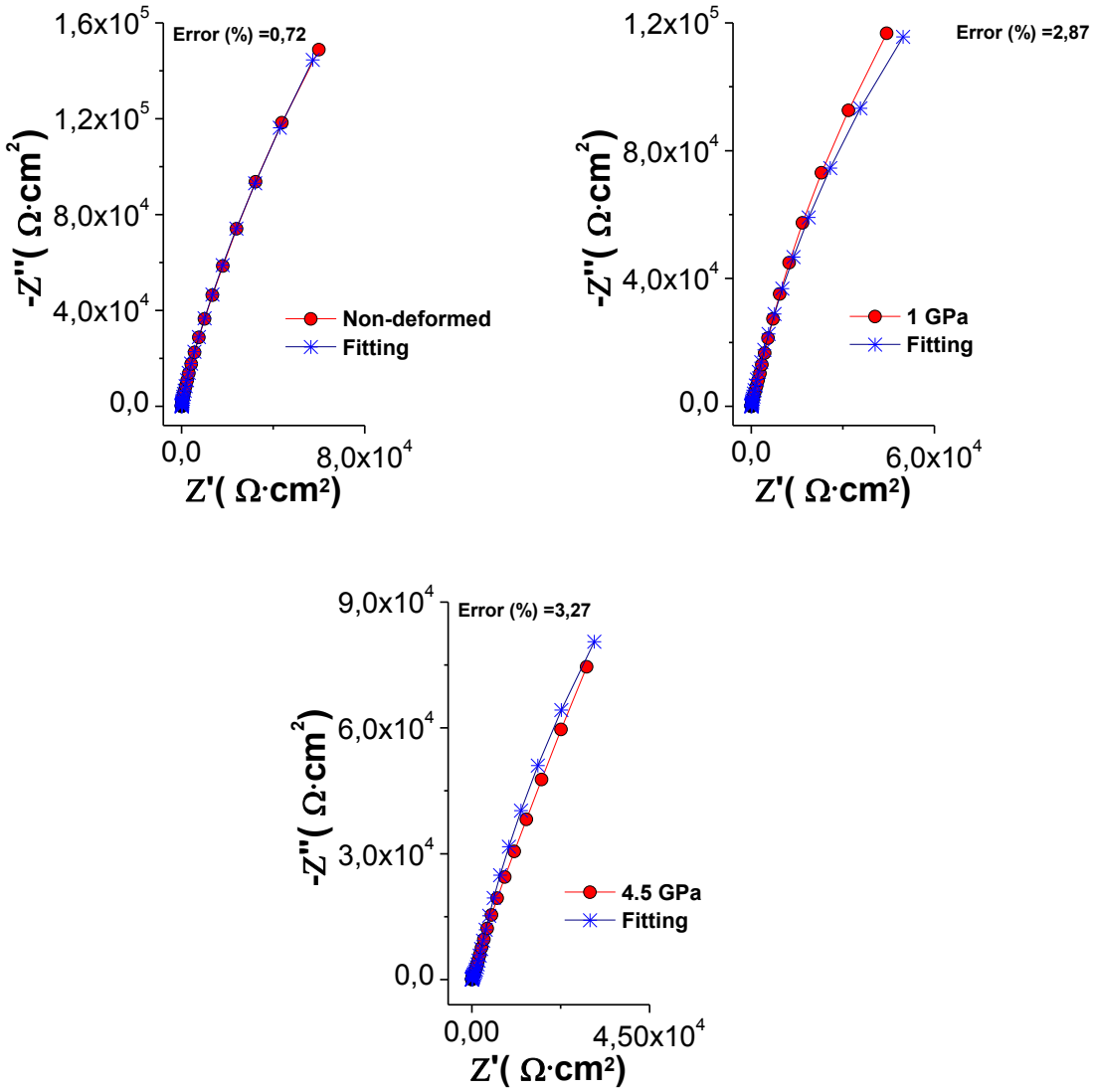

Figure 48: Nyquist diagrams of experimental data and simulated curves obtained by the Simad software for samples of Ti13Nb13Zr alloy chemically treated by HCl and NaOH at ND, HPT1GPa, and HPT4.5GPa conditions.

The equivalent circuit parameters obtained when fitting EIS data of samples of Ti13Nb13Zr alloy chemically treated by HCl and NaOH are shown in Table 17. Further, the effective capacitance associated with the CPE was calculated with the equation derived by Brug et al. (Eq.20). These capacitance values are given in Table 17.

Table 17: Equivalent circuit parameters and effective capacitance associated with the CPEs obtained when fitting EIS data of samples of Ti13Nb13Zr alloy chemically treated by HCl and NaOH according to the EEC in Figure 47.

	Condition		
Element	**Non-deformed**	**1 GPa**	**4.5 GPa**
R_s (Ω· cm^2)	22	20	20
Q_b (μF ·s(αb-1))	52	28	43
α_b	0.70	0.76	0.72
R_b (Ω· cm^2)	28	15	15
$C_{eff(b)}$ (μF/ cm^2)	2.2	2.0	2.0
Q_a (μF ·s(αa-1))	19	11	55
α_a	0.70	0.75	0.70
R_a (Ω· cm^2)	7	2	10
$C_{eff(a)}$ (μF/ cm^2)	0.4	0.3	0.5
Q_{dl} (μF ·s(αdl-1))	21	39	19
α_{dl}	0.98	0.90	0.96
R_{ct} (Ω· cm^2)	7.6E+05	6.8E+05	6.0E+05
$C_{eff(dl)}$ (μF/cm^2)	19	18	14

It can be seen from the data in Table 17, high R_{ct} values, which implies high corrosion resistance. The exponent of the CPE, α_b in the case of Q_b equals a value in between 0.70 and 0.76, while α_a equals a value in between 0.70 and 0.75 in the case of Q_a. These exponent values indicate a highly porous interfacial range between the outer layer and the substrate [186]. The exponent of the CPE related to the double layer was between 0.90 and 0.98, which suggest that the dense inner

layer of samples chemically treated by HCl and NaOH displays a near capacitive behavior.

On the other hand, the capacitance values for the double layer ($C_{eff(dl)}$) were between 14 to 19 $\mu F \cdot cm^{-2}$ (see Table 17). These values are in the typical range, 10–40 $\mu F/cm^{-2}$. The capacitance values for the porous outer layer ($C_{eff(b)}$) and intermediate porous layer ($C_{eff(a)}$) were lower than $C_{eff(dl)}$.

The thickness of the protective film δ (in nm) can be obtained from equation 22. Then, Eq. (22) gives the inner protective film thickness of 4.05, 4.30 and 5.41 nm for chemically treated Ti13Nb13Zr alloy, at ND, HPT1GPa and HPT4.5GPa conditions, respectively. These results show that the chemical treatment, by HCl etching and NaOH activation, contributes to increasing the inner layer thickness comparing with polished samples. Also, the deformation by HPT of Ti13Nb13Zr alloy contributes to increasing the thickness of this inner layer.

The results obtained by fitting EIS data indicate that the deformed and non-deformed Ti13Nb13Zr alloy chemically treated by HCl and NaOH, behaved in a very similar way. The differences are rather small, and this can be explained by the fact that the passive film formed on these alloys is mostly of the same nature.

5.3.4 EEC proposed to samples chemically treatment by H_3PO_4 etching and NaOH activation

The equivalent circuit is shown in Figure 47 also was used to fitting the EIS data of samples of Ti13Nb13Zr alloy chemically treated by H_3PO_4 and NaOH. These fitting are shown in Figure 49. The errors measured for the experimental and simulated data were 1.69% for the non-deformed sample and 1.19% for the 4.5 GPa deformed sample, indicating that data adjusted well to the proposed equivalent circuit.

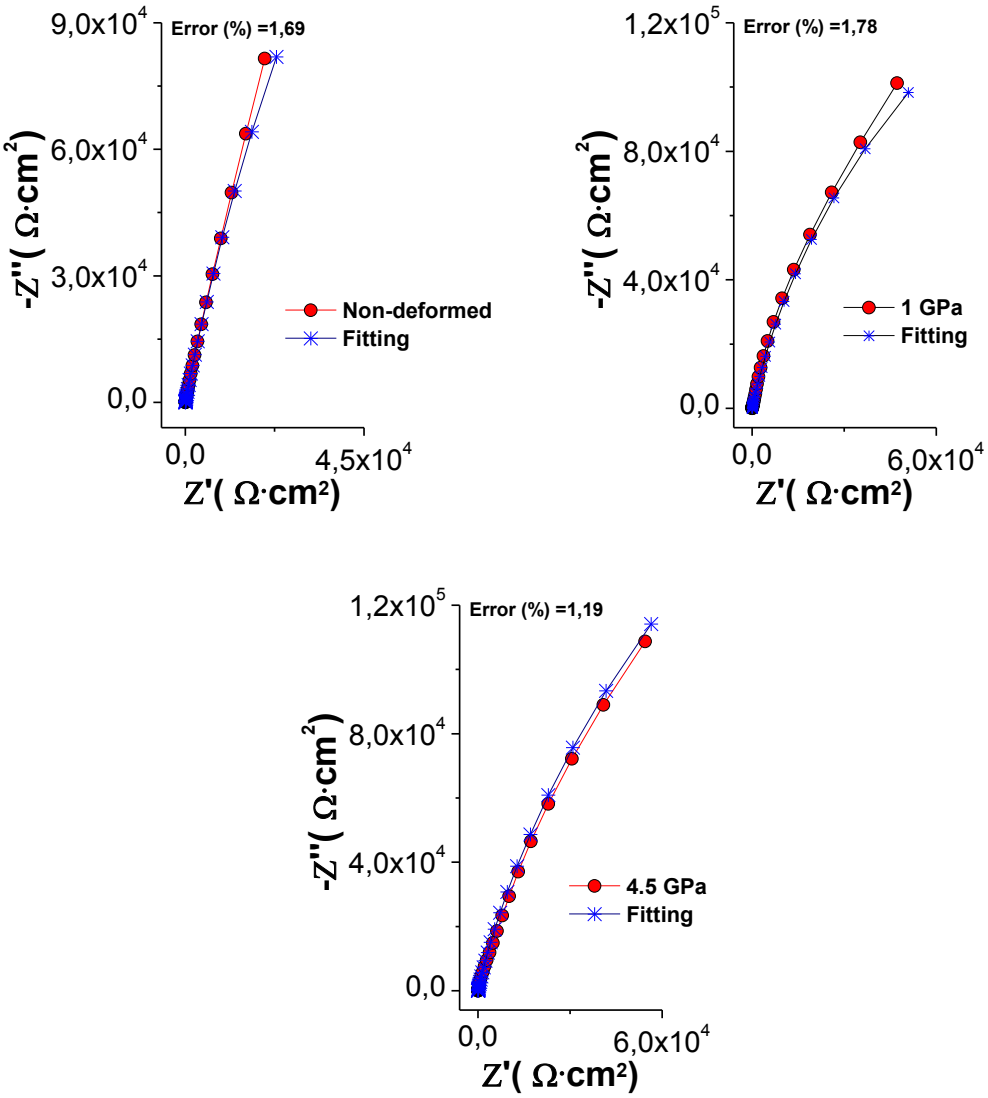

Figure 49: Nyquist diagrams of experimental data and simulated curves obtained by the Simad software for samples of Ti13Nb13Zr alloy chemically treated by H_3PO_4 and NaOH at ND, HPT1GPa, and HPT4.5GPa conditions.

The equivalent circuit parameters and effective capacitance (calculated by an equation derived by Brug et al.) associated with the CPEs obtained are shown in Table 18.

Table 18: Equivalent circuit parameters and effective capacitance associated with the CPEs obtained when fitting EIS data of samples of Ti13Nb13Zr alloy chemically treated by H_3PO_4 and NaOH according to the EEC in Figure 47.

	Condition		
Element	**Non-deformed**	**1 GPa**	**4.5 GPa**
R_s (Ω· cm^2)	20	20	20
Q_b (μF ·s(αb-1))	42	15	15
α_b	0.72	0.81	0.78
R_b (Ω· cm^2)	13	2	10
$C_{eff(b)}$ (μF/ cm^2)	1.9	1.3	1.2
Q_a (μF ·s(αa-1))	65	42	14
α_a	0.78	0.82	0.77
R_a (Ω· cm^2)	78	44	20
$C_{eff(a)}$ (μF/ cm^2)	9	8	1.0
Q_{dl} (μF ·s(αdl-1))	14	12	32
α_{dl}	0.96	0.98	0.91
R_{ct} (Ω· cm^2)	5.1E+05	4.5E+05	7.1E+05
$C_{eff(dl)}$ (μF/cm^2)	10	10	15

It can be seen from the data in Table 18, high R_{ct} values. These results indicate that a highly stable film was formed on the surface of samples chemically treated by H_3PO_4 and NaOH immersed in SBF. Moreover, the α_{dl} values were close to 0.95, which suggest that the samples chemically treated displays a near capacitive behavior. The same behavior was observed as the samples with acid-etched with HCl, where the values of α_b and α_a were between 0.72 and 0.82, which was a consequence of frequency dispersion of the outer layer [187].

On the other hand, the capacitance values for the double layer ($C_{eff(dl)}$) were between 10 to 15 μF·cm^{-2} (see Table 17). These values are in the typical range, 10–40 μF·cm^{-2}. The capacitance values for the porous outer layer ($C_{eff(b)}$) and intermediate porous layer ($C_{eff(a)}$) were lower than $C_{eff(dl)}$.

The thickness of the protective film δ (in nm) can be obtained from equation 22. The thickness values were of 7.62, 7.43, and 5.03 nm for Ti13Nb13Zr alloy at ND, HPT1GPa and HPT4.5GPa conditions, respectively. These results show that the chemical treatment contributes to increasing the inner layer.

The results obtained by fitting EIS data indicate that the deformed and non-deformed Ti13Nb13Zr alloy chemically treated by H_3PO_4 and NaOH behaved in a very similar way.

5.4 Bioactivity of Ti13Nb13Zr alloy

In order to characterize the bioactivity of the Ti13Nb13Zr alloy, the amount of hydroxyapatite (HAp) spontaneously deposited on the surface of the samples was measured. The samples were immersed in SBF for 1, 7, and 14 days.

5.4.1 Bioactivity of polished samples

Figure 50 shown SEM-FEG observations of polished samples, subjected to the bioactivity tests, after 1, 7, and 14 days immersed in SBF.

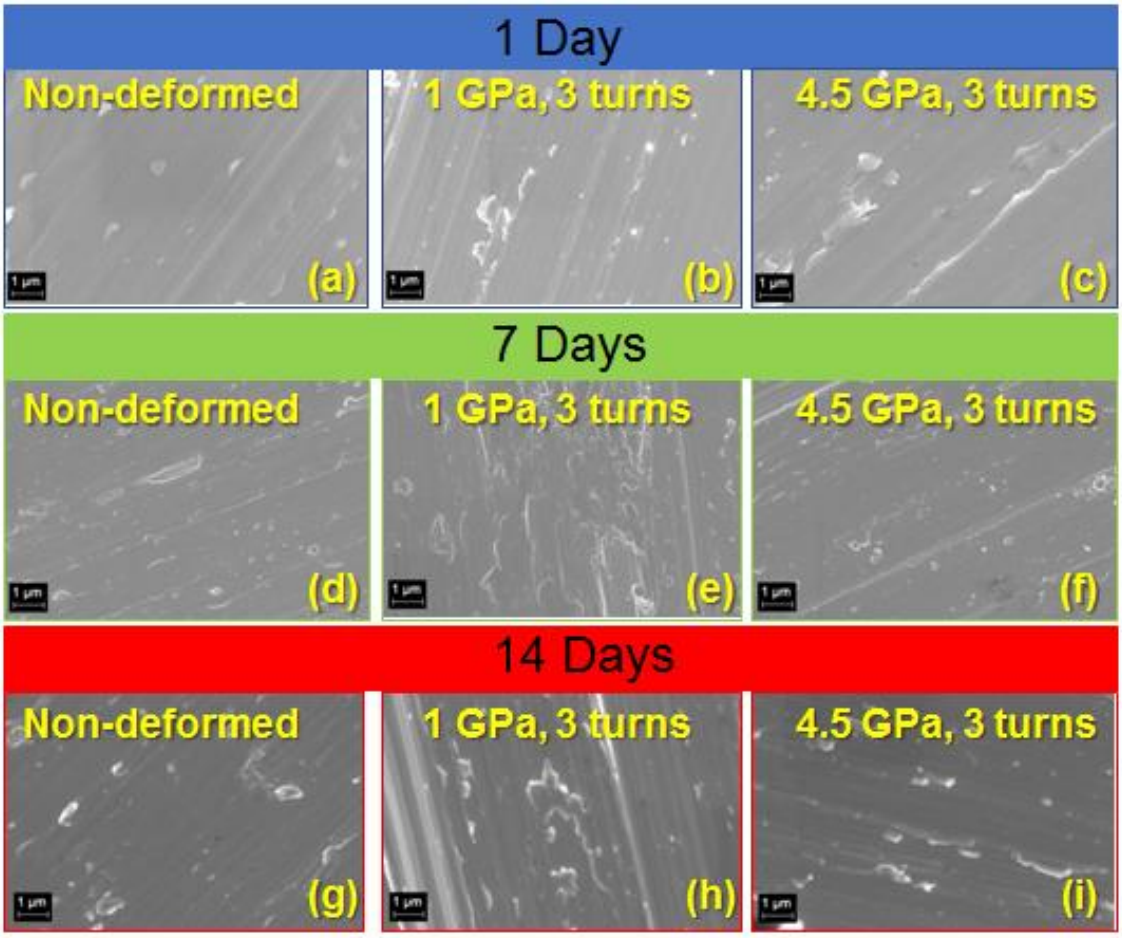

Figure 50: SEM-FEG observations (scale bar 1 μm) of polished samples of Ti13Nb13Zr alloy, non-deformed, and deformed by HPT, subjected to the bioactivity tests after 1, 7, and 14 days immersed in SBF.

From Figure 50, one can see that even after 14 days of immersion in the physiological solution, no apatite was detected on any surfaces of the polished samples of Ti13Nb13Zr alloy.

Table 19 shows the EDS analysis performed for each condition. The results confirm that there was no apatite formation on the surface of the samples.

Table 19: The quantitative chemical EDS analysis of Ti13Nb13Zr alloy non-deformed and deformed by HPT after soaking in SBF solution for 1, 7, and 14 days.

		Chemical element (at %)					
Soaking time	**Condition**	**Ti**	**Zr**	**Nb**	**O**	**Ca**	**P**
1 day	Non-deformed	77.58	8.82	8.68	4.92	-	-
	1 GPa	76.03	9.10	8.95	5.92	-	-
	4.5 GPa	75.64	9.54	8.95	5.87	-	-
7 days	Non-deformed	73.65	7.21	7.26	11.88	-	-
	1 GPa	73.29	7.57	7.92	11.22	-	-
	4.5 GPa	74.24	7.36	7.08	11.32	-	-
14 days	Non-deformed	71.40	7.20	7.19	14.21	-	-
	1 GPa	70.39	7.13	7.19	15.29	-	-
	4.5 GPa	70.12	7.26	7.16	15.46	-	-

The Ca/P ratio in the HAp, $Ca_{10}(PO_4)_6(OH)_2$, concerning stoichiometric value is 1.67 [188]. From the data in Table 19, it can be seen that neither calcium nor phosphorus were identified. Therefore, there was no formation of a film based on calcium and phosphorus on the surface of samples without surface treatments (polished samples). Furthermore, the polished samples were also weighed in order to verify the mass gain due to the formation of a HAp film. There was no change in the mass after 14 days of immersion in SBF.

5.4.2 Bioactivity of anodized samples

Figure 51 shows SEM-FEG observations of anodized samples, subjected to the bioactivity tests, after 1, 7 and 14 days immersed in SBF.

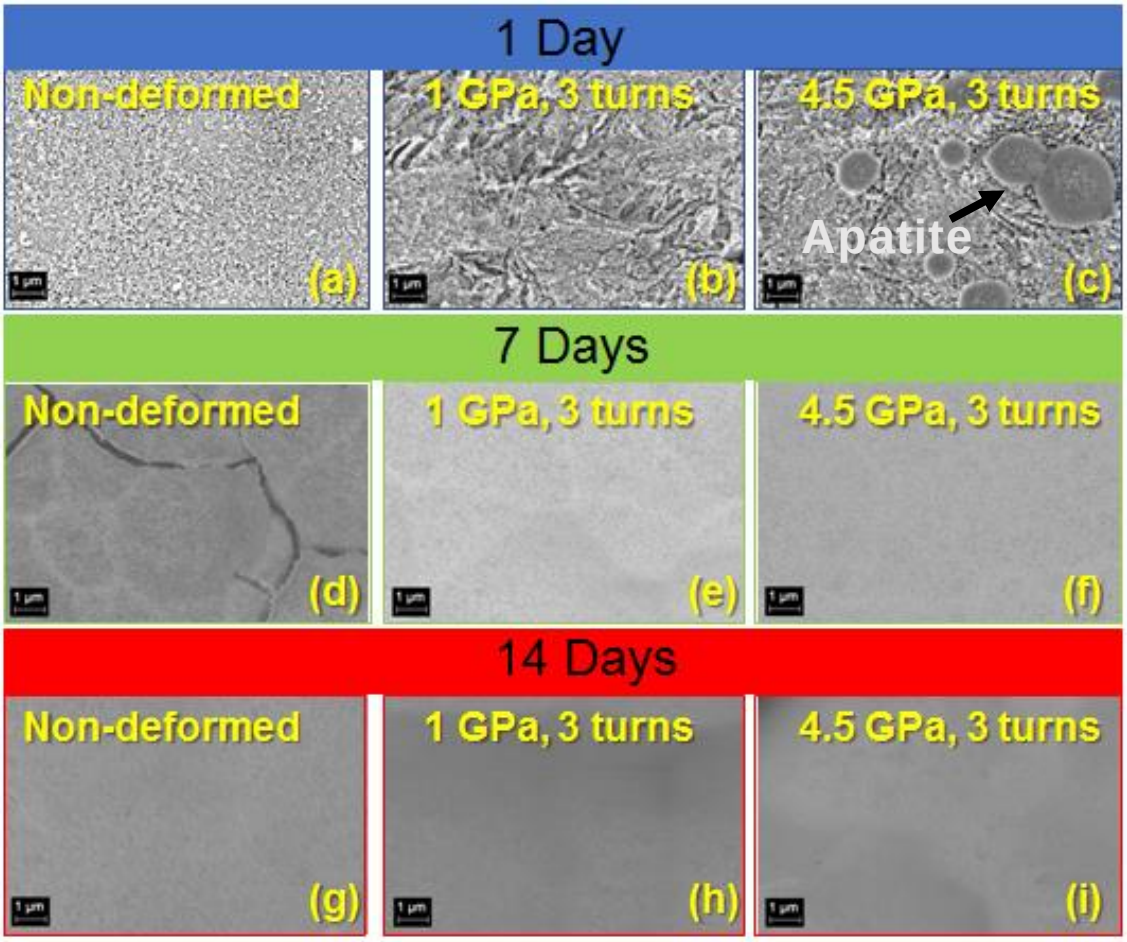

Figure 51: SEM-FEG observations (scale bar 1 µm) of anodized samples of Ti13Nb13Zr alloy, non-deformed, and deformed by HPT, subjected to the bioactivity tests after 1, 7, and 14 days immersed in SBF.

From Figure 51(c), it can be seen that only in the samples deformed at 4.5 GPa, there was the formation of apatite deposits from 24 hours of immersion in SBF. Homogeneous deposits of apatite were observed in all the conditions at 7 and 14 days of immersion in SBF.

Table 20 shows the EDS analysis performed for each condition and confirms that there is apatite formation from the first day for the deformed condition at 4.5 GPa and then for the 7 and 14 days for all the other conditions.

Table 20: Quantitative EDS analysis results and Ca/P molar ratio of anodized samples of Ti13Nb13Zr alloy, non-deformed and deformed by HPT, subjected to the bioactivity tests after 1, 7 and 14 days immersed in SBF.

		Chemical element (at %)								
Soaking time	**Condition**	**Ti**	**Zr**	**Nb**	**O**	**Na**	**Mg**	**Ca**	**P**	**Ca/P Molar Ratio**
1 day	Non-deformed	25.10	2.58	3.31	68.62	0.09	0.09	0.18	0.03	-
	1 GPa	24.89	2.62	3.42	68.68	0.08	0.09	0.19	0.03	-
	4.5 GPa	9.30	1.29	1.17	69.27	-	-	12.23	6.74	1.81
7 days	Non-deformed	0.57	-	-	66.87	0.33	0.92	19.36	11.95	1.62
	1 GPa	0.27	0.42	-	66.71	0.42	0.98	19.73	11.47	1.72
	4.5 GPa	0.05	0.42	-	68.66	0.30	0.85	18.97	10.75	1.76
14 days	Non-deformed	0.90	0.49	-	66.05	0.47	0.84	20.64	10.61	1.95
	1 GPa	0.47	0.50	-	66.21	0.46	0.86	20.65	10.85	1.90
	4.5 GPa	0.05	0.49	-	66.37	0.46	0.88	20.66	11.09	1.86

The molar ratio of Ca / P was calculated in Table 20. This molar ratio of Ca / P was approximately 1.80, which is higher than the stoichiometric ratio of 1.67, which indicates that the newly formed calcium phosphate is a type B carbonate apatite, in which PO_4^{3-} substitutes for CO_3^{2-}[189]. A more detailed explanation will be shown in the result's discussion section. On the other hand, to verify the mass gain by the formation of a hydroxyapatite film, the samples were weighed, and their results are shown in Figure 52.

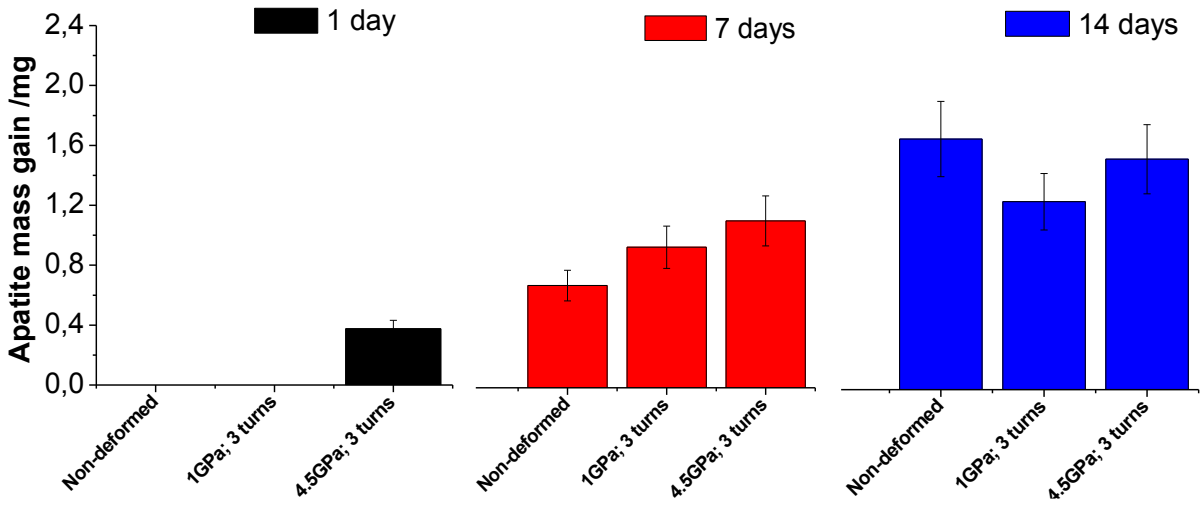

Figure 52: The weight change of anodized samples of Ti13Nb13Zr alloy, non-deformed, and deformed by HPT, after soaking in SBF for 1, 7 and14 days.

It was observed that from the first-day apatite is formed in the sample with 4.5 GPa deformation. From the seventh day, all samples show a mass gain due to the formation of an apatite film. At 14 days, the samples have an increase in mass, which shows that there is an increase in the growth of this film.

5.4.3 Bioactivity of samples chemically treatment by HCl etching and NaOH activation

Figure 53 shows SEM-FEG observations of samples chemically treatment by HCl etching and NaOH activation, subjected to the bioactivity tests, after 1, 7, and 14 days immersed in SBF.

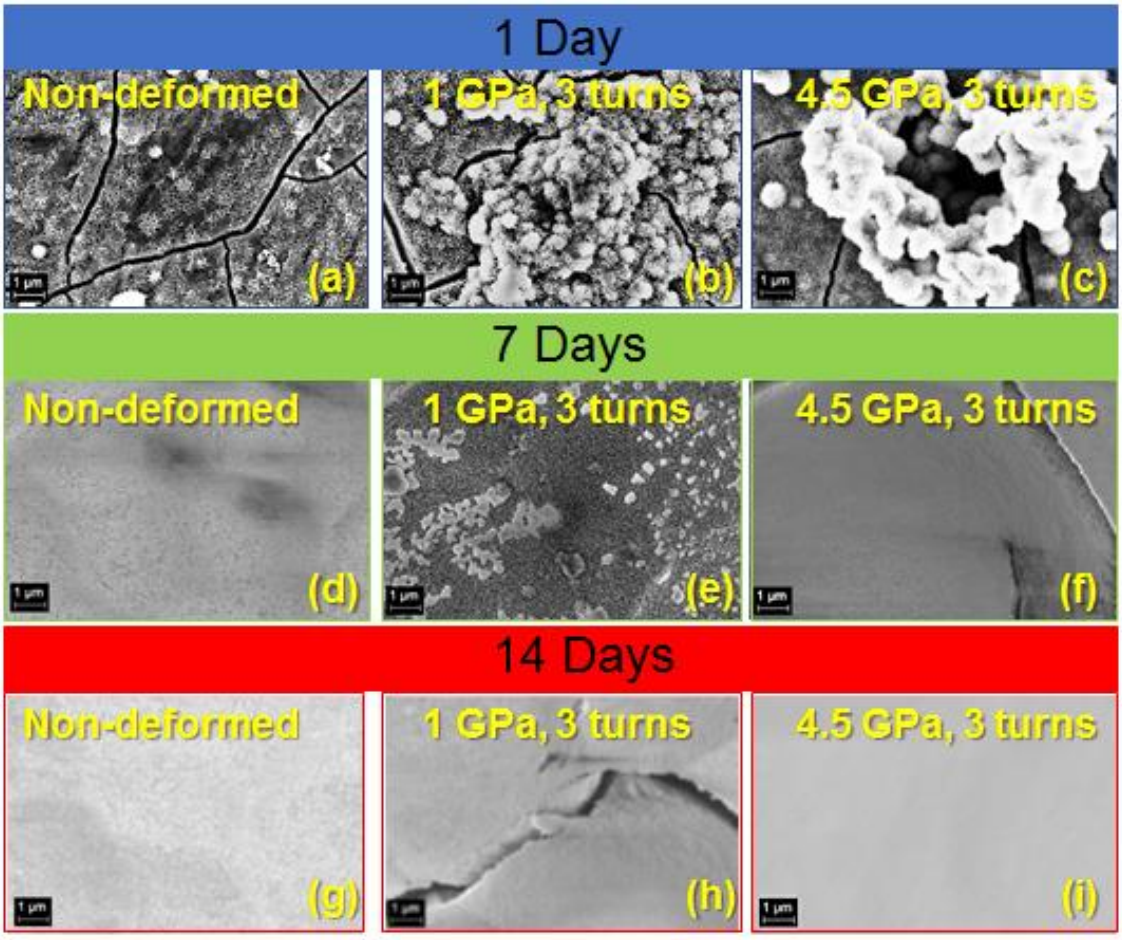

Figure 53: SEM-FEG observations (scale bar 1 µm) for samples of Ti13Nb13Zr alloy chemically treated, by HCl etching and NaOH activation, non-deformed and deformed by HPT, subjected to the bioactivity tests after 1, 7 and 14 days immersed in SBF.

From Figure 53, it is observed that after 7 days of immersion in the physiological solution, apatite was detected on all surfaces of samples chemically treatment by HCl and NaOH.

Table 21 shows the EDS analysis performed for each condition and confirms that there is apatite formation from 7 and 14 days for all conditions.

Table 21: Quantitative EDS analysis results and Ca/P molar ratio for samples of Ti13Nb13Zr alloy chemically treated by HCl and NaOH, non-deformed and deformed by HPT, subjected to the bioactivity tests after 1, 7 and 14 days immersed in SBF.

		Chemical element (at %)								
Soaking time	**Condition**	**Ti**	**Zr**	**Nb**	**O**	**Na**	**Mg**	**Ca**	**P**	**Ca/P Molar Ratio**
1 day	Non-deformed	23.95	1.21	2.41	67.28	0.56	0.59	3.57	0.43	-
	1 GPa	24.12	1.18	2.52	67.32	0.62	0.74	2.98	0.52	-
	4.5 GPa	22.78	1.24	2.64	68.42	0.52	0.65	3.33	0.42	-
7 days	Non-deformed	0.22	0.49	-	68.09	0.72	0.98	18.98	10.52	1.80
	1 GPa	22.49	1.05	2.11	67.42	0.72	0.63	3.56	2.03	1.76
	4.5 GPa	0.24	0.62	-	67.89	0.78	0.57	18.96	10.94	1.73
14 days	Non-deformed	0.16	0.47	-	67.36	0.49	0.85	19.24	11.43	1.68
	1 GPa	0.21	0.78	-	66.08	0.42	0.76	20.50	11.25	1.82
	4.5 GPa	0.12	0.38	-	65.66	0.42	0.82	20.24	12.36	1.64

The molar ratio of Ca / P was calculated in Table 21. This molar ratio of Ca / P was approximately 1.74, which indicates that the newly formed calcium phosphate is a type B carbonate apatite, in which PO_4^{3-} substitutes for CO_3^{2-}. On the other hand, to verify the mass gain by the formation of a hydroxyapatite film, the samples were weighed, and their results are shown in Figure 54.

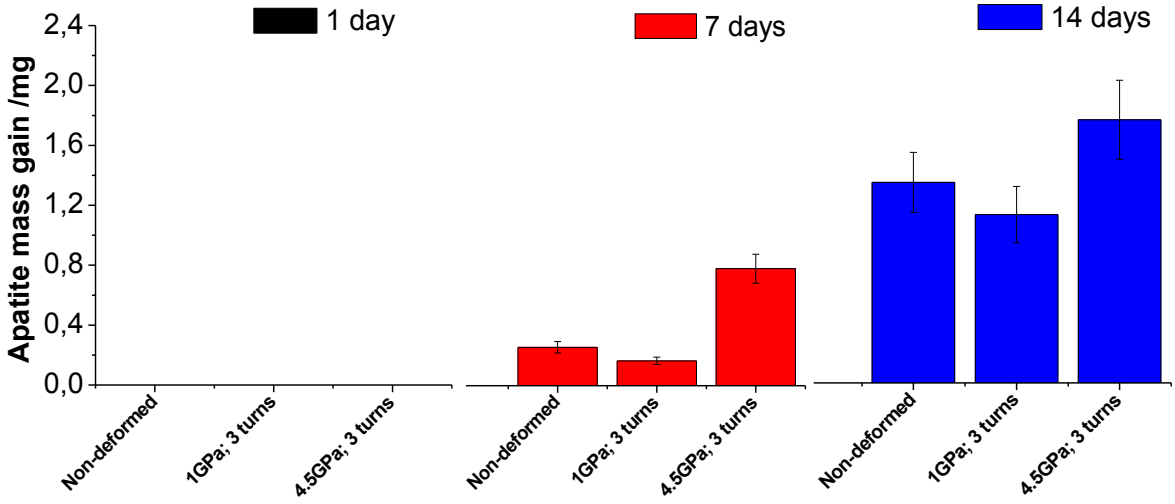

Figure 54: The weight change for samples of Ti13Nb13Zr alloy chemically treated by HCl and NaOH, non-deformed and deformed by HPT, subjected to the bioactivity tests after 1, 7 and 14 days immersed in SBF.

It was observed that from the seventh day, all samples show a mass gain due to the formation of an apatite film. At 14 days, the samples increase their mass, which shows that there is an increase in the growth of this film.

5.4.4 Bioactivity of samples chemically treatment by H_3PO_4 etching and NaOH activation

Figure 55 shows SEM-FEG observations of samples chemically treated by H_3PO_4 and NaOH, subjected to the bioactivity tests, after 1, 7, and 14 days immersed in SBF.

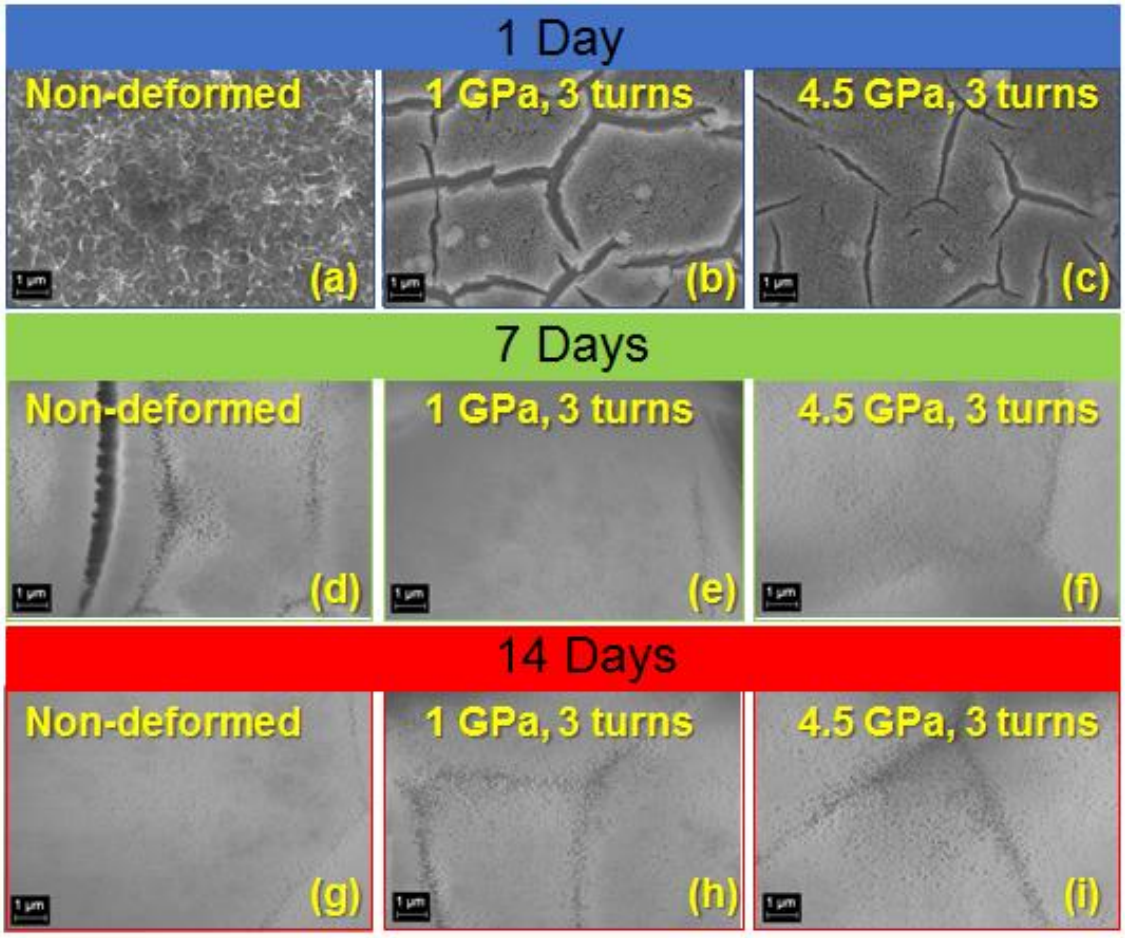

Figure 55: SEM-FEG observations (scale bar 1 µm) for samples of Ti13Nb13Zr alloy chemically treated by H_3PO_4 and NaOH, non-deformed and deformed by HPT, subjected to the bioactivity tests after 1, 7 and 14 days immersed in SBF.

Figure 55 shows that after 7 days of immersion in the physiological solution, apatite was detected on all surfaces of samples chemically treatment by H_3PO_4 and NaOH.

Table 22 shows the ESD analysis performed for each condition and confirms that there is apatite formation from 7 and 14 days for all conditions.

Table 22: Quantitative EDS analysis results and Ca/P molar ratio for samples of Ti13Nb13Zr alloy chemically treated by H_3PO_4 and NaOH, non-deformed and deformed by HPT, subjected to the bioactivity tests after 1, 7 and 14 days immersed in SBF.

		Chemical element (at %)								
Soaking time	**Condition**	**Ti**	**Zr**	**Nb**	**O**	**Na**	**Mg**	**Ca**	**P**	**Ca/P Molar Ratio**
1 day	Non-deformed	26.98	1,31	2,72	65,38	1,40	0,61	1,55	0,05	-
	1 GPa	26,01	1,53	2,62	66,14	1,30	0,72	1,38	0,30	-
	4.5 GPa	27,14	1,12	2,48	66,23	1,12	0,18	1,45	0,28	-
7 days	Non-deformed	0,06	0,29	-	70,24	0,36	0,69	17,64	10,72	1,65
	1 GPa	0,38	0,15	-	62,29	0,46	1,09	21,48	14,15	1,52
	4.5 GPa	0,25	0,19	-	67,48	0,40	0,86	18,77	12,06	1,56
14 days	Non-deformed	0,15	0,24	-	68,86	0,38	0,78	18,20	11,39	1,60
	1 GPa	0,27	0,19	-	65,58	0,42	0,93	19,84	12,77	1,55
	4.5 GPa	0,22	0,22	-	66,27	0,41	0,89	19,56	12,44	1,57

The molar ratio of Ca / P was calculated in Table 22. This molar ratio of Ca / P was approximately 1.58. If the Ca/P is lower than 1.67, β-tricalcium phosphate (TCP) and other phases, such as Tetracalcium phosphate (TTCP), will be present with HA. On the other hand, to verify the mass gain by the formation of a hydroxyapatite film, the samples were weighed, and their results are shown in Figure 56.

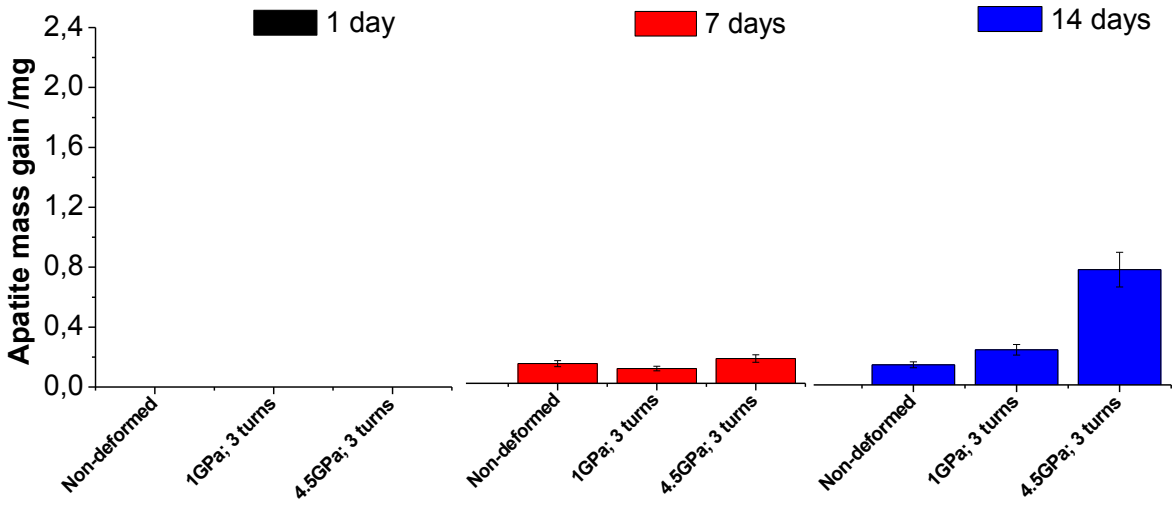

Figure 56: The weight change for samples of Ti13Nb13Zr alloy chemically treated, by H_3PO_4 etching and NaOH activation, non-deformed and deformed by HPT, subjected to the bioactivity tests after 1, 7 and 14 days immersed in SBF.

It was observed that from the seventh day, all samples show a mass gain due to the formation of an apatite film. At 14 days, the samples increase their mass, which shows that there is an increase in the growth of this film.

6 EXPERIMENTAL RESULTS: Ti35Nb7Zr5Ta ALLOY

In this section, the results of Ti35Nb7Zr5Ta alloy in the conditions non-deformed, deformed by HPT, and with different surface conditions will be presented. The results about their microstructural characterization will be presented first, then their electrochemical characterization and finally, the results about bioactivity.

6.1 Microstructural and mechanical characterizations

In this section, the microstructural and mechanical characterization of samples of Ti35Nb7Zr5Ta alloy non-deformed and deformed by HPT will be presented.

6.1.1 Polished samples

Figure 57 shows XRD patterns of Ti35Nb7Zr5Ta alloy at the non-deformed condition (ND) and deformed by HPT, conditions HPT1GPa, and HPT4.5GPa. The indexation of XRD patterns reveals that, before deformation, the Ti35Nb7Zr5Ta alloy is mostly composed by the BCC β (ISCD # 645545) phase with the presence some residual HCP α (ICSD # 43416) phase, which practically vanishes after mechanical processing, also probably due to solute redistribution during HPT. The peak broadening observed after deformation, at both pressure conditions, points to very high grain refinement in the Ti35Nb7Zr5Ta alloy.

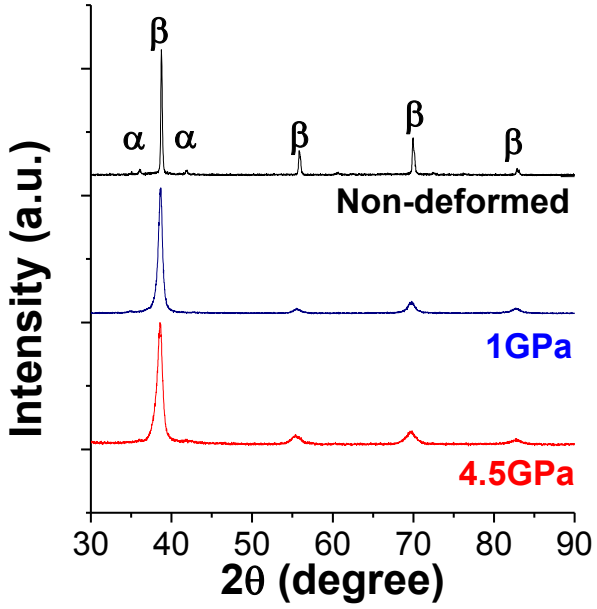

Figure 57: XRD patterns of Ti35Nb7Zr5Ta alloy in the conditions ND, HPT1GPa, and HPT4.5GPa.

The microstructures of Ti-35Nb-7Zr alloy at (a) ND and deformed by HPT (b) HPT GPa and (c) HPT4.5 GPa are shown in Figure 58.

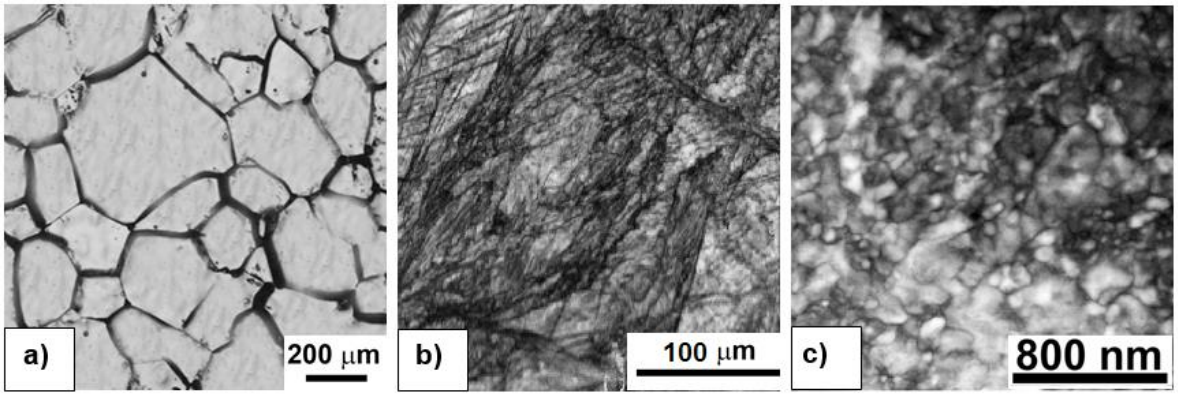

Figure 58: Microstructures of Ti35Nb7Zr5Ta alloy at (a) the non-deformed condition, and deformed by HPT (b) HPT1GPa and (c) HPT4.5GPa.

Figure 58(a) is an image obtained by confocal laser microscopy (CLM), and it shows a single β phase with equiaxed grains after heating and quenching. This result is coherent with the one presented in Figure 57 because the amount of the

residual hcp α phase appears to be very small when comparing peak intensities in such a figure. After image analysis, the grain size was evaluated to be around 240 μm on average.

Figure 58(b) is an image obtained by CLM. This image corresponds to the condition HPT1GPa and shows a grain refinement after being processed. The grain size distribution was determined for the sample after processing by HPT, and the average grain sizes measured was ~ 89 um.

Figure 58(c) present the equivalent TEM bright field image from the surface of the as-received sample. This figure shows a very high grain refinement due to HPT4.5GPa processing. Furthermore, it is possible to observe a non-homogeneous distribution of grains/subgrains sizes as compared with Figure 58(a). The grain size distribution for the sample after processing by HPT was determined, and the measured average grain size was ~112 nm.

Figure 59 presents hardness mappings for the Ti35Nb7Zr5Ta alloy in the conditions ND, HPT1GPa, and HPT4.5GPa.

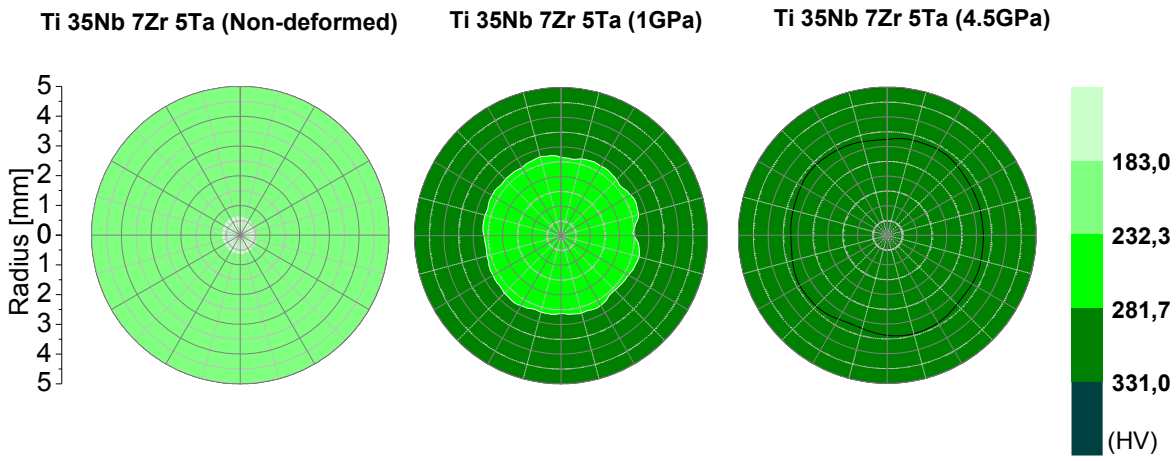

Figure 59: Hardness mappings for Ti35Nb7Zr5Ta alloy in the conditions ND, HPT1GPa, and HPT4.5GPa.

As shown in Figure 59, the same behavior was observed as in the Ti13Nb13Zr alloy, where the hardness increases with deformation and its values

increase from the center to the edge. Consequently, it can be inferred that the HPT process produces materials with smaller grains at the edge than at the center [20].

On the other hand, the mean hardness value obtained for the Ti35Nb7Zr5Ta alloy at the ND condition was a mean value of 183 HV. When the samples were deformed by HPT at 1 GPa, the hardness value increased between 232 and 282 HV. In the same way, after processing by HPT at 4.5 GPa, the hardness value increased between 295 and 331 HV, which represents an increase in the hardness of approximately 75%.

Figure 60 shows the elastic modulus measured for Ti35Nb7Zr5Ta alloy at the conditions of ND, HPT1 GPa, and HPT4.5GPa. All the elastic modulus values are very close to the values reported for human bones (10–30 GPa [190]). The values showed in Figure 60 are the result of a statistical analysis of 3 measurements (mean and standard deviation).

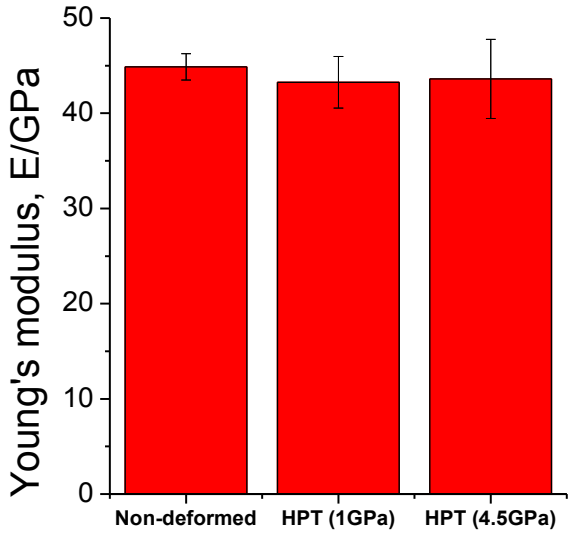

Figure 60: Graph comparing elastic modulus values for the Ti35Nb7Zr5Ta alloy at the conditions ND, HPT1GPA and HPT4.5GPa, and three turns.

6.1.2 Anodized samples

Figure 61 shows the XRD patterns of anodized samples of Ti35Nb7Zr5Ta alloy in the conditions ND, HPT1GPa, and HPT4.5GPa. These XRD patterns indicate that TiO_2 nanostructures obtained during anodization are amorphous. However, when TiO_2 nanostructures were heat-treated at 550 °C for two hours, an anatase-rutile mixture was obtained (Figure 62). The indexing of the Bragg peaks indicates the presence of the anatase TiO_2 phases (2θ = 25.4 °, 38.3 °, 48.1 °, and 55.2 °) [126] and TiO_2 -rutile phases (2θ = 27.4 ° and 36.0 °)[127].

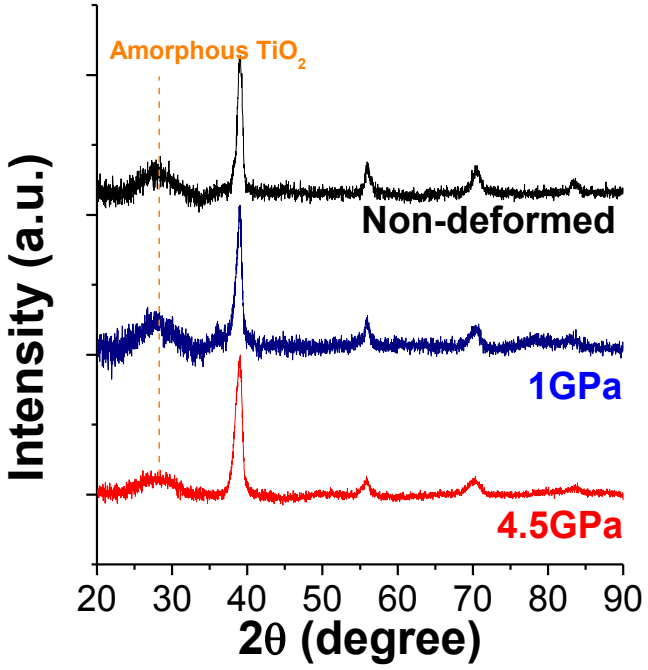

Figure 61: XRD patterns of anodized samples of Ti35Nb7Zr5Ta alloy in the ND, HPT1GPa, and HPT4.5GPa conditions.

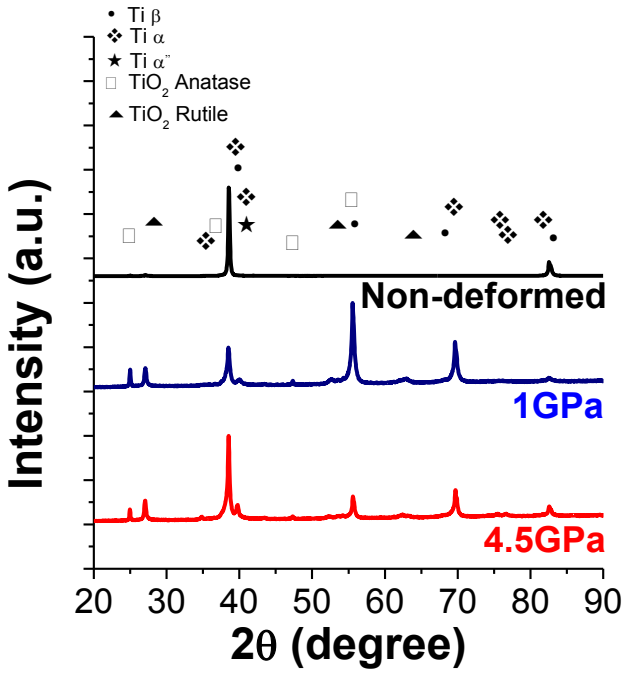

Figure 62: XRD pattern of anodized and annealed samples of Ti35Nb7Zr5Ta alloy in the ND, HPT1GPa, and HPT4.5GPa conditions. TiO_2 nanostructures were annealed at 550 °C in air.

TiO_2 nanostructures morphologies were investigated by SEM. Figure 63 shows the top and lateral views of anodized and annealed samples of Ti35Nb7Zr5Ta alloy (a and b) ND (c and d) HPT1GPa and (e and f) HPT4.5GPa.

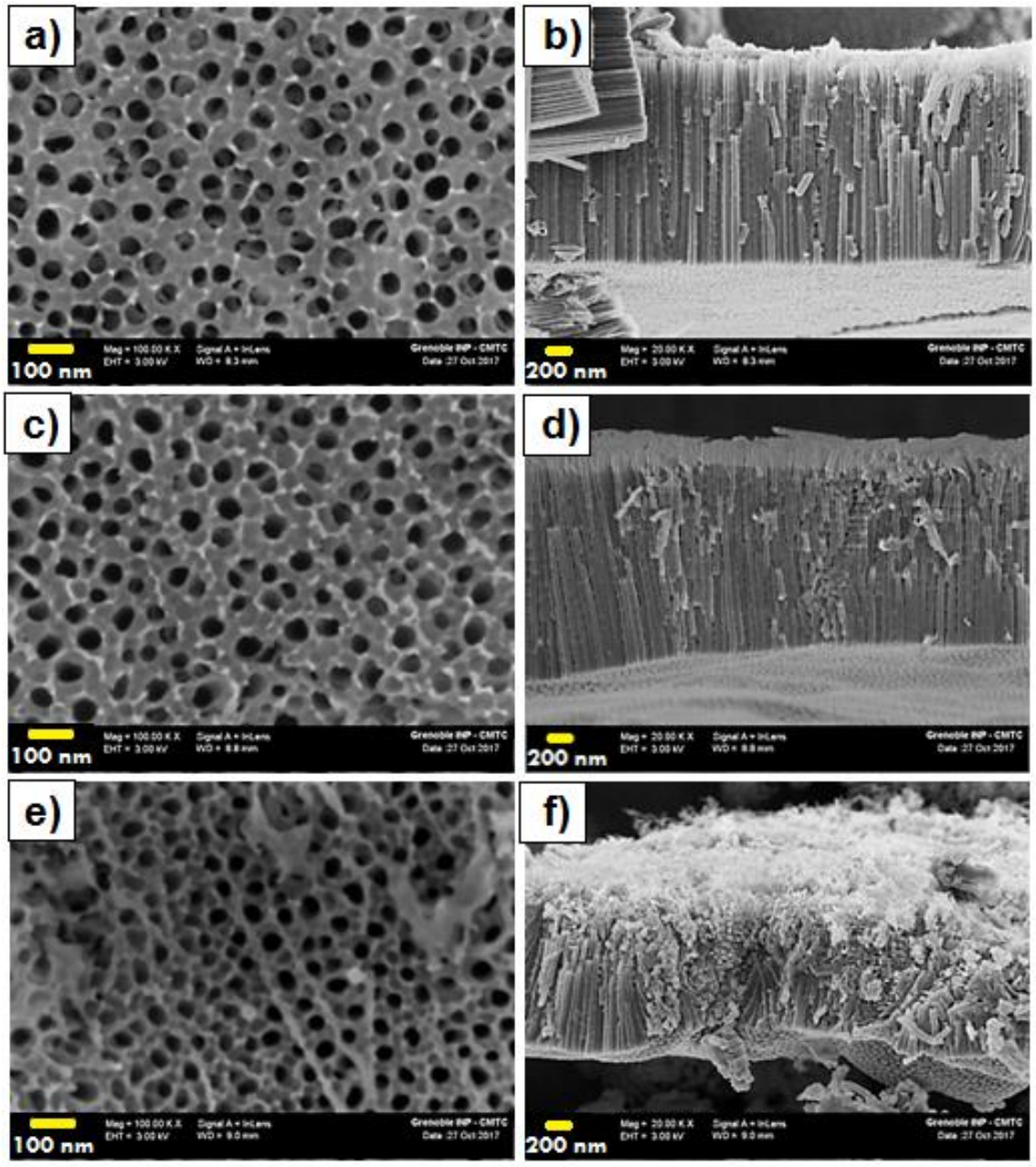

Figure 63: SEM micrographs of anodized and annealed samples of Ti35Nb7Zr5Ta alloy at non-deformed condition, (a) Top and (b) Lateral views, deformed by HPT at 1 GPa, (c) Top and (d) Lateral views and deformed at 4.5 GPa, (e) Top and (f) Lateral views.

Figure 63(a) shows self-organized TiO_2 nanoporous in the β phase of Ti35Nb7Zr5Ta alloy in the ND condition. The lateral view of these nanostructures (Figure 63(b)) shows self-organized arrays of nanoporous whose dimensions are presented in Table 23.

Table 23: Summary of observed morphologies and dimensions of the formed nanostructures observed in Figure 63 for samples of Ti35Nb7Zr5Ta alloy at different conditions.

Ti35Nb7Zr5Ta alloy				
Condition	**Morphology**	**Diameter (nm)**		**Length (nm)**
		Internal	**External**	
Non-deformed	Nanopores	47 ± 7	82 ± 14	2494 ± 23
1 GPa	Nanopores	45 ± 7	81 ± 13	2459 ± 112
4.5 GPa	Nanopores	36 ± 10	69 ± 7	1742 ± 149

In the same way, the samples deformed by HPT, shown in Figures 63(c) and (e), presented nanoporous. However, since processing by HPT caused a refinement of the β phase, the nanoporous presented in these samples are not so organized and are deformed in their longitudinal direction, suggesting that their growth follow the spatial distortion of the β phase.

6.1.3 Samples chemically treated by HCl etching and NaOH activation

The surface morphology of samples of Ti35Nb7Zr5Ta alloy, chemically treated by HCl and NaOH, was examined by scanning electron microscopy (SEM). The secondary electron (SE) detection mode with an acceleration voltage of 25 kV was selected for SEM analysis. Figure 64 shows SEM images of Ti35Nb7Zr5Ta alloy, chemically treated, at the ND, HPT1GPA, and HPT4.5GPa. Figures 64(b), (d) and (f) are SEM images of higher magnification to give more details of surface morphology.

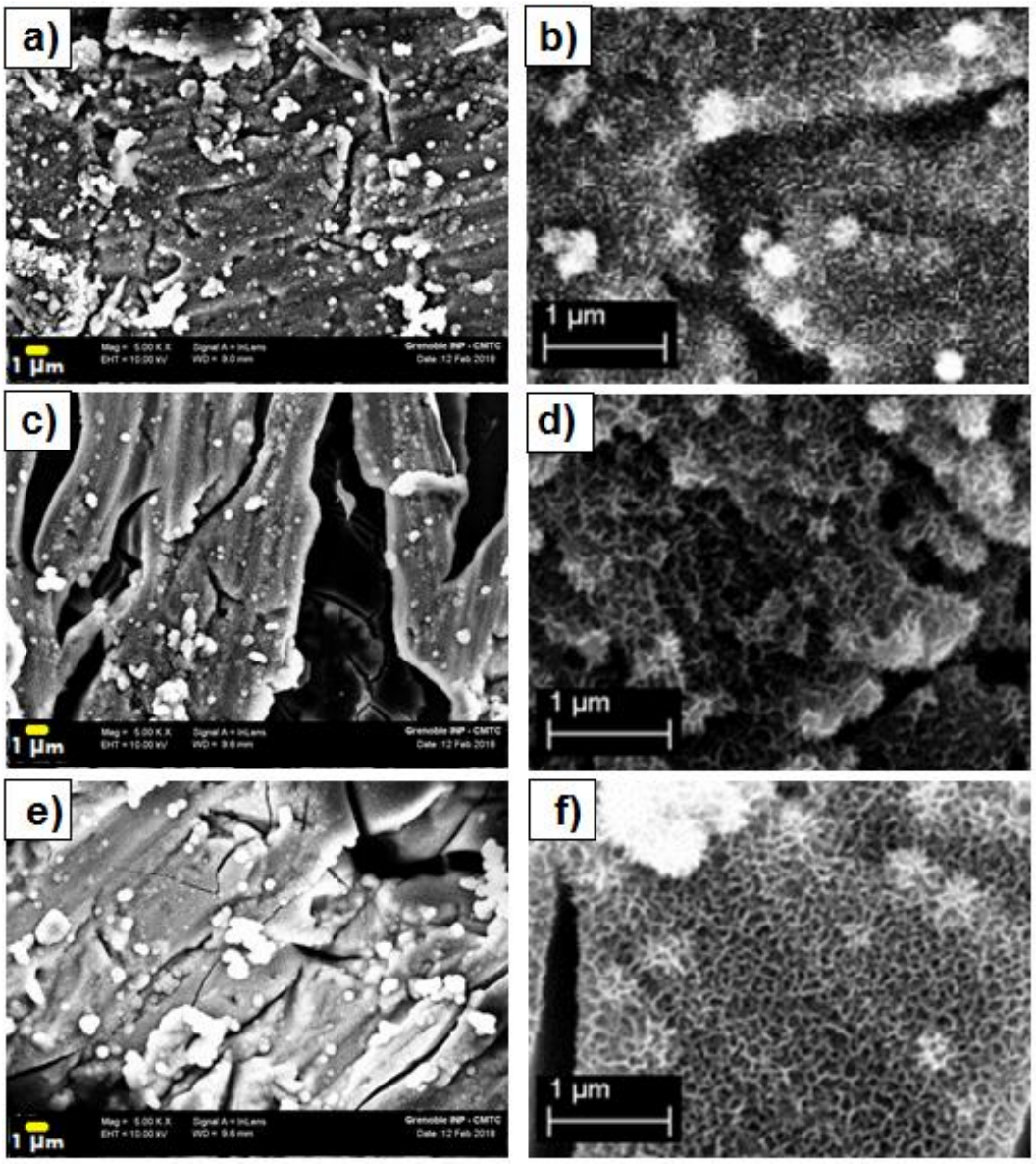

Figure 64: SEM images of Ti35Nb7Zr5Ta alloy, chemically treated by HCl etching and NaOH activation, (a and b) non-deformed condition, deformed by HPT at (c and d) 1 GPa and deformed by HPT at (e and f) 4.5 GPa.

As one may observe in Figure 64, the chemical treatment (HCl etching and NaOH activation) induced the formation of a nano topographic sponge-like morphology on the samples' surface, and, as observed before, surfaces are whole cracked. In order to obtain an analysis of the surface compositions of the samples, EDS analysis was performed. The results are shown in Table 24.

Table 24: Quantitative chemical EDS analysis of samples chemically treated by HCl and NaOH.

	Ti35Nb7Zr5Ta (at %)		
Chemical element	**Non-deformed**	**1 GPa**	**4.5 GPa**
O	59.82	55.89	56.02
Na	1.98	2.06	2.02
Zr	0.78	0.16	0.65
Nb	6.35	4.99	6.18
Ti	24.2	28.06	27.28
Cl	6.56	8.67	7.55
Ta	0.31	0.17	0.30

On the other hand, Raman spectroscopy was used to identify the crystalline phases present on the surface of samples of Ti35Nb7Zr5Ta alloy chemically treated. The results shown in Figure 65 indicate that sodium titanate, anatase, and rutile are the main phases present in all the samples.

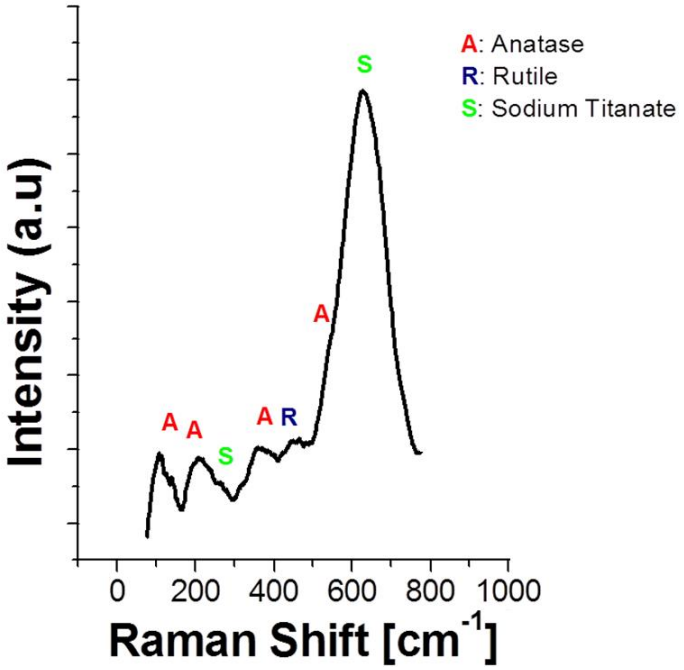

Figure 65: Raman spectra of the surface of Ti35Nb7Zr5Ta alloy chemically treated by HCl etching and NaOH activation.

6.1.4 Samples chemically treated by H_3PO_4 etching and NaOH activation

The surface morphology of samples of Ti35Nb7Zr5Ta alloy, chemically treated by H_3PO_4 etched, and NaOH activated, was examined by scanning electron microscopy (SEM). Figure 66 shows SEM images of chemically modified surfaces of Ti35Nb7Zr5Ta alloy in the ND, HPT1GPA, and HPT4.5GPa conditions. Figures 66(b), (d) and (f) are SEM images of higher magnification to give more details about surface morphology.

In the same way, as samples treated with HCl, the treatment by H_3PO_4 etching and NaOH activation induced the formation of a nano topographic sponge-like morphology on the samples' surface, with the presence of cracks on the surface. Moreover, Raman results also indicate sodium titanate, anatase, and rutile phases in the samples, see Figure 67. Table 25 presents the quantitative EDS chemical analysis of samples chemically treated with H_3PO_4 followed by NaOH.

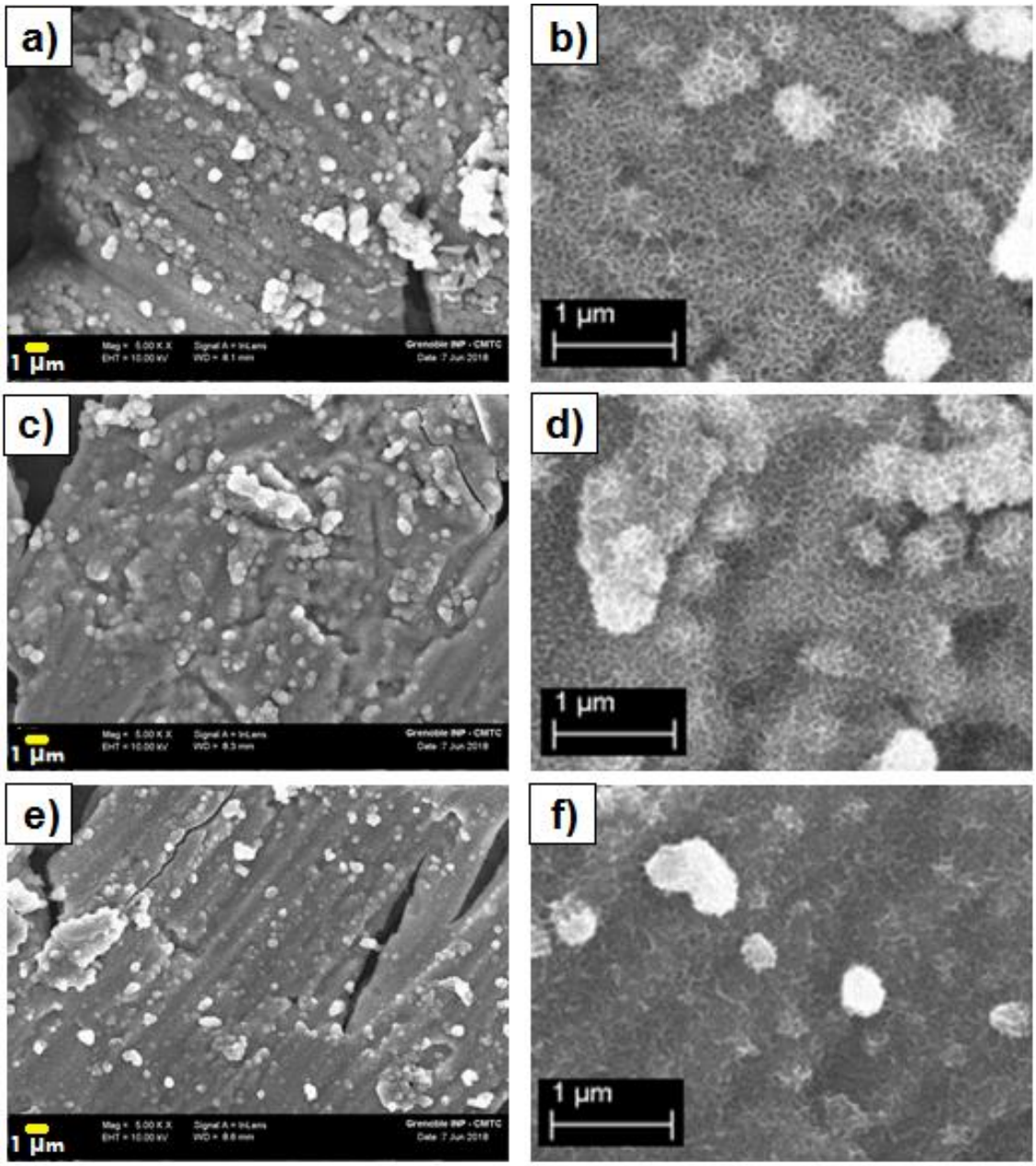

Figure 66: SEM images of Ti35Nb7Zr5Ta alloy, chemically treated by H_3PO_4 etched and NaOH activated, (a and b) non-deformed condition, deformed by HPT at (c and d) 1 GPa and deformed by HPT at (e and f) 4.5 GPa.

Table 25: Quantitative chemical EDS analysis of samples, chemically treated by H_3PO_4 etching, and NaOH activation.

	Ti35Nb7Zr5Ta (at %)		
Chemical element	**Non-deformed**	**1 GPa**	**4.5 GPa;**
O	70.22	70.03	69.89
Na	1.22	1.35	1.12
Zr	0.98	0.87	0.52
Nb	3.62	3.68	3.76
Ti	23.48	23.64	24.19
Ta	70.22	70.03	69.89

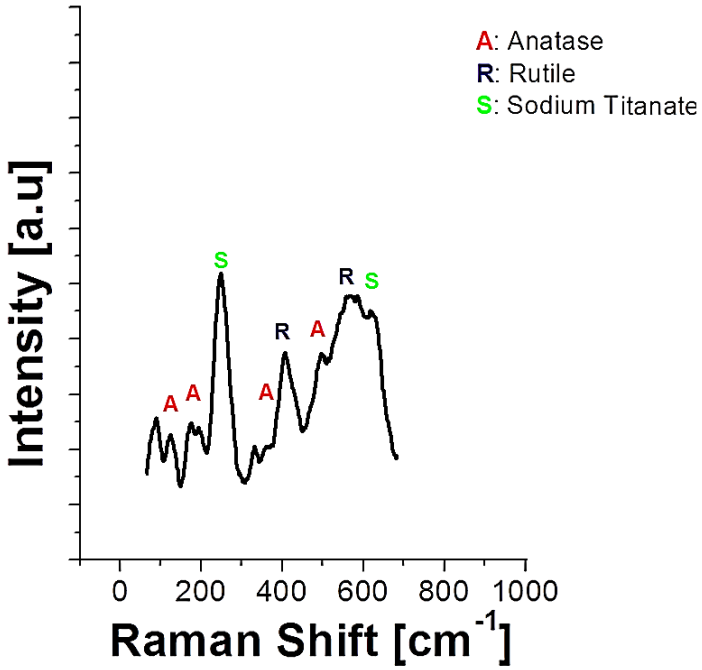

Figure 67 Raman spectra of the surface of Ti35Nb7Zr5Ta alloy chemically treated by H_3PO_4 and NaOH.

6.2 Electrochemistry characterization

6.2.1 Polished samples

6.2.1.1 Open circuit potential (OCP) measures

Table 26 summarizes the values of open circuit potential (or corrosion potential, E_{corr}) recorded after one hour of immersion in simulated body fluid (SBF) for Ti35Nb7Zr5Ta alloy, in the conditions ND, HPT1GPa and HPT4.5GPa. The values are the result of a statistical analysis of 3 measurements (mean and standard deviation).

Table 26: OCP measurements after 1-hour immersion in SBF at 37 °C of the polished surfaces of Ti35Nb7Zr5Ta alloy in the conditions ND, HPT1GPa, and HPT4.5GPa samples.

Condition	OCP or E_{corr} (mV vs. SCE)
Non-deformed	-503 ± 50
1 GPa	-379 ± 45
4.5 GPa	-465 ± 56

A variation of open circuit potential is observed for deformed conditions. The OCP of Ti13Nb13Zr alloy, at ND condition, was - 503 mV vs. SCE, while samples with severe plastic deformation at 1 GPa and 4.5 GPa showed a slight increase, -379 mV vs. SCE and - 465 mV vs. SCE, respectively. Therefore, regardless of the crystal structure, it appears that severe plastic deformation causes an increase in the corrosion potential compared to the samples non-deformed

6.2.1.2 Potentiodynamic polarization curves

Figure 68 shows the anodic polarization curves, recorded in SBF at 37 ºC, for the polished samples of ND, HPT1GPa, and HPT4.5GPa samples. The polarization curve for each sample represents a single measure, arbitrarily chosen from a series of three measurements carried out under the same conditions.

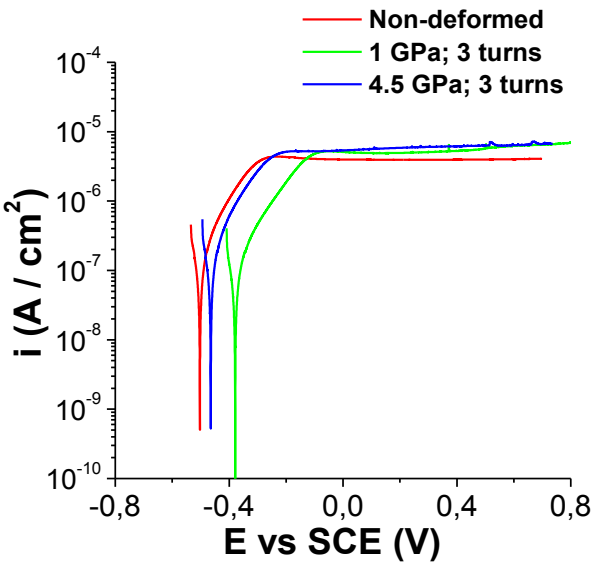

Figure 68: Anodic polarization curves, recorded in SBF at 37 °C of the polished surfaces of Ti35Nb7Zr5Ta alloy in the conditions ND, HPT1GPa, and HPT4.5GPa samples.

Current densities were calculated by dividing the current measured by the geometric area (0.283 cm²). The current measured in the anode region is mainly due to the oxidation reaction of the substrates to TiO_2, which contributes to the thickening of the passive layer. In this reaction, which takes place in the metal/ oxide interface, the area in which it happens is then equal to the geometric area.

The passivation current density (i_{pass}) values, of Ti35Nb7Zr5Ta alloy non-deformed and deformed by HPT at 1 GPa and 4.5 GPa, were graphically established and summed up in Table 27. It shows the mean current density values of three points at the current plateau in the polarization curves and their standard deviations.

Table 27: Passivation current density of the polished samples of Ti35Nb7Zr5Ta alloy in the conditions ND, HPT1GPa, and HPT4.5GPa.

Conditions	i_{pass} (μA/cm^2)
Non-deformed	3.52 ± 0.11
1 GPa	5.18 ± 0.31
4.5 GPa	6.03 ± 0.28

The passivation current density of the non-deformed Ti35Nb7Zr5Ta alloy was 3.52 μA/cm^2, while samples HPT1GPa and HPT4.5GPa showed a slight increase, 5.18 μA/cm^{2,} and 6.03 μA/cm^2, respectively. Therefore, it appears that the increase in the pressure from 1 GPa to 4.5 GPa causes an increase in the passivation current Ti35Nb7Zr5Ta alloy.

6.2.1.3 Electrochemical impedance measurements (EIS)

Figure 69 shows the EIS graphs in the (a) Nyquist and (b) Bode representation of the Ti35Nb7Zr5Ta alloy in the conditions ND, HPT1GPa, and HPT4.5GPa.

The impedance spectra in Nyquist diagrams of Figure 69(a) show the typical shape (arc) for a capacitive-resistive system (associations of capacitive phenomena, accumulation of charges, and resistive phenomena, load transfers or resistance of a layer). Moreover, it can be seen from Figure 69(a) that the spectrum of ND samples has a higher amplitude, which indicates that SPD process displays a slight effect on the formation of the protective layer in Ti35Nb7Zr5Ta alloy. It can be explained by the inhomogeneous strain distribution induced by the HPT [191], as well as by the increase in the dislocation density in deformed samples. Therefore, inhomogeneous strain distribution can cause a selective dissolution of specimens in zones of high strain, which tends to shift the corrosion potential of the alloy to a more active value [191]. Additionally, increasing dislocation density accelerates the release of atoms into electrolyte [133].

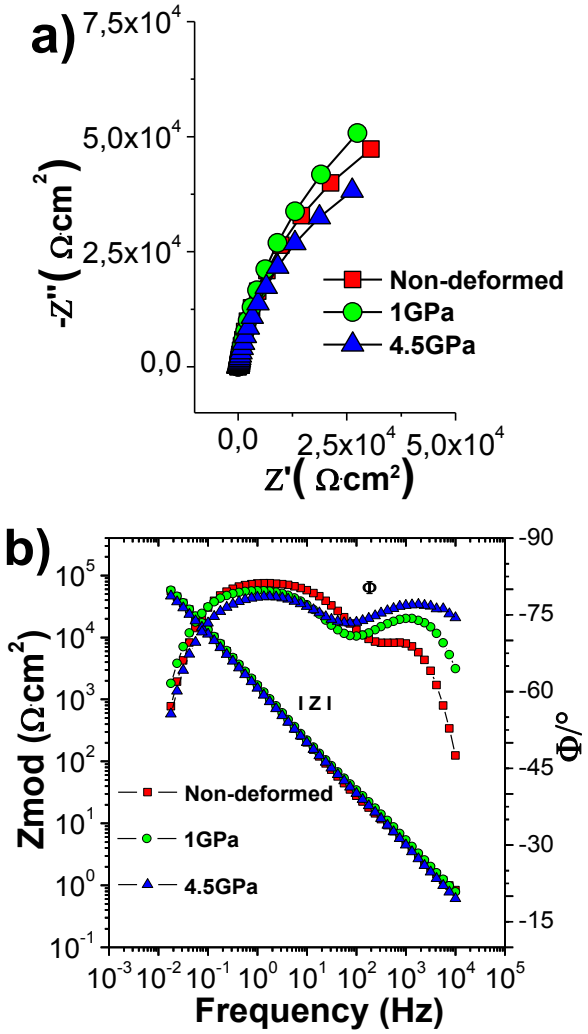

Figure 69: EIS graphs in the Nyquist diagrams (a) and Bode diagrams (b) of the polished samples of Ti35Nb7Zr5Ta alloy in the conditions ND, HPT1GPa, and HPT4.5GPa.

On the other hand, the effect of the SPD was more significant for samples deformed at 4.5 GPa (spectrum with the lowest amplitude). This can be explained by the fact that in this alloy deformed at 4.5 GPa, it could have more zones of high strain, which are favorable to the dissolution of the passive layer.

The Bode diagrams, in Figure 69(b), show a capacitive behavior from medium to low frequencies with phase angles approaching – 80°. It is typical of passive materials [136]. Moreover, high values of |Z| at low frequencies, above 10^4 $\Omega \cdot cm^2$, suggesting that the passive film formed offers high corrosion resistance.

This behavior is consistent with the low passivation current determined in polarization tests. On the other hand, from the Bode phase angle plot for all samples, two plateaus can be identified.

In general, the results obtained from impedance measurement indicate that all tested substrates behaved in a very similar way. The differences are rather small, and this can be ascribed to the fact that the passive film formed on these alloys is basically of the same nature.

6.2.2 Anodized samples

In this section, the effect of the SPD by HPT as well as TiO_2 nanostructures on the electrochemical properties of Ti35Nb7Zr5Ta alloy will be studied. The samples anodized were annealed according to section 4.3.1.2.

6.2.2.1 Open circuit potential measures

Table 28 summarizes the values of E_{corr} recorded after 1 hour of immersion in SBF for anodized Ti35Nb7Zr5Ta alloy in the conditions ND, HPT 1GPa and HPT4.5GPa. The values are the result of a statistical analysis of 3 measurements (mean and standard deviation).

Table 28: OCP measurements, after 1-hour immersion in SBF at 37° C for the anodized samples of Ti35Nb7Zr5Ta alloy in the conditions ND, HPT1GPa and HPT4.5GPa.

Condition	OCP or E_{corr} (mV vs. SCE)
Non-deformed	-125 ± 25
1 GPa	-88 ± 21
4.5 GPa	-82 ± 30

The OCP of anodized Ti35Nb7Zr5Ta alloy, at the ND condition, was - 125 mV vs. SCE, while anodized samples deformed by HPT at 1 GPa and 4.5 GPa showed an increase in their corrosion potential, - 88 mV vs. SCE and - 82 mV vs.

SCE, respectively. Therefore, samples of Ti35Nb7Zr5Ta alloy deformed and anodized showed the noblest corrosion potential (the nobler and more stable surface in SBF).

On the other hand, the E_{corr} of the samples anodized showed a drastic increase compared to samples without TiO_2 nanostructures (Table 26), meaning that electrochemical anodization of Ti35Nb7Zr5Ta alloy, non-deformed or deformed by HPT, ennobled its surface.

6.2.2.2 Potentiodynamic polarization curves

Figure 70 shows the anodic polarization curves, recorded in SBF at 37 ºC, of anodized samples of Ti35Nb7Zr5Ta alloy in the conditions ND, HPT1GPa, and HPT4.5GPa.

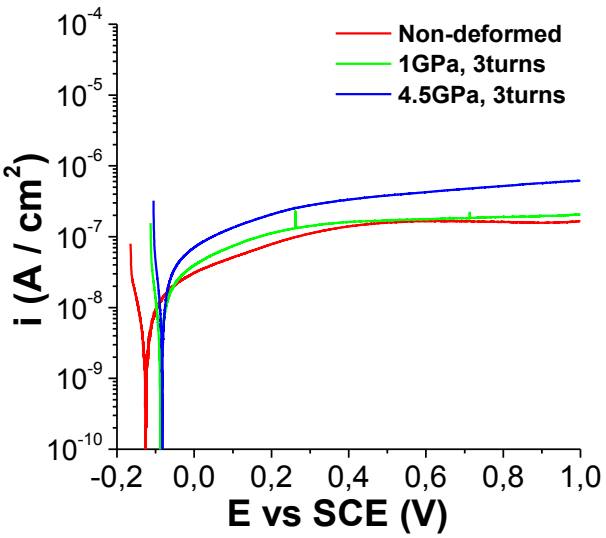

Figure 70: Anodic polarization curves, recorded in SBF at 37 °C for the anodized Ti35Nb7Zr5Ta samples in the conditions ND, HPT1GPa, and HPT4.5GPa.

From Figure 70, it can be seen a current plateau in a wide range of potentials, which corresponds to a limitation of the current by mass transport through the oxide layer [25]. In fact, this behavior is characteristic of passive materials. The i_{pass} values, of anodized samples of Ti35Nb7Zr5Ta alloy non-

deformed and deformed by HPT at 1 GPa and 4.5 GPa, were graphically established and summed up in Table 29. It shows the mean current density values of three points at the current plateau in the polarization curves and their standard deviations.

Table 29: Passivation current density for the anodized Ti35Nb7Zr5Ta samples in the conditions ND, HPT1GPa, and HPT4.5GPa.

Condition	i_{pass} (µA/cm^2)
Non-deformed	0.16 ± 0.02
1 GPa	0.19 ± 0.05
4.5 GPa	0.52 ± 0.06

The passivation current density of anodized Ti35Nb7Zr5Ta alloy, non-deformed, was 0.16 µA/cm^2, while samples deformed by HPT at 1 GPa and 4.5 GPa showed a slight increase, 0.19 µA/cm^2 and 0.52 µA/cm^2, respectively. Therefore, it appears that severe plastic deformation causes a slight increase in the passivation current of anodized Ti35Nb7Zr5Ta alloy.

6.2.2.3 Electrochemical impedance measurements (EIS)

Figure 71 shows the EIS graphs in the (a) Nyquist and (b) Bode representation of anodized samples of Ti35Nb7Zr5Ta alloy non-deformed and deformed by HPT at 1 GPa and 4.5 GPa.

The impedance spectra in Nyquist diagrams of Figure 71(a) show a pseudocapacitive shape (inclined straight). This behavior suggests that the electron exchanges, and therefore, the reactions, are minimal or that the oxide layer is very resistive [137]. Additionally, it can be seen from Figure 71(a) that the amplitude of spectra is much higher than in non-anodized samples (Figure 69(a)). It suggests that the nanoporous arrays on the samples improved the protection of the surface in Ti35Nb7Zr5Ta alloy.

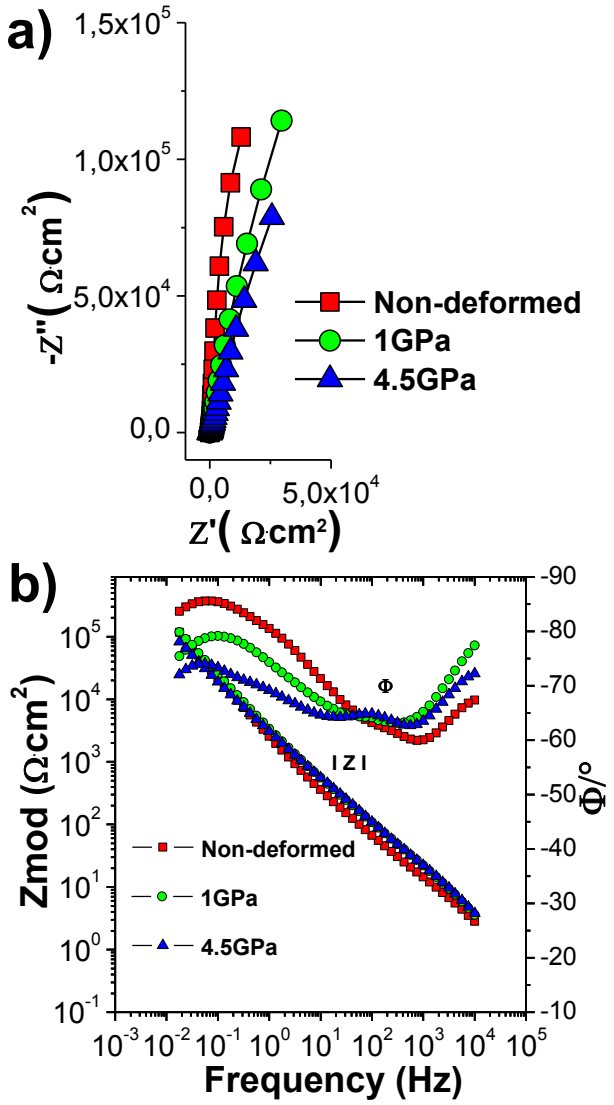

Figure 71: Nyquist diagrams (a) and Bode diagrams (b) for the anodized Ti35Nb7Zr5Ta samples in the conditions ND, HPT1GPa, and HPT4.5GPa.

On the other hand, the Nyquist spectra indicate that the amplitude of the spectra of ND is higher than that of the deformed samples, this can be explained by the lower dislocation density in samples without deformation.

The Bode diagrams, in Figure 71(b), show a capacitive behavior with the maximum phase angles close to −80° and high values of |Z| above 10^5 Ω·cm^2 in the low frequencies region, suggesting that the passive film formed offers high

corrosion resistance, which is consistent with the low passivation current determined in polarization tests. On the other hand, from the Bode phase angle plot for all samples, three plateaus can be identified.

6.2.3 Samples chemically treated by HCl etching and NaOH activation

In this section, the effect of the SPD by HPT as well as, surface modification treatment by HCl etching and subsequent NaOH activation, on the electrochemical properties of Ti35Nb7Zr5Ta alloy will be studied.

6.2.3.1 Open circuit potential measures

Table 30 summarizes the values of E_{corr} for samples non-deformed and deformed by HPT as well as chemically treated by HCl etching and NaOH activation. The values are the result of a statistical analysis of 3 measurements (mean and standard deviation).

Table 30: OCP measurements, after 1-hour immersion in SBF at 37° C of samples of Ti35Nb7Zr5Ta alloy chemically treated by HCl and NaOH in the conditions ND, HPT1GPa and HPT4.5GPa.

Condition	Corrosion potential (mV vs SCE)
Non-deformed	-388 ± 47
1 GPa	-232 ± 28
4.5 GPa	-137 ± 16

The OCP of Ti35Nb7Zr5Ta alloy chemically treated by HCl and NaOH, ND, was - 388 mV vs. SCE, while anodized samples deformed by HPT at 1 GPa and 4.5 GPa showed an increase in their corrosion potential, - 232 mV vs. SCE and - 137 mV vs. SCE, respectively. Therefore, samples of Ti35Nb7Zr5Ta alloy deformed and anodized showed the noblest corrosion potential.

On the other hand, the E_{corr} of chemically treated samples also showed an increase compared to polished samples (Table 26), indicating that the chemical

treatment by HCl etching and NaOH activation turns nobler and more stable the surface of Ti35Nb7Zr5Ta alloy.

6.2.3.2 Potentiodynamic polarization curves

Figure 72 shows the anodic polarization curves for samples non-deformed and deformed as well as chemically treated by HCl and NaOH.

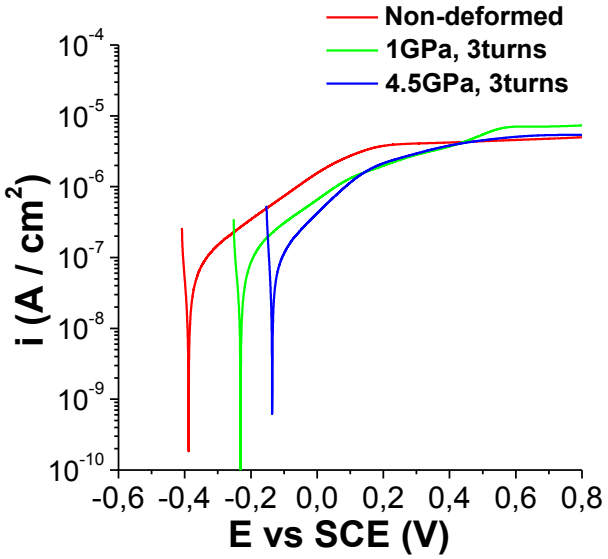

Figure 72: Anodic polarization curves, recorded in SBF at 37 °C for samples of Ti35Nb7Zr5Ta alloy chemically treated by HCl and NaOH in the conditions ND, HPT1GPa, and HPT4.5GPa.

From Figure 72, it can be seen that the behavior of the samples chemically treated by HCl and NaOH, in a physiological environment is characteristic of a passive state. The i_{pass} values of samples chemically treated by HCl and NaOH were graphically established and summed up in Table 31. It shows the mean current density values of three points at the current plateau in the polarization curves and their standard deviations.

Table 31: Passivation current density of samples of Ti35Nb7Zr5Ta alloy chemically treated by HCl and NaOH in the conditions ND, HPT1GPa, and HPT4.5GPa.

Condition	i_{pass} (μA/cm²)
Non-deformed	4.58 ± 0.41
1 GPa	7.20 ± 0.20
4.5 GPa	5.21 ± 0.16

The passivation current of samples chemically treated by HCl etching and NaOH activation, non-deformed, was 4.58 μA/cm^2, while samples deformed by HPT at 1 GPa and 4.5 GPa showed a slight increase, 7.20 μA/cm^2 and 5.21 μA/cm^2, respectively. Therefore, it appears that severe plastic deformation causes a slight increase in the passivation current of the chemically treated Ti35Nb7Zr5Ta samples.

6.2.3.3 Electrochemical impedance measurements (EIS)

Figure 73 shows the EIS graphs in the (a) Nyquist and (b) Bode representation of samples of Ti35Nb7Zr5Ta alloy chemically treated by HCl and NaOH.

The impedance spectra in Nyquist diagrams of Figure 73(a) show a typical behavior of a capacitive-resistive system that indicates corrosion protection. Also, these Nyquist diagrams indicate that the amplitude of the spectra of ND is higher than that of the deformed samples, which means that the ND samples show better corrosion resistance. This can be explained because the resistance of the passive film is more affected in samples with more grain boundaries such as those deformed at 4.5 GPa. These results are likely to be related to a more active dissolution of the passive film at the surface near the grain boundaries [140].

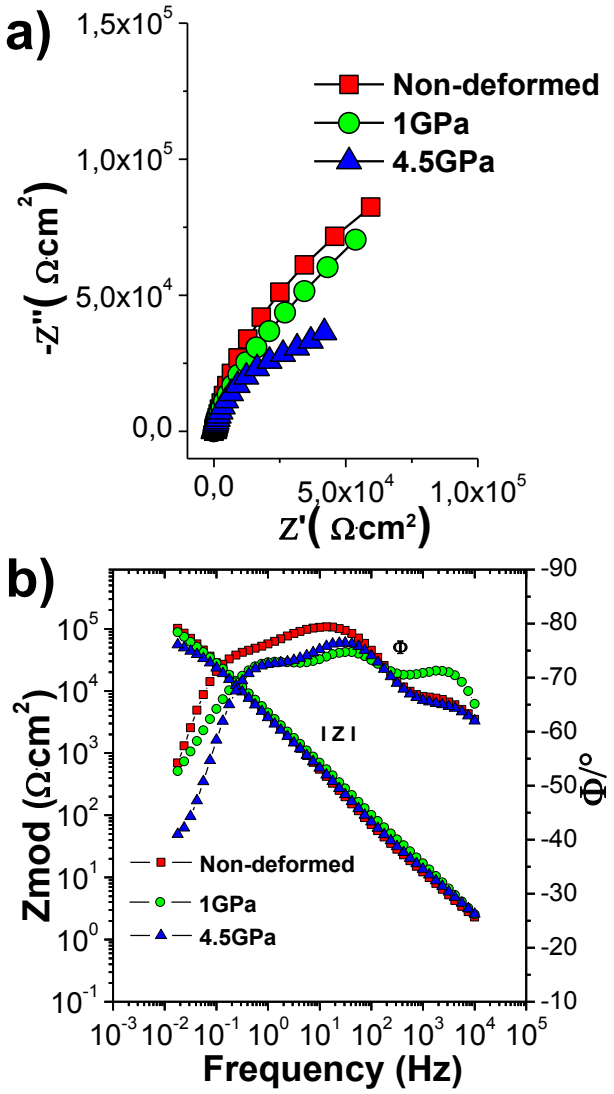

Figure 73: Nyquist diagrams (a) and Bode diagrams (b) for samples of Ti35Nb7Zr5Ta alloy chemically treated by HCl and NaOH in the conditions ND, HPT1GPa, and HPT4.5GPa.

On the other hand, the Bode diagrams, in Figure 73(b), show a capacitive behavior with the maximum phase angles close to −80° and high values of |Z| above 10^4 Ω·cm^2 in the low frequencies region, suggesting that the passive film formed offers high corrosion resistance. From the Bode phase angle plot for all samples, three plateaus can be identified.

6.2.4 Samples chemically treated by H_3PO_4 etching and NaOH activation

In this section, the effect of the SPD by HPT as well as, surface modification treatment by H_3PO_4 etching and subsequent NaOH activation, on the electrochemical properties of Ti35Nb7Zr5Ta alloy will be studied.

6.2.4.1 Open circuit potential measures

Table 32 summarizes the values of Ecorr for samples non-deformed and deformed by HPT as well as chemically treated by H_3PO_4 and NaOH. The values are the result of a statistical analysis of 3 measurements (mean and standard deviation).

Table 32: OCP measurements, after 1-hour immersion in SBF at 37° C of samples of Ti35Nb7Zr5Ta alloy chemically treated by H_3PO_4 and NaOH in the conditions ND, HPT1GPa and HPT4.5GPa.

Condition	Corrosion potential (mV vs SCE)
Non-deformed	-421 ± 51
1 GPa	-406 ± 49
4.5 GPa	-211± 35

The OCP of Ti35Nb7Zr5Ta alloy chemically treated by H_3PO_4 and NaOH, non-deformed, was - 421 mV vs. SCE, while the corrosion potentials for samples deformed at 1 GPa and 4.5 GPa were -406 mV vs. SCE and -211 mV vs. SCE, respectively. Therefore, it appears that the corrosion potential is nobler for substrates chemically treated, by H_3PO_4 etching and NaOH activation, when they were previously deformed (for high pressures).

6.2.4.2 Potentiodynamic polarization curves

Figure 74 shows the anodic polarization curves for samples non-deformed and deformed as well as chemically treated by H_3PO_4 and NaOH.

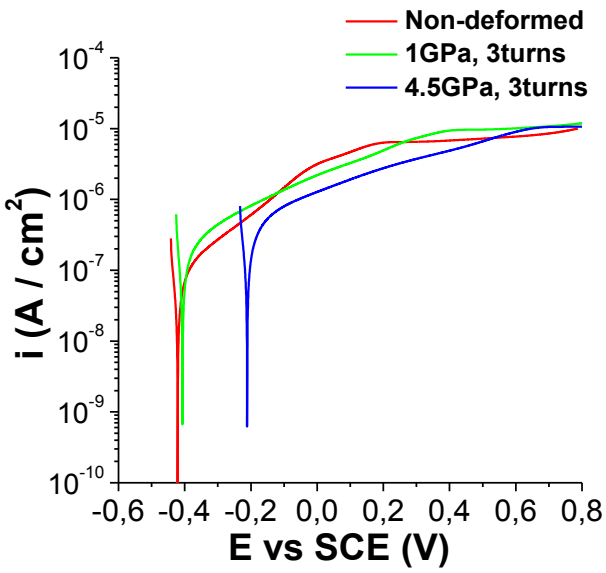

Figure 74: Anodic polarization curves, recorded in SBF at 37 °C for samples of Ti35Nb7Zr5Ta alloy chemically treated by H_3PO_4 and NaOH in the conditions ND, HPT1GPa, and HPT4.5GPa.

The polarization curves show, for potentials higher than $E_{corr,}$ a wide active region of at least 400 mV. These results suggest that the chemical treatment, by H_3PO_4 etching and NaOH activation impairs the passivation of the Ti35Nb7Zr5Ta alloy.

The i_{pass} values of samples chemically treated, by H_3PO_4 etching and NaOH activation, were graphically established and summed up in Table 33. It shows the mean current density values of three points at the current plateau in the polarization curves and their standard deviations.

Table 33: Passivation current density of samples of Ti35Nb7Zr5Ta alloy chemically treated by H_3PO_4 and NaOH in the conditions ND, HPT1GPa, and HPT4.5GPa.

Condition	i_{pass} (μA/cm²)
Non-deformed	8.24 ± 0.53
1 GPa	10.8 ± 0.52
4.5 GPa	10.8 ± 0.20

The passivation current of samples chemically treated by H_3PO_4 and NaOH, non-deformed, was 8.24 μA/cm², while samples deformed by HPT at 1 GPa and 4.5 GPa showed a slight increase, 10.8 μA/cm², and 10.8 μA/cm², respectively. Therefore, it appears that severe plastic deformation causes a slight increase in the passivation current compared to Ti35Nb7Zr5Ta alloy non-deformed.

On the other hand, the i_{pass} of the samples chemically treated by H_3PO_4 etching and NaOH activation showed an increase of i_{pass} compared with samples without chemical treatment (Table 27).

6.2.4.3 Electrochemical impedance measurements (EIS)

Figure 75 shows the EIS graphs in the (a) Nyquist and (b) Bode representation of samples of Ti35Nb7Zr5Ta alloy chemically treated by H_3PO_4 and NaOH.

The same behavior is observed as the samples with acid etching with HCl, where the Nyquist diagrams in Figure 75(a) indicate that the ND samples show better resistance to corrosion.

The substrates show capacitive-like behavior with the maximum phase angles close to −80° and high values of |Z| above 10^4 Ω·cm² in the region of low frequencies, concerning the Bode plots (Figure 75(b)), suggesting that the passive films formed to offer high corrosion resistance. On the other hand, samples with severe plastic deformation have a lower value of |Z|, which indicates that the

treatment of the chemical modification plus the deformation decreases the resistance to corrosion. From Bode phase angle plot for all samples, three plateaus can be identified.

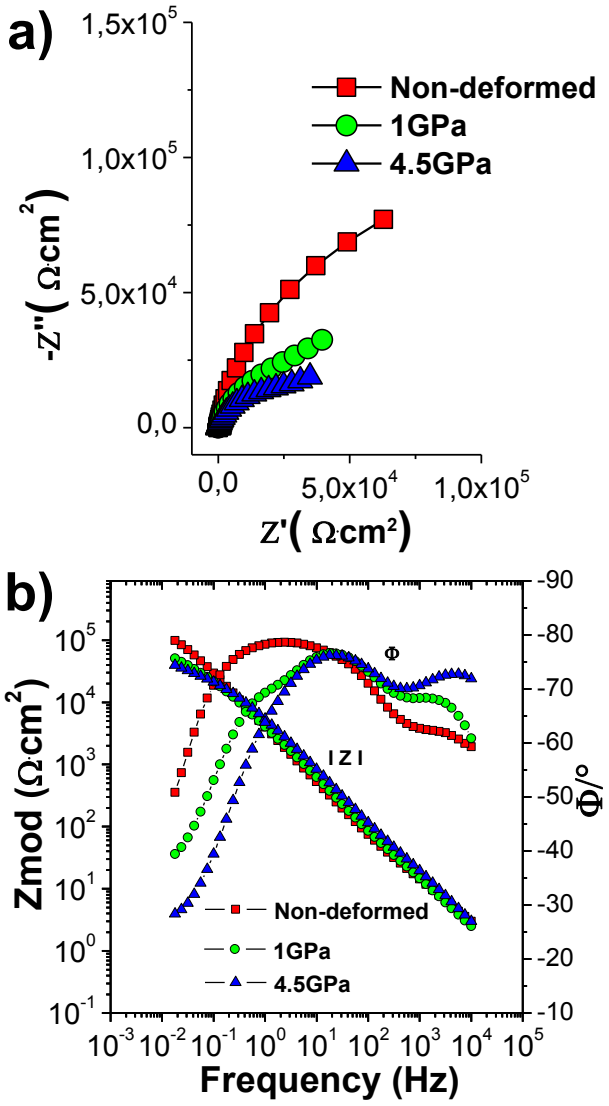

Figure 75: Nyquist diagrams (a) and Bode diagrams (b) for samples of Ti35Nb7Zr5Ta alloy chemically treated by H_3PO_4 and NaOH in the conditions ND, HPT1GPa, and HPT4.5GPa.

6.3 Modeling of impedance spectra for samples of Ti35Nb7Zr5Ta alloy

This section is focused on modeling the electrochemical impedance spectrums by equivalent electrical circuits (EEC) and by transmission line model.

6.3.1 EEC proposed for polished samples

The physical and equivalent circuit model, previously used for polished samples of Ti13Nb13Zr shown in Figure 40, were also chosen to describe the electrochemical behavior of polished samples of Ti35Nb7Zr5Ta alloy immersed in SBF.

This physical model represents a two-layer structure composed of a dense inner layer and a porous outer layer on the surface Ti35Nb7Zr5Ta alloy. It can be represented by the following EEC [142],

$$R_s + Q_a / (R_a + (Q_{dl} / R_{ct})$$

where R_s is the electrolyte resistance, R_a is the resistance of the porous outer layer, Q_a is the constant-phase element for the porous layer, R_{ct} represents the resistance of charge-transfer and Q_{dl} is the constant-phase element for the double layer at the dense inner layer-electrolyte interface.

The fitting of EIS data as Nyquist representations is shown in Figure 76. The error between experimental and simulated data was around 0.27%, indicating that data adjusted well to the proposed equivalent circuit.

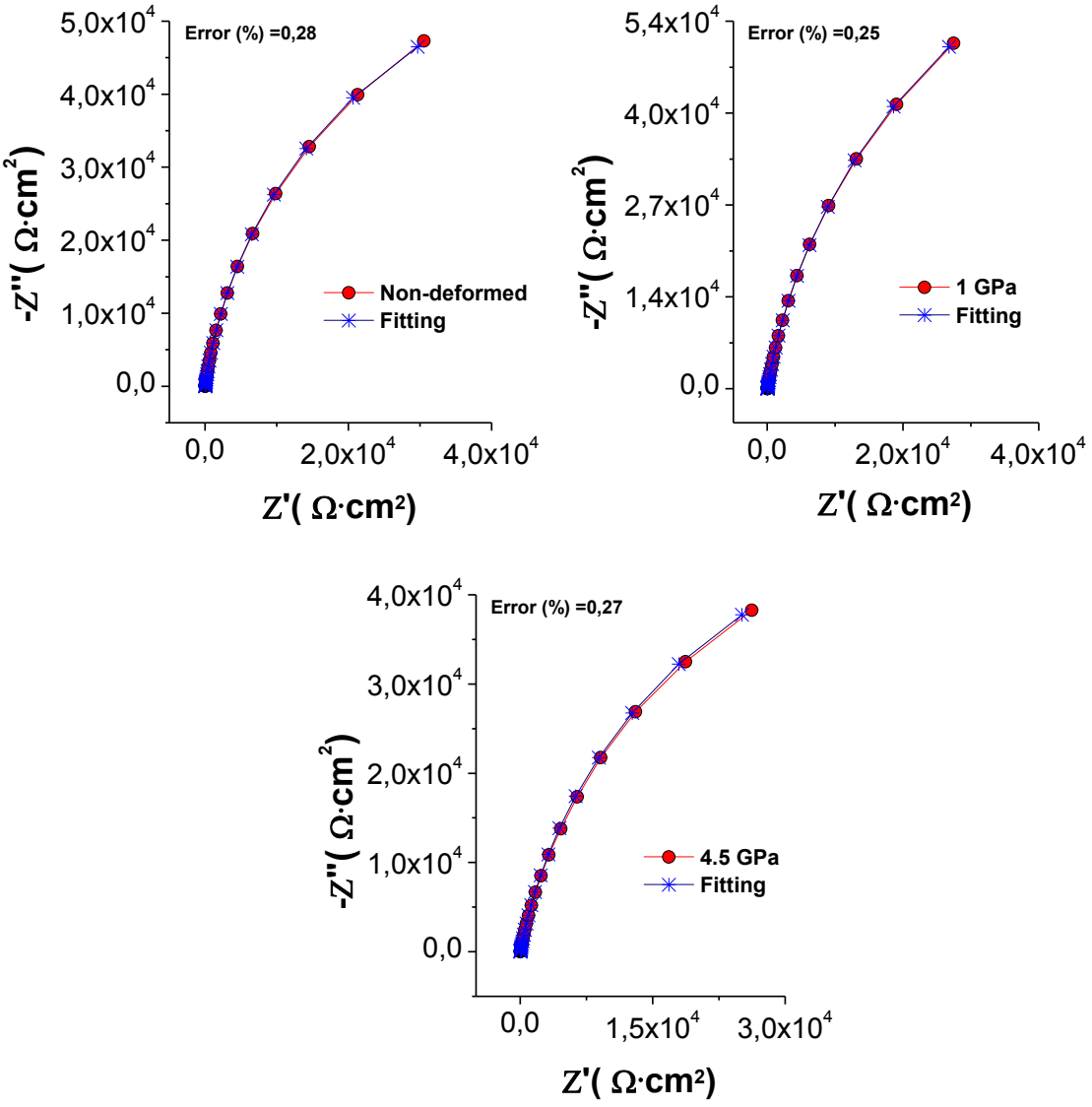

Figure 76: Nyquist diagrams of experimental data and simulated curves obtained by the Simad software for the polished surfaces of Ti35Nb7Zr5Ta alloy at ND, HPT1GPa, and HPT4.5GPa conditions.

The equivalent circuit parameters obtained when fitting EIS data of polished samples of Ti35Nb7Zr5Ta alloy (see section 6.2.1.3, Figure 69) at the ND, HPT1GPA, and HPT4.5GPa conditions, are shown in Table 34. Additionally, the equation derived by Brug et al. Eq. (20) was used to calculate the effective capacitance associated with each CPE ($C_{eff(a)}$ and $C_{eff(dl)}$). These capacitance values are also shown in Table 34.

Table 34: Equivalent circuit parameters and effective capacitance associated with the CPEs obtained when fitting EIS data of polished samples of Ti35Nb7Zr5Ta alloy according to the model in Figure 40.

Condition	Rs $\Omega \cdot cm^2$	Qa $\mu F \cdot s^{(\alpha a-1)}$	α_a	Ra $\Omega \cdot cm^2$	$C_{eff(a)}$ $\mu F/cm^2$	Qdl $\mu F \cdot s^{(\alpha dl-1)}$	α_{dl}	Rct $\Omega \cdot cm^2$	$C_{eff(dl)}$ $\mu F/cm^2$
Non-deformed	20	10	0.91	77	17	23	0.93	1.1E+05	49
1 GPa	21	10	0.89	129	15	22	0.91	1.7E+05	40
4.5 GPa	21	9	0.89	186	12	28	0.89	1.1E+05	44

It can be seen from the data in Table 34, high R_{ct} values, as well as low Q_a and Q_{dl} values. These results suggest a high corrosion resistance in the electrolyte used, and are indicative of a stable passive oxide film present on the surface of the polished samples of Ti35Nb7Zr5Ta alloy, non-deformed and deformed by HPT. Moreover, the α values were close to 0.9, which suggest that the passive film formed displays a near capacitive behavior.

On the other hand, the capacitance values for the double layer ($C_{eff(dl)}$) were between 40 to 49 $\mu F \cdot cm^{-2}$ (see Table 34). These values are in the typical range, 10-40 $\mu F \cdot cm^{-2}$. The capacitance values for the porous layer ($C_{eff(a)}$) were lower than ($C_{eff(dl)}$), between 12 to 17 $\mu F \cdot cm^{-2}$.

The film thickness, δ (in nm), were obtained from the dense inner layer capacitance. The thickness values were of 1.52, 1.90 and 1.70 nm for Ti35Nb7Zr5Ta alloy, at ND, HPT1GPa and HPT4.5GPa conditions, respectively. These results show that the passive films the deformation by HPT of Ti35Nb7Zr5Ta alloy contributes to increasing the passive film thickness.

The results obtained by fitting EIS data indicate that Ti35Nb7Zr5Ta alloy, non-deformed, and deformed by HPT, behaved in a very similar way. The differences are rather small, and this can be ascribed to the fact that the passive film formed on these alloys is primarily of the same nature.

6.3.2 EEC proposed for anodized samples

The transmission lines model used for the anodized samples of the Ti13Nb13Zr alloy was also chosen to describe the electrochemical behavior of anodized samples of Ti35Nb7Zr5Ta alloy, soaked in SBF. The model used is the following:

$$Z = R_s + \frac{1}{x_1 + x_2}\left[\lambda(x_1 + x_2)S_\lambda + (Z_A + Z_B)C_\lambda + \frac{1}{\lambda(x_1 + x_2)}Z_A Z_B S_\lambda\right]^{-1} \times \left(L\lambda x_1 x_2 (x_1 + x_2)S_\lambda + x_1[\lambda x_1 S_\lambda + L x_2 C_\lambda]Z_A + x_2[\lambda x_2 S_\lambda + L x_1 C_\lambda]Z_B + \frac{1}{x_1 + x_2} \times \left[2x_1 x_2 + ({x_1}^2 + {x_2}^2)C_\lambda + \frac{L}{\lambda}x_1 x_2 S_\lambda\right]Z_A Z_B\right)$$

Where the notations $x_1 = r_1 + Z_w$, $x_2 = r_2$, $C_\lambda = cosh\left(\frac{L}{\lambda}\right)$, $S_\lambda = sinh\left(\frac{L}{\lambda}\right)$, $Z_A = R_A$, $Z_B = \frac{1}{Q_B}(i\omega)^{-n}$, $\xi = \frac{r_3}{1+r_3 q_3 (i\omega)^\beta}$, and $\lambda = [\xi/(x_1 + x_2)]^{1/2}$ have been used. Figure 44 outlines the transmission line model used.

The fitting of EIS data as Nyquist representations is shown in Figure 77. The errors measured for the experimental and simulated data were 0.69% for the non-deformed sample and 3.10% for the 4.5 GPa deformed sample, which is quite reasonable.

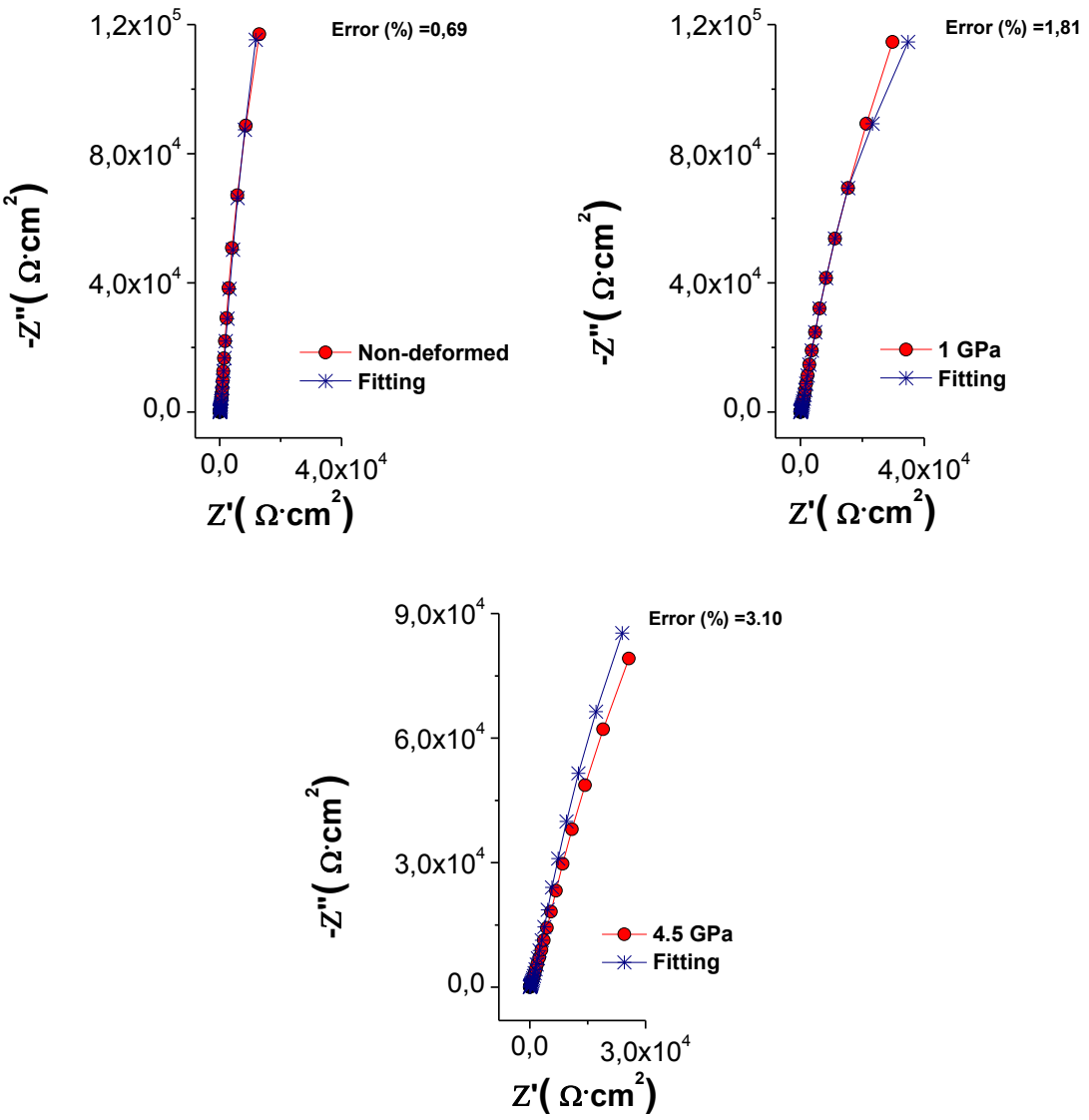

Figure 77: Nyquist diagrams of experimental data and simulated curves obtained by the Simad software for the anodized samples of Ti35Nb7Zr5Ta alloy at ND, HPT1GPa, and HPT4.5GPa conditions.

The equivalent circuit parameters obtained when fitting EIS data of anodized samples of Ti35Nb7Zr5Ta alloy (see section 6.2.2.3, Figure 71), at ND, HPT1GPa and HPT4.5GPa conditions, are shown in Table 35. Further, the effective capacitance was calculated by the equation derived from Hsu-Mansfeld et al. The capacitance values are also given in Table 35.

Table 35: Equivalent circuit parameters and effective capacitance associated with the CPEs obtained when fitting EIS data of anodized samples of Ti35Nb7Zr5Ta alloy

Condition	χ^1	χ^2	ξ				Z_A	Z_B			R_s
	R_1 (Ω)	R_2 (Ω)	R_3 (Ω)	Q_3 ($F^{\beta-1}$)	β	C_β μF/cm^2	R_A (Ω)	Q_B (F^{n-1})	n	C_n μF/cm^2	R_s (Ω)
Non-deformed	7	143	2.1E+15	2.0E-06	0.98	33	8.5E+06	1.2E-06	0.98	2	70.0
1 GPa	1	255	2.2E+15	1.9E-06	0.97	41	2.0E+06	1.0E-06	0.96	3	70.0
4.5 GPa	1	100	1.8E+15	3.1E-06	0.97	66	2.3E+06	1.6E-06	0.96	4	70.0

according to the model in Figure 44.

It can be seen from the data in Table 35, high R_A values, as well as low Q_3 and Q_B values. These results indicate that a highly stable film was formed on the surface of the anodized samples of Ti35Nb7Zr5Ta alloy, non-deformed and deformed by HPT, immersed in SBF. Moreover, the n values were close to 0.96, which suggest that the TiO_2 nanostructures formed displays a near capacitive behavior.

On the other hand, as the anodized samples of Ti13Nb13Zr alloy, it can be seen that internal resistance (R_2) of the solid channel was lower to the sample deformed at 4.5GPa. This result may be explained by the fact that the nanopores layer is thicker in the samples deformed at 1 GPa and ND (see Table 23). Therefore, it seems that there is a proportional relationship between TiO_2 nanoporous length and corrosion resistance.

The effective interfacial capacitance (C_β) associated with the ξ element, for all conditions, are between 33 and 66 μF·cm^{-2} (Table 35), which are typical values for double layer capacitances. Moreover, these values are higher than the effective capacitance (C_n) associated with the boundary CPE, between 2 and 4 μF·cm^{-2}. These values are in the order of magnitude of a passive film capacitance.

Concerning the passive film thickness, they were obtained from passive film capacitance (C_n). The thickness values were of 47.4, 34.3 and 22.3 nm for

Ti35Nb7Zr5Ta alloy, at ND, HPT1GPa and HPT4.5GPa conditions, respectively. These results show that the anodization of Ti35Nb7Zr5Ta alloy contributes to increasing the passive film thickness. The passive film thickness, as well as the length of the nanostructures, are affected by the deformation by HPT.

Finally, the experimental EIS data obtained for the anodized Ti35Nb7Zr5Ta alloy were satisfactory fitting by the model proposed in Figure 44. Therefore, the physical behavior of the system was well described by this transmission line model.

6.3.3 EEC proposed for samples chemically treated by HCl etching and NaOH activation

The electrochemical behavior of samples of Ti35Nb7Zr5Ta alloy, chemically treated, by HCl etching and NaOH activation, was also described by the EEC show in Figure 47, for samples with three different layers, consisting of a compact inner layer of titanium dioxide (TiO_2), an intermediate TiO_2 layer and an outer layer of sodium titanate ($Na_2Ti_5O_{11}$).

The EIS data were fitted using the following EEC:

$$R_s + (Q_b / R_b) + Q_a / (R_a + (Q_{dl} / R_{ct})),$$

where R_s represents the electrolyte resistance, R_b represents the resistance of the outer layer, Q_b is the constant-phase element for the outer layer, R_a is the resistance of the intermediate layer, Q_a is the constant-phase element for the intermediate layer, R_{ct} represents the resistance of charge-transfer, Q_{dl} is the constant-phase element for the double layer at the dense inner layer-electrolyte interface.

The fitting of EIS data as Nyquist representations is shown in Figure 78. The errors measured for the experimental and simulated data were 1.28% for the non-deformed sample and 3.95% for the 4.5 GPa deformed sample, which is quite reasonable.

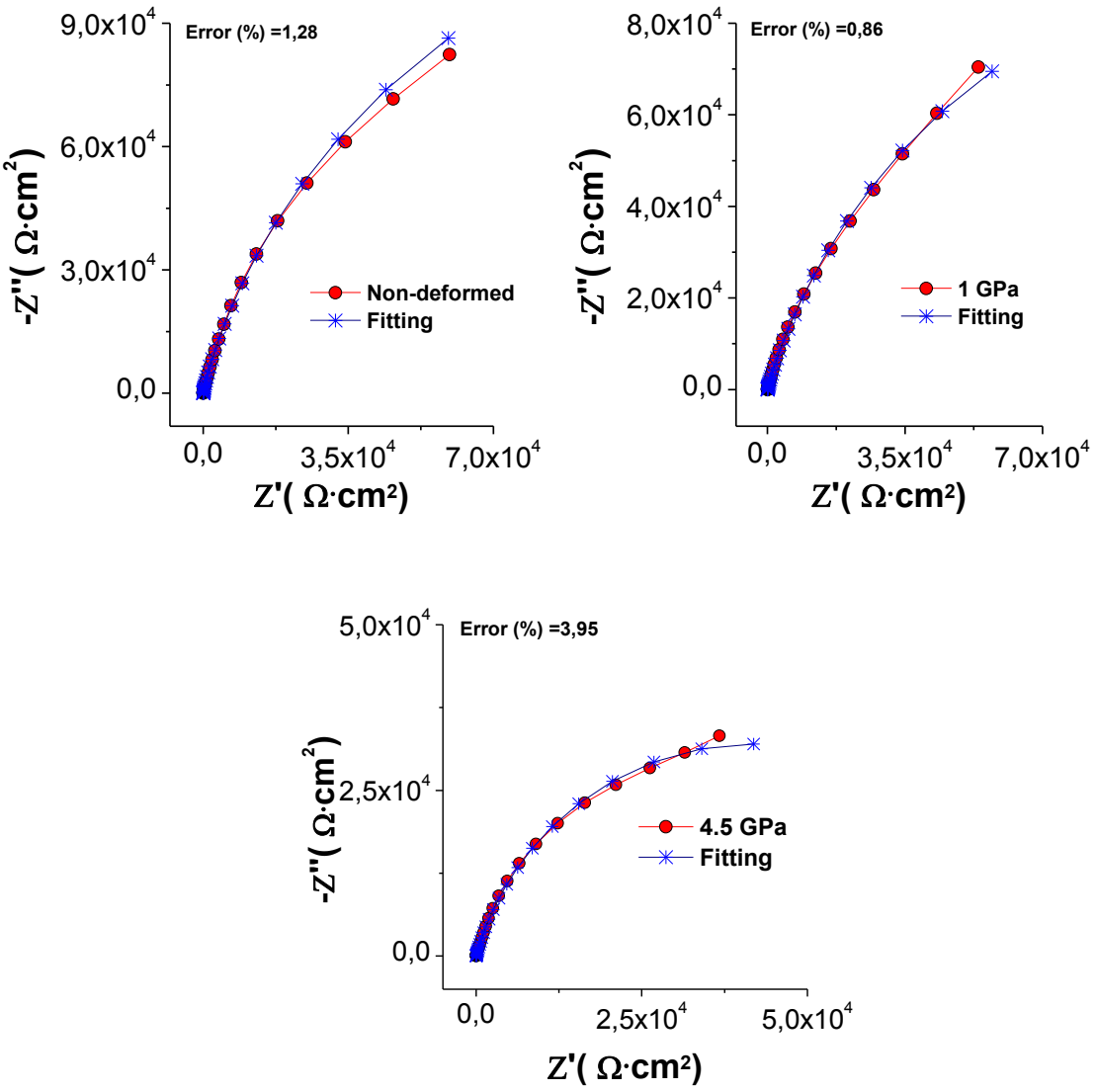

Figure 78: Nyquist diagrams of experimental data and simulated curves obtained by the Simad software for samples of Ti35Nb7Zr5Ta alloy chemically treated by HCl and NaOH at ND, HPT1GPa, and HPT4.5GPa conditions.

The equivalent circuit parameters obtained when fitting EIS data of samples of Ti35Nb7Zr5Ta alloy chemically treated by HCl and NaOH, are shown in Table 36. Further, the effective capacitance associated with the CPE was calculated with the equation derived by Brug et al. (Eq.20). These capacitance values are given in Table 36.

Table 36: Equivalent circuit parameters and the effective capacitance associated with the CPEs obtained when fitting EIS data of samples of Ti35Nb7Zr5Ta alloy chemically treated by HCl and NaOH, according to the EEC in Figure 47.

	Condition		
Element	**Non-deformed**	**1 GPa**	**4.5 GPa**
Rs ($\Omega \cdot cm^2$)	21	20	20
Qb ($\mu F \cdot s^{(\alpha b-1)}$)	42	40	40
α_b	0.72	0.72	0.72
Rb ($\Omega \cdot cm^2$)	10	9	3
$C_{eff(b)}$ ($\mu F/cm^2$)	1.8	1.6	1.1
Qa ($\mu F \cdot s^{(\alpha a-1)}$)	19	33	47
α_a	0.70	0.71	0.80
Ra ($\Omega \cdot cm^2$)	1	1	24
$C_{eff(a)}$ ($\mu F/cm^2$)	0.2	0.5	7.3
Qdl ($\mu F \cdot s^{(\alpha dl-1)}$)	32	17	12
α_{dl}	0.93	0.93	0.98
Rct ($\Omega \cdot cm^2$)	3.3E+05	2.7E+05	8.4E+04
$C_{eff(dl)}$ ($\mu F/cm^2$)	18	10	10

It can be seen from data in Table 36 that the α_{dl} value was higher than 0.92, which suggest that the samples chemically treated displays a near capacitive behavior. Also, as samples chemically treated of the Ti35Nb7Zr5Ta alloy, the values of α_b and α_a were between 0.70 and 0.80, which was caused by interfacial heterogeneity.

On the other hand, the capacitance values for ($C_{eff(dl)}$) were between 10 to 18 $\mu F \cdot cm^{-2}$ (see Table 36). These values are in the typical range 10-40 $\mu F \cdot cm^{-2}$. The capacitance values for the porous outer layer ($C_{eff(b)}$) and intermediate porous layer ($C_{eff(a)}$) were lower than $C_{eff(dl)}$.

The passive film thickness, δ (in nm), were also obtained from passive film capacitance. The values of the thickness were of 4.07, 7.87 and 7.43 nm for chemically treated Ti35Nb7Zr5Ta alloy, at ND, HPT1GPa and HPT4.5GPa

conditions, respectively. These results show that the chemical treatment and the deformation by HPT contribute to increasing the passive films thickness.

6.3.4 EEC proposed for samples chemically treated by H_3PO_4 etching and NaOH activation

The equivalent circuit shown in Figure 47 was also used to fitting the EIS data of samples of Ti35Nb7Zr5Ta alloy chemically treated by H_3PO_4 and NaOH. The fitting of EIS data as Nyquist representations is shown in Figure 79. The errors measured for the experimental and simulated data were 2.14% for the non-deformed sample and 3.88% for the 4.5 GPa deformed sample, indicating that data adjusted well to the proposed equivalent circuit.

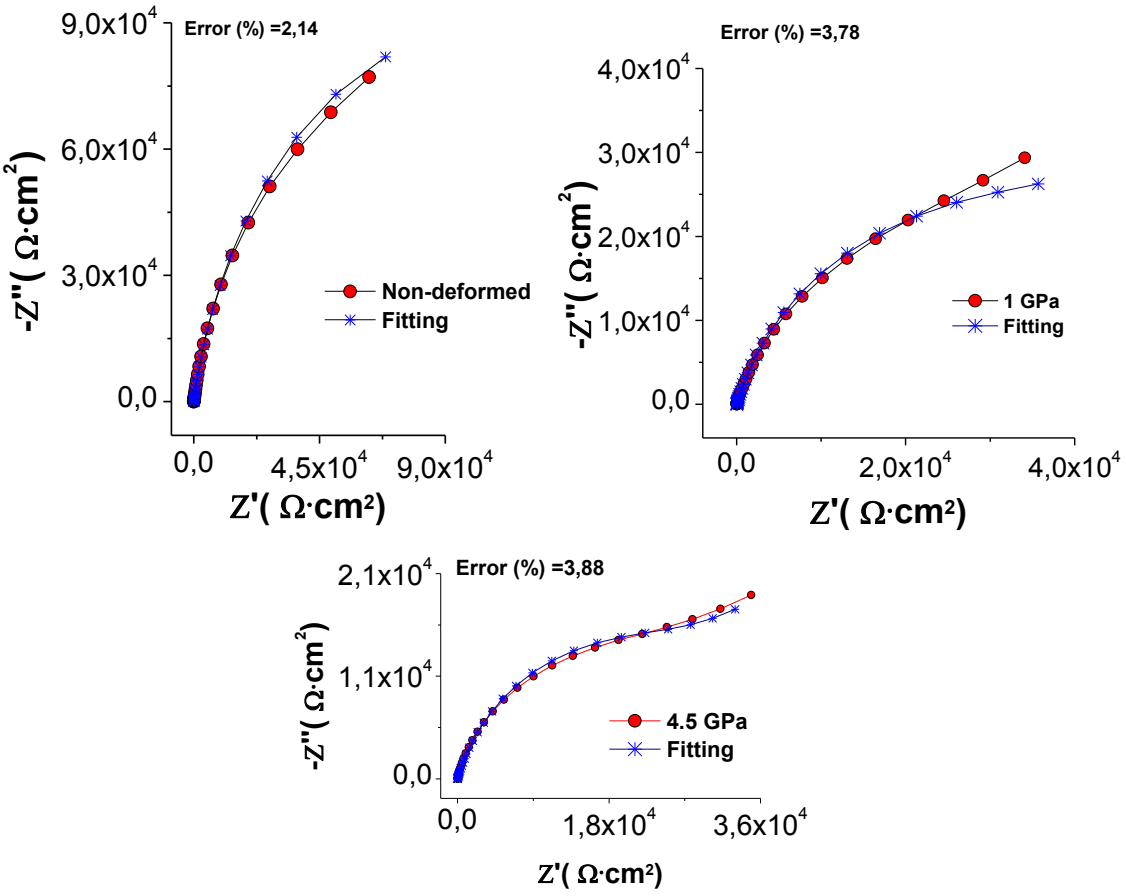

Figure 79: Nyquist diagrams of experimental data and simulated curves obtained by the Simad software for samples of Ti35Nb7Zr5Ta alloy chemically treated by H_3PO_4 and NaOH at ND, HPT1GPa, and HPT4.5GPa conditions.

The equivalent circuit parameters and effective capacitance (calculated by an equation derived by Brug et al.) associated with the CPEs obtained are shown in Table 37.

Table 37: Equivalent circuit parameters and the effective capacitance associated with the CPEs obtained when fitting EIS data of samples of Ti35Nb7Zr5Ta alloy chemically treated by H_3PO_4 and NaOH, according to the EEC in Figure 47.

	Condition		
Element	**Non-deformed**	**1 GPa**	**4.5 GPa**
Rs ($\Omega \cdot cm^2$)	20	20	20
Qb ($\mu F \cdot s^{(\alpha b-1)}$)	40	53	15
α_b	0.73	0.70	0.80
Rb ($\Omega \cdot cm^2$)	9	7	4
$C_{eff(b)}$ ($\mu F/cm^2$)	1.8	1.6	1.3
Qa ($\mu F \cdot s^{(\alpha a-1)}$)	6	6	37
α_a	0.72	0.78	0.84
Ra ($\Omega \cdot cm^2$)	3	1	10
$C_{eff(a)}$ ($\mu F/cm^2$)	0.1	4.3	7.5
Qdl ($\mu F \cdot s^{(\alpha dl-1)}$)	47	54	54
α_{dl}	0.88	0.80	0.80
Rct ($\Omega \cdot cm^2$)	2.2E+05	1.0E+05	2.5E+04
$C_{eff(dl)}$ ($\mu F/cm^2$)	19	10	10

It can be seen from the data in Table 37 that the α_{dl} values were between 0.80 and 0.88, which suggest that the samples chemically treated displays a near capacitive behavior. The same behavior was observed as all the samples with chemical treatment, where the values of α_b and α_a were between 0.70 and 0.84, which was a consequence of an interfacial heterogeneity of the outer layer.

On the other hand, the capacitance values for the double layer $C_{eff(dl)}$ were between 10 to 19 $\mu F \cdot cm^{-2}$ (see Table 37). These values are in the typical range 10-40 $\mu F \cdot cm^{-2}$. The capacitance values for the porous outer layer ($C_{eff(b)}$) and intermediate porous layer ($C_{eff(a)}$) were lower than $C_{eff(dl)}$.

The passive film thickness, δ (in nm), were obtained from dense inner layer capacitance. The thickness values were of 3.98, 7.62 and 7.69 nm for Ti35Nb7Zr5Ta alloy, at ND, HPT1GPa and HPT4.5GPa conditions, respectively.

The results obtained by fitting EIS data indicate that Ti35Nb7Zr5Ta alloy chemically treated by H_3PO_4 and NaOH behaved in a very similar way.

6.4 Bioactivity of Ti35Nb7Zr5Ta alloy

In order to characterize the bioactivity of Ti35Nb7Zr5Ta alloy, the amount of hydroxyapatite (HAp) spontaneously deposited on the surface of the samples was measured. The samples were immersed in SBF for 1, 7, and 14 days.

6.4.1 Bioactivity of polished samples

Figure 80 shown SEM-FEG observations of polished samples, subjected to the bioactivity tests, after 1, 7, and 14 days immersed in SBF.

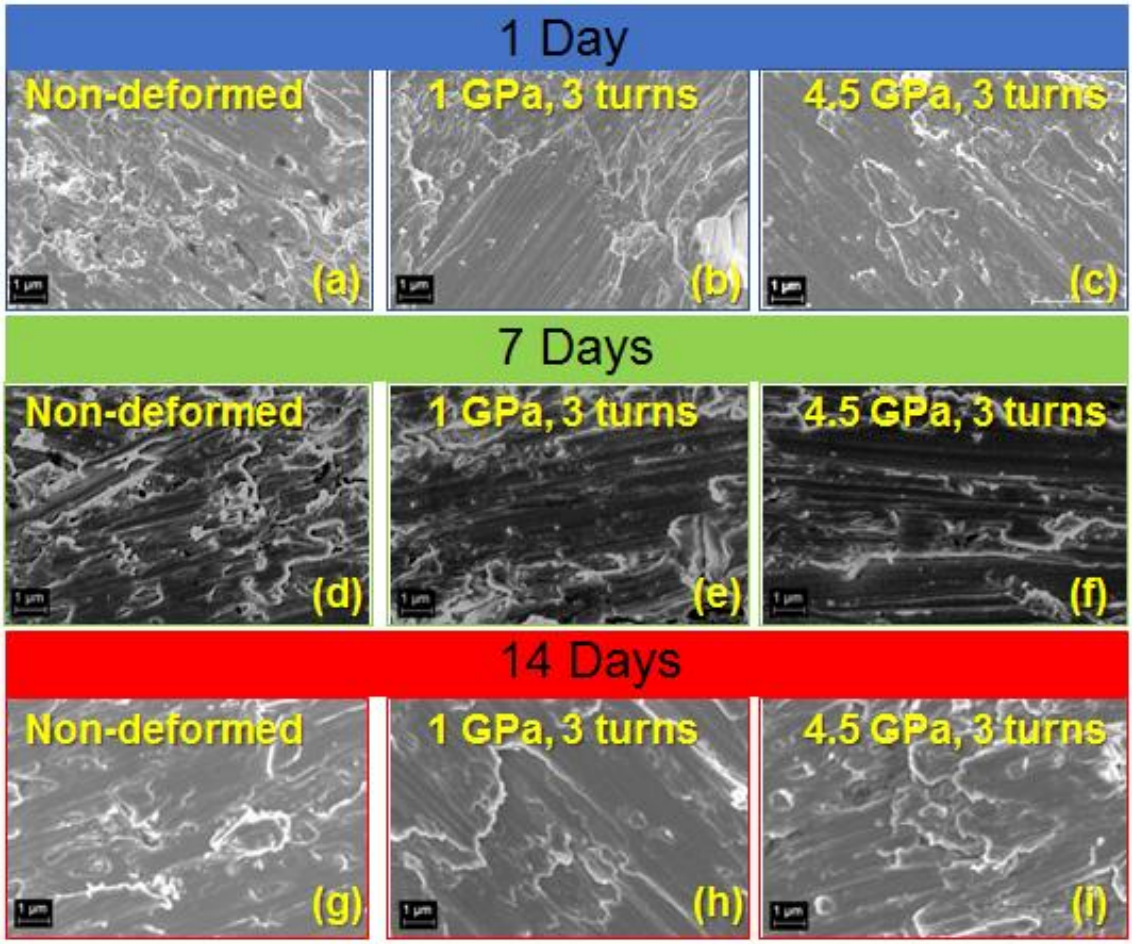

Figure 80: SEM-FEG observations (scale bar 1 µm) of polished samples of Ti35Nb7Zr5Ta alloy, non-deformed, and deformed by HPT, subjected to the bioactivity tests after 1, 7, and 14 days immersed in SBF.

From Figure 80, one may observe that even after 14 days of immersion in the physiological solution, no apatite was detected on any surfaces of the polished samples of Ti35Nb7Zr5Ta alloy.

Table 38 shows the EDS analysis performed for each condition. The results confirm that there was no apatite formation on the surface of the samples.

Table 38: The quantitative chemical EDS analysis of Ti35Nb7Zr5Ta alloy non-deformed and deformed by HPT after soaking in SBF solution for 1, 7, and 14 days.

		Chemical element (at %)								
Soaking time	**Condition**	**Ti**	**Zr**	**Nb**	**O**	**Ta**	**Na**	**Cl**	**Ca**	**P**
1 day	Non-deformed	64.91	3.02	18.74	11.96	1.18	-	-	0.03	0.16
	1 GPa	64.18	3.17	18.18	12.56	1.68	-	-	0.04	0.19
	4.5 GPa	66.21	2.82	18.24	10.89	1.64	-	-	0.03	0.17
7 days	Non-deformed	61.90	3.01	18.26	14.90	1.71	-	-	0.09	0.13
	1 GPa	62.40	3.04	18.56	13.87	1.91	-	-	0.06	0.16
	4.5 GPa	62.42	3.07	18.37	14.02	1.89	-	-	0.06	0.17
14 days	Non-deformed	50.01	2.36	14.42	21.20	1.70	5.10	4.77	0.18	0.26
	1 GPa	50.28	2.75	14.23	20.36	1.89	5.20	4.80	0.17	0.32
	4.5 GPa	50.56	2.42	14.15	21.03	1.76	4.98	4.67	0.16	0.27

The Ca/P ratio in the HAp, $Ca_{10}(PO_4)_6(OH)_2$, concerning stoichiometric value is 1.67 [188]. From the data in Table 19, it can be seen that very low levels of calcium and phosphorus were measured. Therefore, there was no formation of a film based on calcium and phosphorus on the surface of samples without surface treatments (polished samples). On the other hand, the polished samples were weighed in order to verify the mass gain due to the formation of a HAp film. There was no change in the mass after 14 days of immersion in SBF.

6.4.2 Bioactivity of samples anodized

Figure 81 shown SEM-FEG observations of anodized samples, subjected to the bioactivity tests, after 1, 7, and 14 days immersed in SBF.

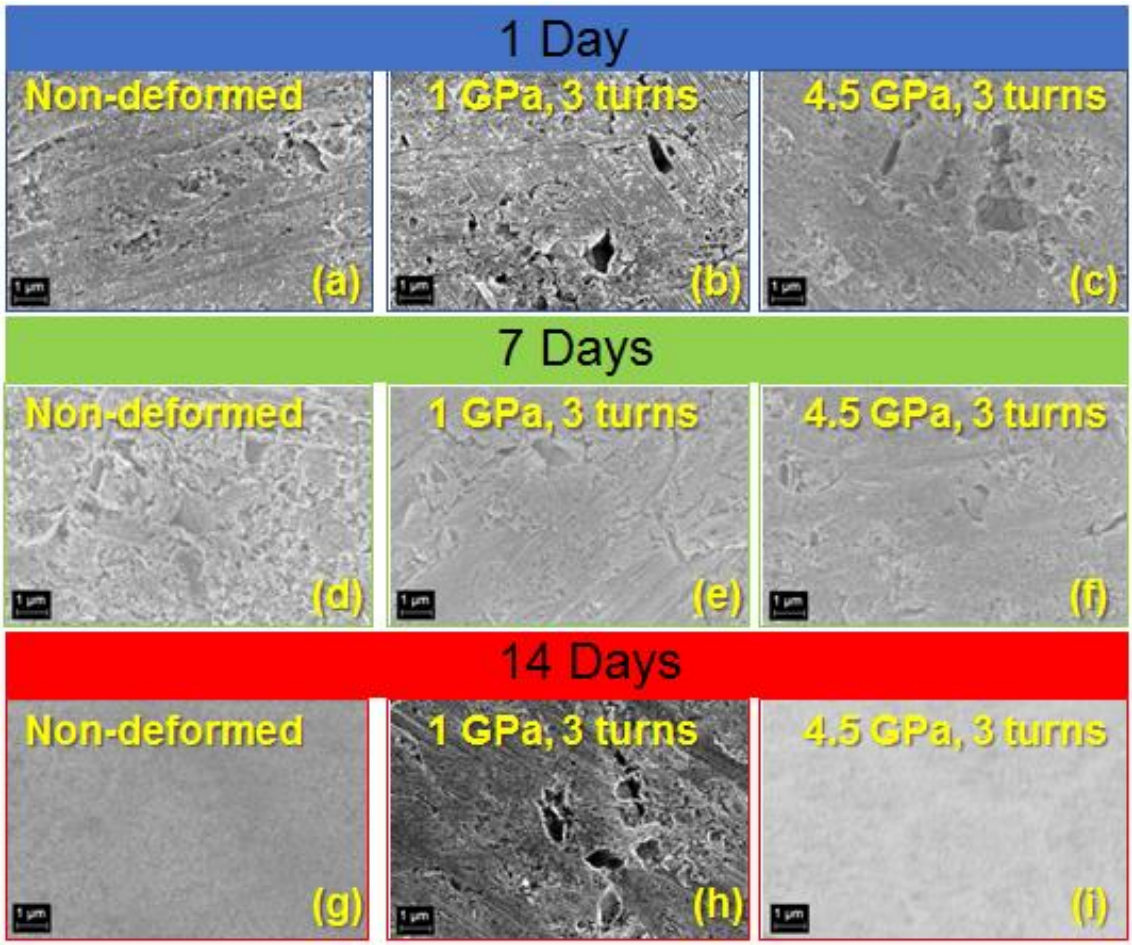

Figure 81: SEM-FEG observations (scale bar 1 µm) of anodized samples of Ti35Nb7Zr5Ta alloy, non-deformed, and deformed by HPT, subjected to the bioactivity tests after 1, 7, and 14 days immersed in SBF.

Figures 81((g) and (i)) show that only apatite deposits were formed from the fourteenth day of immersion in SBF.

Table 39 shows the EDS analysis performed for each condition and confirms that there is apatite formation from the fourteenth day on immersion in SBF for the deformed condition at 4.5 GPa and non-deformed samples.

Table 39: The quantitative EDS analysis spectrum and Ca/P molar ratio of anodized samples of Ti35Nb7Zr5Ta alloy, non-deformed and deformed by HPT, subjected to the bioactivity tests after 1, 7 and 14 days immersed in SBF.

		Chemical element (at %)									
Soaking time	**Condition**	**Ti**	**Zr**	**Nb**	**O**	**Ta**	**Na**	**Mg**	**Ca**	**P**	**Ca/P Molar Ratio**
1 day	Non-deformed	23.10	1.25	7.89	66.54	0.68	-	-	0.41	0.13	-
	1 GPa	22.21	1.09	7.64	67.89	0.62	-	-	0.42	0.13	-
	4.5 GPa	22.55	1.25	7.83	67.16	0.57	-	-	0.48	0.16	-
7 days	Non-deformed	22.77	1.11	7.78	67.05	0.72	-	-	0.42	0.14	-
	1 GPa	22.04	1.12	7.88	67.88	0.51	-	-	0.45	0.12	-
	4.5 GPa	21.82	1.23	7.80	68.10	0.42	-	-	0.47	0.16	-
14 days	Non-deformed	0.20	-	-	64.80	-	0.38	0.90	21.46	12.26	1.75
	1 GPa	22.48	1.14	8.04	67.24	0.52	-	-	0.44	0.14	-
	4.5 GPa	0.20	-	-	64.42	-	0.37	0.88	22.10	12.03	1.84

The molar ratio of Ca / P was calculated in Table 39. This molar ratio of Ca / P was approximately 1.80, which is higher than the stoichiometric ratio of 1.67, indicating that the newly formed calcium phosphate is a type B carbonate apatite, in which PO_4^{3-} substitutes for CO_3^{2-}. On the other hand, to verify the mass gain by the formation of a hydroxyapatite film, the samples were weighed, and their results are presented in Figure 82, which shows that from the fourteenth-day apatite is formed in the sample non-deformed, and the sample deformed at 4.5 GPa.

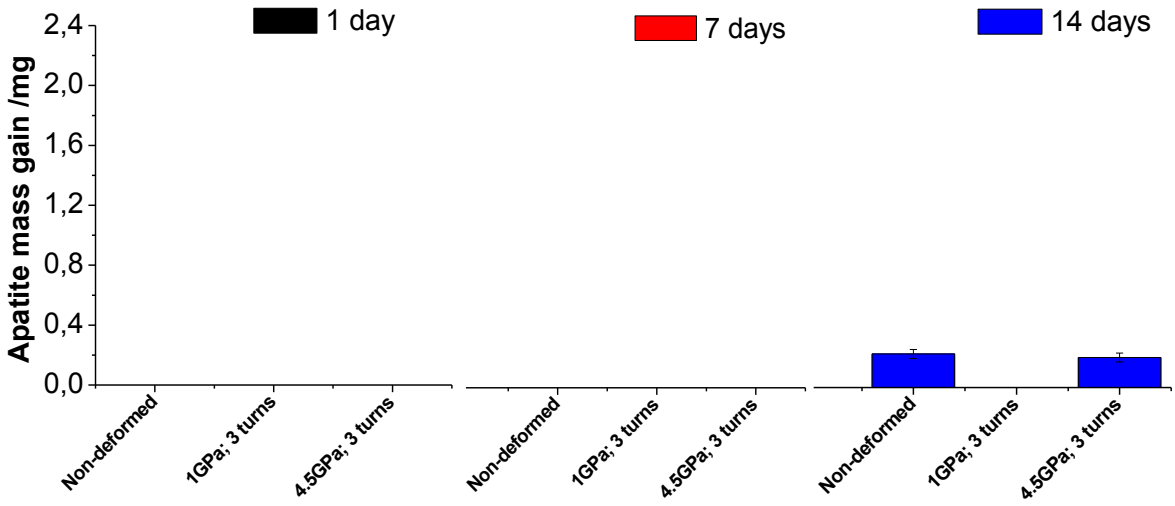

Figure 82: The weight change of samples of the Ti35Nb7Zr5Ta alloy with TiO_2 nanotubes unprocessed and processed by HPT after soaking in SBF for 1, 7 and14 days.

6.4.3 Bioactivity of samples chemically treated by HCl etching and NaOH activation

Figure 83 shown SEM-FEG observations of samples chemically treatment by HCl and NaOH, subjected to the bioactivity tests, after 1, 7 and 14 days immersed in SBF.

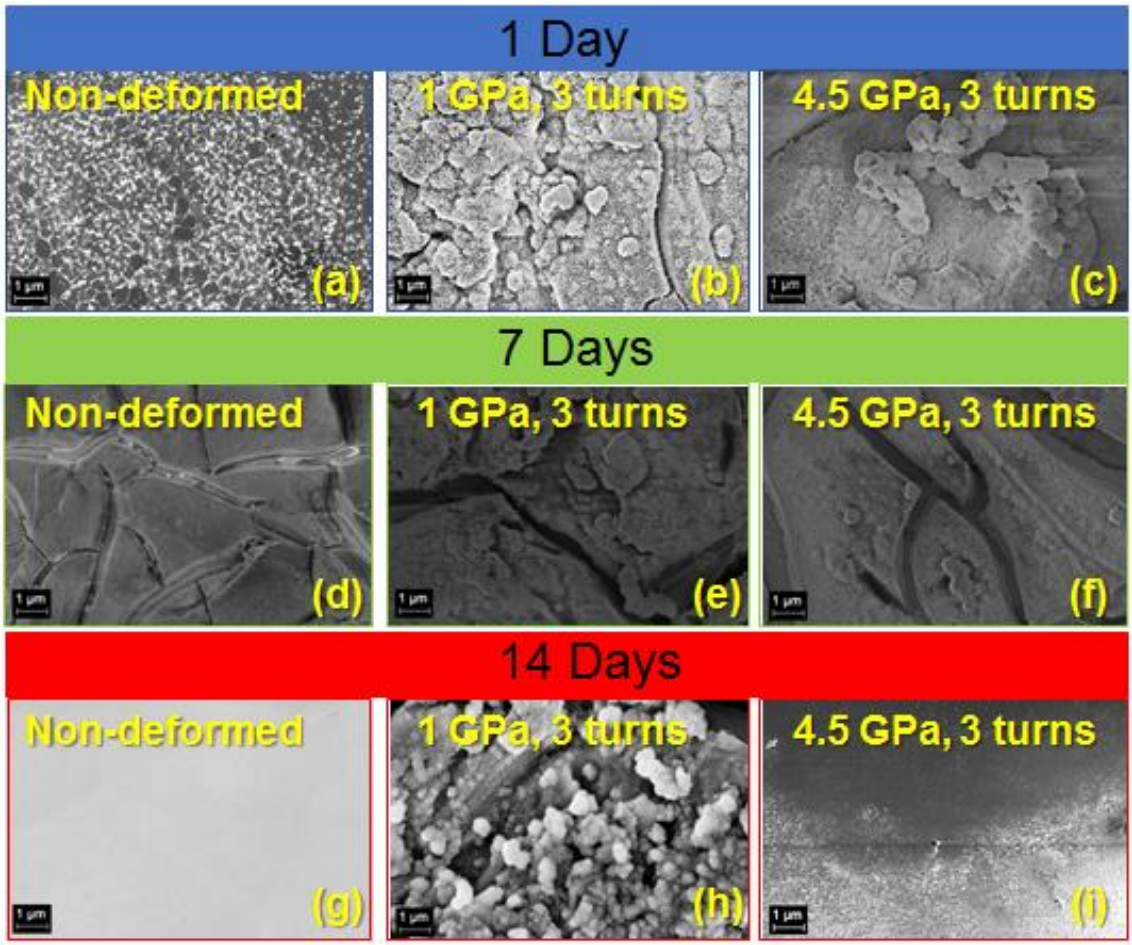

Figure 83: SEM-FEG observations (scale bar 1 µm) for samples of Ti35Nb7Zr5Ta alloy chemically treated by HCl and NaOH, non-deformed and deformed by HPT, subjected to the bioactivity tests after 1, 7, and 14 days immersed in SBF.

Figures 83((g) and (i)) confirm that only apatite deposits were formed from the fourteenth day of immersion in SBF.

Table 40 shows the EDS analysis performed for each condition and confirms that there is apatite formation from the fourteenth day on immersion in SBF for the deformed condition at 4.5 GPa and non-deformed samples.

Table 40: The quantitative EDS analysis spectrum and Ca/P molar ratio for samples of Ti35Nb7Zr5Ta alloy chemically treated by HCl and NaOH, non-deformed and deformed by HPT, subjected to the bioactivity tests after 1, 7 and 14 days immersed in SBF.

		Chemical element (at %)									
Soaking time	**Condition**	**Ti**	**Zr**	**Nb**	**O**	**Ta**	**Na**	**Mg**	**Ca**	**P**	**Ca/P Molar Ratio**
1 day	Non-deformed	16.23	0.25	2.17	71.65	0.32	0.62	0.70	6.65	1.41	-
	1 GPa	16.43	0.26	2.16	71.30	0.31	0.63	0.71	6.74	1.43	-
	4.5 GPa	16.45	0.25	2.40	71.20	0.31	0.62	0.70	6.65	1.41	-
7 days	Non-deformed	18.62	0.34	2.79	69.76	0.92	0.92	0.68	5.51	2.06	-
	1 GPa	19.10	0.41	2.68	68.74	0.92	0.68	0.57	5.01	1.89	-
	4.5 GPa	18.29	0.52	2.37	67.89	1.08	0.72	0.69	6.14	2.30	-
14 days	Non-deformed	0.21	-	-	64.80	-	0.37	0.90	21.46	12.26	1.75
	1 GPa	19.55	0.74	2.92	70.50	0.28	1.86	0.48	3.65	0.02	-
	4.5 GPa	0.01	-	-	67.45	0.02	0.35	1.17	19.89	11.11	1.79

The molar ratio of Ca / P was calculated in Table 40. This molar ratio of Ca / P was approximately 1.77, which indicates that the newly formed calcium phosphate is a type B carbonate apatite, in which PO_4^{3-} substitutes for CO_3^{2-}. On the other hand, to verify the mass gain by the formation of a hydroxyapatite film, the samples were weighed, and their results are introduced in Figure 84, showing that from the fourteenth-day apatite is formed in the non-deformed samples and the samples deformed at 4.5 GPa.

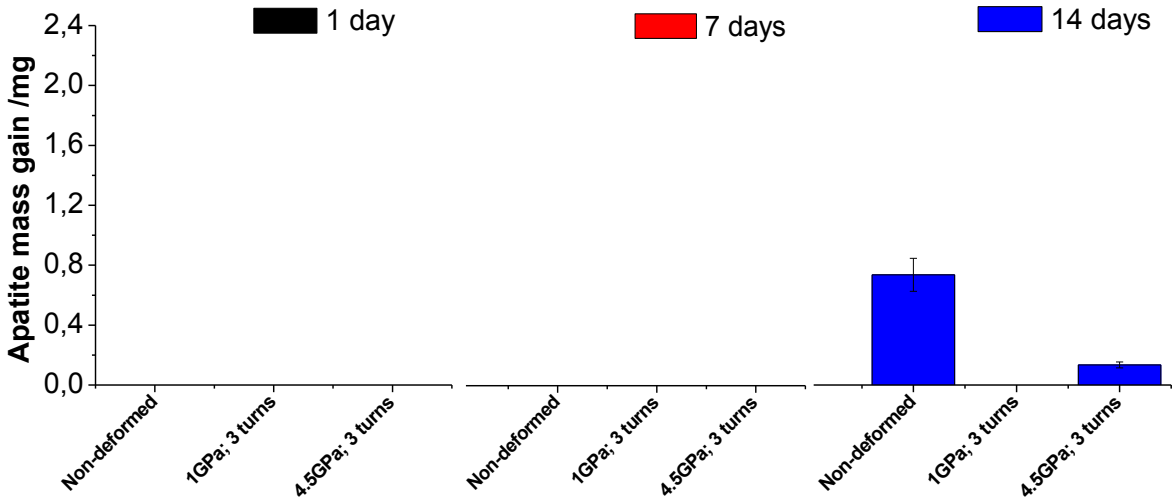

Figure 84: The weight change for samples of Ti35Nb7Zr5Ta alloy chemically treated, by HCl etching and NaOH activation, non-deformed and deformed by HPT, subjected to the bioactivity tests after 1, 7 and 14 days immersed in SBF.

6.4.4 Bioactivity of samples chemically treated by H_3PO_4 etching and NaOH activation

Figure 85 shown SEM-FEG observations of samples chemically treatment by H_3PO_4 and NaOH, subjected to the bioactivity tests, after 1, 7, and 14 days immersed in SBF.

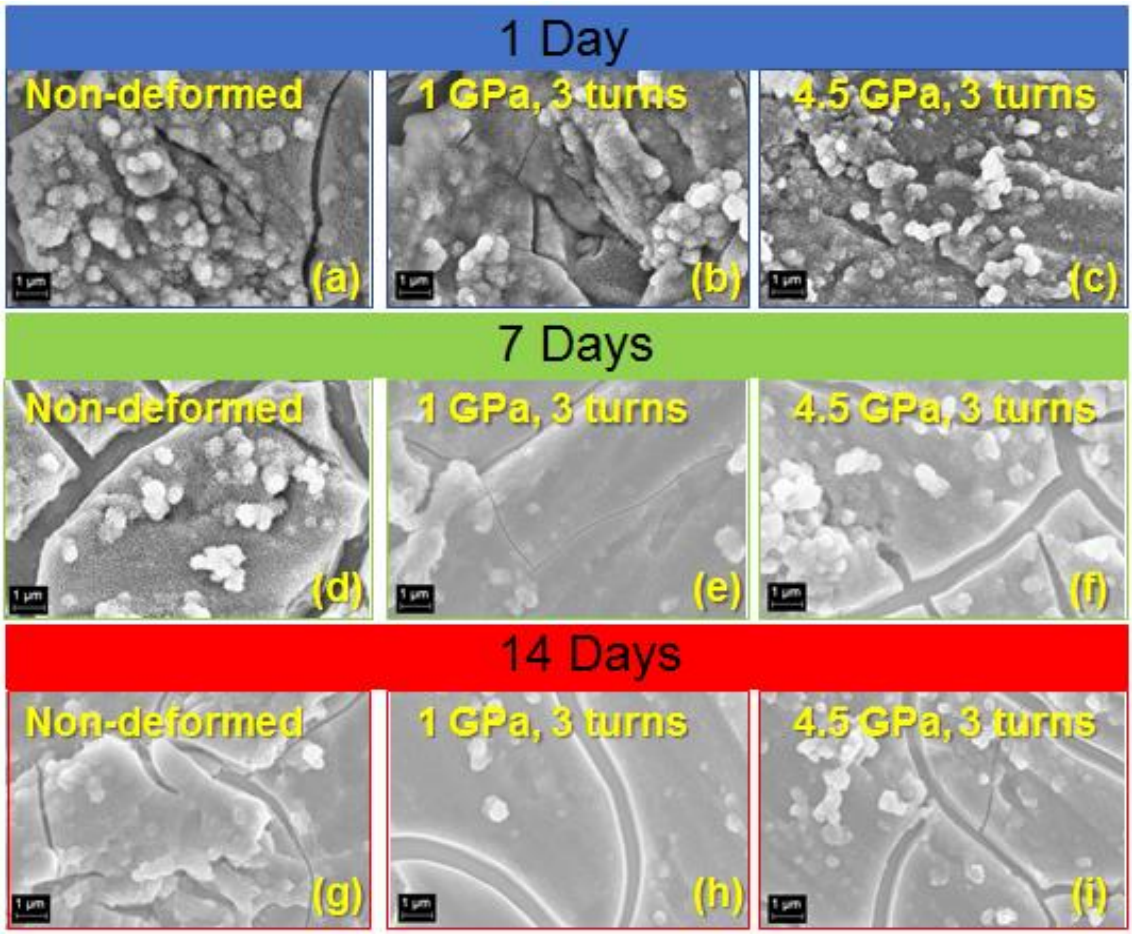

Figure 85: SEM-FEG observations (scale bar 1 µm) for samples of Ti35Nb7Zr5Ta alloy chemically treated by H_3PO_4 and NaOH, non-deformed and deformed by HPT, subjected to the bioactivity tests after 1, 7, and 14 days immersed in SBF.

Figure 85 indicates that even after 14 days of immersion in the physiological solution, no apatite was detected on any surfaces of Ti35Nb7Zr5Ta alloy chemically treated, by H_3PO_4 etching and NaOH activation.

Table 41 shows the EDS analysis performed for each condition. The results confirm that there was no apatite formation on the surface of the samples.

Table 41: The quantitative chemical EDS analysis for samples of Ti35Nb7Zr5Ta alloy chemically treated by H_3PO_4 and NaOH, non-deformed and deformed by HPT, subjected to the bioactivity tests after 1, 7 and 14 days immersed in SBF.

		Chemical element (at %)								
Soaking time	**Condition**	**Ti**	**Zr**	**Nb**	**O**	**Ta**	**Na**	**Mg**	**Ca**	**P**
1 day	Non-deformed	22,09	0,41	4,37	69,02	0,11	1,47	0,51	1,61	0,41
	1 GPa	22,14	0,38	2,58	70,88	0,16	1,43	0,70	1,42	0,31
	4.5 GPa	22,68	0,36	3,75	69,31	0,10	1,35	0,48	1,59	0,38
7 days	Non-deformed	21,91	0,59	4,13	66,34	1,19	1,20	0,43	3,70	0,51
	1 GPa	22,52	1,14	5,58	63,26	0,99	1,75	0,79	3,74	0,23
	4.5 GPa	21,82	0,80	4,88	65,06	0,62	1,85	0,60	3,88	0,49
14 days	Non-deformed	24,55	0,76	5,54	62,29	0,72	1,49	0,52	3,73	0,40
	1 GPa	22,99	0,95	5,05	64,66	0,69	1,26	0,44	3,66	0,30
	4.5 GPa	24,02	1,47	5,96	63,43	0,76	1,06	0,27	2,91	0,12

From the data in Table 41, it can be seen the same behavior as in the polished samples with very low levels of calcium and phosphorus being observed. Therefore, there was no formation of a film based on calcium and phosphorus on the surface of Ti35Nb7Zr5Ta alloy chemically treated. On the other hand, the chemically treated samples were weighed in order to verify the mass gain due to the formation of a HAp film. There was no change in the mass after 14 days of immersion in SBF.

7 DISCUSSION

The grain size was measured before and after the deformations by HPT for the different samples of the alloys Ti13Nb13Zr (α'+β) and Ti35Nb7Zr5Ta (β). Initially, the Ti13Nb13Zr had an average grain size of 250 µm, after being deformed with 1 GPa the size is reduced to 89 µm and finally to 203 nm for the pressure of 4.5 GPa. For the (β) alloy the same behavior is observed where initially an average size of 240 µm is observed, and when deformed with 1 GPa it is reduced to 89 µm, and, finally, grain sizes of 112 nm are observed after deformation of 4.5 GPa. The HPT process produces ultrafine grain size (UFG) in nanometric ranges for high pressures and also generates a high amount of dislocation density [192]. Grain refinement is formed by subdividing the original grains into subgrains into the early stages of deformation as illustrated in Figure 86, and recovering and migrating from these subgrains to form high-angle contours in the following stages of plastic deformation.

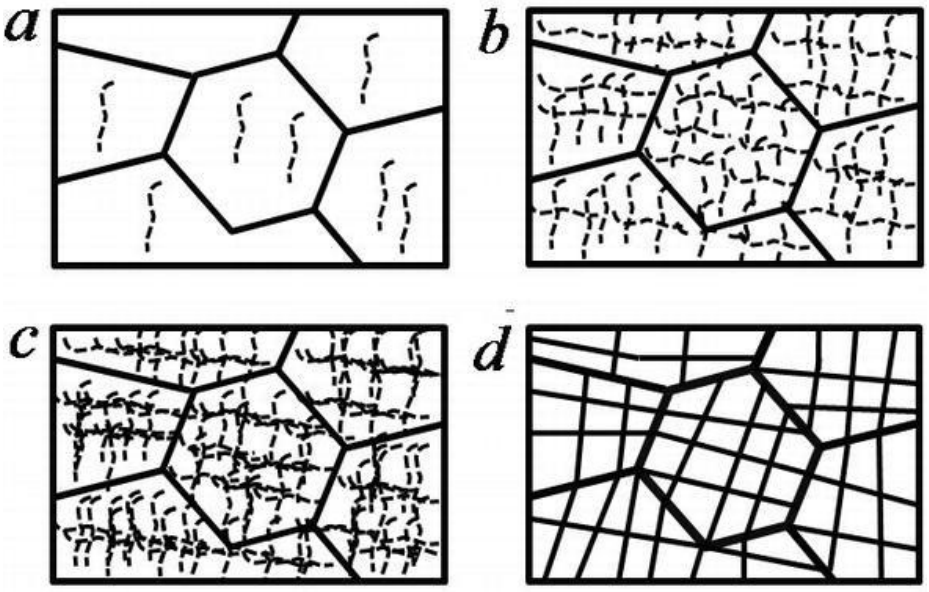

Figure 86: Scheme of grain refinement during deformation by HPT describing in sequence the processes of (a) the generation of dislocations, (b) the formation of subgrains boundaries, (c) the increase in the disorientation angle, and (d) the division of grains into subgrains. Adapted from Borodachenkova et al., (2017) [193].

The hardness in the processed state by HPT was reported for alloys of Ti13Nb13Zr and Ti35Nb7Zr5Ta. The hardness in the processed HPT state becomes higher for high pressures, which is related to the decrease in grain size. Initially, microhardness value was 265 HV in the non-deformed state and 390 HV in the HPT-processed state at 4.5 GPa for the alloy Ti13Nb13Zr and values of 183 HV in the non-deformed state and 320 HV in the HPT-processed state at 4.5 GPa for the alloy of Ti35Nb7Zr5Ta. The microhardness measurements for all the samples have confirmed that the hardness increases with the distance from the center of the disk to the edge because, as the processing is torsional, the deformation decreases from the edge towards the center, leading to smaller grains on the edge that in the center [20]. This analysis is per the study of Wang and Langdon [194], in which the same behavior is observed for the alloy Ti6Al4V deformed by HPT.

The effect of HPT on Young's modulus was investigated. Young's modulus is a measure of interatomic bonds force and depends only slightly on the microstructure morphology of materials [195]. In fact, in the alloys Ti13Nb13Zr and Ti35Nb7Zr5Ta deformed by HPT, the degree of plastic deformation and the size of grains have no significant influence on the value of Young's modulus. For the Ti13Nb13Zr alloy values of Young's modulus were observed between 58 to 63 GPa and Ti35Nb7Zr5Tabetween 44 and 45 GPa for the Ti35Nb7Zr5Ta alloy.

Methods of surface modification are of great interest in this work. The nanostructures in alloys of Ti13Nb13Zr and Ti35Nb7Zr5Ta with different degrees of deformations were fabricated by the surface modification technique known as anodization. The effect of the SPD on the morphology, crystal phase, and size of nanostructures was investigated. Nanostructures arrays with uniform diameter were achieved by using an organic electrolyte (glycerol) containing fluoride ions and a few percentages of water, indicating that the electrolyte composition will influence the arrangement of TiO_2 nanostructures arrays. XRD analysis confirmed that as-anodized amorphous nanostructures crystallize into a mixture of anatase and rutile when annealed at 550°C, without significant morphological changes in

the surface phases. The anodization of the biphasic (α'+β) Ti13Nb13Zr alloy form arrays of TiO_2 nanotubes with well-defined circular geometry in the α' phase, while nanopores of TiO_2 are formed in the β phase. After anodization, formed self-organized arrays of nanotubes were obtained with the following average dimensions in the range: diameter of 62-90 nm, a length of 1.5-1.9 mm and a thickness of 18-26 nm. The HPT processing caused the refinement and spatial redistribution of α' and β phases. The formation of the nanotubes was kept sole within the α' phase, however, with the difference that nanotubes are not so organized and are deformed in their longitudinal direction suggesting that their growth follow the spatial distortion of the α' phase. Such distortion also influences the length of the nanostructures, due to it is observed a greater length of nanotubes in the non-deformed state (uniform arrays) and a shorter length for more significant deformations (arrays with spatial distortion).

The distinct nanostructures obtained in the Ti13Nb13Zr alloy is a result of competition between electrochemical oxide formation and chemical dissolution of oxide by fluoride ions. The oxidation reaction at the interface of the Ti13Nb13Zr alloy surface and electrolyte at a constant applied potential is given by [196]:

$$M \leftrightarrow M^{n+} + ne^{-} (M = Ti, Nb\ and\ Zr)$$

Followed by:

$$xH_2O \leftrightarrow xO^{2-} + 2xH^{+}$$

Then,

$$2M^{n+} + nO^{2-} \leftrightarrow M_nO_n$$

In the presence of a fluorine anion, chemical dissolution occurs:

$$Ti^{4+} + 6F^{-} \leftrightarrow [TiF_6]^{2-}$$

$$Nb^{5+} + 7F^{-} \leftrightarrow [NbF_7]^{2-}$$

$$Zr^{4+} + 6F^{-} \leftrightarrow [ZrF_6]^{2-}$$

Consequently, β and α' phases will inevitably produce different nanostructures due to the high solubility of Ti-F or Ti-O-F compounds in aqueous media, unlike Nb-F and Zr-F species that are much less soluble. Thus, an ordered nanoporous oxide will be formed on the Ti-poorer β phase (less Ti fluorides), but nanotubular morphology will be found for the Ti-richer α' phase (more Ti fluorides).

On the other hand, the anodization of the monophasic alloy (β) Ti35Nb7Zr5Ta forms arrays of TiO_2 nanopores with a well-defined circular geometry. After anodization, formed self-organized arrays of nanotubes were obtained with the following average dimensions in the range: diameter of 66-75 nm, a length of 1.7-2.4 mm and a thickness of 22-32 nm. As a result, the nanoporous grown on the Ti35Nb7Zr5Ta alloy after severe plastic deformation by HPT had a smaller diameter and larger wall thickness. The formation of the nanoporous not so organized was observed in substrates deformed by HPT, suggesting that their growth follow the spatial distortion of the β phase. As it was observed for the Ti13Nb13Zr, the spatial distortion also affects the length of the nanostructures leading to a greater length of nanoporous in the non-deformed state (uniform arrays) and a shorter length for larger deformations (arrays with spatial distortion).

Chemical treatment by acid etching and NaOH activation were carried out in Ti13Nb13Zr and Ti35Nb7Zr5Ta alloys with different degrees of deformations. Two different etching procedures were performed: (i) samples were etched in HCl, (ii) samples were etched in H_3PO_4. Subsequently, all specimens were soaked in NaOH. The acid plus alkali treatment induced the formation of a nano topographic sponge-like morphology on all samples' surfaces. Such surfaces were full of cracks. However, it is noticeable that sponges' tentacles have quite different sizes, depending on the sample composition and mechanical processing condition. In other words, they decrease from Ti13Nb13Zr to Ti35Nb7Zr5Ta and after processing by HPT.

The quantity of Na^+ incorporated into the Ti13Nb13Zr surface after NaOH activation was comparable for the two different acid etching procedures and the

amounts to 2,81±0,62 at% for HCl treated and 1,24±0,11 at% for H_3PO_4 treated samples. The amount of Na^+ ions is related to the formation of sodium titanate ($Na_2Ti_5O_{11}$) on the surface of the substrates. Similarly, the results of Na^+ incorporated into the Ti35Nb7Zr5Ta surface after NaOH activation was comparable for the two different acid etching procedures and the amounts to 2,02±0,03 at% for HCl treated and 1,23±0,09 at% for H_3PO_4 treated samples. Therefore, the samples with acid etching with HCl of both alloys have a more considerable amount of Na^+ ions, and the alloy Ti13Nb13Zr is the one that has more Na^+ ions.

The evaluation of the corrosion resistance was carried out for both alloys Ti13Nb13Zrin the undeformed and Ti35Nb7Zr5Ta deformed conditions, on polished, anodized, and chemically treated surfaces.

Figure 87 summarizes open circuit potential measurements after soaking 1 hour in SBF for all samples presented in this work. The anodized samples of both alloys have a higher open circuit potential. That means that anodized samples have a more stable and protective oxide film on the surface. Apparently, there is a tendency to increase the OCP in the samples of both alloys with acid etching plus alkali treatment when severe plastic deformation is applied. The increase of the potential can indicate the stability of the passive film, suggesting that the severe plastic deformation accelerates the formation of this film.

Figure 88 shows the current passivation (i_{pass}) for the (α'+β) and (β) alloys. The conditions non-deformed and deformed by HPT were plotted and also the different surface modification treatments. The passivation currents for the samples with polished surface and the samples with chemical treatment (HCl, H_3PO_4 + NaOH) are of the same order of magnitude (10^{-6} A $\cdot cm^{-2}$). On the other hand, no significant differences were observed for passivation currents between non-deformed and deformed samples (except anodized samples), suggesting that cracks formed on the surface of chemically treated samples exposed the surfaces, which dominated the passivation phenomenon. Thus, the passive oxide film formed on the samples' surface is responsible for providing high resistance to corrosion.

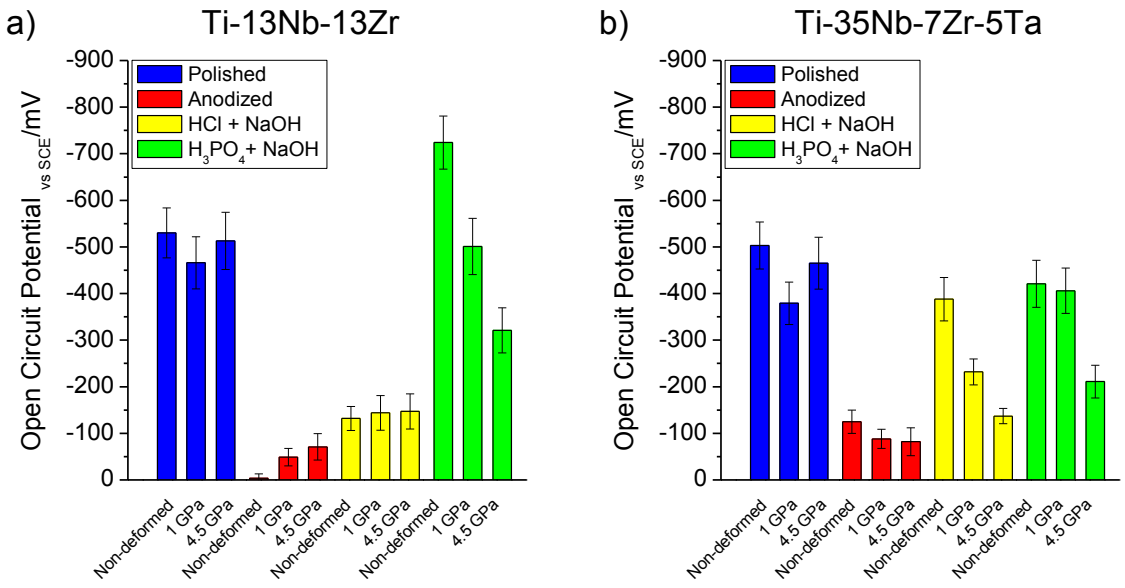

Figure 87: Open circuit potential measurements after 1-hour immersion in SBF at 37 ° C; (a) OCP measurements for samples of Ti13Nb13Zr alloy non-deformed and deformed by HPT with different surface modification treatment and (b) OCP measurements for samples of Ti35Nb7Zr5Ta alloy non-deformed and deformed by HPT with different surface modification treatment.

Regarding the anodized samples, two results are observed: (i) Treatment of modification of surface with lower value of the passivation current, Ti13Nb13Zr and Ti35Nb7Zr5Ta alloys exhibited average values: 10^{-8} and 10^{-7} A $\cdot cm^{-2}$, respectively and (ii) There is a tendency to increment the passivation current by increasing the pressure applied in the HPT process. Such a current increase may be related to the thickness of the nanostructured TiO_2 layer formed on the surfaces of (α'+β) and (β) alloys. Such thicknesses showed to be dependent on the degree of deformation, being smaller for samples with more considerable straining. In other words, the larger the film thickness, the better the resistance to corrosion.

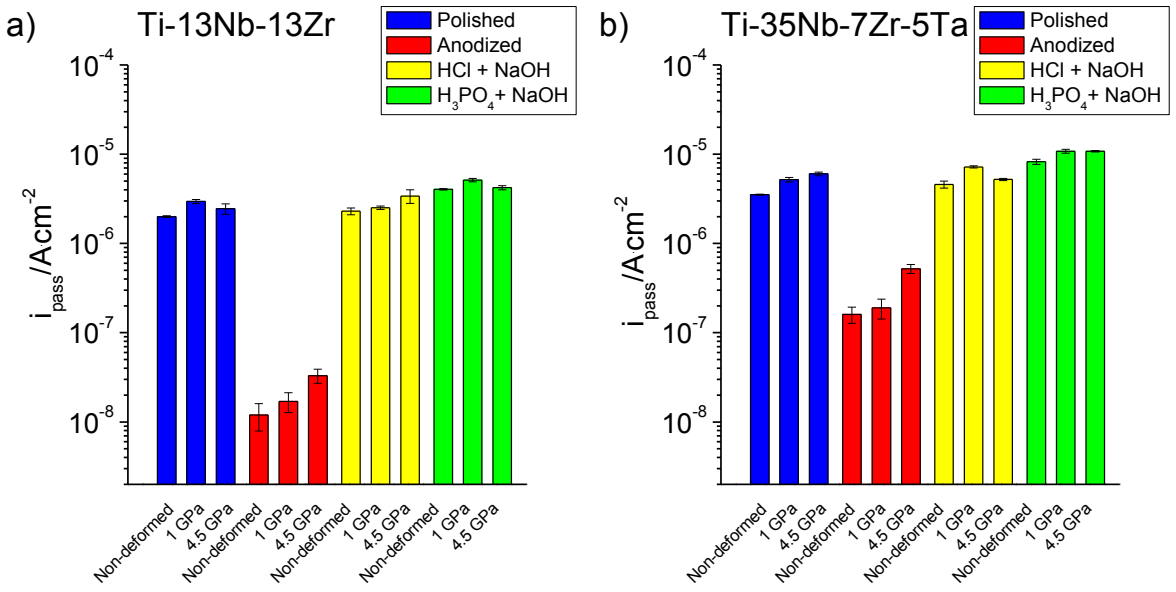

Figure 88: Passivation current (i_{pass}) measurements in SBF at 37 ° C; (a) i_{pass} measurements for samples of Ti13Nb13Zr alloy non-deformed and deformed by HPT with different surface modification treatment and (b) i_{pass} measurements for samples of Ti35Nb7Zr5Ta alloy non-deformed and deformed by HPT with different surface modification treatment.

To discuss the results of EIS in a comparative way for both alloys and conditions of interest of this work (deformation by HPT and surface modification treatments), it is relevant to study in more detail the average values (from a statistical analysis) of the impedance modules |Z| at low frequency for each type of sample. Thus, Figure 89 presents the values of |Z| measured at 20 mHz, associated with the specific surface area of each sample, and calculated according to the relationship:

$$|Z| = \sqrt{((Z' x\, S_s - R_e)^2 + (Z'' x S_s)^2)}$$

Where Z 'and Z' '(in Ω) are respectively the real and imaginary parts of the impedance at 20 mHz, S_S is the specific area exposed to the solution in cm².

The presence of TiO_2 nanostructures causes an increase of |Z| relative to the substrate, meaning better properties of the protective oxide layer. This increase is better observed in the Ti13Nb13Zr alloy, where the maximum values of |Z| were

present. There is a tendency to decrease the value of |Z| when increasing the deformation pressure. This reduced corrosion resistance may be attributed to the non-equilibrium nanostructures formed during the processing by HPT. On the other hand, chemical treatments tend to decrease more the value of |Z|. Such behavior may be attributed to crack formation on the surface and to the increase of the pressure during HPT processing, leading to non-equilibrium microstructures. The preceding mentioned causes the outer layer of the oxide film to be more susceptible to dissolution than the inner layer, indicating a more defective structure of the outer layer.

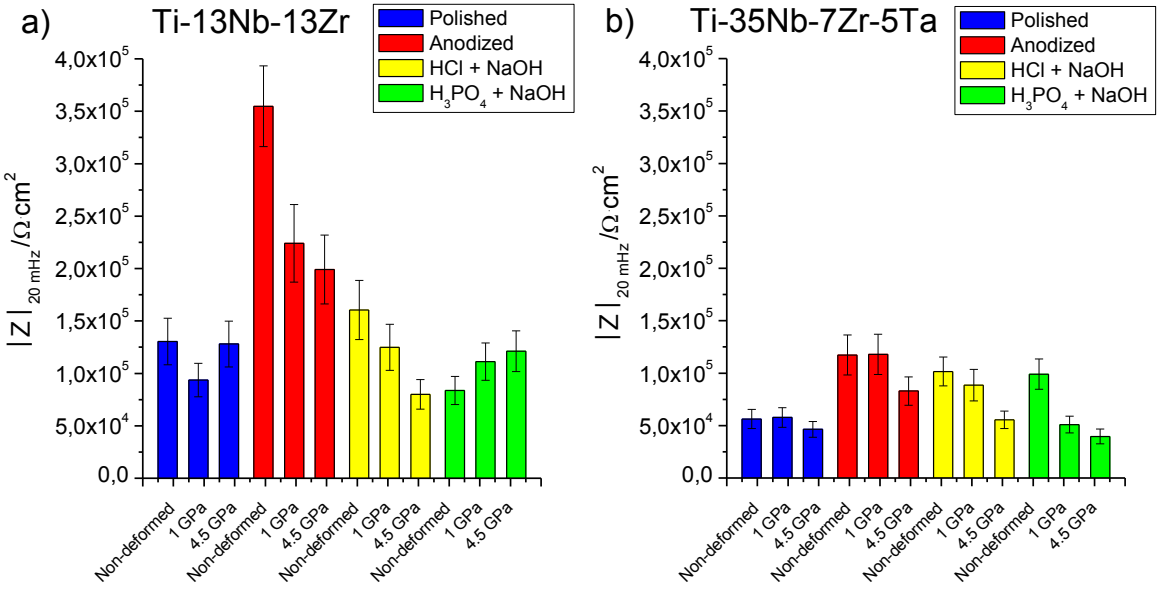

Figure 89: Impedance module |Z| at low frequency (20 mHz); (a) measurements for samples of Ti13Nb13Zr alloy non-deformed and deformed by HPT with different surface modification treatment and (b) measurements for samples of Ti35Nb7Zr5Ta alloy non-deformed and deformed by HPT with different surface modification treatment.

Implants should allow to osseointegration to supply bone-bonding ability. Such capability is ascribed to the development of a bone-like apatite layer on the implant surface, which must start after the implantation [197]. The osseointegration the material is usually tested in vitro using simulated body fluid (SBF) [197], thus verifying its efficacy of apatite production. Therefore, the bone-bonding ability of

samples with treated surfaces correlated to polished surfaces was evaluated by immersing them for 1, 7, and 14 days in SBF.

The formation of an apatite layer was assessed by SEM-EDS chemical microanalysis. For samples evidencing the apatite layer formation, the ratio Ca/P was calculated (Table 42), which were inside or, at least, near the theoretical relationship for hydroxyapatite of 1.67 ($Ca_5(PO_4)_3(OH)$ Ca/P = 5/3 = 1.67).

Table 42: Ca/P molar ratios obtained from the EDS results on the polished surfaces and surface treated of deformed and undeformed samples after different times in SBF.

			Surface modification treatments		
		Polished	Anodized	HCl + NaOH	H_3PO_4 + NaOH
Soaking time	**Condition**	**Ca/P Molar Ratio**	**Ca/P Molar Ratio**	**Ca/P Molar Ratio**	**Ca/P Molar Ratio**
1 Day	Ti13Nb13Zr; Non-deformed	-	-	-	-
	Ti13Nb13Zr; 1 GPa	-	-	-	-
	Ti13Nb13Zr; 4.5 GPa	-	1.81	-	-
	Ti35Nb7Zr5Ta; Non-deformed	-	-	-	-
	Ti35Nb7Zr5Ta; 1 GPa	-	-	-	-
	Ti35Nb7Zr5Ta; 4.5 GPa	-	-	-	-
7 Days	Ti13Nb13Zr; Non-deformed	-	1.62	1.80	1.65
	Ti13Nb13Zr; 1 GPa	-	1.72	1.76	1.52
	Ti13Nb13Zr; 4.5 GPa	-	1.76	1.73	1.56
	Ti35Nb7Zr5Ta; Non-deformed	-	-	-	-
	Ti35Nb7Zr5Ta; 1 GPa	-	-	-	-
	Ti35Nb7Zr5Ta; 4.5 GPa	-	-	-	-
14 Days	Ti13Nb13Zr; Non-deformed	-	1.95	1.68	1.60
	Ti13Nb13Zr; 1 GPa	-	1.90	1.82	1.55
	Ti13Nb13Zr; 4.5 GPa	-	1.86	1.64	1.57
	Ti35Nb7Zr5Ta; Non-deformed	-	1.75	1.75	-
	Ti35Nb7Zr5Ta; 1 GPa	-	-	-	-
	Ti35Nb7Zr5Ta; 4.5 GPa	-	1.84	1.79	-

SEM-EDS chemical microanalysis (Table 42) showed that the Ti13Nb13Zr and Ti35Nb7Zr5Ta alloys even after soaking for 14 days, in the polished condition did form apatite, i.e., they are not bioactive. This behavior confirms that the first

inert TiO_2 layer created on the surface of the polished substrates was not sufficient to promote bone formation.

The above behavior was also observed for samples of the Ti35Nb7Zr5Ta alloy treated with acid etching using H_3PO_4 and activated with NaOH, indicating that, even starting with phosphate on the surface, this material does not acquire bioactivity using such a surface treatment. Contrarily, regarding the same surface treatment, samples' surfaces of the Ti13Nb13Zr alloy showed bioactivity between one and seven days for deformed and undeformed conditions.

Anodized surfaces of samples of the undeformed Ti13Nb13Zr alloy started producing an apatite layer between seven and fourteen days, while deformed samples showed to be bioactive since the first 24 hours. However, the same surface treatment proved to be not as successful for specimens of the Ti35Nb7Zr5Ta alloy. In this case, samples (deformed or not) only started producing some apatite between the seventh and the fourteen days.

On the other hand, depending on the surface treatment performed, the apatite composition can vary. The relation between Ca and P (Ca / P) obtained from Table 44 is in the range of 1.52 to 1.95. As previously mentioned, hydroxyapatite has a Ca / P ratio of 1.67, due to this, other CaP phases were formed on the surfaces of the substrates. Table 43 [198] presents the potential phases that can be present and their respective formulas.

Table 43: Summary of CaP phases, their corresponding Ca/P molar ratios, abbreviations, and chemical formulas.

Compounds	Chemical formula	Abbreviation	Ca/P Molar Ratio
Hydroxyapatite	$Ca_{10}(PO_4)_6(OH)_2$	HAp	1.67
Amorphous phase	N/A	ACP	
Alpha tricalcium phosphate	α-$Ca_3(PO_4)_2$	α-TCP	1.5
Beta tricalcium phosphate	β-$Ca_3(PO_4)_2$	β-TCP	1.5
Tetracalcium phosphate	$Ca_4P_2O_9$	TTCP	2.0
Oxyhydroxyapatite	$Ca_{10}(PO_4)_6(OH)_{2-2x}(O)_x(h)_x$	OHA	1.67
Calcium-deficient hydroxyapatite	$Ca_{10-x}(HPO_4)_x(PO_4)_{6-x}(OH)_{2-x}$ $(0 < x < 1)$	CDHA or Ca-def HA	1.5–1.67

In general, two different ranges of Ca / P ratio are observed: (i) Samples with Ca / P higher than 1.67, (ii) Samples with Ca / P less than 1.67. Samples with a ratio of Ca / P higher than 1.67 are the following: (i) Ti13Nb13Zr and Ti35Nb7Zr5Ta alloys non-deformed and deformed by HPT with the anodized surface and (ii) Ti13Nb13Zr and Ti35Nb7Zr5Ta alloys non-deformed and deformed by HPT with the surface etched with HCl and activated with NaOH.

Samples with a ratio of Ca / P lower than 1.67 are the following:(i) Ti13Nb13Zr and Ti35Nb7Zr5Ta alloys non-deformed and deformed by HPT with the surface etched with H_3PO_4 and activated with NaOH. For instance, the Ca / P molar ratios 1.75-1.79 are commonly calculated for biomimetic CaP precipitated onto calcium deficient hydroxyapatite [189]. In this case, the Ca/P ratio is higher than 1.67, which indicates the formation of a calcium phosphate that is a B-type carbonate apatite. This type of apatite replaces the PO_4^{3-} for CO_3^{2-} and commonly occurs during biological mineralization processes [189].

The general formula for calcium deficient hydroxyapatite can be written as [199]:

$$Ca_{10-x}(HPO_4)_X(PO_4)_{6-X}(OH)_{2-X}$$

With 0 ≤ x ≤ 1. For stoichiometric HA (x = 0) the molar Ca/P ratio is 1.67. If HPO_4^{2-} is incorporated into the structure, the Ca/P ratio decreases to a minimum of 1.5 at x= 1. CO_3^{2-} can easily substitute HPO_4^{2-} due to the same charge [199]. This results in:

$Ca_8(CO_3)_2(PO_4)_4$; Ca/P ratio = 2.

Therefore, other phases, such as B-type carbonate apatite, will be present with hydroxyapatite.

Samples with an acid attack with H_3PO_4 and activation with NaOH have a Ca / P ratio of less than 1.67. As expected, these samples form calcium deficient hydroxyapatite with HPO_4^{2-} incorporated into its structure. This results in:

$Ca_9(HPO_4)(PO_4)_5(OH)$; Ca/P ratio = 1.5

Therefore, other phases, such as calcium-deficient hydroxyapatite, will be present with hydroxyapatite.

In addition to the previous qualitative analysis performed by SEM-EDS, apatite disposition was quantitatively estimated by weighing of samples before and after SBF soaking. Such an evaluation is summarized in Figure 90, which presents the means value of three weighings. Error bars display the standard deviation.

As it can be observed, the quantitative analysis of Figure 90 endorses the above qualitative one, regarding apatite deposition or not, on polished or treated surfaces, deformed or nondeformed, inside the periods afore-discussed.

It is noticeable that even having some bioactivity, the surfaces of anodized samples of deformed and mechanically processed Ti35Nb7Zr5Ta alloy produced

an undermost amount of apatite after 14 days. In a whole, for the Ti35Nb7Zr5Ta alloy, it can be inferred that, unfortunately, even with these two kinds of surface treatment, its bioactivity in the deformed and non-deformed conditions is unsatisfactory. One reason for such behavior is probably the contamination of the surfaces by other oxides. Surface layers of the alloys enriched with niobium, tantalum, and zirconium oxides could decrease surface potential under physiological conditions [200]. This surface potential decrease could be the reason why the treated alloys did not form apatite as a result of suppression of the sequence adsorption of phosphate and calcium ions.

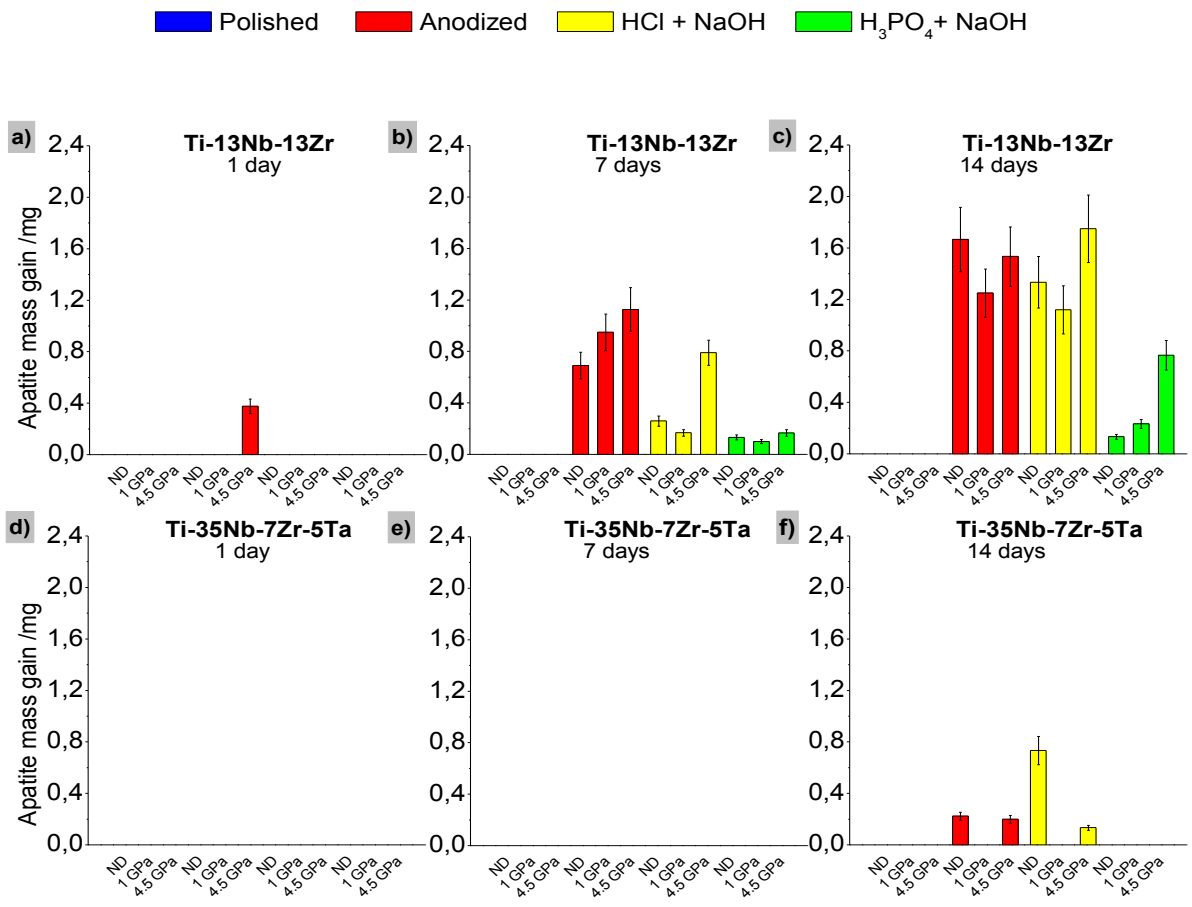

Figure 90: Graphs showing the apatite mass gain after soaking specimens in SBF as a function of the immersion time, comparing polished surfaces and surface treated of deformed and undeformed samples.

Concerning the behavior of the Ti13Nb13Zr alloy after anodization, as can be seen, there was no precipitation of apatite on the surface of undeformed Ti13Nb13Zr alloy during the first day of soaking, while, on deformed samples at 4.5 GPa, the apatite mass gain raised with the immersion time from the early 24 hours. This behavior leads one inferring that the smaller the grain size, the more significant the mass gain, which also proves the consequence of the kind of surface for bioactivity, and, in this case, the redistribution and refinement of α' and β phases on the sample surface caused by HPT.

In this study, it was shown that the TiO_2 nanostructures formed on samples deformed grew longitudinally following the texture induced by the HPT process. Thus, the refinement presented in samples deformed at 4.5 GPa probably caused the formation of TiO_2 nanostructures more distorted. This behavior could favor higher wettability of samples deformed when in contact with the SBF, and then speed up the formation of apatite.

Regarding the behavior of the chemically treated surfaces of the Ti13Nb13Zr alloy, one may observe that such a treatment is not as useful for activating the surface of undeformed samples, being the bioactivation much better for deformed ones. This behavior was already observed in the samples with anodized ultrafine granulation. Therefore, it can be inferred that for the biphasic sample of Ti13Nb13Zr, the grain refinement improves bioactivity due to a greater apatite mass gain.

On the other hand, the amount of Na^+ observed on the surface of the chemically modified samples affects the formation of apatite. These sodium ions come from the sodium titanate layer formed by the chemical treatment. As mentioned, chemical treatment of etching by HCl and activation with NaOH forms a higher quantity of Na^+ ions. This condition was the one that most formed apatite on samples' surface, indicating that the apatite formation on chemically treated titanium alloys seems to be similar to that bioactive glasses [128]. The exchange of Na^+ from glass by H^+ or H_3O^+ from the fluid leads to the formation of a Si-OH layer that was described to induce apatite nucleation via incorporation of Ca2+. The

consumption of H3O+ causes an increase in pH, and apatite will be precipitated [201].

Finally, to discuss the results of surface modification treatments in a similar way for both alloys, HPT deformation will not be considered in this analysis. Regarding electrochemical characterization, one may observe that the anodizing treatment clearly showed an improvement in electrochemical properties, which can be observed in Figures 87, 88 and 89, which correspond to the graphs of open circuit potential, passivation currents and modulus of impedance respectively. These samples showed the noblest open circuit potential, lowest passivation current and the highest impedance module at lower frequency (20 mHz). On the other hand, the values of passivation current and impedance modulus of samples chemically treated were similar to those of polished samples.

The surface modification treatments activated the surface of the sample to form apatite, which was not observed in samples in the polished condition. The surface modification treatments that formed apatite in both alloys were anodization and HCl etching followed by NaOH activation. The treatment with H_3PO_4 followed by NaOH activation formed lower amount of apatite in the Ti13Nb13Zr alloy and did not form apatite in the Ti35Nb7Zr5Ta alloy. These results were positive and showed high potential for the surface modification treatments in biomedical applications.

8 SUMMARY AND CONCLUSIONS:

Two commercial Ti alloys, Ti13Nb13Zr and Ti35Nb7Zr5Ta, were heat treated and rapidly quenched. Part of the samples was severely deformed by HPT, using 3 rpm and 3 turns, with loads of 1GPa and 4.5 GPa. The samples had their surface modified using different methods (anodization, chemical etching (HCl and H_3PO_4) and activation with NaOH). The specimens, in all conditions, were structurally, microstructurally, mechanically, and electrochemically characterized using several different methods as a function of the microstructural refinement, phases present and the kind of surface modification. Finally, bioactivity tests were also accomplished for all sample conditions. After analyzing and discussing the results, the following conclusions can be drawn:

Heat-treatment

- ✓ After heat treatment, the Ti13Nb13Zr alloy acquired a biphasic microstructure containing the α' and β phases. The Ti35Nb7Zr5Ta alloy also presented a biphasic microstructure composed mainly by the β phase and a small amount of α.

Processing by HPT

- ✓ HPT processing significantly reduced grain sizes, resulting in ultra-fine microstructures in both alloys. The initial grain sizes of the two alloys were about 250 μm, which were reduced to ~ to 89 μm, ~203 nm and ~112 nm for the Ti13Nb13Zr and Ti35Nb7Zr5Ta alloys, respectively.
- ✓ Another feature produced by HPT was the increase of the β phase in the Ti13Nb13Zr alloy and a decrease of α in the Ti35Nb7Zr5Ta, making it almost a single phase.
- ✓ Grain refinement led to increased hardness in both samples, changing from ~265 HV and ~183 HV to ~390 HV and ~320 HV, respectively.
- ✓ In the same sample sense as for hardness and outstanding (low) values of the elastic modulus were obtained, they were reduced a bit. However, considering

error bars, they stayed in the range of 60 GPa and 44 GPa before and after deformation, respectively for the Ti13Nb13Zr and Ti35Nb7Zr5Ta specimens.

Surface treatments

- ✓ The anodization of the Ti13Nb13Zr alloy indicates that there is the formation of two different nanostructures, where nanotubes for the α'-phase and nanopores for the β-phase are observed, irrespective to the spatial distribution of both phases or their refinement. In the case of the Ti35Nb7Zr5Ta alloy, only nanopores were observed.
- ✓ As-anodized surfaces were amorphous. After annealing at 550°C, they crystallize into a mixture of anatase and rutile, without significant morphological changes in the nanostructures produced on the surfaces.
- ✓ Surfaces of the samples were modified using acid etching followed by alkaline treatment, resulting in a sodium titanate sponge-like layer. Sponges' tentacles sizes depended on the grain size, surface chemistry, and structure. In general, tentacles were thicker for undeformed samples and much thinner for samples processed by HPT.

Corrosion Behavior

- ✓ The anodized samples of both alloys have a higher open circuit potential, meaning that they have a more stable and protective oxide film on the surface. Apparently, there is a tendency to increase the OCP in the samples of both alloys with acid etching plus alkali treatment when severe plastic deformation is applied leading to the conclusion that SPD can accelerate the formation of the passivation film.
- ✓ Anodized samples presented very small passivation currents (between one to two orders of magnitude lower than polished surfaces). Even being inside of the same order of magnitude, passivation currents tend to increase with the HPT pressure. Such a current increase may be related to the thickness of the nanostructured TiO_2, which was smaller for samples with higher loads.

- ✓ The passivation currents for the samples with polished surface and the samples with chemical treatment (HCl, H_3PO_4 + NaOH) are of the same order of magnitude (10^{-6} A cm^{-2}). Such behavior was associated to cracks formed on the surface that exposed it, suggesting that the only responsible for the passivation is the oxide film formed on the samples' surface and not the titanate layer formed after chemical treatment. Thus, natural TiO_2 is the only responsible for providing high resistance to corrosion.

EIS Analysis

- ✓ |Z| increases compared to the substrate when samples are anodized, which means better properties of the protective oxide layer.
- ✓ |Z| tends to decrease with the increase of the deformation pressure. Such behavior was attributed to the non-equilibrium nanostructures formed during the processing by HPT.
- ✓ |Z| is more decreased after any surface chemical treatment. Such a decrease is emphasized with the increase of the HPT pressure. Both behaviors were linked with crack formation on the surface and, as it was for TiO_2 nanostructures, also to non-equilibrium microstructures.

Bioactivity

- ✓ Samples with polished surfaces did not form apatite, i.e., they are not bioactive.
- ✓ In general, results of bioactivity tests indicated that TiO_2 nanostructures could activate the surfaces of both samples, but the bioactivity of the Ti13Nb13Zr alloy is much higher than for the Ti35Nb7Zr5Ta alloy, which did not present any bioactivity when chemical treatment was used. Contrarily, Ti13Nb13Zr alloy was active after both treatments, but much better for TiO_2 nanostructures and samples deformed by HPT.
- ✓ Reasons for apatite forming-ability behavior were given, which, finally, were related to different charges arising on the surfaces due to the presence of

other oxides in both kinds of surface treatment and tentacle sizes in the case of chemically treated surfaces.

9 REFERENCES

[1] A. Rosenfeld, M. Dvorachek, I. Rotstein, Bronze single crown-like prosthetic restorations of teeth from the Late Roman period, J. Archaeol. Sci. 27 (2000) 641–644. doi:10.1006/jasc.1999.0517.

[2] G. Manivasagam, D. Dhinasekaran, A. Rajamanickam, Biomedical implants: Corrosion and its Prevention-A Review, Recent Patents Corros. Sci. 2 (2010) 40–54. doi:10.2174/1877610801002010040.

[3] M. Ribeiro, F.J. Monteiro, M.P. Ferraz, Infection of orthopedic implants with emphasis on bacterial adhesion process and techniques used in studying bacterial-material interactions, Biomatter. 2 (2012) 176–194. doi:10.4161/biom.22905.

[4] C. Schank, Titanium Metal: Titanium Medical Metal of Choice – Supra Alloys, Http://Www.Supraalloys.Com/Medical-Titanium.Php. (n.d.). http://www.supraalloys.com/medical-titanium.php.

[5] F. Guillemot, Recent advances in the design of titanium alloys for orthopedic applications, Expert Rev. Med. Devices. 2 (2005) 741–748. doi:10.1586/17434440.2.6.741.

[6] C. Oldani, A. Dominguez, Titanium as a Biomaterial for Implants, in: Recent Adv. Arthroplast., InTech, 2012: pp. 149–162. doi:10.5772/27413.

[7] P.G. Coelho, J.E. Lemons, Physico/chemical characterization and in vivo evaluation of nanothickness bioceramic depositions on alumina-blasted/acid-etched Ti-6Al-4V implant surfaces, J. Biomed. Mater. Res. Part A An Off. J. Soc. Biomater. Japanese Soc. Biomater. Aust. Soc. Biomater. Korean Soc. Biomater. 90 (2009) 351–361. doi:10.1002/jbm.a.32097.

[8] S. Taksali, J.N. Grauer, A.R. Vaccaro, Material considerations for

intervertebral disc replacement implants, Spine J. 4 (2004) S231–S238. doi:10.1016/j.spinee.2004.07.012.

[9] A. Bansiddhi, D.C. Dunand, Titanium and NiTi foams for bone replacement, in: Bone Substit. Biomater., Elsevier, 2014: pp. 142–179. doi:10.1533/9780857099037.2.142.

[10] D.R. Crapper, S.S. Krishnan, S. Quittkat, Aluminium, neurofibrillary degeneration and Alzheimer's disease, Brain a J. Neurol. 99 (1976) 67–80. doi:10.1093/brain/99.1.67.

[11] M. Niinomi, D. Kuroda, K. Fukunaga, M. Morinaga, Y. Kato, T. Yashiro, A. Suzuki, Corrosion wear fracture of new β type biomedical titanium alloys, Mater. Sci. Eng. A. 263 (1999) 193–199. doi:10.1016/S0921-5093(98)01167-8.

[12] M. Niinomi, Mechanical properties of biomedical titanium alloys, Mater. Sci. Eng. A. 243 (1998) 231–236. doi:10.1016/S0921-5093(97)00806-X.

[13] A. Najdahmadi, A. Zarei-Hanzaki, E. Farghadani, Mechanical properties enhancement in Ti–29Nb–13Ta–4.6 Zr alloy via heat treatment with no detrimental effect on its biocompatibility, Mater. Des. 54 (2014) 786–791. doi:10.1016/j.matdes.2013.09.007.

[14] K.K. Wang, L.J. Gustavson, J.H. Dumbleton, Microstructure and properties of a new beta titanium alloy, Ti-12Mo-6Zr-2Fe, developed for surgical implants, in: Med. Appl. Titan. Its Alloy. Mater. Biol. Issues, ASTM International, 1996.

[15] P.L. Ferrandini, F.F. Cardoso, S.A. Souza, C.R. Afonso, R. Caram, Aging response of the Ti–35Nb–7Zr–5Ta and Ti–35Nb–7Ta alloys, J. Alloys Compd. 433 (2007) 207–210. doi:10.1016/j.jallcom.2006.06.094.

[16] H.J. Rack, J.I. Qazi, Titanium alloys for biomedical applications, 26 (2006) 1269–1277. doi:10.1016/j.msec.2005.08.032.

[17] S. Zherebtsov, G. Salishchev, R. Galeyev, K. Maekawa, Mechanical properties of Ti–6Al–4V titanium alloy with submicrocrystalline structure produced by severe plastic deformation, Mater. Trans. 46 (2005) 2020–2025. doi:10.2320/matertrans.46.2020.

[18] a. Azushima, R. Kopp, a. Korhonen, D.Y. Yang, F. Micari, G.D. Lahoti, P. Groche, J. Yanagimoto, N. Tsuji, a. Rosochowski, a. Yanagida, Severe plastic deformation (SPD) processes for metals, CIRP Ann. - Manuf. Technol. 57 (2008) 716–735. doi:10.1016/j.cirp.2008.09.005.

[19] Y.T. Zhu, T.G. Langdon, The fundamentals of nanostructured materials processed by severe plastic deformation, Jom. 56 (2004) 58–63. doi:10.1007/s11837-004-0294-0.

[20] D.A.G. Pérez, J. Junior, A. Moreira, C.S. Kiminami, C. Bolfarini, W.J. Botta, Ultrafine-Grained Ti-13Nb-13Zr Alloy Produced by Severe Plastic Deformation, Mater. Res. 20 (2017) 404–410. doi:10.1590/1980-5373-mr-2017-0037.

[21] K. Sharman, P. Bazarnik, T. Brynk, A. Gunay Bulutsuz, M. Lewandowska, Y. Huang, T.G. Langdon, Enhancement in mechanical properties of a β-titanium alloy by high-pressure torsion, J. Mater. Res. Technol. 4 (2015) 79–83. doi:10.1016/j.jmrt.2014.10.010.

[22] M. Kulkarni, A. Mazare, E. Gongadze, Š. Perutkova, V. Kralj-Iglič, I. Milošev, P. Schmuki, A. Iglič, M. Mozetič, Titanium nanostructures for biomedical applications, Nanotechnology. 26 (2015) 62002. doi:10.1088/0957-4484/26/6/062002.

[23] R.Z. Valiev, I.P. Semenova, V. V. Latysh, H. Rack, T.C. Lowe, J. Petruzelka, L. Dluhos, D. Hrusak, J. Sochova, Nanostructured titanium for biomedical applications, Adv. Eng. Mater. 10 (2008) 15–17. doi:10.1002/adem.200800026.

[24] H. Miyamoto, Corrosion of Ultrafine Grained Materials by Severe Plastic Deformation, an Overview, Mater. Trans. 57 (2016) 559–572. doi:10.2320/matertrans.M2015452.

[25] F. Hilario, Synthèse et caractérisations de nanotubes de TiO2 pour applications biomédicales: propriétés électrochimiques et bioactivité, (2017).

[26] J. Lu, Y. Zhang, W. Huo, W. Zhang, Y. Zhao, Y. Zhang, Electrochemical corrosion characteristics and biocompatibility of nanostructured titanium for implants, Appl. Surf. Sci. 434 (2018) 63–72. doi:10.1016/j.apsusc.2017.10.168.

[27] J.M. Hernández-López, A. Conde, J. de Damborenea, M.A. Arenas, Correlation of the nanostructure of the anodic layers fabricated on Ti13Nb13Zr with the electrochemical impedance response, Corros. Sci. 94 (2015) 61–69. doi:10.1016/j.corsci.2015.01.041.

[28] M. Takeuchi, Y. Abe, Y. Yoshida, Y. Nakayama, M. Okazaki, Y. Akagawa, Acid pretreatment of titanium implants, 24 (2003) 1821–1827. doi:10.1016/S0142-9612(02)00576-8.

[29] R.Z. Legeros, R.G. Craig, Strategies to affect bone remodeling: osteointegration, J. Bone Miner. Res. 8 (1993) S583–S596. doi:10.1002/jbmr.5650081328.

[30] T. Albrektsson, A. Wennerberg, Oral implant surfaces: Part 1--review focusing on topographic and chemical properties of different surfaces and in vivo responses to them, Int. J. Prosthodont. 17 (2004).

[31] T. Albrektsson, B. Albrektsson, Osseointegration of bone implants: A review of an alternative mode of fixation, Acta Orthop. Scand. 58 (1987) 567–577. doi:10.3109/17453678709146401.

[32] W.F. Oliveira, I.R.S. Arruda, G.M.M. Silva, G. Machado, L.C.B.B. Coelho, M.T.S. Correia, Functionalization of titanium dioxide nanotubes with

biomolecules for biomedical applications, Mater. Sci. Eng. C. 81 (2017) 597–606. doi:10.1016/j.msec.2017.08.017.

[33] J.E.G. Hulshoff, K. Van Dijk, J.E. De Ruijter, F.J.R. Rietveld, L.A. Ginsel, J.A. Jansen, Interfacial phenomena: An in vitro study of the effect of calcium phosphate (Ca-P) ceramic on bone formation, J. Biomed. Mater. Res. 40 (1998) 464–474. doi:10.1002/(SICI)1097-4636(19980605)40:3<464::AID-JBM18>3.0.CO;2-J.

[34] S. Nishiguchi, T. Nakamura, M. Kobayashi, H.-M. Kim, F. Miyaji, T. Kokubo, The effect of heat treatment on bone-bonding ability of alkali-treated titanium, Biomaterials. 20 (1999) 491–500. doi:10.1016/S0142-9612(98)90203-4.

[35] M.J. Filiaggi, N.A. Coombs, R.M. Pilliar, Characterization of the interface in the plasma-sprayed HA coating/Ti-6Al-4V implant system, J. Biomed. Mater. Res. 25 (1991) 1211–1229. doi:10.1002/jbm.820251004.

[36] K.S. Brammer, C.J. Frandsen, S. Jin, TiO2 nanotubes for bone regeneration, Trends Biotechnol. 30 (2012) 315–322. doi:10.1016/j.tibtech.2012.02.005.

[37] F.H. Froes, Titanium: Physical Metallurgy, Processing, and Applications, ASM International, 2015.

[38] S. Malinov, W. Sha, Application of artificial neural networks for modelling correlations in titanium alloys, Mater. Sci. Eng. A. 365 (2004) 202–211. doi:10.1016/j.msea.2003.09.029.

[39] G. Lütjering, J. Williams, Titanium, (2003). doi:10.1007/978-3-540-73036-1.

[40] W. Sha, S. Malinov, Titanium alloys: modelling of microstructure, properties and applications, (2009). doi:10.1017/S0001924000037829.

[41] E. Urba, A. Krz, A. Kazek-k, J. Michalska, A. Stolarczyk, G. Dercz, W. Simka, Electrochemical modi fi cation of Ti-13Nb-13Zr alloy surface in phosphate based solutions, 291 (2016) 79–88. doi:10.1016/j.surfcoat.2016.02.025.

[42] T.C. Niemeyer, C.R. Grandini, L.M.C. Pinto, A.C.D. Angelo, S.G. Schneider, Corrosion behavior of Ti-13Nb-13Zr alloy used as a biomaterial, 476 (2009) 172–175. doi:10.1016/j.jallcom.2008.09.026.

[43] D.A.G. Pérez, A.M.J. Junior, G.H. Asato, J.-C. Lepretre, V. Roche, C. Bolfarini, W.J. Botta, Surface anodization of the biphasic Ti13Nb13Zr biocompatible alloy: Influence of phases on the formation of TiO2 nanostructures, J. Alloys Compd. 796 (2019) 93–102. doi:10.1016/j.jallcom.2019.04.167.

[44] O. Florêncio, P.S.S. Jr, R. Ribeiro, J.M. Chaves, F.H. Sá, F.X. Melo, S.G. Schneider, Effect of different annealing on the anelastic relaxation in Ti – 13Nb – 13Zr alloy, 522 (2009) 351–353. doi:10.1016/j.msea.2008.09.136.

[45] A.K. Mishra, J.A. Davidson, R.A. Poggie, P. Kovacs, J. Ted, Mechanical and tribological properties and biocompatibility of diffusion hardenen Ti-13Nb-13Zr A new Titanium alloy for surgical implants, (1996) 96–113.

[46] M. Geetha, U. Kamachi Mudali, A.K. Gogia, R. Asokamani, B. Raj, Influence of microstructure and alloying elements on corrosion behavior of Ti-13Nb-13Zr alloy, Corros. Sci. 46 (2004) 877–892. doi:10.1016/S0010-938X(03)00186-0.

[47] M.A. Khan, R.L. Williams, D.F. Williams, The corrosion behaviour of Ti–6Al–4V, Ti–6Al–7Nb and Ti–13Nb–13Zr in protein solutions, Biomaterials. 20 (1999) 631–637. doi:10.1016/S0142-9612(98)00217-8.

[48] N.T.C. Oliveira, E.A. Ferreira, T. Duarte, S.R. Biaggio, R.C. Rocha-filho, N. Bocchi, Corrosion resistance of anodic oxides on the Ti – 50Zr and Ti – 13Nb – 13Zr alloys, 51 (2006) 2068–2075. doi:10.1016/j.electacta.2005.07.015.

[49] M.A. Khan, R.L. Williams, D.F. Williams, Conjoint corrosion and wear in titanium alloys, Biomaterials. 20 (1999) 765–772. doi:10.1016/S0142-9612(98)00229-4.

[50] K.S. Suresh, N.P. Gurao, S. Singh D., S. Suwas, K. Chattopadhyay, S. V. Zherebtsov, G.A. Salishchev, Effect of equal channel angular pressing on grain refinement and texture evolution in a biomedical alloy Ti13Nb13Zr, Mater. Charact. 82 (2013) 73–85. doi:10.1016/j.matchar.2013.05.003.

[51] A. Stróż, B. Łosiewicz, M. Zubko, B. Chmiela, K. Balin, G. Dercz, M. Gawlikowski, T. Goryczka, Production, structure and biocompatible properties of oxide nanotubes on Ti13Nb13Zr alloy for medical applications, Mater. Charact. 132 (2017) 363–372. doi:https://doi.org/10.1016/j.matchar.2017.09.004.

[52] D. Cáceres, C. Munuera, C. Ocal, J.A. Jiménez, A. Gutiérrez, M.F. López, Nanomechanical properties of surface-modified titanium alloys for biomedical applications, Acta Biomater. 4 (2008) 1545–1552. doi:10.1016/j.actbio.2008.04.009.

[53] M.A. Khan, R.L. Williams, D.F. Williams, The corrosion behaviour of Ti—6Al—4V, Ti—6Al—7Nb and Ti—13Nb—13Zr in protein solutions, 20 (1999) 631–637.

[54] M.A. Baker, S.L. Assis, O.Z. Higa, I. Costa, Nanocomposite hydroxyapatite formation on a Ti – 13Nb – 13Zr alloy exposed in a MEM cell culture medium and the effect of H 2 O 2 addition, Acta Biomater. 5 (2009) 63–75. doi:10.1016/j.actbio.2008.08.008.

[55] Y. Okazaki, E. Nishimura, H. Nakada, K. Kobayashi, Surface analysis of Ti-15Zr-4Nb-4Ta alloy after implantation in rat tibia, Biomaterials. 22 (2001) 599–607. doi:10.1016/S0142-9612(00)00221-0.

[56] S. Nag, Influence of beta instabilities on the early stages of nucleation and growth of alpha in beta titanium alloys, (2008).

[57] V.R. Jablokov, N.G.D. Murray, H.J. Rack, H.L. Freese, Influence of oxygen content on the mechanical properties of Titanium-35Niobium-7Zirconium-

5Tantalum beta titanium alloy, in: Titanium, Niobium, Zirconium, Tantalum Med. Surg. Appl., ASTM International, 2006.

[58] S. Ozan, J. Lin, Y. Li, R. Ipek, C. Wen, Development of Ti-Nb-Zr alloys with high elastic admissible strain for temporary orthopedic devices, Acta Biomater. 20 (2015) 176–187. doi:10.1016/j.actbio.2015.03.023.

[59] M. Long, H.J. Rack, Titanium alloys in total joint replacement—a materials science perspective, Biomaterials. 19 (1998) 1621–1639. doi:10.1016/S0142-9612(97)00146-4.

[60] M. Atapour, A.L. Pilchak, G.S. Frankel, J.C. Williams, Corrosion behavior of β titanium alloys for biomedical applications, Mater. Sci. Eng. C. 31 (2011) 885–891. doi:10.1016/j.msec.2011.02.005.

[61] Y.J. Bai, Y.B. Wang, Y. Cheng, F. Deng, Y.F. Zheng, S.C. Wei, Comparative study on the corrosion behavior of Ti–Nb and TMA alloys for dental application in various artificial solutions, Mater. Sci. Eng. C. 31 (2011) 702–711. doi:10.1016/j.msec.2010.12.010.

[62] S. Samuel, S. Nag, S. Nasrazadani, V. Ukirde, M. El Bouanani, A. Mohandas, K. Nguyen, R. Banerjee, Corrosion resistance and in vitro response of laser-deposited Ti-Nb-Zr-Ta alloys for orthopedic implant applications, J. Biomed. Mater. Res. Part A. 94 (2010) 1251–1256. doi:10.1002/jbm.a.32782.

[63] M. Niinomi, Mechanical biocompatibilities of titanium alloys for biomedical applications, J. Mech. Behav. Biomed. Mater. 1 (2008) 30–42. doi:10.1016/j.jmbbm.2007.07.001.

[64] I. Dimić, I. Cvijović-Alagić, B. Völker, A. Hohenwarter, R. Pippan, D. Veljović, M. Rakin, B. Bugarski, Microstructure and metallic ion release of pure titanium and Ti-13Nb-13Zr alloy processed by high pressure torsion, Mater. Des. 91 (2016) 340–347. doi:10.1016/j.matdes.2015.11.088.

[65] R.. Valiev, R.. Islamgaliev, I.. Alexandrov, Bulk nanostructured materials from severe plastic deformation, 2000. doi:10.1016/S0079-6425(99)00007-9.

[66] A.P. Zhilyaev, T.G. Langdon, Using high-pressure torsion for metal processing: Fundamentals and applications, Prog. Mater. Sci. 53 (2008) 893–979. doi:10.1016/j.pmatsci.2008.03.002.

[67] I. Sabirov, N.A. Enikeev, M.Y. Murashkin, R.Z. Valiev, Bulk Nanostructured Materials with Multifunctional Properties, First Ed., Springer Inter. Pub. (2015) 27–100. doi:10.1007/978-3-319-19599-5.

[68] A. Tiwari, A.N. Nordin, Advanced biomaterials and biodevices, John Wiley & Sons, 2014. doi:10.1002/9781118774052.

[69] L. Mishnaevsky, E. Levashov, R.Z. Valiev, J. Segurado, I. Sabirov, N. Enikeev, S. Prokoshkin, A. V Solov'yov, A. Korotitskiy, E. Gutmanas, Nanostructured titanium-based materials for medical implants: modeling and development, Mater. Sci. Eng. R Reports. 81 (2014) 1–19. doi:10.1016/j.mser.2014.04.002.

[70] X. Liu, P.K. Chu, C. Ding, Surface modification of titanium , titanium alloys , and related materials for biomedical applications, 47 (2005) 49–121. doi:10.1016/j.mser.2004.11.001.

[71] O.P. Ferreira, A.G. Souza Filho, J. Mendes Filho, O.L. Alves, Unveiling the structure and composition of titanium oxide nanotubes through ion exchange chemical reactions and thermal decomposition processes, J. Braz. Chem. Soc. 17 (2006) 393–402.

[72] P. Roy, S. Berger, P. Schmuki, TiO2nanotubes: Synthesis and applications, Angew. Chemie - Int. Ed. 50 (2011) 2904–2939. doi:10.1002/anie.201001374.

[73] N.S. Allen, M. Edge, G. Sandoval, J. Verran, J. Stratton, J. Maltby, Photocatalytic Coatings for Environmental Applications, Photochem.

Photobiol. 81 (2005) 279–290. doi:10.1562/2004-07-01-RA-221.

[74] Y. Cheng, H. Yang, Y. Yang, J. Huang, K. Wu, Z. Chen, X. Wang, C. Lin, Y. Lai, Progress in TiO 2 nanotube coatings for biomedical applications: a review, J. Mater. Chem. B. 6 (2018) 1862–1886. doi:10.1039/C8TB00149A.

[75] O. Ola, M.M. Maroto-Valer, Review of material design and reactor engineering on TiO2 photocatalysis for CO2 reduction, J. Photochem. Photobiol. C Photochem. Rev. 24 (2015) 16–42. doi:10.1016/j.jphotochemrev.2015.06.001.

[76] H. Tsuchiya, J.M. Macak, L. Müller, J. Kunze, F. Müller, P. Greil, S. Virtanen, P. Schmuki, Hydroxyapatite growth on anodic TiO2 nanotubes, J. Biomed. Mater. Res. Part A. 77A (2006) 534–541. doi:10.1002/jbm.a.30677.

[77] V.P. Parkhutik, V.I. Shershulsky, Theoretical modelling of porous oxide growth on aluminium, J. Phys. D. Appl. Phys. 25 (1992) 1258. doi:10.1088/0022-3727/25/8/017.

[78] G.K. Grimes, Craig A., Mor, TiO2 nanotube arrays: synthesis, properties, and applications, 2009. doi:10.1007/978-1-4419-0068-5.

[79] A. Jaroenworaluck, D. Regonini, C.R. Bowen, R. Stevens, D. Allsopp, Macro, micro and nanostructure of TiO 2 anodised films prepared in a fluorine-containing electrolyte, J. Mater. Sci. 42 (2007) 6729–6734. doi:10.1007/s10853-006-1474-9.

[80] S. Minagar, C.C. Berndt, J. Wang, E. Ivanova, C. Wen, A review of the application of anodization for the fabrication of nanotubes on metal implant surfaces, Acta Biomater. 8 (2012) 2875–2888. doi:10.1016/j.actbio.2012.04.005.

[81] B.J. Hwang, J.R. Hwang, Kinetic model of anodic oxidation of titanium in sulphuric acid, J. Appl. Electrochem. 23 (1993) 1056–1062. doi:10.1007/BF00266129.

[82] V. Etacheri, C. Di Valentin, J. Schneider, D. Bahnemann, S.C. Pillai, Visible-light activation of TiO2 photocatalysts: Advances in theory and experiments, J. Photochem. Photobiol. C Photochem. Rev. 25 (2015) 1–29. doi:10.1016/j.jphotochemrev.2015.08.003.

[83] K. Huo, B. Gao, J. Fu, L. Zhao, P.K. Chu, Fabrication, modification, and biomedical applications of anodized TiO2 nanotube arrays, Rsc Adv. 4 (2014) 17300–17324. doi:10.1039/c4ra01458h.

[84] J.M. Macak, H. Tsuchiya, A. Ghicov, K. Yasuda, R. Hahn, S. Bauer, P. Schmuki, TiO2 nanotubes: Self-organized electrochemical formation, properties and applications, Curr. Opin. Solid State Mater. Sci. 11 (2007) 3–18. doi:10.1016/j.cossms.2007.08.004.

[85] K. Indira, U.K. Mudali, T. Nishimura, N. Rajendran, A Review on TiO2 Nanotubes: Influence of Anodization Parameters, Formation Mechanism, Properties, Corrosion Behavior, and Biomedical Applications, J. Bio- Tribo-Corrosion. 1 (2015) 1–22. doi:10.1007/s40735-015-0024-x.

[86] L. Le Guéhennec, A. Soueidan, P. Layrolle, Y. Amouriq, Surface treatments of titanium dental implants for rapid osseointegration, Dent. Mater. 23 (2007) 844–854. doi:10.1016/j.dental.2006.06.02.

[87] S.A. Cho, K.T. Park, The removal torque of titanium screw inserted in rabbit tibia treated by dual acid etching, Biomaterials. 24 (2003) 3611–3617. doi:10.1016/S0142-9612(03)00218-7.

[88] J.Y. Park, J.E. Davies, Red blood cell and platelet interactions with titanium implant surfaces, Clin. Oral Implants Res. 11 (2000) 530–539. doi:10.1034/j.1600-0501.2000.011006530.x.

[89] H. Kim, F. Miyaji, T. Kokubo, T. Nakamura, Preparation of bioactive Ti and its alloys via simple chemical surface treatment, J. Biomed. Mater. Res. An Off. J. Soc. Biomater. Japanese Soc. Biomater. 32 (1996) 409–417.

doi:10.1002/(sici)1097-4636(199611)32:3<409::aid-jbm14>3.0.co;2-.

[90] T. Kokubo, H. Kim, M. Kawashita, Novel bioactive materials with different mechanical properties, 24 (2003) 2161–2175. doi:10.1016/S0142-9612(03)00044-9.

[91] S. Thomas, R. Thomas, A.K. Zachariah, R.K. Mishra, Spectroscopic Methods for Nanomaterials Characterization, Elsevier, 2017.

[92] C. Duret-Thual, Understanding corrosion: basic principles, Underst. Biocorrosion Fundam. Appl. (2014) 1. doi:10.1533/9781782421252.1.3.

[93] Y.S. Jiménez, M.T. Gil, M.T. Guerra, L. Baltes, J.M. Rosca, Interpretation of open circuit potential of two titanium alloys for a long time immersion in physiological fluid, Bull. Transilv. Univ. Braşov• Vol. 2 (2009) 51.

[94] J. Tafel, Über die Polarisation bei kathodischer Wasserstoffentwicklung, Zeitschrift Für Phys. Chemie. 50 (1905) 641–712. doi:10.1515/zpch-1905-5043.

[95] R.A. Buchanan, E.E. Stansbury, 4-Electrochemical Corrosion, (2012). doi:10.1016/B978-1-4377-3455-3.00004-3.

[96] R.M. Cardoso, R.M. Dornellas, A.P. Lima, R.H.O. Montes, E.M. Richter, R.A.A. Munoz, Batch-Injection Amperometric Determination of Pyrogallol in Biodiesel Using a Multi-Walled Carbon Nanotube Modified Electrode, J. Braz. Chem. Soc. 28 (2017) 1650–1656. doi:10.21577/0103-5053.20160316.

[97] A. Lasia, Electrochemical impedance spectroscopy and its applications, in: Springer, Springer, 2014: pp. 49–52. doi:10.1007/978-1-4614-8933-7.

[98] D. Loveday, P. Peterson, B. Rodgers, Evaluation of organic coatings with electrochemical impedance spectroscopy, JCT Coatings Tech. 8 (2004) 46–52.

[99] G. Instruments, Basics of electrochemical impedance spectroscopy, G. Instruments, Complex Impedance Corros. (2007) 1–30.

[100] M.E. Orazem, B. Tribollet, An integrated approach to electrochemical impedance spectroscopy, Electrochim. Acta. 53 (2008) 7360–7366.

[101] N. Perez, Electrochemistry and Corrosion Science, Elsevier, 2016. doi:10.1007/978-3-319-24847-9.

[102] J.R. Macdonald, Impedence Spectroscopy--Emphasizing Solid Materials and Systems, Wiley-Interscience, John Wiley Sons,. (1987) 1–346.

[103] B. Hirschorn, M.E. Orazem, B. Tribollet, V. Vivier, I. Frateur, M. Musiani, Determination of effective capacitance and film thickness from constant-phase-element parameters, Electrochim. Acta. 55 (2010) 6218–6227. doi:10.1016/j.electacta.2009.10.065.

[104] B. Torres, A. Seyeux, S. Zanna, B. Tribollet, P. Marcus, I. Frateur, Influence of BSA adsorption on the oxide layers developed on 70Cu-30Ni alloy in static artificial seawater, Matériaux Tech. 101 (2013) 106.

[105] M.E. Orazem, I. Frateur, B. Tribollet, V. Vivier, S. Marcelin, N. Pébère, A.L. Bunge, E.A. White, D.P. Riemer, M. Musiani, Dielectric properties of materials showing constant-phase-element (CPE) impedance response, J. Electrochem. Soc. 160 (2013) C215–C225.

[106] G. Sha, L. Yao, X. Liao, S.P. Ringer, Z.C. Duan, T.G. Langdon, Segregation of solute elements at grain boundaries in an ultrafine grained Al–Zn–Mg–Cu alloy, Ultramicroscopy. 111 (2011) 500–505. doi:10.1016/j.ultramic.2010.11.013.

[107] C. Xu, M. Furukawa, Z. Horita, T.G. Langdon, Influence of ECAP on precipitate distributions in a spray-cast aluminum alloy, Acta Mater. 53 (2005) 749–758. doi:10.1016/j.actamat.2004.10.026.

[108] Y. Miyajima, M. Mitsuhara, S. Hata, H. Nakashima, N. Tsuji, Quantification of internal dislocation density using scanning transmission electron microscopy in ultrafine grained pure aluminium fabricated by severe plastic deformation, Mater. Sci. Eng. A. 528 (2010) 776–779. doi:10.1016/j.msea.2010.09.058.

[109] I.J. Beyerlein, R.A. Lebensohn, C.N. Tome, Modeling texture and microstructural evolution in the equal channel angular extrusion process, Mater. Sci. Eng. A. 345 (2003) 122–138. doi:10.1016/S0921-5093(02)00457-4.

[110] S. Parithimarkalaignan, T. V Padmanabhan, Osseointegration: an update, J. Indian Prosthodont. Soc. 13 (2013) 2–6. doi:10.1007/s13191-013-0252-z.

[111] E.M. Rivera-Muñoz, R. Velázquez-Castillo, S. Alonso-Sierra, J.R. Alanís-Gómez, B. Millán-Malo, L. Bucio-Galindo, R. Huirache-Acuña, A. Manzano-Ramírez, R. Nava, M. Apátiga-Castro, HAp Nanofibers Grown with Crystalline Preferential Orientation and Its Influence in Mechanical Properties of Organic-Inorganic Composite Materials, in: Hydroxyapatite-Advances Compos. Nanomater. Biomed. Appl. Its Technol. Facet., InTech, 2018. doi:10.5772/intechopen.71850.

[112] J. Venkatesan, S.-K. Kim, Chitosan composites for bone tissue engineering—an overview, Mar. Drugs. 8 (2010) 2252–2266. doi:10.3390/md8082252.

[113] C. Zhao, X. Zhang, P. Cao, Mechanical and electrochemical characterization of Ti–12Mo–5Zr alloy for biomedical application, J. Alloys Compd. 509 (2011) 8235–8238. doi:10.1016/j.jallcom.2011.05.090.

[114] G. Lütjering, Influence of processing on microstructure and mechanical properties of (α+ β) titanium alloys, Mater. Sci. Eng. A. 243 (1998) 32–45. doi:10.1016/S0921-5093(97)00778-8.

[115] P. Majumdar, S.B. Singh, M. Chakraborty, The role of heat treatment on

microstructure and mechanical properties of Ti-13Zr-13Nb alloy for biomedical load bearing applications., J. Mech. Behav. Biomed. Mater. 4 (2011) 1132–44. doi:10.1016/j.jmbbm.2011.03.023.

[116] J. Davidson, A. Mishra, New surface-hardened, low-modulus, corrosion-resistant Ti-13Nb-13Zr alloy for total hip arthroplasty, Bio-Medical Mater. 4 (1994) 231–243. doi:10.3233/BME-1994-4310.

[117] J. Qazi, V. Tsakiris, B. Marquardt, H. Rack, Effect of aging treatments on the tensile properties of Ti-35Nb-7Zr-5Ta-(0.06-0.7)O alloys, 2004. doi:10.1520/JAI12780.

[118] F. Hilario, V. Roche, R.P. Nogueira, A.M.J. Junior, Influence of morphology and crystalline structure of TiO2 nanotubes on their electrochemical properties and apatite-forming ability, Electrochim. Acta. 245 (2017) 337–349. doi:10.1016/j.electacta.2017.05.160.

[119] A. Sadkowski, J. Diard, On the Fletcher ' s two-terminal equivalent network of a three-terminal electrochemical cell, Electrochim. Acta. 55 (2010) 1907–1911. doi:10.1016/j.electacta.2009.11.008.

[120] T. Kokubo, H. Takadama, How useful is SBF in predicting in vivo bone bioactivity?, Biomaterials. 27 (2006) 2907–2915. doi:10.1016/j.biomaterials.2006.01.017.

[121] R. Kamalian, A. Yazdanpanah, F. Moztarzadeh, R. Ravarian, Z. Moztarzadeh, M. Tahmasbi, M. Mozafari, Synthesis and characterization of bioactive glass/forsterite nanocomposites for bone implants, Ceramics-Silikáty. 56 (2012) 331–340.

[122] E. ASTM, Standard test method for dynamic young's modulus, shear modulus, and poisson's ratio by impulse excitation of vibration, Annu. B. ASTM Stand. 3 (2005).

[123] L.B. Otani, A.H.A. Pereira, J.D.D. Melo, S.C. Amico, Elastic Moduli

characterization of composites using the Impulse Excitation, ATCP Phys. Eng. (2014).

[124] K.N. Fish, M.W. Davidson, Fluorescent Biomarkers in Neurons, in: L.R.B.T.-E. of N. Squire (Ed.), Academic Press, Oxford, 2009: pp. 261–271. doi:https://doi.org/10.1016/B978-008045046-9.02003-9.

[125] H.A. Franco, C.R.M. Silva, J.L.A. Ferreira, J.A. Araújo, Fatigue Strength of Ti-35Nb-7Zr-5Ta, in: Mater. Sci. Forum, Trans Tech Publ, 2012: pp. 73–79. doi:10.4028/www.scientific.net/MSF.727-728.73.

[126] Y. Ji, K.-C. Lin, H. Zheng, J. Zhu, A.C.S. Samia, Fabrication of double-walled TiO2 nanotubes with bamboo morphology via one-step alternating voltage anodization, Electrochem. Commun. 13 (2011) 1013–1015. doi:10.1016/j.elecom.2011.06.030.

[127] A. Ibrahim, W. Mekprasart, W. Pecharapa, Anatase/Rutile TiO2 composite prepared via sonochemical process and their photocatalytic activity, Mater. Today Proc. 4 (2017) 6159–6165. doi:10.1016/j.matpr.2017.06.110.

[128] L. Jonášová, F.A. Müller, A. Helebrant, J. Strnad, P. Greil, Biomimetic apatite formation on chemically treated titanium, Biomaterials. 25 (2004) 1187–1194. doi:10.1016/j.biomaterials.2003.08.009.

[129] J.-H. Yi, C. Bernard, F. Variola, S.F. Zalzal, J.D. Wuest, F. Rosei, A. Nanci, Characterization of a bioactive nanotextured surface created by controlled chemical oxidation of titanium, Surf. Sci. 600 (2006) 4613–4621. doi:10.1016/j.susc.2006.07.053.

[130] F.A. Müller, M.C. Bottino, L. Müller, V.A.R. Henriques, U. Lohbauer, A.H.A. Bressiani, J.C. Bressiani, In vitro apatite formation on chemically treated (P/M) Ti–13Nb–13Zr, Dent. Mater. 24 (2008) 50–56. doi:10.1016/j.dental.2007.02.005.

[131] M.E. Orazem, N. Pébère, B. Tribollet, Enhanced graphical representation of

electrochemical impedance data, J. Electrochem. Soc. 153 (2006) B129–B136. doi:10.1149/1.2168377.

[132] G. Huang, B. Svendsen, Z. Lu, Effect of surface energy on dislocation-induced field in half-space with application to thin film-substrate systems, Acta Mech. Solida Sin. 22 (2009) 436–442. doi:10.1016/S0894-9166(09)60294-9.

[133] E. Rafiee, M. Farzam, M.A. Golozar, A. Ashrafi, An investigation on dislocation density in cold-rolled copper using electrochemical impedance spectroscopy, ISRN Corros. 2013 (2013). doi:10.1155/2013/921825.

[134] R.J. Twiss, Theory and applicability of a recrystallized grain size paleopiezometer, in: Stress Earth, Springer, 1977: pp. 227–244.

[135] S.H. Zahiri, D. Fraser, M. Jahedi, Recrystallization of cold spray-fabricated CP titanium structures, J. Therm. Spray Technol. 18 (2009) 16–22. doi:10.1007/s11666-008-9212-2.

[136] S.L. de Assis, I. Costa, The effect of polarisation on the electrochemical behavior of Ti-13Nb-13Zr alloy, Mater. Res. 10 (2007) 293–296. doi:10.1590/S1516-14392007000300014.

[137] V. Augustyn, P. Simon, B. Dunn, Pseudocapacitive oxide materials for high-rate electrochemical energy storage, Energy Environ. Sci. 7 (2014) 1597–1614. doi:10.1039/C3EE44164D.

[138] A.K. Bhargava, M.K. Banerjee, 2.14 Heat-Treating Copper and Nickel Alloys, (2017). doi:10.1016/B978-0-12-803581-8.09196-7.

[139] Y. Sasikumar, R. Nallaiyan, Effect of Acid Treatment on the Surface Modification of Ti-6Al-7Nb and Ti-5Al-2Nb-1Ta and Its Electrochemical Investigations in Simulated Body Fluid, 2017. doi:10.1007/s40735-017-0096-x.

[140] M. Bettayeb, V. Maurice, L.H. Klein, L. Lapeire, K. Verbeken, P. Marcus, Nanoscale Intergranular Corrosion and Relation with Grain Boundary Character as Studied In Situ on Copper, J. Electrochem. Soc. 165 (2018) C835–C841. doi:10.1149/2.1341811jes.

[141] F.E.-T. Heakal, A.S. Mogoda, A.A. Mazhar, M.S. El-Basiouny, Kinetic studies on the dissolution of the anodic oxide film on titanium in phosphoric acid solutions, Corros. Sci. 27 (1987) 453–462. doi:10.1016/0010-938x(87)90089-8.

[142] I.C. Lavos-Valereto, S. Wolynec, I. Ramires, A.C. Guastaldi, I. Costa, Electrochemical impedance spectroscopy characterization of passive film formed on implant Ti–6Al–7Nb alloy in Hank's solution, J. Mater. Sci. Mater. Med. 15 (2004) 55–59.

[143] I. Milošev, T. Kosec, H.-H. Strehblow, XPS and EIS study of the passive film formed on orthopaedic Ti–6Al–7Nb alloy in Hank's physiological solution, Electrochim. Acta. 53 (2008) 3547–3558. doi:10.1016/j.electacta.2007.12.041.

[144] I. Milošev, M. Metikoš-Huković, H.-H. Strehblow, Passive film on orthopaedic TiAlV alloy formed in physiological solution investigated by X-ray photoelectron spectroscopy, Biomaterials. 21 (2000) 2103–2113. doi:10.1016/S0142-9612(00)00145-9.

[145] M. Aziz-Kerrzo, K.G. Conroy, A.M. Fenelon, S.T. Farrell, C.B. Breslin, Electrochemical studies on the stability and corrosion resistance of titanium-based implant materials, Biomaterials. 22 (2001) 1531–1539. doi:10.1016/S0142-9612(00)00309-4.

[146] S.L. de Assis, S. Wolynec, I. Costa, Corrosion characterization of titanium alloys by electrochemical techniques, Electrochim. Acta. 51 (2006) 1815–1819. doi:10.1016/j.electacta.2005.02.121.

[147] M. De Vittorio, L. Martiradonna, J. Assad, Nanotechnology and neuroscience: nano-electronic, photonic and mechanical neuronal interfacing, Springer, 2014.

[148] F. Hilario, V. Roche, A. Jorge Junior, R. Nogueira, Application of the transmission line model for porous electrodes to analyse the impedance response of TiO 2 nanotubes in physiological environment, 2017. doi:10.1016/j.electacta.2017.09.045.

[149] S.A.A. Yahia, L. Hamadou, A. Kadri, N. Benbrahim, E.M.M. Sutter, Effect of anodizing potential on the formation and EIS characteristics of TiO2 nanotube arrays, J. Electrochem. Soc. 159 (2012) K83–K92. doi:10.1149/2.077204jes.

[150] L. Hamadou, L. Aïnouche, A. Kadri, S.A.A. Yahia, N. Benbrahim, Electrochemical impedance spectroscopy study of thermally grown oxides exhibiting constant phase element behaviour, Electrochim. Acta. 113 (2013) 99–108.

[151] P. Pu, H. Cachet, E.M.M. Sutter, Electrochemical impedance spectroscopy to study photo-induced effects on self-organized TiO2 nanotube arrays, Electrochim. Acta. 55 (2010) 5938–5946. doi:10.1016/j.electacta.2010.05.048.

[152] A.G. Munoz, Semiconducting properties of self-organized TiO2 nanotubes, Electrochim. Acta. 52 (2007) 4167–4176. doi:10.1016/j.electacta.2006.11.035.

[153] W. Yu, Development of nanostructured materials based on manganese oxides and produced by an electrochemical method for water electrolysis, (2016).

[154] M. Stępień, P. Handzlik, K. Fitzner, Electrochemical synthesis of oxide nanotubes on Ti6Al7Nb alloy and their interaction with the simulated body

fluid, J. Solid State Electrochem. 20 (2016) 2651–2661. doi:10.1007/s10008-016-3258-8.

[155] A. Mazare, M. Dilea, D. Ionita, I. Demetrescu, Electrochemical behavior in simulated body fluid of TiO2 nanotubes on TiAlNb alloy elaborated in various anodizing electrolyte, Surf. Interface Anal. 46 (2014) 186–192. doi:10.1002/sia.5364.

[156] C. Liu, Y. Wang, M. Wang, W. Huang, P.K. Chu, Electrochemical stability of TiO2 nanotubes with different diameters in artificial saliva, Surf. Coatings Technol. 206 (2011) 63–67. doi:10.1016/j.surfcoat.2011.06.038.

[157] W. Yu, J. Qiu, F. Zhang, In vitro corrosion study of different TiO2 nanotube layers on titanium in solution with serum proteins, Colloids Surfaces B Biointerfaces. 84 (2011) 400–405. doi:10.1016/j.colsurfb.2011.01.033.

[158] S. Ahmadi, I. Mohammadi, S.K. Sadrnezhaad, Hydroxyapatite based and anodic titania nanotube biocomposite coatings: fabrication, characterization and electrochemical behavior, Surf. Coatings Technol. 287 (2016) 67–75. doi:10.1016/j.surfcoat.2015.12.062.

[159] L. Aïnouche, L. Hamadou, A. Kadri, N. Benbrahim, D. Bradai, Interfacial barrier layer properties of three generations of TiO2 nanotube arrays, Electrochim. Acta. 133 (2014) 597–609. doi:10.1016/j.electacta.2014.04.086.

[160] J.M. Hernández-López, A. Conde, J.J. de Damborenea, M.A. Arenas, Electrochemical response of TiO2 anodic layers fabricated on Ti6Al4V alloy with nanoporous, dual and nanotubular morphology, Corros. Sci. 112 (2016) 194–203. doi:10.1016/j.corsci.2016.07.021.

[161] B. Munirathinam, L. Neelakantan, Titania nanotubes from weak organic acid electrolyte: Fabrication, characterization and oxide film properties, Mater. Sci. Eng. C. 49 (2015) 567–578. doi:10.1016/j.msec.2015.01.045.

[162] B. Munirathinam, L. Neelakantan, Role of crystallinity on the nanomechanical

and electrochemical properties of TiO2 nanotubes, J. Electroanal. Chem. 770 (2016) 73–83. doi:10.1016/j.jelechem.2016.03.032.

[163] B. Munirathinam, H. Pydimukkala, N. Ramaswamy, L. Neelakantan, Influence of crystallite size and surface morphology on electrochemical properties of annealed TiO2 nanotubes, Appl. Surf. Sci. 355 (2015) 1245–1253. doi:10.1016/j.apsusc.2015.08.017.

[164] L. Mohan, C. Anandan, R. Nallaiyan, Electrochemical behavior and effect of heat treatment on morphology, crystalline structure of self-organized TiO2 nanotube arrays on Ti–6Al–7Nb for biomedical applications, Mater. Sci. Eng. C. 50 (2015) 394–401. doi:10.1016/j.msec.2015.02.013.

[165] P. Córdoba-Torres, N.T.C. Oliveira, C. Bolfarini, V. Roche, R.P. Nogueira, Electrochemical impedance analysis of TiO2 nanotube porous layers based on an alternative representation of impedance data, J. Electroanal. Chem. 737 (2015) 54–64. doi:10.1016/j.jelechem.2014.06.034.

[166] R. De Levie, On porous electrodes in electrolyte solutions: I. Capacitance effects, Electrochim. Acta. 8 (1963) 751–780. doi:10.1016/0013-4686(63)80042-0.

[167] R. De Levie, On porous electrodes in electrolyte solutions—IV, Electrochim. Acta. 9 (1964) 1231–1245.

[168] R. De Levie, The influence of surface roughness of solid electrodes on electrochemical measurements, Electrochim. Acta. 10 (1965) 113–130. doi:10.1016/0013-4686(65)87012-8.

[169] J. Bisquert, G.G. Belmonte, F.F. Santiago, N.S. Ferriols, M. Yamashita, E.C. Pereira, Application of a distributed impedance model in the analysis of conducting polymer films, Electrochem. Commun. 2 (2000) 601–605. doi:10.1016/S1388-2481(00)00089-8.

[170] F. Fabregat-Santiago, E.M. Barea, J. Bisquert, G.K. Mor, K. Shankar, C.A.

Grimes, High Carrier Density and Capacitance in TiO2 Nanotube Arrays Induced by Electrochemical Doping, J. Am. Chem. Soc. 130 (2008) 11312–11316. doi:10.1021/ja710899q.

[171] H. Han, P. Sudhagar, T. Song, Y. Jeon, I. Mora-Seró, F. Fabregat-Santiago, J. Bisquert, Y.S. Kang, U. Paik, Three dimensional-TiO2 nanotube array photoanode architectures assembled on a thin hollow nanofibrous backbone and their performance in quantum dot-sensitized solar cells, Chem. Commun. 49 (2013) 2810–2812. doi:10.1039/C3CC40439K.

[172] A. Lasia, Modeling of impedance of porous electrodes, in: Model. Numer. Simulations, Springer, 2008: pp. 67–137. doi:10.1007/978-0-387-49582-8_3.

[173] O.E. Barcia, E. D'Elia, I. Frateur, O.R. Mattos, N. Pébère, B. Tribollet, Application of the impedance model of de Levie for the characterization of porous electrodes, Electrochim. Acta. 47 (2002) 2109–2116. doi:10.1016/S0013-4686(02)00081-6.

[174] J. Bisquert, Influence of the boundaries in the impedance of porous film electrodes, Phys. Chem. Chem. Phys. 2 (2000) 4185–4192. doi:10.1039/B001708F.

[175] J. Bisquert, A. Compte, Theory of the electrochemical impedance of anomalous diffusion, J. Electroanal. Chem. 499 (2001) 112–120. doi:10.1016/S0022-0728(00)00497-6.

[176] J. Garche, C.K. Dyer, P.T. Moseley, Z. Ogumi, D.A.J. Rand, B. Scrosati, Encyclopedia of electrochemical power sources, Newnes, 2013.

[177] J. Landesfeind, J. Hattendorff, A. Ehrl, W.A. Wall, H.A. Gasteiger, Tortuosity determination of battery electrodes and separators by impedance spectroscopy, J. Electrochem. Soc. 163 (2016) A1373–A1387. doi:10.1149/2.1141607jes.

[178] J. Song, M.Z. Bazant, Effects of nanoparticle geometry and size distribution

on diffusion impedance of battery electrodes, J. Electrochem. Soc. 160 (2013) A15–A24. doi:10.1149/2.023301jes.

[179] O.L. Riabokin, O. V Bojchuk, K.D. Pershina, Estimation of the primary batteries state of charge and state of art by frequency characteristics of electrochemical impedance spectra, Перспективні Матеріали Та Процеси в Прикладній Електрохімії-2018. (2018).

[180] S.J. Cooper, A. Bertei, D.P. Finegan, N.P. Brandon, Simulated impedance of diffusion in porous media, Electrochim. Acta. 251 (2017) 681–689. doi:10.1016/j.electacta.2017.07.152.

[181] S. Ban, Y. Iwaya, H. Kono, H. Sato, Surface modification of titanium by etching in concentrated sulfuric acid, Dent. Mater. 22 (2006) 1115–1120. doi:10.1016/j.dental.2005.09.007.

[182] L. Jonášová, F.A. Müller, A. Helebrant, J. Strnad, P. Greil, Hydroxyapatite formation on alkali-treated titanium with different content of Na+ in the surface layer, Biomaterials. 23 (2002) 3095–3101.

[183] H.-M. Kim, F. Miyaji, T. Kokubo, T. Nakamura, Apatite-forming ability of alkali-treated Ti metal in body environment, J. Ceram. Soc. Japan. 105 (1997) 111–116.

[184] S. Tanaka, M. Aonuma, N. Hirose, T. Tanaki, The preparation of porous TiO2 by immersing Ti in NaOH solution, J. Electrochem. Soc. 149 (2002) D167–D171. doi:10.1149/1.1512672.

[185] M.E. Orazem, B. Tribollet, Electrochemical impedance spectroscopy, John Wiley & Sons, 2017.

[186] A. Tiwari, L. Hihara, J. Rawlins, Intelligent coatings for corrosion control, Butterworth-Heinemann, 2014.

[187] S. Tamilselvi, V. Raman, N. Rajendran, Corrosion behaviour of Ti–6Al–7Nb

and Ti–6Al–4V ELI alloys in the simulated body fluid solution by electrochemical impedance spectroscopy, Electrochim. Acta. 52 (2006) 839–846.

[188] H. Nishikawa, T. Hasegawa, A. Miyake, Y. Tashiro, Y. Hashimoto, D.H.A. Blank, G. Rijnders, Relationship between the Ca/P ratio of hydroxyapatite thin films and the spatial energy distribution of the ablation laser in pulsed laser deposition, Mater. Lett. 165 (2016) 95–98. doi:10.1016/j.matlet.2015.11.115.

[189] M. Vallet-Regí, D.A. Navarrete, Nanoceramics in clinical use: from materials to applications, Royal Society of Chemistry, 2015.

[190] E. Wintermantel, S.-W. Ha, Medizintechnik: Life Science Engineering, Springer Science & Business Media, 2009. doi:10.1007/978-3-540-93936-8.

[191] W.Y. Guo, J. Sun, J.S. Wu, Effect of deformation on corrosion behavior of Ti–23Nb–0.7 Ta–2Zr–O alloy, Mater. Charact. 60 (2009) 173–177. doi:10.1016/j.matchar.2008.08.006.

[192] Y. Wang, J. C. Ho, Y. Cao, X. Liao, H. Q. Li, Y. H. Zhao, E. Lavernia, S. Ringer, Y. Zhu, Dislocation density evolution during high pressure torsion of a nanocrystalline NiFe alloy, 2009. doi:10.1063/1.3095852.

[193] M. Borodachenkova, W. Wen, A.M. de Bastos Pereira, High-Pressure Torsion: Experiments and Modeling, in: Sev. Plast. Deform. Tech., IntechOpen, 2017. doi:10.5772/intechopen.69173.

[194] Y.C. Wang, T.G. Langdon, Effect of heat treatment on microstructure and microhardness evolution in a Ti–6Al–4V alloy processed by high-pressure torsion, J. Mater. Sci. 48 (2012) 4646–4652. doi:10.1007/s10853-012-7071-1.

[195] S. Zherebtsov, I.P. Semenova, H. Garbacz, M. Motyka, Chapter 6 - Advanced mechanical properties, in: H. Garbacz, I.P. Semenova, S.

Zherebtsov, M.B.T.-N.T. Motyka (Eds.), Micro Nano Technol., Elsevier, 2019: pp. 103–121. doi:10.1016/B978-0-12-814599-9.00006-7.

[196] S. Minagar, Surface nanoengineering of titanium alloys for biomedical applications, (2015).

[197] X. Liu, P.K. Chu, C. Ding, Surface modification of titanium, titanium alloys, and related materials for biomedical applications, Mater. Sci. Eng. R Reports. 47 (2004) 49–121. doi:10.1016/j.mser.2004.11.001.

[198] M. Mucalo, Hydroxyapatite (HAp) for biomedical applications, Elsevier, 2015.

[199] A. Tampieri, S. Sprio, Bio-Inspired Regenerative Medicine: Materials, Processes, and Clinical Applications, CRC Press, 2016.

[200] S. Yamaguchi, H. Hashimoto, R. Nakai, H. Takadama, Impact of Surface Potential on Apatite Formation in Ti Alloys Subjected to Acid and Heat Treatments, Materials (Basel). 10 (2017) 1127. doi:10.3390/ma10101127.

[201] T. Kokubo, S. Yamaguchi, Novel bioactive titanate layers formed on Ti metal and its alloys by chemical treatments, Materials (Basel). 3 (2010) 48–63. doi:10.3390/ma3010048.

INFLUENCE DE TRAITEMENTS DE SURFACE SUR LES PROPRIETES DE RESISTANCE A LA CORROSION D'ALLIAGES DE TITANE A GRAINS ULTRAFINS POUR DES APPLICATIONS BIOMEDICALES.

RÉSUMÉ DÉTAILLÉ EN FRANÇAIS

INTRODUCTION

Les dispositifs biomédicaux utilisés (prothèses, implants) fonctionnent de manière satisfaisante dans de nombreux cas. Cependant, parfois, le corps réagit à la présence de l'implant ce qui peut entraîner son remplaçant rapide. Dans ce contexte, le titane (Ti) et ses alliages sont les matériaux les plus utilisés pour les implants orthopédiques et dentaires en raison de leur excellente biocompatibilité et résistance à la corrosion [1].

Cependant, les propriétés mécaniques du titane et de ses alliages devraient être proches du tissu osseux, condition préalable au succès des implants orthopédiques. Dans ce contexte, les alliages (α+β) et β ont suscité un intérêt considérable, car ils présentent un faible module d'élasticité, ce qui permet une meilleure interaction entre l'implant et l'os [2]. De plus, les alliages (α+β) et β peuvent être obtenus à partir d'éléments métalliques considérés comme biocompatibles comme Nb, Ta, Zr, Mo et Sn [3].

Les investigations récentes menées sur le module d'élasticité ont permis le développement d'une nouvelle génération d'alliages de titane pour les applications orthopédiques, notamment le Ti29Nb13Ta4.6Zr [4], Ti12Mo6Zr2Fe (TMZF) [5], Ti35Nb7Zr5Ta (TNZT) [6] et Ti13Nb13Zr [7].

En plus du module d'élasticité, d'autres propriétés mécaniques des alliages de titane, tels que la dureté, la résistance et la ductilité, peuvent être considérablement améliorées grâce à l'utilisation de techniques de déformations mécaniques telles que les déformations plastiques sévères (SPD-Severe Plastic Deformation) [8]. Ce procédé permet d'obtenir une microstructure avec des grains

ultrafins [9]. Les techniques de SPD les plus couramment appliquées sont l'extrusion de canaux angulaires ((ECAP-Equal Channel Angular Pressing) et la torsion sous haute pression (HPT-High Pressure Torsion) [10].

Notre équipe a étudié l'article intitulé ***"Ultrafine-Grained Ti13Nb13Zr Alloy produced by Severe Plastic Deformation"*** [11]. Dans ce travail, l'effet de la technique de torsion sous haute pression sur l'augmentation de la micro-dureté de l'alliage Ti13Nb13Zr a été observé. La valeur de micro-dureté a augmenté de manière significative de 220 HV à 402 HV avec une pression appliquée de 4,5 GPa. De plus, un affinement de la taille de grains (200 µm à l'état initial à 130 nm) a également été observé.

D'autre part, des travaux antérieurs sur le titane et les alliages de titane traités par SPD se sont concentrés sur l'étude de la relation entre la microstructure obtenue et les propriétés mécaniques [12–14]. Cependant, peu d'études concernent la microstructure obtenue par le SPD et la résistance à la corrosion des alliages de titane [15].

Le comportement en corrosion des alliages de titane dépend principalement des propriétés du film passif (composition et épaisseur) et de la microstructure du substrat (taille du grain et densité de déplacement) [16]. La faible vitesse de dissolution et l'inertie chimique des produits de dissolution de la couche passive d'oxyde de titane (TiO_2) permettent à l'os de se développer et de se solidifier avec la surface de l'alliage de titane [17].

Ainsi, la réponse biologique d'un implant dépend des propriétés physico-chimiques de la surface [18]. Récemment, des méthodes de modification de la surface des implants en titane ont été étudiées, telles que des revêtements au phosphate de calcium ($Ca_3(PO_4)_2$) [19], des traitements alcalins et thermiques [20], des revêtements au plasma [21] et des nanotubes de TiO_2 [22] pour améliorer l'intégration des implants. Par conséquent, afin de progresser quant à la compréhension des propriétés mécaniques et de la corrosion des matériaux à base de titane pour les applications biomédicales, deux alliages de titane,

l'alliage Ti13Nb13Zr (α'+β) et l'alliage β Ti35Nb7Zr5Ta déformé par la méthode HPT seront étudiés dans des conditions déjà définies dans un travail précédent [11]. En outre, deux traitements de modification de surface différents sont proposés : la croissance de nanotubes de titane (TiO_2) et les traitements chimiques sur des échantillons déformés HPT et des échantillons sans déformation. Enfin, les effets des traitements de déformation plastique sévère et de modification de surface seront évalués par des tests de corrosion et de bioactivité.

Déformation plastique sévère

Une stratégie pour améliorer les propriétés mécaniques du titane et de ses alliages consiste à affiner la granulométrie par une déformation plastique sévère (SPD-Severe Plastic Deformation). Les techniques de SPD les plus développées sont l'extrusion en canal angulaire (ECAP-Equal Channel Angular Pressing), torsion sous haute pression (HPT-High Pressure Torsion) et le laminage cumulatif (ARB-Accumulative Roll Bonding) [9,10].

D'après les méthodes de déformation plastique sévère mentionnées ci-dessus, le traitement HPT a montré un raffinement accru de la microstructure [9]. Les principes du traitement HPT moderne sont décrits schématiquement sur la figure 1 [23].

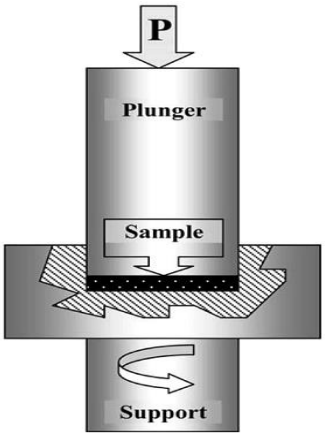

Figure 1 : Schéma de principe de la Torsion sous Haute Pression (HPT). Adapté de Zhilyaev et al., (2008) [23].

L'échantillon en forme de disque est positionné entre deux actionneurs, où il est soumis à la pression appliquée, P, de quelques GPa à température ambiante ou à chaud. Pendant que la pression est appliquée, une déformation par rotation est réalisée sur l'éprouvette. Les forces de frottement sur la surface déforment le disque par cisaillement. Le processus se déroule alors sous une pression presque hydrostatique [23].

Dans ce projet, les alliages Ti13Nb13Zr et Ti35Nb7Zr5Ta sous forme de disques de 10 mm de diamètre et 1 mm d'épaisseur sont traités par HPT. Le traitement est effectué à la température ambiante. Les disques sont traités sous des pressions de 1,0 et 4,5 GPa et trois tours sont appliqués avec une vitesse de rotation de 3 rpm.

Traitements de modification de surface.

Le titane et ses alliages sont largement utilisés dans les dispositifs et composants biomédicaux ainsi que dans les applications cardiaques et cardiovasculaires, en raison de leurs propriétés recherchées, telles que leur module d'élasticité relativement bas, leur bonne résistance à la fatigue, leur usinabilité, résistance à la corrosion et biocompatibilité. Cependant, le titane et ses alliages ne peuvent pas répondre à toutes les exigences cliniques en raison de leurs propriétés tribologiques faibles [24]. Par conséquent, afin d'améliorer les propriétés biologiques, chimiques et mécaniques du titane et des alliages de titane, des traitements de modification de surface sont souvent effectués.

Nanotubes de TiO_2.

Le titane est largement utilisé pour la fabrication de dispositifs biomédicaux et, comme la surface de l'implant est responsable du processus d'ostéointégration, il est essentiel de modifier cette surface pour obtenir une meilleure biocompatibilité. De plus, l'adhérence d'une surface nanostructurée augmente par rapport aux surfaces métalliques usuelles, démontrant ainsi que les nanotubes améliorent l'ostéointégration. Les surfaces contenant des nanotubes de TiO_2

augmentent la croissance cellulaire et les dépôts d'hydroxyapatite (HAp) [25]. L'hydroxyapatite ($Ca_{10}(PO_4)_6(OH)_2$) présente une similitude chimique et structurelle avec le composant inorganique de la matrice osseuse.

Croissance de nanostructures de TiO_2 par anodisation électrochimique.

Les tests d'anodisation sont généralement effectués sur une cellule électrochimique à deux ou trois électrodes avec un alliage en titane comme anode, une grille de platine comme cathode et, dans le cas d'une cellule à trois électrodes avec une électrode Ag / AgCl comme électrode de référence. Un potentiel constant est appliqué à l'aide d'une source d'alimentation en courant continu [13].

Les principaux processus de formation de nanotubes de TiO_2 sont (1) la croissance d'oxydes à la surface du métal due à l'interaction du métal avec les ions O^{2-} ou OH^- [26]. Après formation d'une couche d'oxyde initiale, ces anions migrent à travers la couche d'oxyde pour atteindre l'interface métal / oxyde où ils réagissent avec le métal. (2) migration des ions métalliques (Ti^{4+}) du métal à l'interface métal / oxyde ; les cations Ti^{4+} seront éjectés de l'interface métal / oxyde sous l'application d'un champ électrique qui se déplacera vers l'interface oxyde / électrolyte [27]. (3) Oxydation assistée par le champ électrique de l'oxyde à l'interface oxyde / électrolyte. En raison du champ électrique appliqué, la liaison Ti-O subit une polarisation et est affaiblie, ce qui favorise la dissolution des cations métalliques. Les cations Ti^{4+} se dissolvent dans l'électrolyte et les anions sans O^{2-} migrent vers l'interface métal / oxyde, processus (1), pour interagir avec le métal [27]. (4) Dissolution chimique du métal, ou de l'oxyde, par l'électrolyte acide. La dissolution chimique du TiO_2 dans l'électrolyte HF joue un rôle crucial dans la formation de nanotubes, plutôt que de simples structures nanoporeuses [27].

Dans le présent travail, la formation de nanotubes de TiO_2 par anodisation électrochimique des alliages Ti13Nb13Zr et Ti35Nb7Zr5Ta a été réalisée à l'aide de solutions organiques contenant des fluorures.

Structure cristalline de nanotubes de TiO_2 et traitements thermiques.

Après l'anodisation, les nanotubes de TiO_2 sont généralement amorphes. [28,29]. Après le traitement thermique (généralement sous air ou oxygène), les nanotubes de TiO_2 peuvent cristalliser sous forme anatase ou rutile ; la conversion en structure cristallisée peut avoir un impact significatif sur les propriétés mécaniques, optiques, électroniques, chimiques et biomédicales [30].

Pour ce projet, un traitement thermique a été réalisé sur des surfaces avec des nanotubes de TiO_2, à une température de 550 ° C pendant deux heures pour former un mélange de phases anatase et rutile.

Traitement acide.

Le traitement à l'acide est souvent utilisé pour éliminer l'oxyde et la contamination afin d'obtenir des finitions de surface propres et uniformes, générant également une microrugosité de surface. Takeuchi et al. (2003) ont étudié l'efficacité de décontamination de trois acides, $Na_2S_2O_8$, H_2SO_4 et HCl, pour la surface de titane et ont découvert que HCl était un excellent agent de décontamination, car il pouvait facilement dissoudre les sels de titane et ne fragilisait pas la surface de Ti [17]. Il a été démontré que l'attaque acide améliore grandement l'ostéointégration, car elle favorise la formation de tissu osseux entre l'implant et l'interface osseuse [31]. Pour ce travail, les acides chlorhydriques et phosphorique ont été testés afin de déterminer quel acide favorise la formation d'hydroxyapatite.

Traitement alcalin.

Une méthode chimique simple a été établie pour induire la bioactivité du titane et de ses alliages. Lorsque des substrats en alliage de titane ont été traités avec une solution aqueuse de NaOH 10 M et ensuite traités thermiquement à 60°C, une mince couche de titanate de sodium s'est formée sur ses surfaces [32]. Ainsi, les substrats traités formaient une couche d'apatite dense et uniforme sur leurs surfaces dans un fluide corporel simulé (SBF-Simulated Body Fluid) avec des concentrations ioniques presque égales à celles du plasma sanguin humain [32].

Caractérisation initiale d'échantillons d'alliage Ti13Nb13Zr.

Différentes surface sont étudiées dans ce travail et le tableau 1 résume toutes les surfaces modifiées avec et sans déformation plastique sévère utilisées dans les tests de corrosion et de bioactivité.

Tableau 1 : Surfaces de travail initial de l'alliage Ti13Nb13Zr avec différents traitements de modification de surface et avec et sans traitement par HPT.

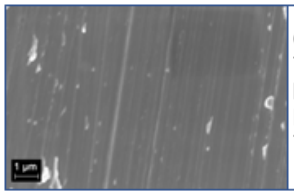	**Condition:** Sans déformation. **Traitement de surface:** Polissage . **Phases cristallines :**α' e β. **Taille de grain:** 250 µm.	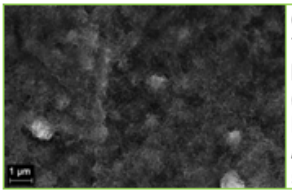	**Condition:** Sans déformation. **Traitement de surface:** Procédés chimiques (HCl + NaOH) . **Phases cristallines :** Anatase, rutile et titanate de sodium.
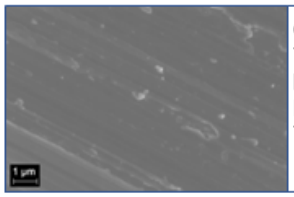	**Condition:** 1 GPa (HPT). **Traitement de surface:** Polissage . **Phases cristallines :**α' e β. **Taille de grain:** 22 µm.	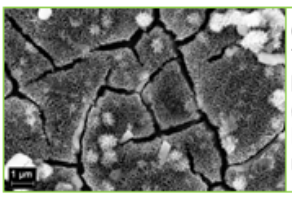	**Condition:** 1 GPa (HPT). **Traitement de surface:** Procédés chimiques (HCl + NaOH) . **Phases cristallines:** Anatase, rutile et titanate de sodium.
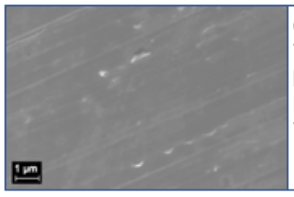	**Condition:** 4.5 GPa (HPT). **Traitement de surface:** Polissage . **Phases cristallines :**α' e β. **Taille de grain:** 203 nm.	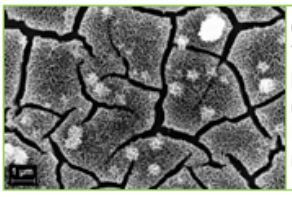	**Condition:** 4.5 GPa (HPT). **Traitement de surface:** Procédés chimiques (HCl + NaOH). **Phases cristallines :**Anatase, rutile et titanate de sodium.
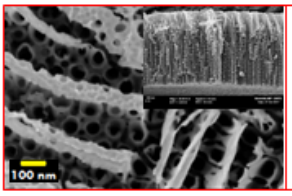	**Condition:** Sans déformation. **Traitement de surface:** Nanotubes de TiO_2. **Phases cristallines :**α', α, β, anatase et rutile. **Longueur:** 1839 nm. **Diamètre:** 96 nm.	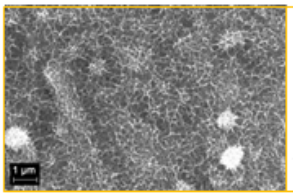	**Condition:** Sans déformation. **Traitement de surface:** Procédés chimiques (H_3PO_4 + NaOH). **Phases cristallines :** Anatase, rutile et titanate de sodium.
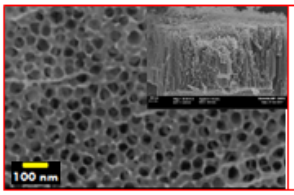	**Condition:** 1 GPa (HPT). **Traitement de surface:** Nanotubes de TiO2. **Phases cristallines :**α', α, β, anatase et rutile. **Longueur:** 1557 nm. **Diamètre:** 67 nm.	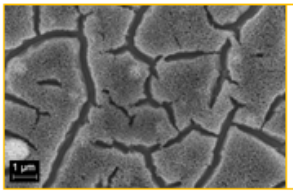	**Condition:** 1 GPa (HPT). **Traitement de surface:** Procédés chimiques (H_3PO_4 + NaOH). **Phases cristallines:** Anatase, rutile et titanate de sodium.
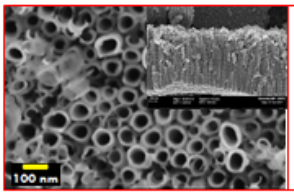	**Condition:** 4.5 GPa (HPT) **Traitement de surface:** Nanotubes de TiO2. **Phases cristallines :**α', α, β, anatase et rutile. **Longueur:** 1492 nm. **Diamètre:** 94 nm.	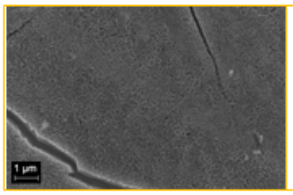	**Condition:** 4.5 GPa (HPT). **Traitement de surface:** Procédés chimiques (H_3PO_4 + NaOH). **Phases cristallines :**Anatase, rutile et titanate de sodium.

Caractérisation électrochimique.

Alliage Ti13Nb13Zr.

Pour reproduire au plus près des conditions du corps humain, les mesures électrochimiques sont effectuées dans un environnement physiologique. Une solution simulant un fluide corporel (SBF-Simulated Body Fluid) a été utilisée comme électrolyte (NaCl 8,035 g L^{-1}, KCl 0,225 g L^{-1}, $NaHCO_3$ 0,355 g L^{-1}, $K_2HPO_4 \cdot 3H_2O$ 0,231 g L^{-1}, $MgCl_2 \cdot 6H_2O$ 0,311 g L^{-1}, $CaCl_2$ 0,292 g L^{-1} e Na_2SO_4 0,072 g L^{-1}). Il reproduit la partie inorganique du plasma sanguin humain (ne contient pas de composition organique ni de cellules). Dans cette étude, la solution de SBF a été préparée, selon le protocole détaillé proposé par Kokubo et al.(2006) [33] et dans la norme ISO 23317:2014.

Les mesures électrochimiques présentées ci-dessous sont donc destinées à évaluer l'impact du traitement de modification de surface et de la déformation plastique sévère sur les propriétés électrochimiques dans la solution SBF pour l'alliage Ti13Nb13Zr. Les conditions pour les tests électrochimiques effectués pour toutes les conditions existantes et pour les deux alliages (Ti13Nb13Zr et Ti35Nb7Zr5Ta) sont les suivantes :

- Afin de reproduire au mieux les conditions physiologiques, toutes les mesures se font à l'obscurité.
- Pour des raisons de reproductibilité, les mesures sont répétées trois fois (sur un échantillon différent à chaque fois, mais avec la même morphologie et la même structure cristalline).
- Les courbes de polarisation sont enregistrées dans une plage de potentiel de -30 mV à +1,20 V par rapport au potentiel de circuit ouvert (OCP), avec une vitesse de balayage de 0,50 mV s-1.
- Les mesures de spectroscopie d'impédance sont enregistrées pour une gamme de fréquences de 20 kHz à 20 mHz. L'amplitude du signal de perturbation sinusoïdale est de 10 mVrms.

- Les simulations des spectres EIS de tous les échantillons ont été réalisées à l'aide du logiciel Simad (développé parle laboratoire LISE).

Échantillons polis.

Les figures 2((a) et (b)) présentent les courbes de polarisation anodiques et les diagrammes de Nyquist, respectivement, dans SBF à 37°C des échantillons de surface poli de l'alliage Ti13Nb13Zr non déformés et déformés par HPT.

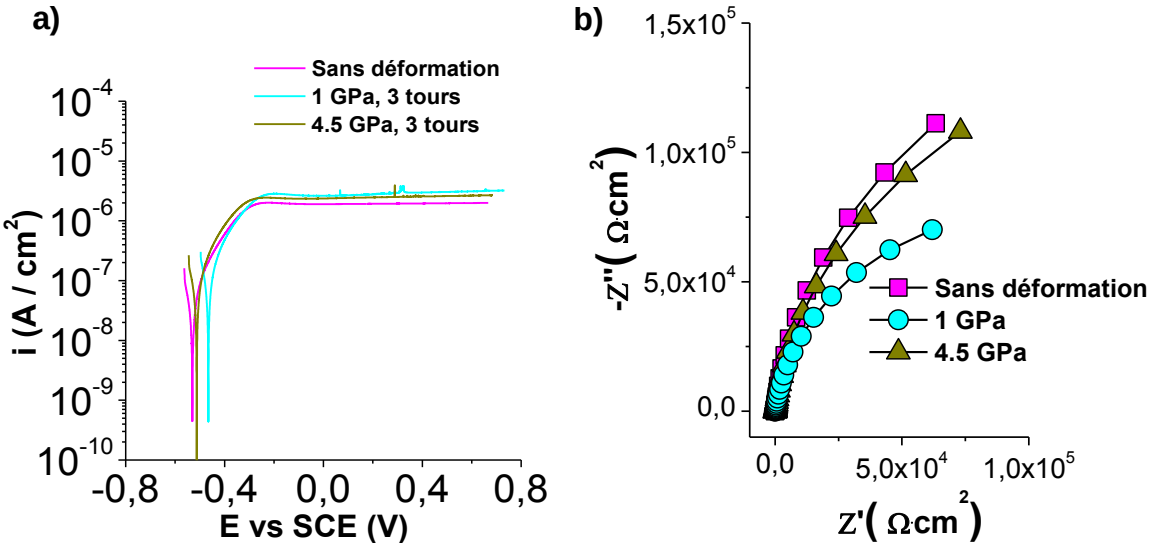

Figure 2 : Courbes de polarisation anodiques (a) et diagrammes de Nyquist (b) des échantillons polis de l'alliage Ti-13Zr-13Nb non déformés et déformés par HPT en milieu physiologique dans une solution de SBF à pH 7,4 à 37 ° C.

Les densités de courant, représentées sur l'axe des ordonnées de la figure 2(a), ont été calculées en divisant le courant mesuré par la surface géométrique (0,283 cm²). On considère que le courant mesuré dans la région anodique est principalement dû à la réaction d'oxydation des substrats en TiO_2, ce qui contribue à l'épaississement de la couche passive. Cette réaction se produit à l'interface métal / oxyde [30].

Les courants de passivation sont similaires pour les conditions non déformées eet déformées par HPT. Initialement pour un échantillon sans

déformation, le courant de passivation a une valeur approximative : 2,00 µA / cm^2. Pour les échantillons présentant une déformation plastique sévère, les courants de passivation sont les suivants: 2,95 µA / cm^2 pour l'échantillon présentant une déformation de 1 GPa et 2,45 µA / cm^2 pour l'échantillon présentant une déformation de 4,5 GPa. Par conséquent, une déformation plastique sévère n'a pas d'effet significatif sur le courant de passivation des échantillons déformés par rapport au échantillons sans déformation.

Afin de compléter la caractérisation électrochimique des surfaces polies, les échantillons ont été soumis à des mesures de spectroscopie d'impédance électrochimique. La figure 2(b) montre les mesures d'impédance en représentation de Nyquist. L'observation des diagrammes de Nyquist révèle que la forme du spectre d'impédance de tous les substrats (arc) est typique d'un système capacitif-résistif (associations de phénomènes capacitifs, c'est-à-dire accumulations de charges et phénomènes résistifs, liés à la charge ou la résistance d'une couche).

Les spectres d'impédance expérimentaux ont été modelisés par un circuit électrique équivalent approprié décrivant les propriétés du système étudié. Nous avons envisagé pour les échantillons un modèle qui représente une structure à deux couches composées d'une couche interne dense et d'une couche externe poreuse sur l'alliage Ti13Nb13Zr. La figure 3 montre le modèle sélectionné qui est représenté par un circuit équivalent $R_s + Q_a / (R_a + (Q_{dl} / R_{ct}))$. Où R_s est la résistance de la solution, R_a est la résistance de la couche externe poreuse, R_{ct} représente la résistance de transfert de charge, Q_a est l'élément à phase constante pour la couche externe poreuse et Qdl est l'élément à phase constante pour la double couche à l'interface couche interne dense-électrolyte.

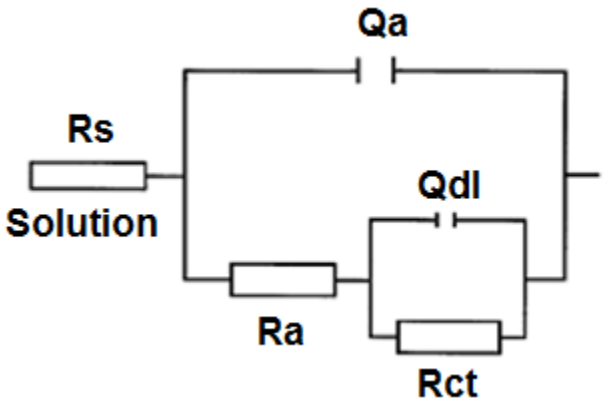

Figure 3 : Circuit électrique équivalent utilisé pour modéliser les résultats d'échantillons d'alliage Ti13Nb13Zr non déformés et déformés par HPT en milieu physiologique dans une solution de SBF à pH 7,4 à 37 ° C.

Les résultats du modèle sont présentés dans le tableau 2. En général, on observe des valeurs de résistance de la solution (résistance d'électrolyte) comprises entre 19 et 22 ($\Omega \cdot cm^2$) ainsi que des valeurs de résistance de transfert de charge élevées entre $1{,}7x10^5$ et $3x10^5$ ($\Omega \cdot cm^2$), indiquant une résistance élevée à la corrosion. De plus, il est possible de calculer des valeurs de capacités effectives (C_{eff}) de la couche externe poreuse et de la couche interne dense à partir des paramètres de l'élément à phase constante, à l'aide de la relation de Brug [34] :

$$C_{eff}(Brug) = Q^{\frac{1}{\alpha}}(R_e^{-1} + R_t^{-1})^{\frac{\alpha-1}{\alpha}}$$

Les valeurs de capacité sont indiquées dans le tableau 2. Le calcul de la capacité effective associée à la couche externe poreuse ($C_{eff(a)}$) donne entre 7 et 16 $\mu F \cdot cm^{-2}$. Par contre, les résultats obtenus pour la couche interne dense ($C_{eff(dl)}$) sont compris entre 17 et 20 $\mu F \cdot cm^{-2}$, qui est une valeur typique d'une capacité de double couche.

Si l'on associe le film passif à un condensateur plan, l'épaisseur de film passif δ (en nm) peut être estimée par la relation suivante :

$$\delta = \frac{\epsilon \cdot \epsilon_0}{C_{eff}}$$

Où ϵ0 est la permittivité du vide (8,8542 × 10^{-14} F/cm) et ϵ la constante diélectrique du matériau. La valeur de la constante diélectrique pour le TiO_2 est comprise entre 18,2 et 173 [35]. Si l'on considère maintenant une valeur moyenne de la constante diélectrique, ϵ = 100, comme déjà choisie par différents auteurs [36,37], conduit des épaisseurs de films passifs protecteurs (associés à la couche interne dense, responsables de la protection du matériau) de 3,75, 4,53 et 3,80 nm pour l'alliage Ti13Nb13Zr, dans des conditions non déformées (ND) et déformées par 1GPa (HPT1GPa) et déformées par 4,5GPa (HPT4.5GPa), respectivement. Ces résultats montrent que les films passifs en alliage Ti13Nb13Zr déformé ont une épaisseur supérieure.

En résumé, les résultats obtenus avec l'ajustement indiquent que tous les substrats testés se sont comportés de manière très similaire.

Tableau 2 : Valeurs des paramètres d'ajustement des mesures d'impédance des échantillons polis d'alliage Ti13Nb13Zr avec le modèle de la Figure 3.

Condition	**Rs** $\Omega \cdot cm^2$	**Qa** $\mu F \cdot s^{(\alpha a-1)}$	α_a	**Ra** $\Omega \cdot cm^2$	$C_{eff(a)}$ $\mu F/cm^2$	**Qdl** $\mu F \cdot s^{(\alpha dl-1)}$	α_{dl}	**Rb** $\Omega \cdot cm^2$	$C_{eff(dl)}$ $\mu F/cm^2$
Sans déformation	22	7	0.94	57	16	9	0.94	3.0E+05	20
1 GPa	19	5	0.90	111	7	12	0.88	1.3E+05	17
4.5 GPa	21	6	0.90	124	9	11	0.91	1.7E+05	20

Echantillons de surface à base de nanotubes de TiO_2

Les figures 4((a) et (b)) présentent les courbes de polarisation anodiques et les diagrammes de Nyquist, respectivement, dans SBF à 37°C des échantillons de surface à base de nanotubes de TiO_2 d'alliage Ti13Nb13Zr non déformés et déformés par HPT.

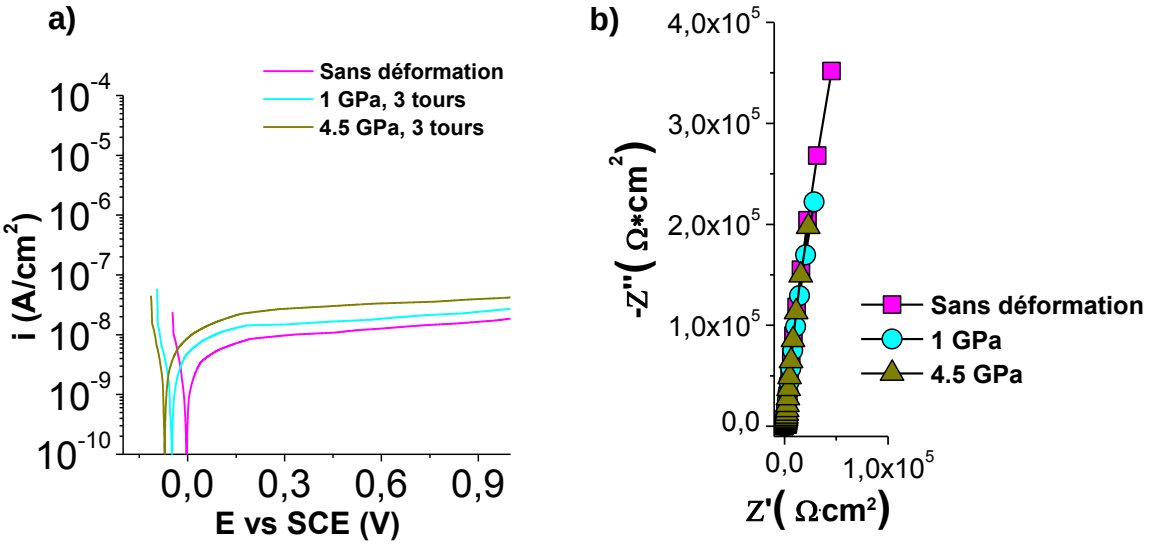

Figure 4 : Courbes de polarisation anodiques (a) et diagrammes de Nyquist (b) des échantillons de surface à base de nanotubes de TiO_2 de l'alliage Ti13Nb13Zr non déformés et déformés par HPT en milieu physiologique dans une solution de SBF à pH 7,4 à 37 ° C.

L'observation générale de la figure 4(a) montre que la forme de la partie anodique des courbes de polarisation présente le comportement caractéristique d'un état passif. Effectivement, pour tous les échantillons, un plateau de courant est présent sur une large plage de potentiels.

Les courants de passivation sont très différents par rapport aux substrats nus. Initialement pour un échantillon sans déformation, le courant de passivation de l'alliage Ti13Nb13Zr avec nanotubes de TiO_2 recuits est de 0,012 µA / cm^2. Pour les échantillons présentant une déformation plastique sévère, les courants de passivation sont les suivants : 0,017 µA / cm^2 pour l'échantillon présentant une déformation de 1 GPa et 0,033 µA / cm^2 pour l'échantillon présentant une déformation de 4,5 GPa. Par conséquent, il semble qu'une déformation plastique sévère entraîne une légère augmentation du courant de passivation par rapport au substrat sans déformation.

La figure 4(b) montre les mesures d'impédance en représentation de Nyquist. L'observation des diagrammes de Nyquist révèle que la forme du spectre d'impédance de tous les substrats est pseudo-capacitive (droite inclinée), c'est-à-dire que les échanges d'électrons et donc les réactions sont très limitées ou que la couche d'oxyde est très résistive.

Les spectres expérimentaux d'impédance sont modélisés au moyen d'un modèle de ligne de transmission développée pour une électrode poreuse décrivant les propriétés du système à l'étude. La figure 5 montre le schéma de la ligne de transmission proposée pour modéliser les mesures d'impédance.

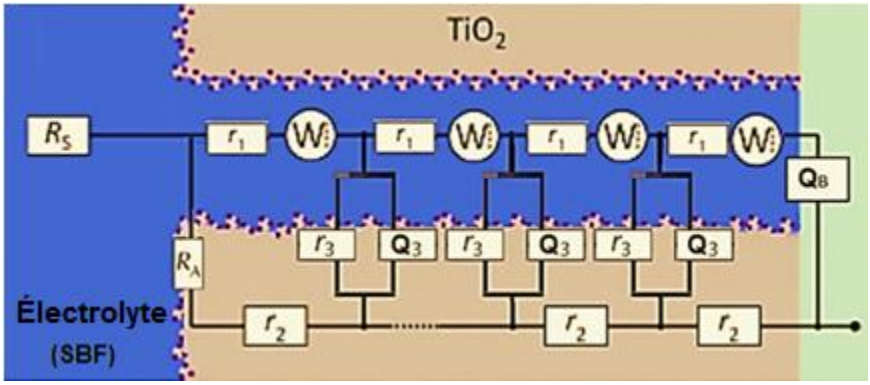

Figure 5 : Schéma de la ligne de transmission proposée pour des échantillons de surface à base de nanotubes de TiO_2 de l'alliage Ti13Nb13Zr non déformés et déformés par HPT dans une solution de SBF à pH 7,4 à 37 ° C.

Les résultats du modèle sont présentés dans le tableau 3. Les résultats du réglage indiquent des valeurs de résistance de la solution proches de 20 ($\Omega \cdot cm^2$) et une élevée résistance associée à la limite supérieure des pores (R_A) comprise entre $2x10^7$ et $3x10^7$ ($\Omega \cdot cm^2$), indiquant une résistance à la corrosion supérieure à celle des substrats polis. Enfin, il a été observé que les substrats avec des nanotubes de TiO_2 plus longs à l'état non déformé présentent une résistance à la corrosion supérieure. De plus, il est possible de calculer des valeurs de capacités effectives à partir des paramètres CPE modélisant les impédances ξ et Z_B, à l'aide de la relation de Hsu-Mansfeld [38] :

$$C_{eff}(H-M) = Q^{\frac{1}{\alpha}}(R_t)^{\frac{1-\alpha}{\alpha}}$$

Les valeurs de capacité sont indiquées dans le tableau 3. Le calcul de la capacité effective interfaciale associée à l'élément ξ (C_{β}) donne entre 14 et 42 $\mu F \cdot cm^{-2}$, qui correspondent aux valeurs correspondant à la capacité de double couche. Par contre, les résultats obtenus pour la capacité effective C_n, associée au CPE de fond de pore sont compris entre 2 et 5 $\mu F \cdot cm^{-2}$, qui est une valeur typique d'une capacité de film passif.

En ce qui concerne l'épaisseur du film passif, elles ont été calculées à partir de la capacité effective. Les valeurs d'épaisseur étaient de 25,5, 39,6 et 17,6 nm pour l'alliage Ti13Nb13Zr dans les conditions ND, HPT1GPa et HPT4.5GPa, respectivement.

Tableau 3 : Valeurs des paramètres d'ajustement des mesures d'impédance des échantillons de surface à base de nanotubes de TiO_2 d'alliage Ti13Nb13Zr avec le modèle de la Figure 5.

Condition	χ1	χ2	ξ				Z_A	Z_B			R_s
	R_1 (Ω)	R_2 (Ω)	R_3 (Ω)	Q_3 ($F^{\beta-1}$)	β	C_{β} μF/cm²	R_A (Ω)	Q_B (F^{n-1})	n	C_n μF/cm²	R_s (Ω)
Sans déformation	1	241	2.3E+15	1.4E-06	0.96	14	3.0E+07	1.4E-06	0.96	3	70.0
1 GPa	6	736	1.8E+15	1.2E-06	0.97	19	3.0E+07	1.0E-06	0.96	2	70.0
4.5 GPa	1	100	1.8E+15	2.4E-06	0.94	42	2.3E+07	2.0E-06	0.96	5	70.0

Échantillons soumis à un traitement acide à l'HCl puis à un traitement alcalin avec NaOH.

Les figures 6((a) et (b)) présentent les courbes de polarisation anodiques et les diagrammes de Nyquist, respectivement, dans SBF à 37°C des échantillons de surface soumis à un traitement acide à l'HCl puis à un traitement alcalin avec NaOH d'alliage Ti13Nb13Zr non déformés et déformés par HPT.

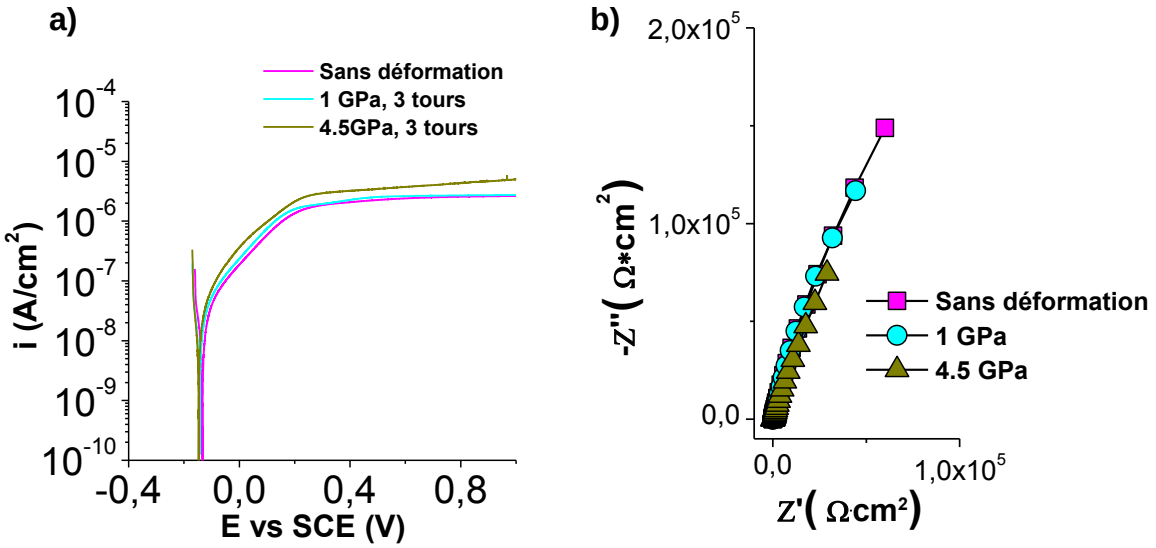

Figure 6 : Courbes de polarisation anodiques (a) et diagrammes de Nyquist (b) des échantillons de surface soumis à un traitement acide à l'HCl puis à un traitement alcalin avec NaOH d'alliage Ti13Nb13Zr non déformés et déformés par HPT en milieu physiologique dans une solution de SBF à pH 7,4 à 37 ° C.

Une observation générale de la forme de la partie anodique des courbes de polarisation représentées à la figure 6(a), montre que le comportement des échantillons dans un environnement physiologique est caractéristique d'un état passif.

Une variation des courants de passivation est observée : initialement les échantillons sans déformation ont une valeur approximative du courant au plateau de passivation de 2,30 µA / cm^2, pour les échantillons présentant une déformation plastique sévère, les courants de passivation sont les suivants : 2,51 µA / cm^2 pour l'échantillon présentant une déformation de 1 GPa et 3,40 µA / cm^2 pour l'échantillon présentant une déformation de 4,5 GPa. Ainsi, une déformation plastique sévère entraîne une légère augmentation du courant de passivation par rapport au substrat sans déformation.

La figure 6(b) montre les mesures d'impédance en représentation de Nyquist. L'observation des diagrammes de Nyquist révèle que la forme du spectre

d'impédance pour tous les substrats (arc) est typique d'un système capacitif-résistif.

Les spectres expérimentaux d'impédance sont modélisés à l'aide d'un circuit électrique équivalent approprier décrivant les propriétés du système étudié.

Les spectres ont été ajustés à l'aide du circuit :

$$R_s + (Q_b / R_b) + Q_a / (R_a + (Q_{dl} / R_{ct})),$$

Où R_s représente la résistance de la solution, R_b et Q_b représentent la résistance et l'élément à phase constante pour la couche externe poreuse, R_a et Q_a représentent la résistance et l'élément à phase constante pour la couche intermédiaire poreuse, R_{ct} et Q_{dl} représentent la résistance de transfert de charge et l'élément à phase constante pour la double couche à l'interface couche interne dense-électrolyte. La figure 7 montre le modèle sélectionné.

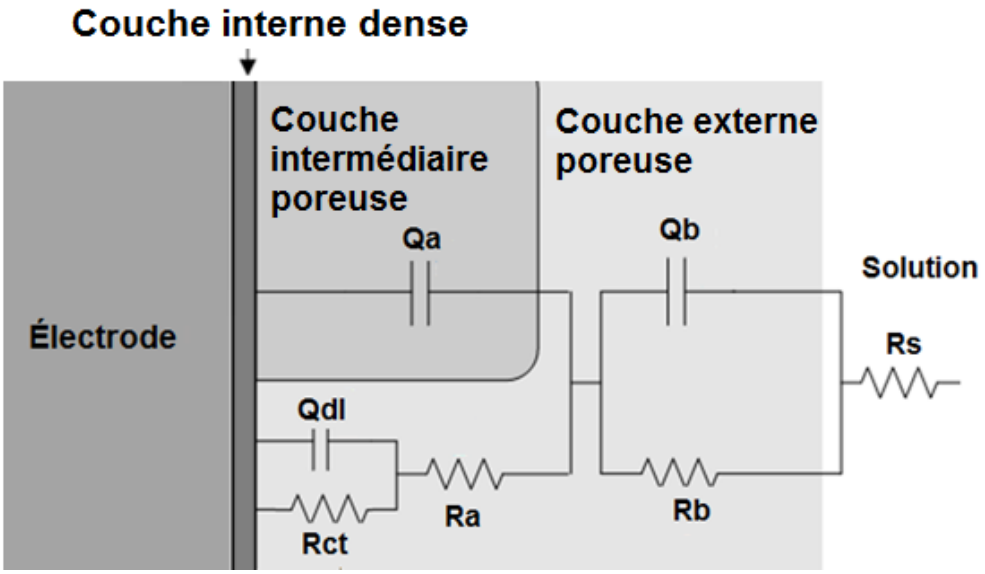

Figure 7 : Circuit équivalent utilisé pour modéliser les résultats d'impédance d'échantillons de surface soumis à un traitement acide à l'HCl puis à un traitement alcalin avec NaOH d'alliage Ti13Nb13Zr non déformés et déformés par HPT en milieu physiologique dans une solution de SBF à pH 7,4 à 37 ° C.

Les résultats de l'ajustement du modèle et de la capacité effective associée au CPE calculé avec l'équation de Brug sont donnés dans le tableau 4. L'ajustement permet d'obtenir des valeurs de résistance de solution comprises entre 20 et 22 ($\Omega \cdot cm^2$) ainsi que des valeurs élevées de résistance de transfert de charge (R_{ct}) comprises entre $6x10^5$ et $8x10^5$ ($\Omega \cdot cm^2$), indiquant une résistance élevée à la corrosion avec des valeurs légèrement supérieures à des échantillons nus.

En ce qui concerne les capacités, les valeurs pour la double couche ($Ceff_{(dl)}$) étaient comprises entre 14 et 19 $\mu F \cdot cm^{-2}$ (voir tableau 4). Les valeurs de capacité pour la couche externe poreuse ($Ceff_{(b)}$) et la couche poreuse intermédiaire ($Ceff_{(a)}$) étaient inférieures à $Ceff_{(dl)}$. De plus, l'épaisseur du film passif, δ (en nm), a été obtenue à partir de la capacité de la couche interne dense. Les valeurs d'épaisseur sont respectivement de 4,05, 4,30 et 5,41 nm pour l'alliage Ti13Nb13Zr, dans les conditions ND, HPT1GPa et HPT4.5GPa, respectivement. Ces résultats montrent que le film passif en alliage Ti13Nb13Zr sans déformation a une épaisseur inférieure et que le traitement chimique augmente le film passif par rapport aux échantillons nus.

Tableau 4 : Valeurs des paramètres d'ajustement des mesures d'impédance d'échantillons de surface soumis à un traitement acide à l'HCl puis à un traitement alcalin avec NaOH d'alliage Ti13Nb13Zr avec le modèle de la Figure 7.

	Condition		
Élément	**Sans déformation**	**1 GPa**	**4.5 GPa**
R_s (Ω· cm^2)	22	20	20
Q_b (μF ·s(αb-1))	52	28	43
α_b	0.70	0.76	0.72
R_b (Ω· cm^2)	28	15	15
$C_{eff(b)}$ (μF/ cm^2)	2.2	2.0	2.0
Q_a (μF ·s(αa-1))	19	11	55
α_a	0.70	0.75	0.70
R_a (Ω· cm^2)	7	2	10
$C_{eff(a)}$ (μF/ cm^2)	0.4	0.3	0.5
Q_{dl} (μF ·s(αdl-1))	21	39	19
α_{dl}	0.98	0.90	0.96
R_{ct} (Ω· cm^2)	7.6E+05	6.8E+05	6.0E+05
$C_{eff(dl)}$ (μF/cm^2)	19	18	14

Échantillons soumis à un traitement acide à l'H_3PO_4 puis à un traitement alcalin avec NaOH.

Les figures 8((a) et (b)) présentent les courbes de polarisation anodiques et les diagrammes de Nyquist, respectivement, dans SBF à 37°C des échantillons de surface soumis à un traitement acide à l'H_3PO_4 puis à un traitement alcalin avec NaOH d'alliage Ti13Nb13Zr non déformés et déformés par HPT.

Le comportement observé est différent des surfaces nues ou avec nanotubes montrant un comportement passif des échantillons en SBF au potentiel de corrosion pour les alliages avec nanotubes et près du potentiel de corrosion pour les surfaces nues (zone de corrosion active réduite) mais assez similaire à

celui des alliages traités en milieu acide bien que la partie active s'étale sur une plus large gamme de potentiels la partie anodique des courbes de polarisation.

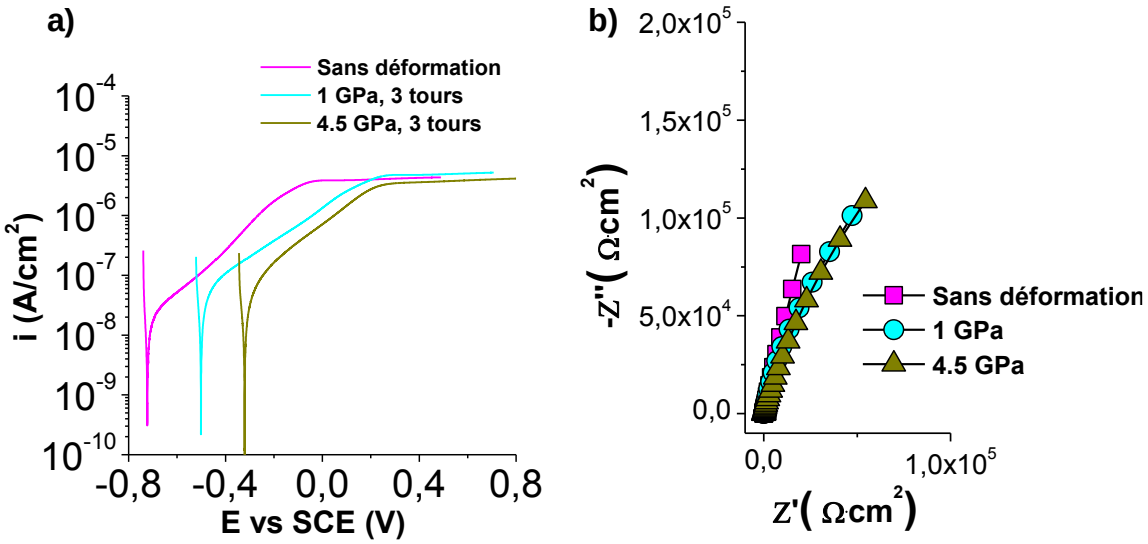

Figure 8 : Courbes de polarisation anodiques (a) et diagrammes de Nyquist (b) des échantillons de surface soumis à un traitement acide à l'H_3PO_4 puis à un traitement alcalin avec NaOH d'alliage Ti13Nb13Zr non déformés et déformés par HPT en milieu physiologique dans une solution de SBF à pH 7,4 à 37 ° C.

Initialement les échantillons sans déformation ont une valeur de courants de passivation approximative de : 4,05 µA / cm^2. Pour les échantillons présentant une déformation plastique sévère, les courants de passivation sont les suivants : 5,13 µA / cm^2 pour l'échantillon présentant une déformation de 1 GPa et 5,13 µA / cm^2 pour l'échantillon présentant une déformation de 4,5 GPa. Par conséquent, il apparaît qu'une déformation plastique sévère n'a pas d'effet sur le courant de passivation par rapport au substrat sans déformation.

La figure 8(b) montre les mesures d'impédance. L'observation des diagrammes de Nyquist révèle que la forme du spectre d'impédance de tous les substrats est caractéristique d'un système capacitif-résistif. Les spectres d'impédance expérimentaux sont analysés en ajustant le même circuit électrique équivalent à celui utilisé pour les échantillons de surface soumis à un traitement

acide à l'HCl puis à un traitement alcalin avec NaOH d'alliage Ti13Nb13Zr (voir figure 7).

Les résultats de l'ajustement du modèle et de la capacité effective associée au CPE calculé avec l'équation de Brug sont donnés dans le tableau 5. L'ajustement permet d'obtenir des valeurs de résistance de solution de 20 ($\Omega \cdot cm^2$) ainsi que des valeurs élevées de résistance de transfert de charge (R_{ct}) comprises entre $5x10^5$ et $7x10^5$ ($\Omega \cdot cm^2$), indiquant une résistance élevée à la corrosion avec des valeurs légèrement supérieures à des échantillons nus.

En ce qui concerne les capacités, les valeurs pour la double couche ($Ceff_{(dl)}$) étaient comprises entre 10 et 15 $\mu F \cdot cm^{-2}$. Les valeurs de capacité pour la couche externe poreuse ($Ceff_{(b)}$) et la couche poreuse intermédiaire ($Ceff_{(a)}$) étaient inférieures à $Ceff_{(dl)}$. De plus, l'épaisseur du film passif, δ (en nm), a été obtenue à partir de la capacité de la couche interne dense. Les valeurs d'épaisseur sont respectivement de 7,62, 7,43 et 5,03 nm pour l'alliage Ti13Nb13Zr, dans les conditions ND, HPT1GPa et HPT4.5GPa, respectivement. Ces résultats montrent que le traitement chimique contribue à augmenter l'épaisseur du film passif.

Tableau 5 : Valeurs des paramètres d'ajustement des mesures d'impédance d'échantillons de surface soumis à un traitement acide à l'H_3PO_4 puis à un traitement alcalin avec NaOH d'alliage Ti13Nb13Zr avec le modèle de la Figure 7.

	Condition		
Élément	**Sans déformation**	**1 GPa**	**4.5 GPa**
R_s (Ω· cm^2)	20	20	20
Q_b (μF ·s(αb-1))	42	15	15
α_b	0.72	0.81	0.78
R_b (Ω· cm^2)	13	2	10
$C_{eff(b)}$ (μF/ cm^2)	1.9	1.3	1.2
Q_a (μF ·s(αa-1))	65	42	14
α_a	0.78	0.82	0.77
R_a (Ω· cm^2)	78	44	20
$C_{eff(a)}$ (μF/ cm^2)	9	8	1.0
Q_{dl} (μF ·s(αdl-1))	14	12	32
α_{dl}	0.96	0.98	0.91
R_{ct} (Ω· cm^2)	5.1E+05	4.5E+05	7.1E+05
$C_{eff(dl)}$ (μF/cm^2)	10	10	15

Tests de bioactivité sur l'alliage Ti13Nb13Zr

Le principe des essais de bioactivité est d'évaluer l'aptitude du matériau à former spontanément de l'apatite à la surface lorsqu'il est immergé dans du SBF. Cette capacité est un critère essentiel pour déterminer la biocompatibilité d'un matériau. Dans cette étude, les dépôts d'apatite ont été examinés après 1, 7 et 14 jours d'immersion dans du SBF pour des échantillons de l'alliage Ti13Nb13Zr avec une modification de surface différente, ainsi que différents niveaux de déformation par HPT.

Échantillons polis.

Les observations au microscope électronique à balayage (MEB) présentées sur la la figure 9 indiquent que, même après 14 jours d'immersion dans la solution physiologique, aucune formation d'apatite n'est détectée à la surface des substrats polis.

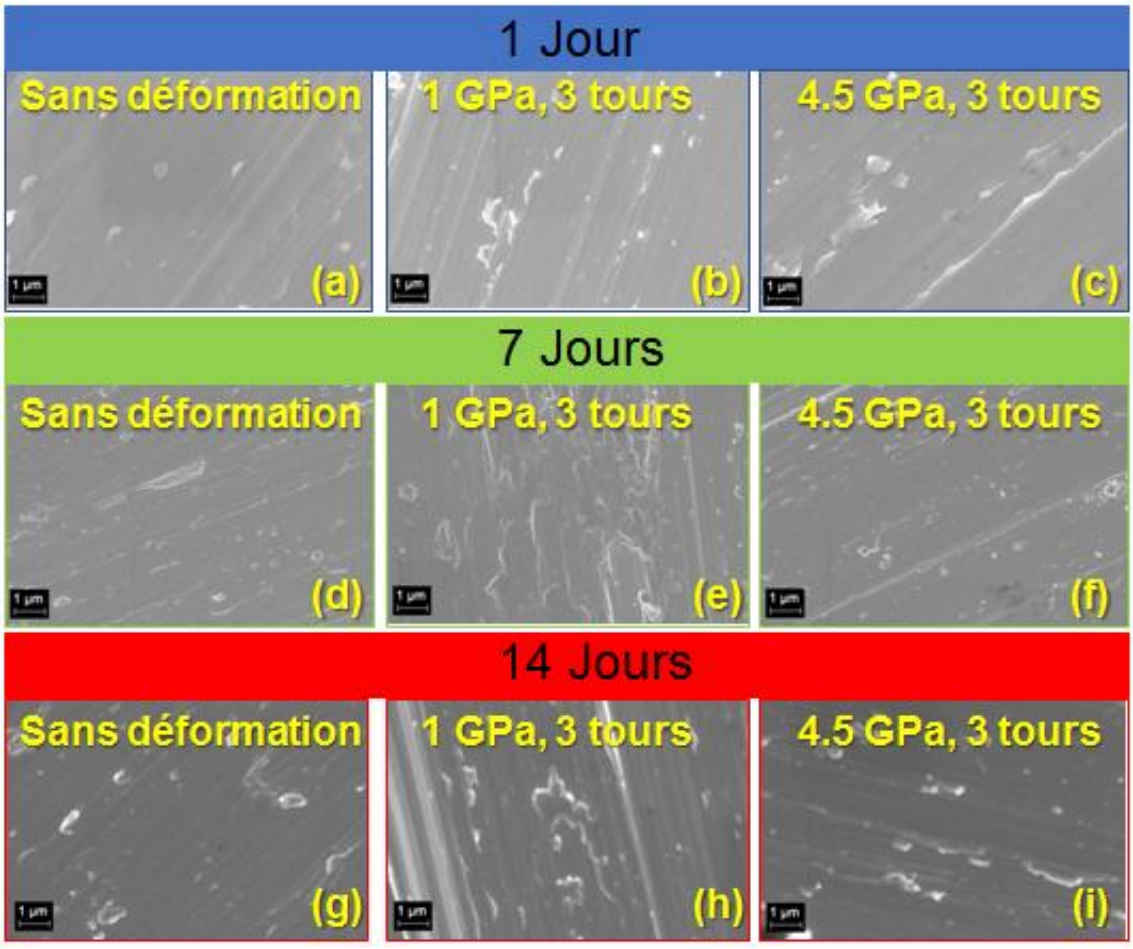

Figure 9 : Observations MEB-FEG des échantillons de surface polies (nues) d'alliage Ti13Nb13Zr non déformés et déformés par HPT soumis à des tests de bioactivité de 1, 7 et 14 jours dans du SBF.

Echantillons de surface à base de nanotubes de TiO_2

Dès le premier jour d'immersion dans une solution de SBF, l'apatite est visible dans de petites zones sur des substrats de l'alliage Ti13Nb13Zr déformé

par HPT pour une déformation de 4,5 GPa (Figure 10(c)). Des dépôts homogènes d'apatite sont observés dans tous les échantillons lorsqu'ils sont immergés dans du SBF pendant sept et 14 jours.

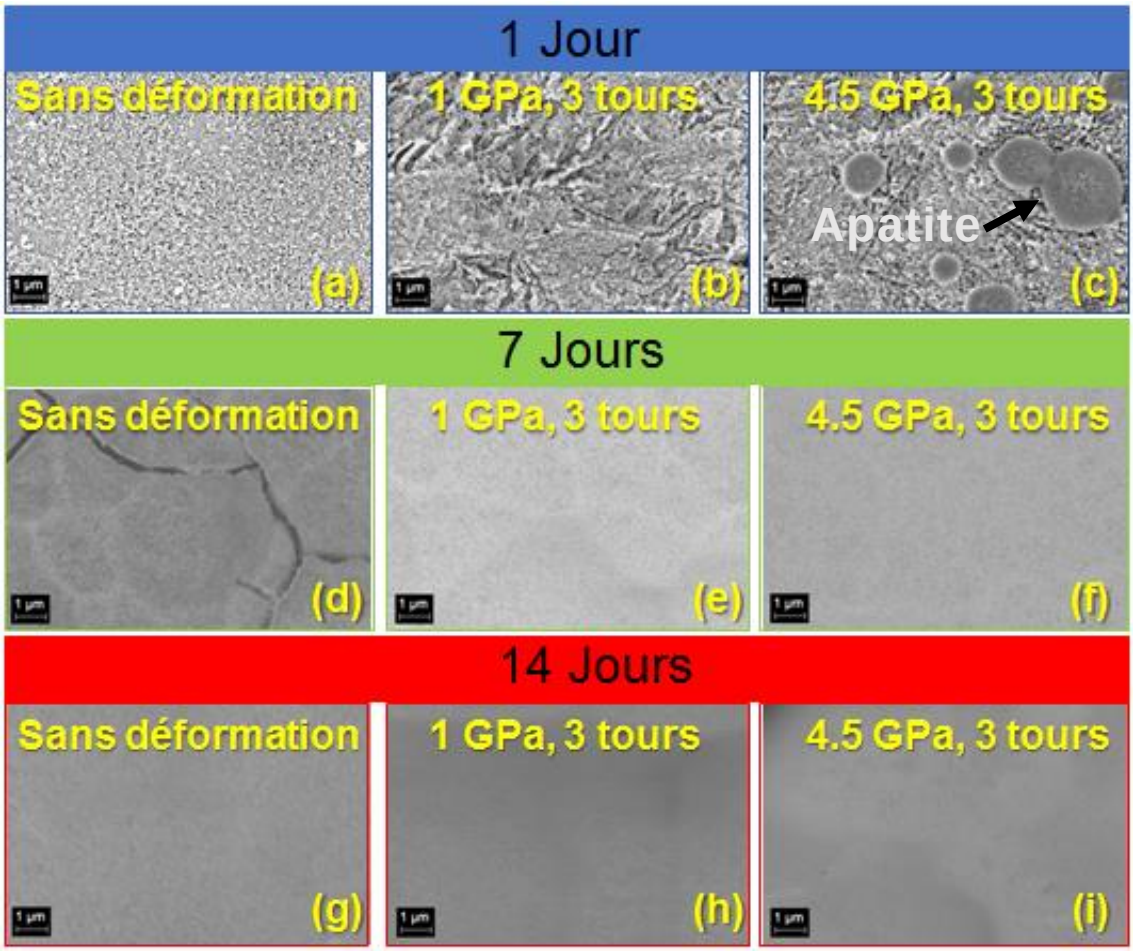

Figure 10 : Observations MEB-FEG des surfaces d'alliage Ti13Nb13Zr avec nanotubes de TiO2 non déformé et déformé par HPT soumises à des tests de bioactivité pendant 1, 7 et 14 jours dans du SBF.

Échantillons soumis à un traitement acide à l'HCl puis à un traitement alcalin avec NaOH.

Les observations MEB-FEG illustrées à la figure 11 montrent qu'à partir du septième jour d'immersion dans une solution de SBF, des dépôts d'apatite sont visibles sur tous les échantillons de l'alliage Ti13Nb13Zr.

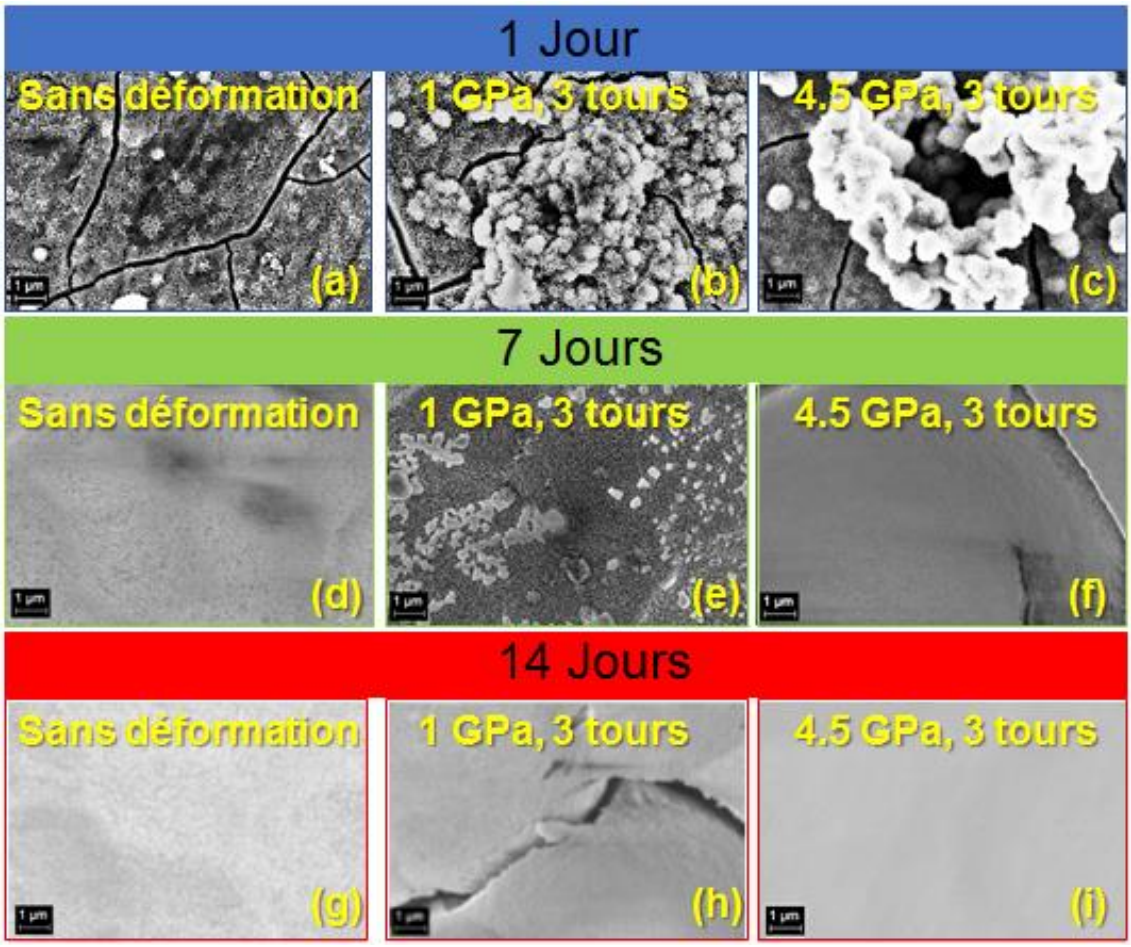

Figure 11 : Observations MEB-FEG des surfaces soumises à un traitement acide à l'HCl puis à un traitement alcalin avec NaOH d'alliage Ti13Nb13Zr non déformées et déformées par HPT suite aux tests de bioactivité pendant 1, 7 et 14 jours dans du SBF.

Échantillons soumis à un traitement acide à l'H_3PO_4 puis à un traitement alcalin avec NaOH.

Les observations SEM-FEG illustrées à la figure 12 montrent le même comportement que pour les échantillons attaqués avec HCl : à partir du septième jour d'immersion dans une solution de SBF, des dépôts d'apatite sont visibles sur tous les échantillons de l'alliage Ti13Nb13Zr.

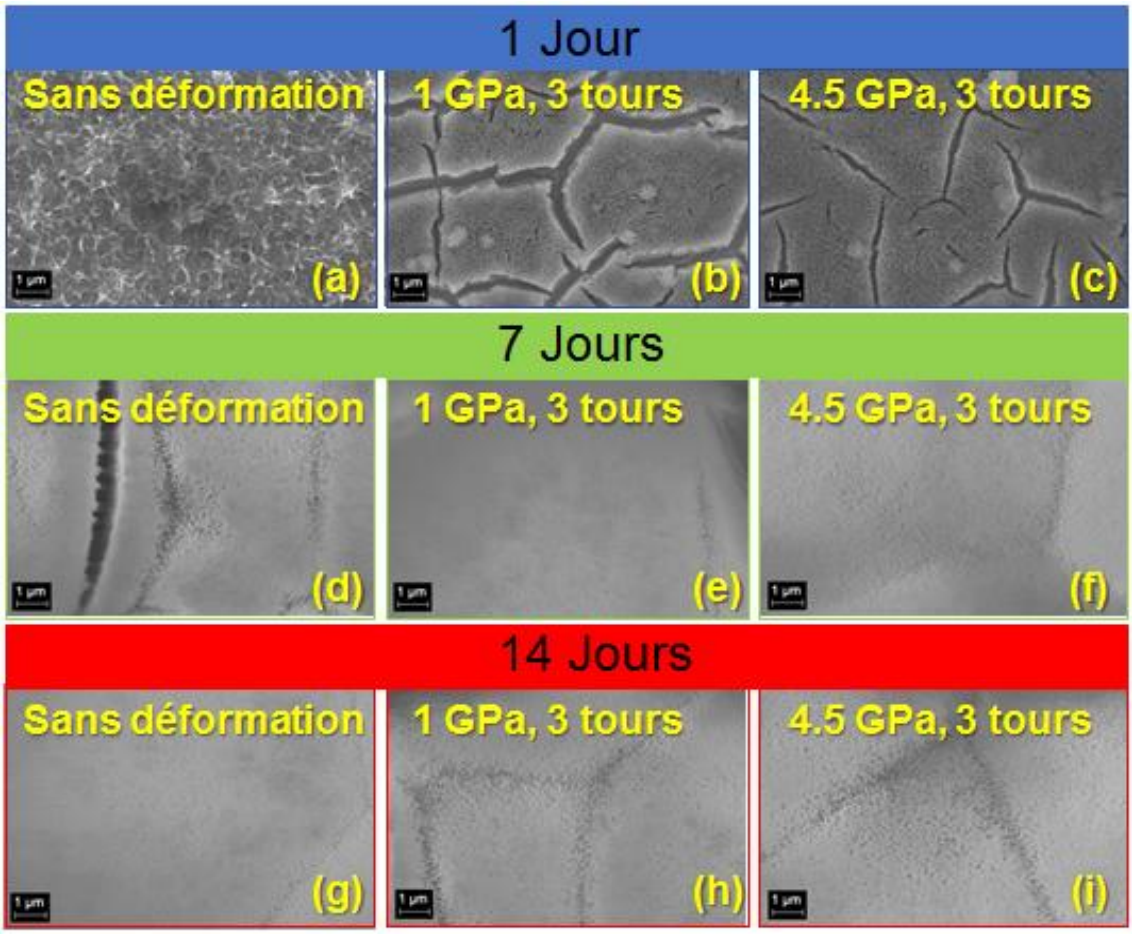

Figure 12 : Observations MEB-FEG des surfaces soumises à un traitement acide à l'H_3PO_4 puis à un traitement alcalin avec NaOH d'alliage Ti13Nb13Zr non déformées et déformées par HPT suite aux tests de bioactivité réalisés pendant 1, 7 et 14 jours dans du SBF.

Caractérisation initiale d'échantillons d'alliage Ti35Nb7Zr5Ta.

Différentes conditions de surface sont étudiées dans ce travail afin de résumer toutes les surfaces modifiées avec et sans déformation plastique sévère. Le tableau 6 montre toutes les surfaces de travail utilisées dans les tests de corrosion et de bioactivité.

Tableau 6 : Surfaces de travail initial en alliage Ti35Nb7Zr5Ta avec différents traitements de modification de surface et avec et sans traitement par HPT.

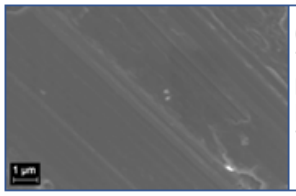	**Condition:** Sans déformation. **Traitement de surface:** Polissage. **Phases cristallines :**β. **Taille de grain:** 240 µm.	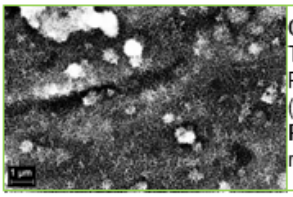	**Condition:** Sans déformation. **Traitement de surface:** Procédés chimiques (HCl + NaOH) . **Phases cristallines:**Anatase, rutile et titanate de sodium.
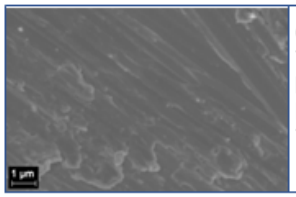	**Condition:** 1 GPa (HPT). **Traitement de surface:** Polissage. **Phases cristallines :**β. **Taille de grain:** 89 µm.	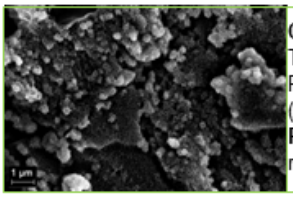	**Condition:** 1 GPa (HPT). **Traitement de surface:** Procédés chimiques (HCl + NaOH) . **Phases cristallines:**Anatase, rutile et titanate de sodium.
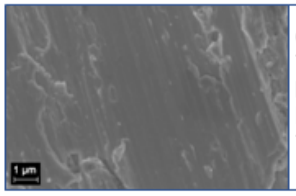	**Condition:** 4.5 GPa (HPT). **Traitement de surface:** Polissage. **Phases cristallines :**β. **Taille de grain:** 112 nm.	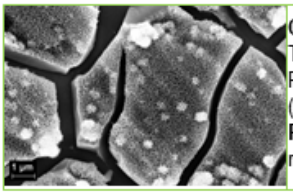	**Condition:** 4.5 GPa (HPT). **Traitement de surface:** Procédés chimiques (HCl + NaOH) . **Phases cristallines:**Anatase, rutile et titanate de sodium.
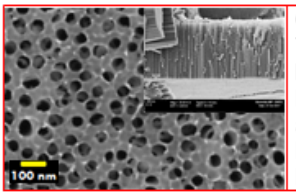	**Condition:** Sans déformation. **Traitement de surface:** Nanotubes de TiO2. **Phases cristallines :**α', α, β, anatase et rutile. **Longueur:** 2494 nm. **Diamètre:** 82 nm.	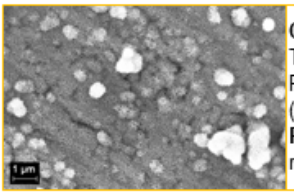	**Condition:** Sans déformation. **Traitement de surface:** Procédés chimiques (H3PO4 + NaOH) . **Phases cristallines:**Anatase, rutile et titanate de sodium.
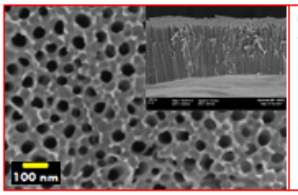	**Condition:** 1 GPa (HPT). **Traitement de surface:** Nanotubes de TiO2. **Phases cristallines :**α', α, β, anatase et rutile. **Longueur:** 2459 nm. **Diamètre:** 81 nm.	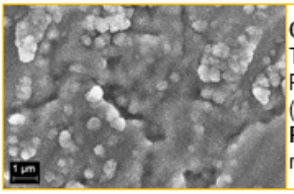	**Condition:** 1 GPa (HPT). **Traitement de surface:** Procédés chimiques (H3PO4 + NaOH) . **Phases cristallines:**Anatase, rutile et titanate de sodium.
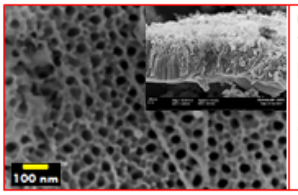	**Condition:** 4.5 GPa (HPT). **Traitement de surface:** Nanotubes de TiO2. **Phases cristallines :**α', α, β, anatase et rutile. **Longueur:** 1742 nm. **Diamètre:** 69 nm.	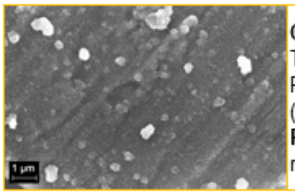	**Condition:** 4.5 GPa (HPT). **Traitement de surface:** Procédés chimiques (H3PO4 + NaOH) . **Phases cristallines:**Anatase, rutile et titanate de sodium.

Caractérisation électrochimique.

Alliage Ti35Nb7Zr5Ta.

Les mesures électrochimiques présentées ci-dessous sont donc destinées à évaluer l'impact du traitement de modification de surface et des déformations plastiques sévères sur les propriétés électrochimiques dans du SBF pour l'alliage Ti35Nb7Zr5Ta.

Échantillons polis.

Les figures 13((a) et (b)) présentent les courbes de polarisation anodiques et les diagrammes de Nyquist, respectivement, dans SBF à 37°C des échantillons de surface poli de l'alliage Ti35Nb7Zr5Ta non déformés et déformés par HPT.

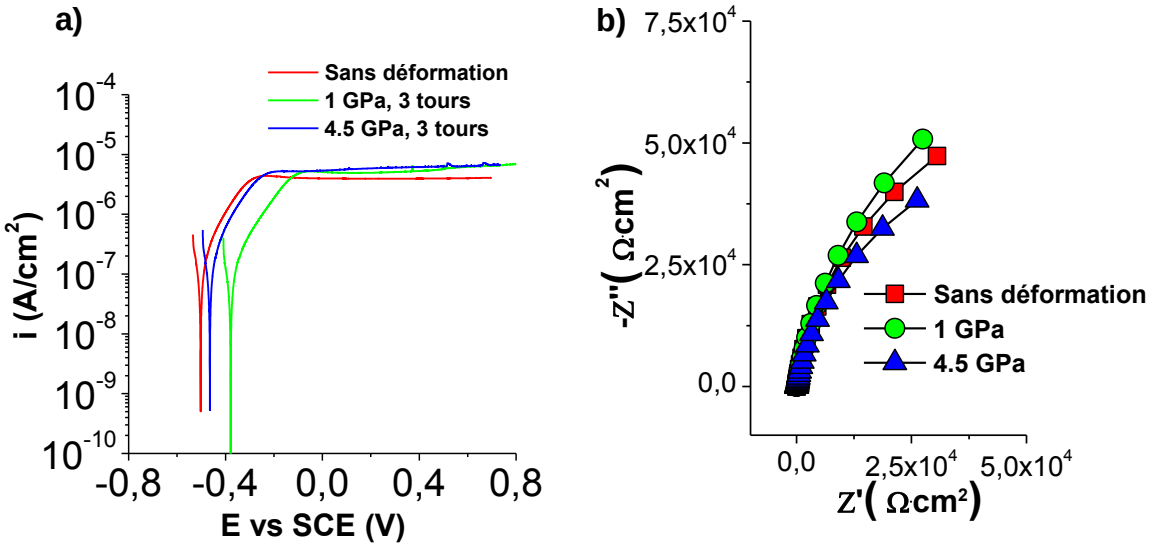

Figure 13 : Courbes de polarisation anodiques (a) et diagrammes de Nyquist (b) des échantillons polis de l'alliage Ti35Nb7Zr5Ta non déformés et déformés par HPT en milieu physiologique dans une solution de SBF à pH 7,4 à 37 ° C.

On considère que le courant mesuré dans la région anodique est principalement dû à la réaction d'oxydation des substrats en TiO_2, ce qui contribue à l'épaississement de la couche passive.

Une légère variation des courants de passivation est observé. Où initialement les échantillons sans déformation ont une valeur approximative de : 3,52 µA / cm^2. Pour les échantillons présentant une déformation plastique sévère, les courants de passivation sont les suivants : 5,18 µA / cm^2 pour l'échantillon présentant une déformation de 1 GPa et 6,03 µA / cm^2 pour l'échantillon présentant une déformation de 4,5 GPa. Ainsi, une déformation plastique sévère entraîne une légère augmentation du courant de passivation par rapport au substrat sans déformation.

La figure 13(b) montre les mesures d'impédance à l'aide du diagramme de Nyquist. L'observation des diagrammes de Nyquist révèle que la forme du spectre d'impédance de tous les substrats sont caractéristiques d'un système capacitif-résistif. Les spectres d'impédance expérimentaux sont analysés en ajustant le même circuit électrique équivalent qu'utiliser pour les échantillons de surface poli de l'alliage Ti13Nb13Zr (voir figure 3).

Les résultats de l'ajustement du modèle et de la capacité effective associée au CPE calculé avec l'équation de Brug sont donnés dans le tableau 7. En général, on observe des valeurs de résistance d'électrolyte d'environ 21 ($\Omega \cdot cm^2$) ainsi que des valeurs élevées de résistance de transfert de charge entre $1x10^5$ et $1.7x10^5$ ($\Omega \cdot cm^2$), indiquant une résistance élevée à la corrosion. Le calcul de la capacité effective associée à la couche passive poreuse ($C_{eff(a)}$) donne entre 12 et 17 $\mu F \cdot cm^{-2}$. Par contre, les résultats obtenus pour la couche interne dense ($C_{eff(dl)}$) sont compris entre 40 et 49 $\mu F \cdot cm^{-2}$, qui est une valeur typique d'une capacité de double couche.

De plus, l'épaisseur du film passif, δ (en nm), a été obtenue à partir de la capacité de la couche interne dense. Les valeurs d'épaisseur sont respectivement de 1,52, 1,90 et 1,70 nm pour l'alliage Ti35Nb7Zr5Ta, dans les conditions ND, HPT1GPa et HPT4.5GPa, respectivement. Ces résultats montrent que les films passifs en alliage Ti35Nb7Zr5Ta déformé ont une épaisseur supérieure.

Tableau 7 : Valeurs des paramètres d'ajustement des mesures d'impédance des échantillons polis de l'alliage Ti35Nb7Zr5Ta avec le modèle de la Figure 3.

Condition	Rs $\Omega \cdot cm^2$	Qa $\mu F \cdot s^{(\alpha 2-1)}$	α_a	Ra $\Omega \cdot cm^2$	$C_{eff(a)}$ $\mu F/cm^2$	Qb $\mu F \cdot s^{(\alpha 3-1)}$	α_b	Rb $\Omega \cdot cm^2$	$C_{eff(b)}$ $\mu F/cm^2$
Sans déformation	20	10	0.91	77	17	23	0.93	1.1E+05	49
1 GPa	21	10	0.89	129	15	22	0.91	1.7E+05	40
4.5 GPa	21	9	0.89	186	12	28	0.89	1.1E+05	44

Echantillons de surface à base de nanotubes de TiO_2

Les figures 14((a) et (b)) présentent les courbes de polarisation anodiques et les diagrammes de Nyquist, respectivement, dans SBF à 37°C des échantillons de surface à base de nanotubes de TiO_2 d'alliage Ti35Nb7Zr5Ta non déformés et déformés par HPT.

La figure 14(a) montre que la forme de la partie anodique des courbes de polarisation présente le comportement caractéristique d'un état passif. Pour tous les échantillons, un plateau de courant s'établit sur une large plage de potentiels, ce qui pourrait correspondre à une limitation du courant par le transport de matière à travers la couche d'oxyde.

Les courants de passivation diffèrent de ceux mesurés sur les substrats polis. Initialement pour un échantillon sans déformation, le courant de passivation de l'alliage Ti13Nb13Zr avec nanotubes de TiO_2 recuits a à peu près la valeur : 0,16 µA / cm^2. Pour les échantillons présentant une déformation plastique sévère, les courants de passivation sont les suivants : 0,19 µA / cm^2 pour l'échantillon présentant une déformation de 1 GPa et 0,52 µA / cm^2 pour l'échantillon présentant une déformation de 4,5 GPa. Par conséquent, il semble qu'une déformation plastique sévère entraîne une légère augmentation du courant de passivation par rapport au substrat sans déformation.

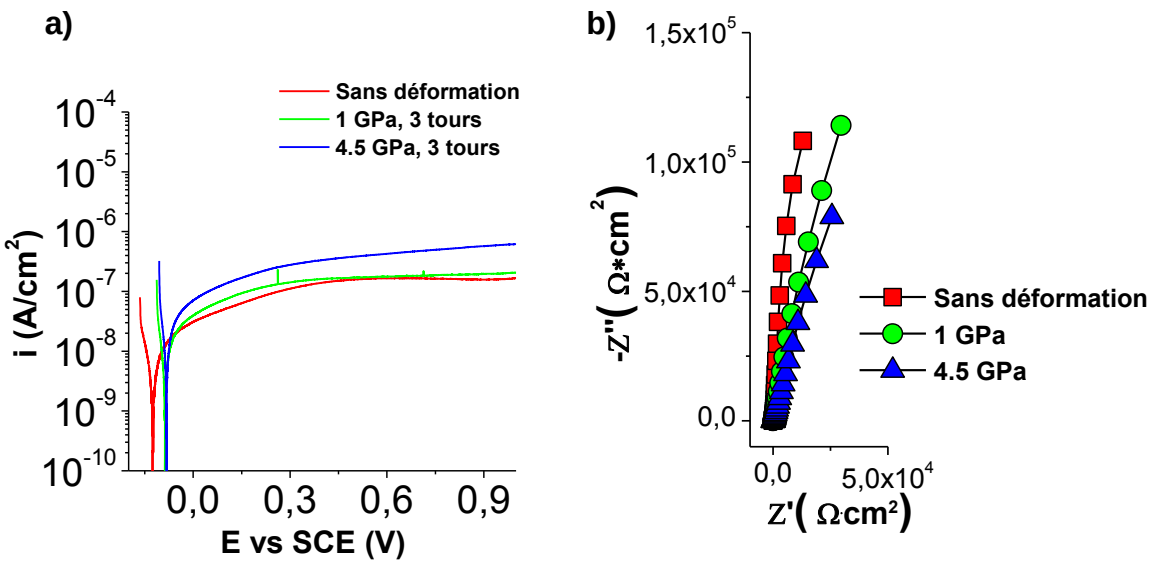

Figure 14 : Courbes de polarisation anodiques (a) et diagrammes de Nyquist (b) des échantillons de surface à base de nanotubes de TiO_2 de l'alliage Ti35Nb7Zr5Ta non déformés et déformés par HPT en milieu physiologique dans une solution de SBF à pH 7,4 à 37 ° C.

La figure 14(b) montre les mesures d'impédance. L'observation des diagrammes de Nyquist révèle que la forme du spectre d'impédance de tous les substrats est pseudo-capacitive (droite inclinée), c'est-à-dire que les échanges d'électrons et donc les réactions sont très limitées ou que la couche d'oxyde est très résistive.

Les spectres d'impédance expérimentaux sont analysés en utilisant le même modèle de ligne de transmission que celui utilisé pour l'alliage Ti13Nb13Zr avec des nanotubes de TiO_2. Les résultats de l'ajustement du modèle et de la capacité effective associée au CPE calculé avec l'équation de Hsu-Mansfeld sont donnés dans le tableau 8. Les résultats d'ajustement indiquent des valeurs de résistance de la solution proches de 21 ($\Omega \cdot cm^2$) et une élevée résistance associée à la limite supérieure des pores (R_A) comprise entre $2x10^6$ et $8x10^6$ ($\Omega \cdot cm^2$), indiquant une résistance à la corrosion supérieure à celle des substrats polis.

Le calcul de la capacité effective interfaciale associée à l'élément ξ (C_β) donne entre 33 et 66 $\mu F \cdot cm^{-2}$, qui correspondent aux valeurs correspondant à la

capacité de double couche. Par contre, les résultats obtenus pour la capacité effective C_n, associée au CPE de fond de pore sont compris entre 2 et 4 $\mu F \cdot cm^{-2}$, qui est une valeur typique d'une capacité de film passif.

En ce qui concerne l'épaisseur du film passif, elles ont été calculées à partir de la capacité effective. Les valeurs d'épaisseur étaient de 47,4, 34,3 et 22,3 nm pour l'alliage Ti35Nb7Zr5Ta dans les conditions ND, HPT1GPa et HPT4.5GPa, respectivement.

Enfin, il a été observé que les substrats avec des nanotubes de TiO_2 plus longs à l'état non déformé présentent une résistance à la corrosion supérieure.

Tableau 8 : Valeurs des paramètres d'ajustement des mesures d'impédance des échantillons de surface à base de nanotubes de TiO_2 d'alliage Ti35Nb7Zr5Ta avec le modèle de la Figure 5.

Condition	$\chi 1$	$\chi 2$	ξ				Z_A	Z_B			R_s
	R_1 (Ω)	R_2 (Ω)	R_3 (Ω)	Q_3 ($F^{\beta-1}$)	β	C_β µF/cm²	R_A (Ω)	Q_B (F^{n-1})	n	C_n µF/cm²	R_s (Ω)
Sans déformation	7	143	2.1E+15	2.0E-06	0.98	33	8.5E+06	1.2E-06	0.98	2	70.0
1 GPa	1	255	2.2E+15	1.9E-06	0.97	41	2.0E+06	1.0E-06	0.96	3	70.0
4.5 GPa	1	100	1.8E+15	3.1E-06	0.97	66	2.3E+06	1.6E-06	0.96	4	70.0

Échantillons soumis à un traitement acide à l'HCl puis à un traitement alcalin avec NaOH.

Les figures 15((a) et (b)) présentent les courbes de polarisation anodiques et les diagrammes de Nyquist, respectivement, dans SBF à 37°C des échantillons de surface soumis à un traitement acide à l'HCl puis à un traitement alcalin avec NaOH d'alliage Ti35Nb7Zr5Ta non déformés et déformés par HPT.

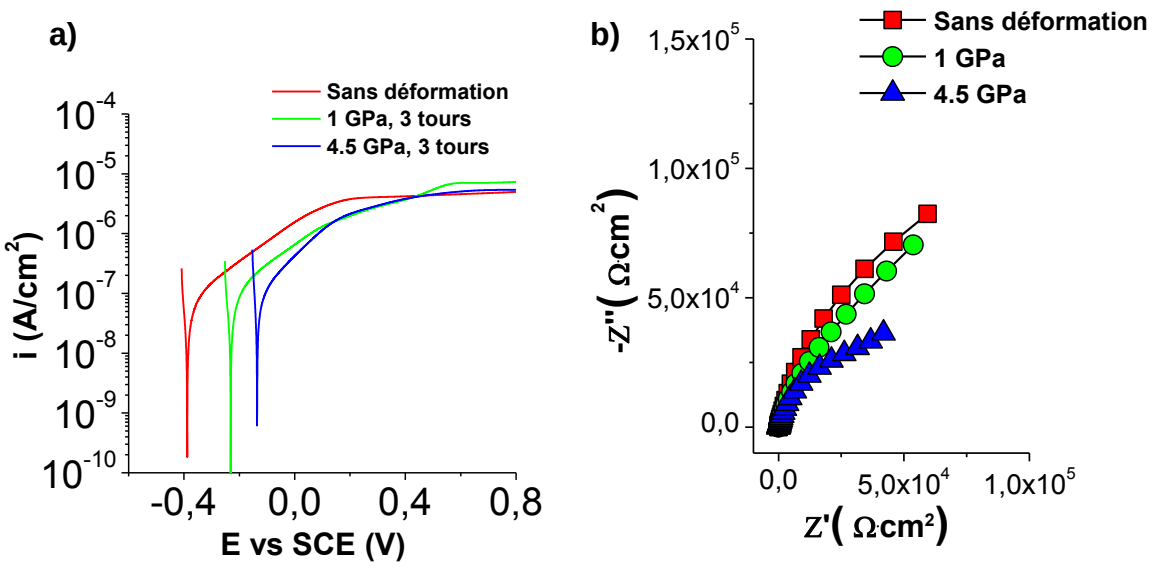

Figure 15 : Courbes de polarisation anodiques (a) et diagrammes de Nyquist (b) des échantillons de surface soumis à un traitement acide à l'HCl puis à un traitement alcalin avec NaOH d'alliage Ti35Nb7Zr5Ta non déformés et déformés par HPT en milieu physiologique dans une solution de SBF à pH 7,4 à 37 ° C.

La forme de la partie anodique des courbes de polarisation représentées à la figure 15(a), elle montre que le comportement des échantillons dans un environnement physiologique est caractéristique d'un état passif.

Une variation des courants de passivation est observée : initialement les échantillons sans déformation ont une valeur approximative de 4,58 µA / cm^2, pour les échantillons présentant une déformation plastique sévère, les courants de passivation sont les suivants : 7,20 µA / cm^2 pour l'échantillon présentant une déformation de 1 GPa et 3,40 µA / cm^2 et 5,21 µA / cm^2 pour l'échantillon présentant une déformation de 4,5 GPa. Ainsi, une déformation plastique sévère entraîne une légère augmentation du courant de passivation par rapport au substrat sans déformation.

La figure 15(b) montre les mesures d'impédance à l'aide du diagramme de Nyquist. L'observation des diagrammes de Nyquist révèle que la forme du spectre d'impédance de tous les substrats sont caractéristiques d'un système capacitif-

résistif. Les spectres d'impédance expérimentaux sont analysés en ajustant le même circuit électrique équivalent qu'utiliser pour les 'alliages Ti13Nb13Zr soumis à un traitement acide à l'HCl puis à un traitement alcalin avec NaOH (voir figure 7).

Les résultats de l'ajustement du modèle et de la capacité effective associée au CPE calculé avec l'équation de Brug sont donnés dans le tableau 9.

Tableau 9 : Valeurs des paramètres d'ajustement des mesures d'impédance d'échantillons de surface soumis à un traitement acide à l'HCl puis à un traitement alcalin avec NaOH d'alliage Ti35Nb7Zr5Ta avec le modèle de la Figure 7.

	Condition		
Elément	**Sans déformation**	**1 GPa**	**4.5 GPa**
Rs ($\Omega \cdot cm^2$)	21	20	20
Qb ($\mu F \cdot s^{(\alpha b-1)}$)	42	40	40
α_b	0.72	0.72	0.72
Rb ($\Omega \cdot cm^2$)	10	9	3
$C_{eff(b)}$ ($\mu F/cm^2$)	1.8	1.6	1.1
Qa ($\mu F \cdot s^{(\alpha a-1)}$)	19	33	47
α_a	0.70	0.71	0.80
Ra ($\Omega \cdot cm^2$)	1	1	24
$C_{eff(a)}$ ($\mu F/cm^2$)	0.2	0.5	7.3
Qdl ($\mu F \cdot s^{(\alpha dl-1)}$)	32	17	12
α_{dl}	0.93	0.93	0.98
Rct ($\Omega \cdot cm^2$)	3.3E+05	2.7E+05	8.4E+04
$C_{eff(dl)}$ ($\mu F/cm^2$)	18	10	10

L'ajustement permet d'obtenir des valeurs de résistance de solution comprises entre 20 et 21 ($\Omega \cdot cm^2$) ainsi que des valeurs élevées de résistance de transfert de charge (R_{ct}) comprises entre $8,4x10^4$ et $3x10^5$ ($\Omega \cdot cm^2$).

En ce qui concerne les capacités, les valeurs pour la double couche ($Ceff_{(dl)}$) étaient comprises entre 10 et 18 $\mu F \cdot cm^{-2}$. Les valeurs de capacité pour la couche externe poreuse ($Ceff_{(b)}$) et la couche poreuse intermédiaire ($Ceff_{(a)}$)

étaient inférieures à Ceff ($_{dl}$). De plus, l'épaisseur du film passif, δ (en nm), a été obtenue à partir de la capacité de la couche interne dense. Les valeurs d'épaisseur sont respectivement de 4,07, 7,87 et 7,43 nm pour l'alliage Ti35Nb7Zr5Ta, dans les conditions ND, HPT1GPa et HPT4.5GPa, respectivement. Ces résultats montrent que le traitement chimique et la déformation contribuent à augmenter l'épaisseur du film passif.

Échantillons soumis à un traitement acide à l'H_3PO_4 puis à un traitement alcalin avec NaOH.

Les figures 16((a) et (b)) présentent les courbes de polarisation anodiques et les diagrammes de Nyquist, respectivement, dans SBF à 37°C des échantillons de surface soumis à un traitement acide à l'H_3PO_4 puis à un traitement alcalin avec NaOH d'alliage Ti35Nb7Zr5Ta non déformés et déformés par HPT.

Le même comportement observé pour les autres courbes de polarisation est observé, où la partie anodique des courbes de polarisation montre un comportement passif des échantillons en SBF.

Une variation des courants de passivation est observée : initialement les échantillons sans déformation ont une valeur approximative de 8,24 µA / cm^2 et pour les échantillons présentant une déformation plastique sévère, les courants de passivation sont les suivants : 10,80 µA / cm^2 pour l'échantillon présentant une déformation de 1 GPa et 10,80 µA / cm^2 pour l'échantillon présentant une déformation de 4,5 GPa. Ainsi, une déformation plastique sévère entraîne une légère augmentation du courant de passivation par rapport au substrat sans déformation.

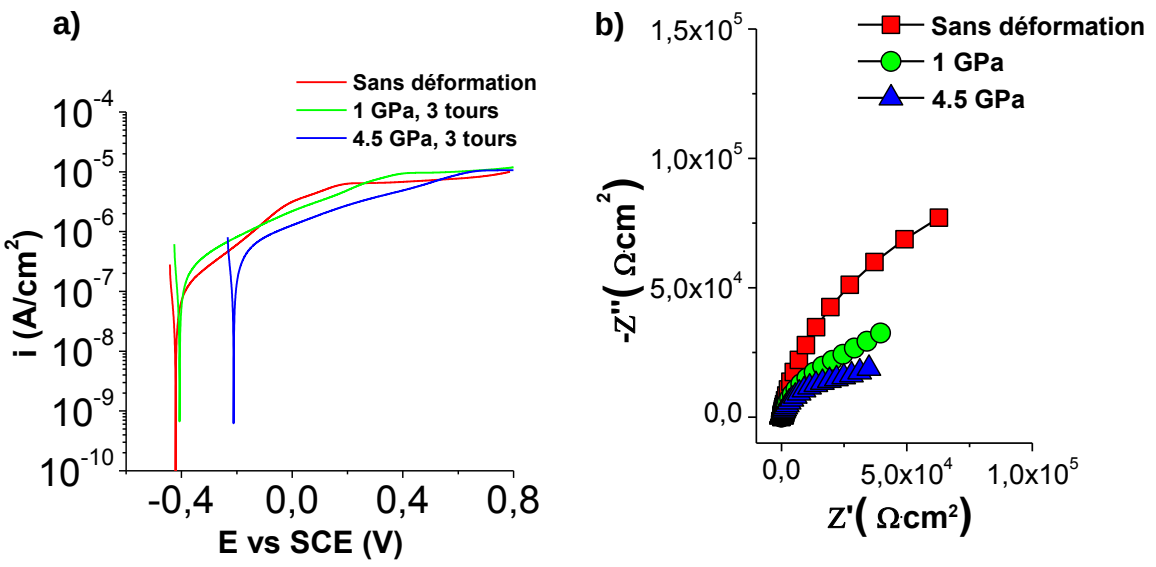

Figure 16 : Courbes de polarisation anodiques (a) et diagrammes de Nyquist (b) des échantillons de surface soumis à un traitement acide à l'H_3PO_4 puis à un traitement alcalin avec NaOH d'alliage Ti35Nb7Zr5Ta non déformés et déformés par HPT en milieu physiologique dans une solution de SBF à pH 7,4 à 37 ° C.

L'observation des diagrammes de Nyquist (figure 16 b) révèle que la forme du spectre d'impédance de tous les substrats est caractéristique d'un système capacitif-résistif. Les spectres d'impédance expérimentaux sont analysés avec le même circuit électrique équivalent que celui utilisé pour les échantillons de surface soumis à un traitement acide à l'HCl puis à un traitement alcalin avec NaOH pour les alliages Ti13Nb13Zr (voir figure 7).

Les résultats de l'ajustement du modèle et de la capacité effective associée au CPE calculé avec l'équation de Brug sont donnés dans le tableau 10. L'ajustement permet d'obtenir des valeurs de résistance de solution de 20 ($\Omega \cdot cm^2$) ainsi que des valeurs élevées de résistance de transfert de charge (R_{ct}) comprises entre $2x10^4$ et $2x10^5$ ($\Omega \cdot cm^2$).

En ce qui concerne les capacités, les valeurs pour la double couche ($Ceff_{(dl)}$) étaient comprises entre 10 et 19 $\mu F \cdot cm^{-2}$. Les valeurs de capacité pour la couche externe poreuse ($Ceff_{(b)}$) et la couche poreuse intermédiaire ($Ceff_{(a)}$) étaient inférieures à $Ceff_{(dl)}$. De plus, l'épaisseur du film passif, δ (en nm), a été

obtenue à partir de la capacité de la couche interne dense. Les valeurs d'épaisseur sont respectivement de 3,98, 7,62 et 7,69 nm pour l'alliage Ti35Nb7Zr5Ta, dans les conditions ND, HPT1GPa et HPT4.5GPa, respectivement. Ces résultats montrent que le traitement chimique et la déformation contribuent à augmenter l'épaisseur du film passif.

Tableau 10 : Valeurs des paramètres d'ajustement des mesures d'impédance d'échantillons de surface soumis à un traitement acide à l'H_3PO_4 puis à un traitement alcalin avec NaOH d'alliage Ti13Nb13Zr avec le modèle de la Figure 7.

	Condition		
Elément	**Sans déformation**	**1 GPa**	**4.5 GPa**
Rs ($\Omega \cdot cm^2$)	20	20	20
Qb ($\mu F \cdot s^{(\alpha b-1)}$)	40	53	15
α_b	0.73	0.70	0.80
Rb ($\Omega \cdot cm^2$)	9	7	4
$C_{eff(b)}$ ($\mu F/cm^2$)	1.8	1.6	1.3
Qa ($\mu F \cdot s^{(\alpha a-1)}$)	6	6	37
α_a	0.72	0.78	0.84
Ra ($\Omega \cdot cm^2$)	3	1	10
$C_{eff(a)}$ ($\mu F/cm^2$)	0.1	4.3	7.5
Qdl ($\mu F \cdot s^{(\alpha dl-1)}$)	47	54	54
α_{dl}	0.88	0.80	0.80
Rct ($\Omega \cdot cm^2$)	2.2E+05	1.0E+05	2.5E+04
$C_{eff(dl)}$ ($\mu F/cm^2$)	19	10	10

Tests de bioactivité sur l'alliage Ti35Nb7Zr5Ta

Dans cette étude, les dépôts d'apatite ont été examinés après 1, 7 et 14 jours d'immersion dans la solution SBF pour des échantillons de l'alliage Ti35Nb7Zr5Ta avec différente modification de surface, ainsi que des niveaux de déformation par HPT différents.

Échantillons polis.

Les observations au microscope électronique à balayage (MEB) illustrées à la figure 17 indiquent que, même après 14 jours d'immersion dans la solution physiologique, aucune formation d'apatite n'est détectée à la surface des substrats nus.

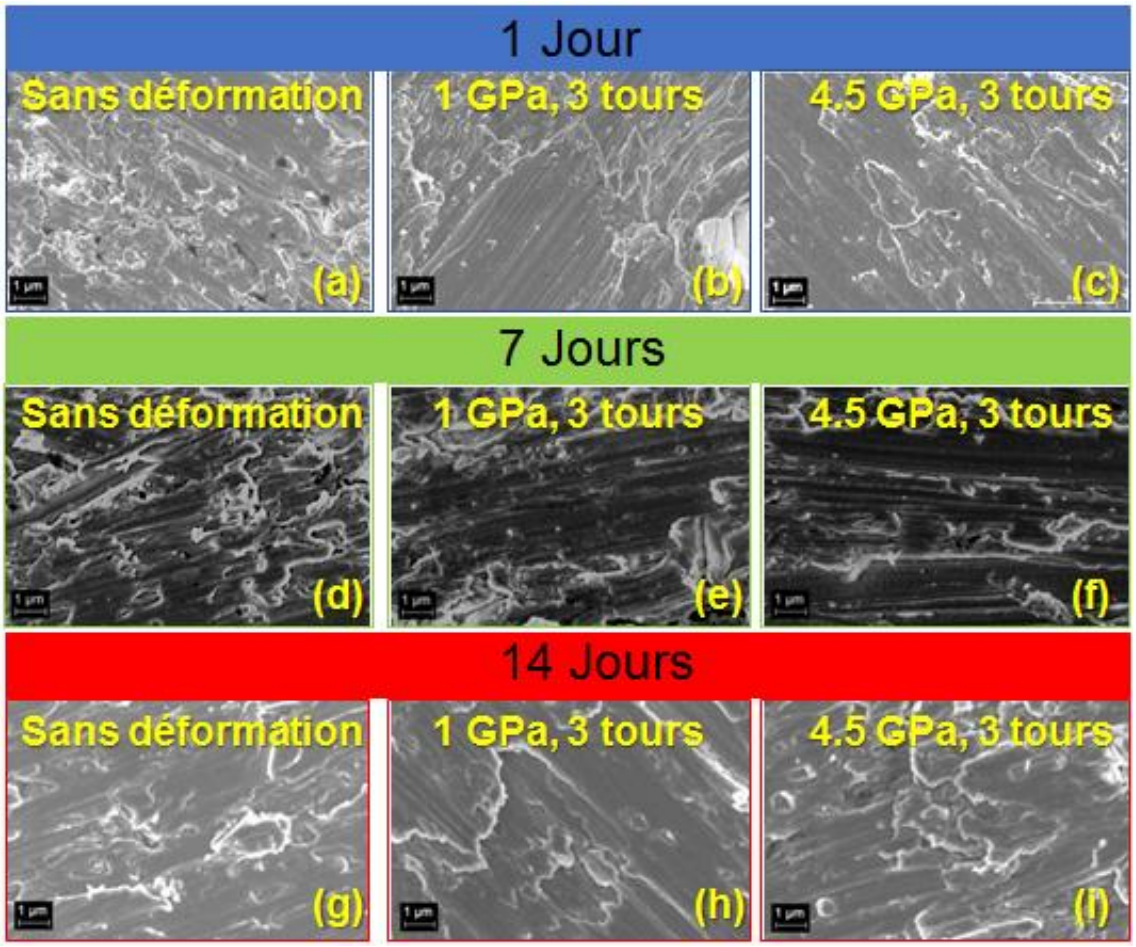

Figure 17 : Observations MEB-FEG des échantillons de surface poli d'alliage Ti35Nb7Zr5Ta non déformé et déformé par HPT suite aux tests de bioactivité pendant 1, 7 et 14 jours dans du SBF.

Échantillons de surface à base de nanotubes de TiO_2.

Les observations au microscope électronique à balayage (SEM) illustrées à la figure 18 indiquent que à partir du quatorzième jour d'immersion dans une solution de SBF, l'apatite est visible sur certains substrats de Ti35Nb7Zr5Ta non déformés et des échantillons déformés par HPT à l'état de 4,5 GPa avec des nanotubes de TiO_2 recuits. (Figures 18((g) et (i)).

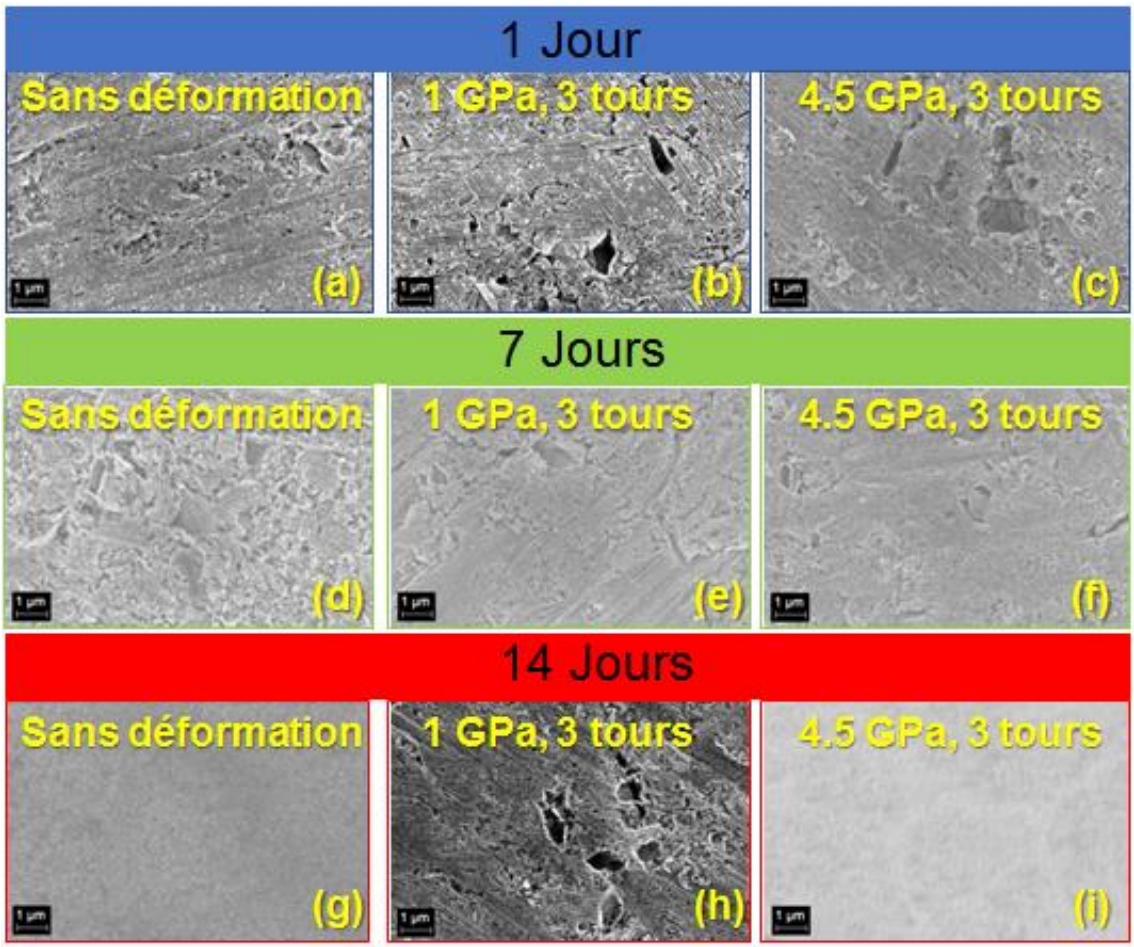

Figure 18 : Observations MEB-FEG des échantillons d'alliage Ti35Nb7Zr5Ta avec nanotubes de TiO_2 non déformé et déformé par HPT suite aux tests de bioactivité à 1, 7 et 14 jours dans du SBF.

Échantillons soumis à un traitement acide à l'HCl puis à un traitement alcalin avec NaOH.

Les observations au microscope électronique à balayage (MEB) illustrées à la figure 19 indiquent le même comportement que celui observé pour les échantillons avec des nanotubes de TiO_2. Cela signifie qu'à partir du quatorzième jour d'immersion dans une solution de SBF, l'apatite est visible dans certains substrats de Ti35Nb7Zr5Ta non déformés et des échantillons déformés par HPT 4,5 GPa.

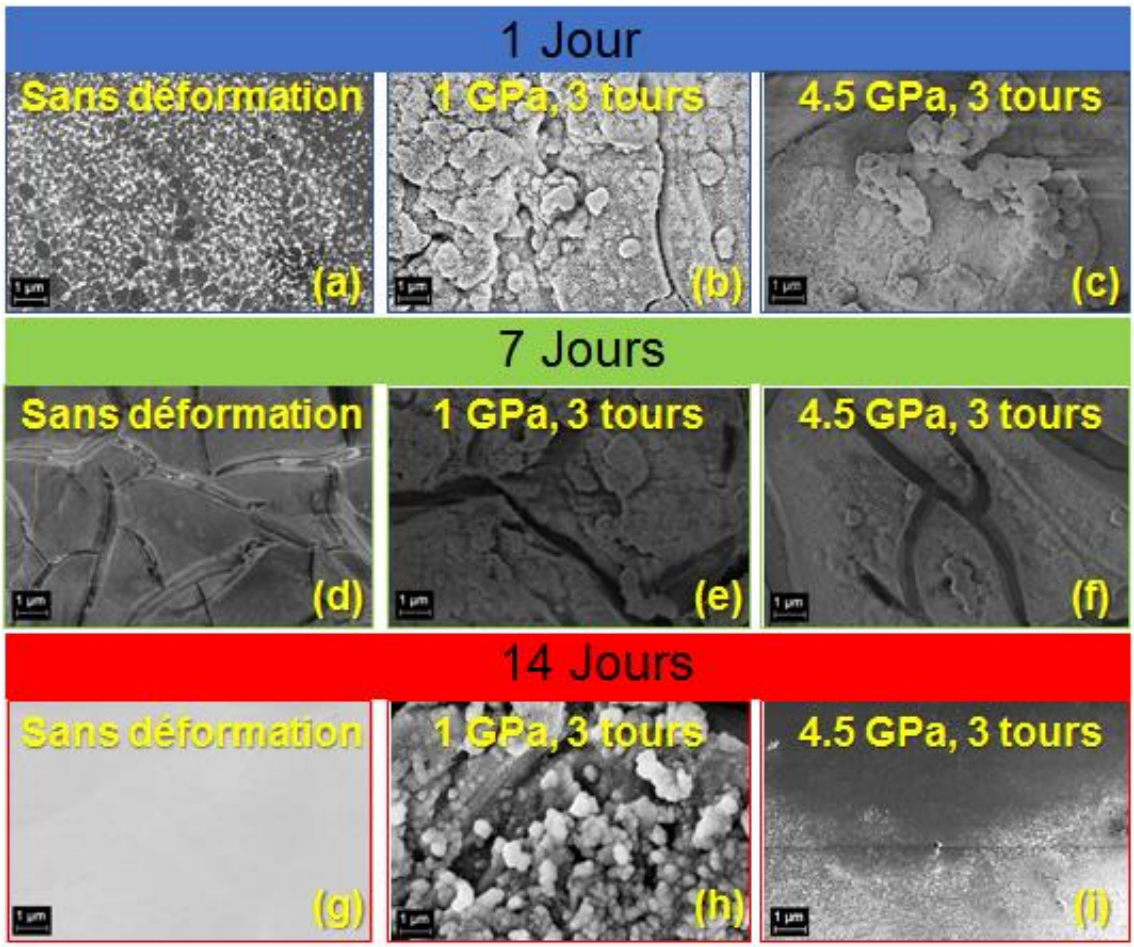

Figure 19 : Observations MEB-FEG des échantillons Ti35Nb7Zr5Ta soumis à un traitement acide à l'HCl puis à un traitement alcalin avec NaOH non déformé et déformé par HPT suite aux tests de bioactivité à 1, 7 et 14 jours dans du SBF.

Échantillons soumis à un traitement acide à l'H_3PO_4 puis à un traitement alcalin avec NaOH.

Les observations au microscope électronique à balayage (MEB) illustrées à la figure 20 indiquent que, même après 14 jours d'immersion dans la solution physiologique, aucune formation d'apatite n'est détectée à la surface des substrats.

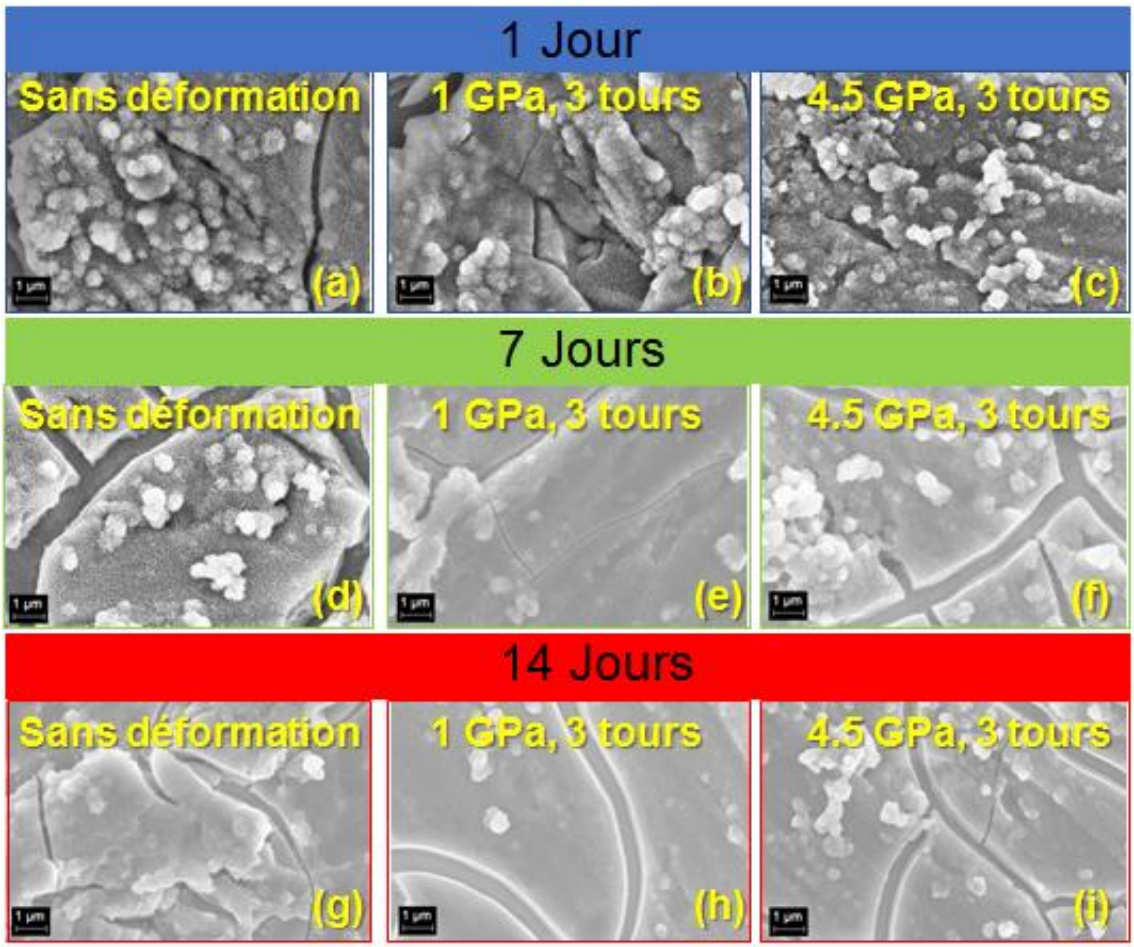

Figure 20 : Observations MEB-FEG des échantillons Ti35Nb7Zr5Ta soumis à un traitement acide à l'H_3PO_4 puis à un traitement alcalin avec NaOH d'alliage non déformé et déformé par HPT suite aux tests de bioactivité à 1, 7 et 14 jours dans du SBF.

Récapitulatif

Les essais de corrosion et test de bioactivité ont été réalisés pour les alliages de Ti13Nb13Zr et Ti35Nb7Zr5Ta avec des surfaces modifiées et déformées par HPT. La caractérisation électrochimique a été réalisée par courbes de polarisation et impédance électrochimique. En ce qui concerne le courant de passivation (I_{pass}) obtenu à partir des courbes de polarisation, il a été observé que les échantillons à surface polie (nue) et les échantillons traités chimiquement (HCl, H_3PO_4 + NaOH) ont des valeurs de Ipass du même ordre de grandeur (10^{-6} A·cm^{-2}).

D'autre part, les échantillons non déformés et les échantillons déformés par HPT ne montrent pas une grande différence entre les valeurs du courant de passivation (à l'exception des échantillons anodisés). Il a été observé que la présence de TiO_2 présente la plus grande valeur de résistance de la couche poreuse externe, ce qui suggère une résistance accrue à la corrosion. Ceci est plus clair pour Ti13Nb13Zr, où les valeurs de résistance présentées sont de l'ordre de $3x10^7$ ($\Omega \cdot cm^2$).

En outre, les traitements chimiques ont tendance à diminuer la valeur de la résistance de la couche d'oxyde protectrice, lorsque la pression de déformation augmente. Cette réduction de la résistance à la corrosion a été attribuée à la microstructure hors équilibre formée par la déformation HPT. De ce fait,le film d'oxyde de la couche la plus externe est plus sensible à la dissolution de la couche interne, ce qui indique une structure plus défectueuse de la couche externe.

Les micrographies obtenues par MEB-FEG ont montré que, pour Ti13Nb13Zr et Ti35Nb7Zr5Ta immergé dans une solution de SBF pendant 14 jours, aucun des échantillons avec des surfaces polies ne présente de formation d'apatite sur la surface, c'est-à-dire qu'ils ne sont pas bioactifs. Cela confirme que la couche de TiO_2 initiale inerte créée sur la surface des substrats polis ne suffit pas pour favoriser la formation de tissu entre l'os et l'implant spontanément.

Le comportement observé pour les substrats polies a également été observé pour les échantillons de surface soumis à un traitement acide à l'H_3PO_4 puis à un traitement alcalin avec NaOH pour l'alliage Ti35Nb7Zr5Ta, ce qui indique que, malgré la présence de phosphate sur la surface, ledit matériau n'acquiert aucune activité biologique. En revanche, au cours du même traitement de surface, les surfaces des échantillons d'alliage Ti13Nb13Zr ont montré une bioactivité pendant des périodes allant de un à sept jours dans des conditions non déformées et déformées.

Les surfaces avec des nanotubes de TiO_2 sur l'alliage de Ti13Nb13Zr dans un état non déformé commence à produire une couche d'apatite entre un et sept jours, tandis que les échantillons déformés ont formé des dépôts de l'apatite à partir des 24 premières heures. Cependant, le même traitement de surface ne s'est pas révélé aussi efficace pour les échantillons de Ti35Nb7Zr5Ta. Dans ce cas, les échantillons (déformés ou non) ont seulement commencé à présenter une couche d'apatite à partir dès le quatorze jours.

Enfin, cette étude a montré que les traitements de modification de surface sont bénéfiques pour promouvoir l'ostéointégration et également que la déformation plastique sévère favorise la bioactivité.

Références

[1] G. Manivasagam, D. Dhinasekaran, A. Rajamanickam, Biomedical implants: Corrosion and its Prevention-A Review, Recent Patents Corros. Sci. 2 (2010) 40–54. doi:10.2174/1877610801002010040.

[2] M. Niinomi, Mechanical properties of biomedical titanium alloys, Mater. Sci. Eng. A. 243 (1998) 231–236. doi:10.1016/S0921-5093(97)00806-X.

[3] M. Niinomi, D. Kuroda, K. Fukunaga, M. Morinaga, Y. Kato, T. Yashiro, A. Suzuki, Corrosion wear fracture of new β type biomedical titanium alloys,

Mater. Sci. Eng. A. 263 (1999) 193–199. doi:10.1016/S0921-5093(98)01167-8.

[4] A. Najdahmadi, A. Zarei-Hanzaki, E. Farghadani, Mechanical properties enhancement in Ti–29Nb–13Ta–4.6 Zr alloy via heat treatment with no detrimental effect on its biocompatibility, Mater. Des. 54 (2014) 786–791. doi:10.1016/j.matdes.2013.09.007.

[5] K.K. Wang, L.J. Gustavson, J.H. Dumbleton, Microstructure and properties of a new beta titanium alloy, Ti-12Mo-6Zr-2Fe, developed for surgical implants, in: Med. Appl. Titan. Its Alloy. Mater. Biol. Issues, ASTM International, 1996.

[6] P.L. Ferrandini, F.F. Cardoso, S.A. Souza, C.R. Afonso, R. Caram, Aging response of the Ti–35Nb–7Zr–5Ta and Ti–35Nb–7Ta alloys, J. Alloys Compd. 433 (2007) 207–210. doi:10.1016/j.jallcom.2006.06.094.

[7] H.J. Rack, J.I. Qazi, Titanium alloys for biomedical applications, 26 (2006) 1269–1277. doi:10.1016/j.msec.2005.08.032.

[8] S. Zherebtsov, G. Salishchev, R. Galeyev, K. Maekawa, Mechanical properties of Ti–6Al–4V titanium alloy with submicrocrystalline structure produced by severe plastic deformation, Mater. Trans. 46 (2005) 2020–2025. doi:10.2320/matertrans.46.2020.

[9] a. Azushima, R. Kopp, a. Korhonen, D.Y. Yang, F. Micari, G.D. Lahoti, P. Groche, J. Yanagimoto, N. Tsuji, a. Rosochowski, a. Yanagida, Severe plastic deformation (SPD) processes for metals, CIRP Ann. - Manuf. Technol. 57 (2008) 716–735. doi:10.1016/j.cirp.2008.09.005.

[10] Y.T. Zhu, T.G. Langdon, The fundamentals of nanostructured materials processed by severe plastic deformation, Jom. 56 (2004) 58–63. doi:10.1007/s11837-004-0294-0.

[11] D.A.G. Pérez, J. Junior, A. Moreira, C.S. Kiminami, C. Bolfarini, W.J. Botta, Ultrafine-Grained Ti-13Nb-13Zr Alloy Produced by Severe Plastic Deformation, Mater. Res. 20 (2017) 404–410. doi:10.1590/1980-5373-mr-2017-0037.

[12] K. Sharman, P. Bazarnik, T. Brynk, A. Gunay Bulutsuz, M. Lewandowska, Y. Huang, T.G. Langdon, Enhancement in mechanical properties of a β-titanium alloy by high-pressure torsion, J. Mater. Res. Technol. 4 (2015) 79–83. doi:10.1016/j.jmrt.2014.10.010.

[13] M. Kulkarni, A. Mazare, E. Gongadze, Š. Perutkova, V. Kralj-Iglič, I. Milošev, P. Schmuki, A. Iglič, M. Mozetič, Titanium nanostructures for biomedical applications, Nanotechnology. 26 (2015) 62002. doi:10.1088/0957-4484/26/6/062002.

[14] R.Z. Valiev, I.P. Semenova, V. V. Latysh, H. Rack, T.C. Lowe, J. Petruzelka, L. Dluhos, D. Hrusak, J. Sochova, Nanostructured titanium for biomedical applications, Adv. Eng. Mater. 10 (2008) 15–17. doi:10.1002/adem.200800026.

[15] H. Miyamoto, Corrosion of Ultrafine Grained Materials by Severe Plastic Deformation, an Overview, Mater. Trans. 57 (2016) 559–572. doi:10.2320/matertrans.M2015452.

[16] J. Lu, Y. Zhang, W. Huo, W. Zhang, Y. Zhao, Y. Zhang, Electrochemical corrosion characteristics and biocompatibility of nanostructured titanium for implants, Appl. Surf. Sci. 434 (2018) 63–72. doi:10.1016/j.apsusc.2017.10.168.

[17] M. Takeuchi, Y. Abe, Y. Yoshida, Y. Nakayama, M. Okazaki, Y. Akagawa, Acid pretreatment of titanium implants, 24 (2003) 1821–1827. doi:10.1016/S0142-9612(02)00576-8.

[18] W.F. Oliveira, I.R.S. Arruda, G.M.M. Silva, G. Machado, L.C.B.B. Coelho, M.T.S. Correia, Functionalization of titanium dioxide nanotubes with biomolecules for biomedical applications, Mater. Sci. Eng. C. 81 (2017) 597–606. doi:10.1016/j.msec.2017.08.017.

[19] J.E.G. Hulshoff, K. Van Dijk, J.E. De Ruijter, F.J.R. Rietveld, L.A. Ginsel, J.A. Jansen, Interfacial phenomena: An in vitro study of the effect of calcium phosphate (Ca-P) ceramic on bone formation, J. Biomed. Mater. Res. 40 (1998) 464–474. doi:10.1002/(SICI)1097-4636(19980605)40:3<464::AID-JBM18>3.0.CO;2-J.

[20] S. Nishiguchi, T. Nakamura, M. Kobayashi, H.-M. Kim, F. Miyaji, T. Kokubo, The effect of heat treatment on bone-bonding ability of alkali-treated titanium, Biomaterials. 20 (1999) 491–500. doi:10.1016/S0142-9612(98)90203-4.

[21] M.J. Filiaggi, N.A. Coombs, R.M. Pilliar, Characterization of the interface in the plasma-sprayed HA coating/Ti-6Al-4V implant system, J. Biomed. Mater. Res. 25 (1991) 1211–1229. doi:10.1002/jbm.820251004.

[22] K.S. Brammer, C.J. Frandsen, S. Jin, TiO_2 nanotubes for bone regeneration, Trends Biotechnol. 30 (2012) 315–322. doi:10.1016/j.tibtech.2012.02.005.

[23] A.P. Zhilyaev, T.G. Langdon, Using high-pressure torsion for metal processing: Fundamentals and applications, Prog. Mater. Sci. 53 (2008) 893–979. doi:10.1016/j.pmatsci.2008.03.002.

[24] X. Liu, P.K. Chu, C. Ding, Surface modification of titanium , titanium alloys , and related materials for biomedical applications, 47 (2005) 49–121. doi:10.1016/j.mser.2004.11.001.

[25] H. Tsuchiya, J.M. Macak, L. Müller, J. Kunze, F. Müller, P. Greil, S. Virtanen, P. Schmuki, Hydroxyapatite growth on anodic TiO_2 nanotubes, J. Biomed. Mater. Res. Part A. 77A (2006) 534–541. doi:10.1002/jbm.a.30677.

[26] V.P. Parkhutik, V.I. Shershulsky, Theoretical modelling of porous oxide growth on aluminium, J. Phys. D. Appl. Phys. 25 (1992) 1258. doi:10.1088/0022-3727/25/8/017.

[27] G.K. Grimes, Craig A., Mor, TiO_2 nanotube arrays: synthesis, properties, and applications, 2009. doi:10.1007/978-1-4419-0068-5.

[28] Y. Bai, I.S. Park, H.H. Park, M.H. Lee, T.S. Bae, W. Duncan, M. Swain, The effect of annealing temperatures on surface properties, hydroxyapatite growth and cell behaviors of TiO_2 nanotubes, Surf. Interface Anal. 43 (2011) 998–1005. doi:10.1002/sia.3683.

[29] P. Roy, S. Berger, P. Schmuki, TiO_2 nanotubes: synthesis and applications, Angew. Chemie. 50 (2011) 2904–2939. doi:10.1002/anie.201001374.

[30] F. Hilario, Synthèse et caractérisations de nanotubes de TiO_2 pour applications biomédicales: propriétés électrochimiques et bioactivité, (2017).

[31] L. Le Guéhennec, A. Soueidan, P. Layrolle, Y. Amouriq, Surface treatments of titanium dental implants for rapid osseointegration, Dent. Mater. 23 (2007) 844–854. doi:10.1016/j.dental.2006.06.02.

[32] H. Kim, F. Miyaji, T. Kokubo, T. Nakamura, Preparation of bioactive Ti and its alloys via simple chemical surface treatment, J. Biomed. Mater. Res. An Off. J. Soc. Biomater. Japanese Soc. Biomater. 32 (1996) 409–417. doi:10.1002/(sici)1097-4636(199611)32:3<409::aid-jbm14>3.0.co;2-.

[33] T. Kokubo, H. Takadama, How useful is SBF in predicting in vivo bone bioactivity?, Biomaterials. 27 (2006) 2907–2915. doi:10.1016/j.biomaterials.2006.01.017.

[34] B. Torres, A. Seyeux, S. Zanna, B. Tribollet, P. Marcus, I. Frateur, Influence of BSA adsorption on the oxide layers developed on 70Cu-30Ni alloy in static artificial seawater, Matériaux Tech. 101 (2013) 106.

[35] F. Hilario, V. Roche, A. Jorge Junior, R. Nogueira, Application of the transmission line model for porous electrodes to analyse the impedance response of TiO_2 nanotubes in physiological environment, 2017. doi:10.1016/j.electacta.2017.09.045.

[36] S.A.A. Yahia, L. Hamadou, A. Kadri, N. Benbrahim, E.M.M. Sutter, Effect of anodizing potential on the formation and EIS characteristics of TiO2 nanotube arrays, J. Electrochem. Soc. 159 (2012) K83–K92. doi:10.1149/2.077204jes.

[37] P. Pu, H. Cachet, E.M.M. Sutter, Electrochemical impedance spectroscopy to study photo-induced effects on self-organized TiO_2 nanotube arrays, Electrochim. Acta. 55 (2010) 5938–5946.

[38] B. Hirschorn, M.E. Orazem, B. Tribollet, V. Vivier, I. Frateur, M. Musiani, Determination of effective capacitance and film thickness from constant-phase-element parameters, Electrochim. Acta. 55 (2010) 6218–6227. doi:10.1016/j.electacta.2009.10.065.

INFLUÊNCIA DOS TRATAMENTOS DE SUPERFÍCIE NAS PROPRIEDADES DE RESISTÊNCIA À CORROSÃO DE LIGAS DE TITÂNIO DE GRÃO ULTRAFINO PARA APLICAÇÕES EM IMPLANTES

RESUMO DETALHADO EM PORTUGUÊS

INTRODUÇÃO

Os dispositivos biomédicos atualmente em uso (próteses, implantes) têm um desempenho satisfatório em muitos casos. No entanto, às vezes, o corpo reage à inserção do dispositivo e pode levar à sua rápida substituição. Neste contexto, titânio (Ti) e as suas ligas são atualmente um dos materiais mais procurados para implantes ortopédicos e dentais devido à sua excelente biocompatibilidade e resistência à corrosão [1].

No entanto, as propriedades mecânicas do titânio e suas ligas devem estar próximas do tecido ósseo como pré-requisito para o sucesso dos implantes ortopédicos. Nesse contexto, as ligas (α+β) e β têm atraído considerável interesse, pois apresentam baixo módulo de elasticidade, que resulta em uma melhor interação entre o implante e o osso [2]. Além disso, as ligas (α+β) e β podem ser obtidas a partir de elementos metálicos considerados biocompatíveis como Nb, Ta, Zr, Mo e Sn [3].

O interesse recente na redução do módulo de elasticidade resultou no desenvolvimento de uma nova geração de ligas de titânio para aplicações ortopédicas, incluindo Ti29Nb13Ta4.6Zr [4], o Ti12Mo6Zr2Fe (TMZF) [5], Ti35Nb7Zr5Ta (TNZT) [6] e Ti13Nb13Zr [7].

Além disso, o módulo de elasticidade, outras propriedades mecânicas das ligas de titânio, tal como a dureza, resistência e ductilidade pode ser melhorada significativamente através da utilização de deformação plástica severa (SPD-Severe Plastic Deformation, em inglês) [8]. Devido à microestrutura de grãos ultrafinos obtida por este processo [9]. As técnicas de SPD mais comumente

aplicadas são extrusão de canal angular (ECAP-Equal Channel Angular Pressing) e torção sob alta pressão (HPT-High Pressure Torsion) [10].

Nosso grupo de pesquisa estudou o acima mencionado no artigo intitulado "Ultrafine-Grained Ti13Nb13Zr Alloy produced by Severe Plastic Deformation" [11]. Neste trabalho, foi observado o efeito da técnica de HPT no aumento da microdureza da liga Ti13Nb13Zr. O valor de microdureza aumentou significativamente de 220 HV para 402 HV para a pressão aplicada de 4,5 GPa. Além disso, o refinamento do tamanho de grão (200 μm no estado inicial a 130 nm) também foi observado.

Por outro lado, os trabalhos anteriores sobre ligas de titânio e titânio processadas por SPD têm se concentrado em estudar a relação entre a microestrutura obtida e as propriedades mecânicas [12–14]. No entanto, poucos estudos relacionam a microestrutura obtida pelo SPD e a resistência à corrosão das ligas de titânio [15].

O comportamento corrosivo das ligas de titânio depende principalmente das propriedades do filme passivo (composição e espessura) e da microestrutura do substrato (tamanho do grão e densidade de discordâncias) [16]. A baixa taxa de dissolução e a inércia química dos produtos de dissolução da camada passiva de óxido de titânio (TiO_2) permitem que o osso se desenvolva e se osseointegre com a superfície da liga de titânio [17].

Desta forma, a resposta biológica de um implante depende das propriedades físico-químicas da superfície [18]. Recentemente, métodos de modificação de superfície de implantes de titânio têm sido estudados, tais como revestimentos de fosfato de cálcio ($Ca_3(PO_4)_2$) [19], tratamentos alcalinos e térmicos [20], revestimentos por plasma [21] e nanotubos de TiO_2 [22]. Como forma de melhorar a integração dos implantes.

Portanto, com o objetivo de avançar no entendimento das propriedades mecânicas e de corrosão de materiais à base de titânio para aplicações

biomédicas neste trabalho, duas ligas de titânio, a liga (α'+ β) Ti13Nb13Zr e a liga (β) Ti35Nb7Zr5Ta deformadas pelo método HPT serão estudadas sob condições já definidas em um trabalho anterior [11]. Além disso, dois tratamentos diferentes de modificação de superfície são propostos, como o crescimento de nanotubos de titânio (TiO_2) e tratamentos químicos em amostras deformadas por HPT e em amostras sem deformação. Finalmente, os efeitos de deformação plástica severa e tratamentos de modificação de superfície foram avaliados por testes de corrosão e bioatividade.

Deformação plástica severa

Uma estratégia para melhorar as propriedades mecânicas do titânio e suas ligas é a refinar a granulação através da deformação plástica severa (SPD-Severe Plastic Deformation, em inglês). As técnicas mais desenvolvidas de SPD são extrusão em canal angular (ECAP-Equal Channel Angular Pressing), torção sob alta pressão (HPT-High Pressure Torsion) e a laminação acumulativa (ARB - Acumulative Roll-bonding) [9,10].

Dos métodos de deformação plástica severa mencionados acima, o processamento por HPT mostrou um maior refinamento da microestrutura [9]. Os princípios do processamento moderno de HPT são descritos esquematicamente na Figura 1 [23].

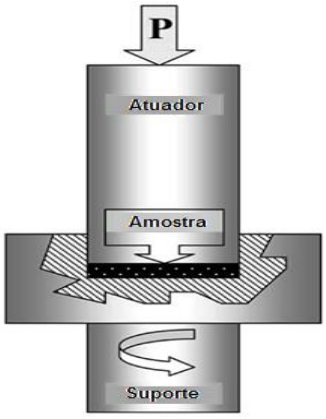

Figura 1: Ilustração esquemática do processamento HPT. Adaptado de Zhilyaev et al., (2008) [23].

O corpo de prova em formato de disco é posicionado entre dois atuadores, onde são submetidos à pressão aplicada, P, de alguns GPa em temperatura ambiente ou a quente. Enquanto a pressão é aplicada, uma deformação através de rotação é realizada no corpo de prova. Forças de atrito na superfície deformam o disco por cisalhamento, assim o processo ocorre sob pressão quase hidrostática [23].

Neste projeto, as ligas de Ti13Nb13Zr e Ti35Nb7Zr5Ta em forma de discos de 10 mm de diâmetro e 1 mm de espessura foram processadas por HPT. O processamento foi realizado à temperatura ambiente. Os discos foram processados sob pressões de 1,0 e 4,5 GPa e três voltas foram aplicadas usando uma velocidade de rotação de 3 rpm.

Tratamentos de modificação de superfície.

Titânio e suas ligas são amplamente utilizados em dispositivos e componentes biomédicos, especialmente como substitutos de tecidos duros, bem como em aplicações cardíacas e cardiovasculares, devido às suas propriedades desejáveis, como módulo de elasticidade relativamente baixo, boa resistência à fadiga, conformabilidade, usinabilidade, resistência à corrosão e biocompatibilidade. No entanto, o titânio e suas ligas não podem atender a todos os requisitos clínicos devido às suas inferiores propriedades tribológicas [24]. Portanto, a fim de melhorar as propriedades biológicas, químicas e mecânicas das ligas do titânio e titânio, os tratamentos de modificação de superfície são frequentemente realizados. Os tratamentos de modificação de superfície usados neste trabalho serão explicados em breve.

Nanotubos de TiO_2

Titânio é amplamente utilizado para a fabricação de dispositivos biomédicos e como a superfície do implante é responsável pelo processo de osseointegração, é essencial modificar essa superfície para obter uma melhor biocompatibilidade. Além disso, a adesão de uma superfície nanoestruturada aumenta em

comparação com as superfícies metálicas usuais, demonstrando que os nanotubos melhoram a osseointegração. Superfícies contendo nanotubos de TiO_2 aumentam o crescimento celular e aumentam a deposição de hidroxiapatita (HAp) [25]. A hidroxiapatita ($Ca_{10}(PO_4)_6(OH)_2$) tem similaridade química e estrutural com o componente inorgânico da matriz óssea.

Crescimento de nanoestruturas de TiO_2 por anodização eletroquímica.

Normalmente, os testes de anodização são realizados em uma célula eletroquímica de dois ou três eletrodos com uma liga de titânio como ânodo, uma folha de platina como o cátodo e, no caso de uma célula de três eletrodos com um eletrodo Ag/AgCl como o eletrodo de referência. Um potencial constante é aplicado usando uma fonte de energia DC [13].

Os principais processos na formação de nanotubos de TiO_2 são (1) o crescimento de óxido sobre a superfície do metal devido à interação do metal com os íons de O^{2-} ou OH^- [26]. Após a formação de uma camada de óxido inicial, estes ânions migram através da camada de óxido para atingir a interface de metal / óxido de onde reagem com o metal. (2) Migração de íons metálicos (Ti^{4+}) do metal na interface metal / óxido; Os cátions Ti^{4+} serão ejetados da interface metal / óxido sob a aplicação de um campo elétrico que se moverá em direção à interface óxido / eletrólito [27]. (3) Oxidação assistida por campo elétrico do óxido na interface óxido / eletrólito. Devido ao campo elétrico aplicado, a ligação Ti-O sofre polarização e é enfraquecida, promovendo a dissolução dos cátions metálicos. Os cátions de Ti^{4+} se dissolvem no eletrólito, e os ânions livres de O^{2-} migram em direção à interface metal / óxido, processo (1), para interagir com o metal [27]. (4) Dissolução química do metal, ou óxido, pelo eletrólito ácido. A dissolução química do TiO_2 no eletrólito de HF desempenha um papel crucial na formação de nanotubos, ao invés de estruturas nanoporosas simples [27].

No presente trabalho foi investigada a formação de nanotubos de TiO_2, por anodização eletroquímica das ligas Ti13Nb13Zr e Ti35Nb7Zr5Ta, utilizando soluções orgânicas contendo fluoretos.

Estrutura cristalina dos nanotubos de TiO_2 e tratamentos térmicos

Posteriormente a anodização, os nanotubos de TiO_2 são geralmente amorfos [28,29]. Após o tratamento térmico (geralmente sob ar ou oxigênio), os nanotubos de TiO_2 podem cristalizar em forma de anatase ou rutilo; a conversão para uma estrutura cristalizada pode ter um impacto significativo nas propriedades mecânicas, ópticas, eletrônicas, químicas e biomédicas [30].

Para este projeto foi realizado tratamento térmico em superfícies com nanotubos de TiO_2, o tratamento térmico foi realizado a uma temperatura de 550 ° C por 2 horas para formar uma mistura de fases de anatase e rutilo.

Tratamento Ácido

O tratamento com ácido é frequentemente usado para remover o óxido e a contaminação para obter acabamentos superficiais limpos e uniformes, gerando também micro rugosidade superficial. Takeuchi et al. investigaram a eficiência de descontaminação de três ácidos, $Na_2S_2O_8$, H_2SO_4 e HCl, para a superfície de titânio e descobriram que o HCl era um excelente agente de descontaminação porque podia facilmente dissolver sais de titânio sem fragilizá-lo [17]. Demonstrou-se que o ataque ácido melhora grandemente a osseointegração devido a que favorece a formação de tecido ósseo entre a interface implante e osso [31]. Para este trabalho, os ácidos clorídrico e fosfórico são de particular interesse, com o objetivo de observar qual ácido favorece a formação da hidroxiapatita.

Tratamento alcalino

Um método químico simples foi estabelecido para induzir a bioatividade do titânio e suas ligas. Quando substratos de ligas de titânio foram tratados com solução aquosa de NaOH 10M e subsequentemente tratados termicamente a 60 ° C, uma camada fina de titanato de sódio foi formada em suas superfícies [32]. Assim, os substratos tratados formaram uma camada de apatita densa e uniforme em suas superfícies em fluido corporal simulado (SBF) com concentrações iônicas quase iguais às do plasma sanguíneo humano [32].

Caracterização inicial das amostras da liga Ti13Nb13Zr

Diferentes condições superfície são estudadas neste trabalho, a fim de resumir todas as superfícies modificadas com e sem deformação plástica severa. A Tabela 1 nos mostra de uma maneira geral todas as superfícies de trabalhos utilizadas nos testes de corrosão e bioatividade.

Tabela 1: Superfícies de trabalho iniciais da liga Ti13Nb13Zr com diferentes tratamentos de modificação de superfície e com e sem processamento por HPT.

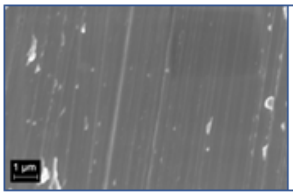	**Condição:** Sem deformar. **Tratamento de Superfície:** Polida. **Fases cristalinas :**α' e β. **Tamanho de grão:** 250 µm.	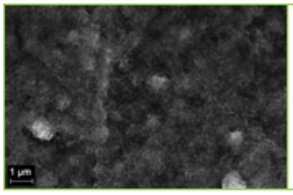	**Condição:** Sem deformar. **Tratamento de Superfície:** Ataque com HCl + NaOH . **Fases cristalinas :** Anatase, rutilo e titanato de sódio.
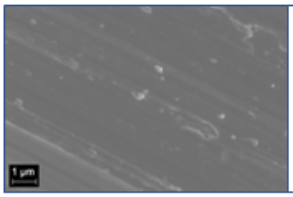	**Condição:** 1 GPa (HPT). **Tratamento de Superfície:** Polida. **Fases cristalinas :**α' e β. **Tamanho de grão:** 22 µm.	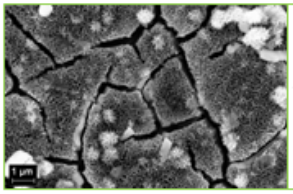	**Condição:** 1 GPa (HPT). **Tratamento de Superfície:** Ataque com HCl + NaOH . **Fases cristalinas:** Anatase, rutilo e titanato de sódio.
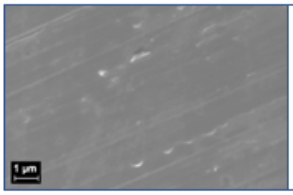	**Condição:** 4.5 GPa (HPT). **Tratamento de Superfície:** Polida. **Fases cristalinas :**α' e β. **Tamanho de grão:** 203 nm.	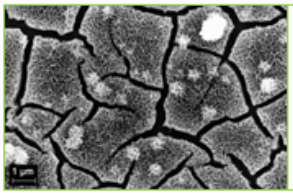	**Condição:** 4.5 GPa (HPT). **Tratamento de Superfície:** Ataque com HCl + NaOH . **Fases cristalinas :**Anatase, rutilo e titanato de sódio.
	**Condição:** Sem deformar. **Tratamento de Superfície:** Nanotubos de TiO_2. **Fases cristalinas :**α', α, β, anatase e rutilo. **Comprimento:** 1839 nm. **Diâmetro:** 96 nm.	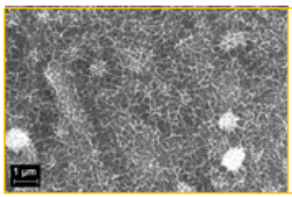	**Condição:** Sem deformar. **Tratamento de Superfície:** Ataque com H_3PO_4 + NaOH. **Fases cristalinas :** Anatase, rutilo e titanato de sódio.
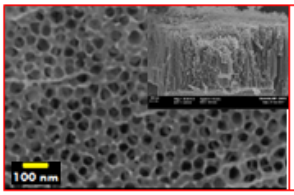	**Condição:** 1 GPa (HPT). **Tratamento de Superfície:** Nanotubos de TiO2. **Fases cristalinas :**α', α, β, anatase e rutilo. **Comprimento:** 1557 nm. **Diâmetro:** 67 nm.	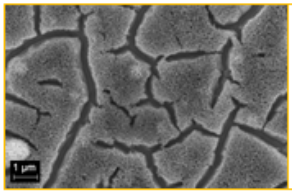	**Condição:** 1 GPa (HPT). **Tratamento de Superfície:** Ataque com H_3PO_4 + NaOH. **Fases cristalinas:** Anatase, rutilo e titanato de sódio.
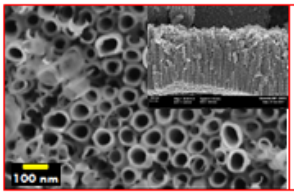	**Condição:** 4.5 GPa (HPT) **Tratamento de Superfície:** Nanotubos de TiO2. **Fases cristalinas :**α', α, β, anatase e rutilo. **Comprimento:** 1492 nm. **Diâmetro:** 94 nm.	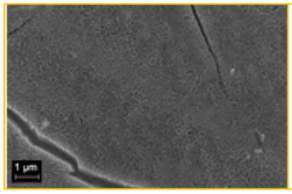	**Condição:** 4.5 GPa (HPT). **Tratamento de Superfície:** Ataque com H_3PO_4 + NaOH. **Fases cristalinas :**Anatase, rutilo e titanato de sódio.

Caracterização eletroquímica da Liga Ti13Nb13Zr

Para reproduzir o mais próximo possível das condições do corpo humano, as medidas eletroquímicas são realizadas em um meio fisiológico. Uma solução que simula o fluido corporal (SBF-Simulated body fluid) foi utilizada como eletrólito (NaCl 8,035 g L^{-1}, KCl 0,225 g L^{-1}, $NaHCO_3$ 0,355 g L^{-1}, $K_2HPO_4 \cdot 3H_2O$ 0,231 g L^{-1}, $MgCl_2 \cdot 6H_2O$ 0,311 g L^{-1}, $CaCl_2$ 0,292 g L^{-1} e Na_2SO_4 0,072 g L^{-1}). Ela reproduz a parte inorgânica do plasma sanguíneo humano (não contém nenhum composto orgânico e células). Neste estudo, a solução SBF foi preparada de acordo com o protocolo detalhado proposto por Kokubo et al. (2006) [33] e a norma ISO 23317: 2014.

As medidas eletroquímicas apresentadas a seguir são, portanto, destinadas a avaliar o impacto do tratamento de modificação de superfície e a deformação plástica severa nas propriedades eletroquímicas em SBF para a liga Ti13Nb13Zr.

Algumas considerações para mencionar dos testes eletroquímicos realizados para todas as condições existentes e para ambas as ligas (Ti13Nb13Zr e Ti35Nb7Zr5Ta) são:

- Para reproduzir as condições fisiológicas da melhor forma possível, todas as medições foram feitas no escuro.
- Por razões de reprodutibilidade, as medidas são repetidas três vezes (em uma amostra diferente a cada vez, mas com a mesma morfologia e mesma estrutura cristalina).
- As curvas de polarização são registradas em um intervalo de potencial de -30 mV a +1.20 V em relação ao OCP (Open Circuit Potential), com uma velocidade de varredura de 0,50 mV s^{-1}.
- As simulações dos espectros EIS para todas as amostras foram realizadas usando o software Simad desenvolvido pelo Laboratório de Interfaces e Sistemas Eletroquímicos (LISE).

- As medidas de espectroscopia de impedância são registradas para uma faixa de frequência de 20 kHz a 20 mHz. A amplitude do sinal de perturbação sinusoidal é de 10 mVrms.

Amostras polidas

As Figuras 2((a) e (b)) mostram as curvas de polarização anódicas e os diagramas de Nyquist respectivamente em SBF a 37 ° C dos substratos com superfície polida da liga Ti13Nb13Zr não processadas e processadas por HPT.

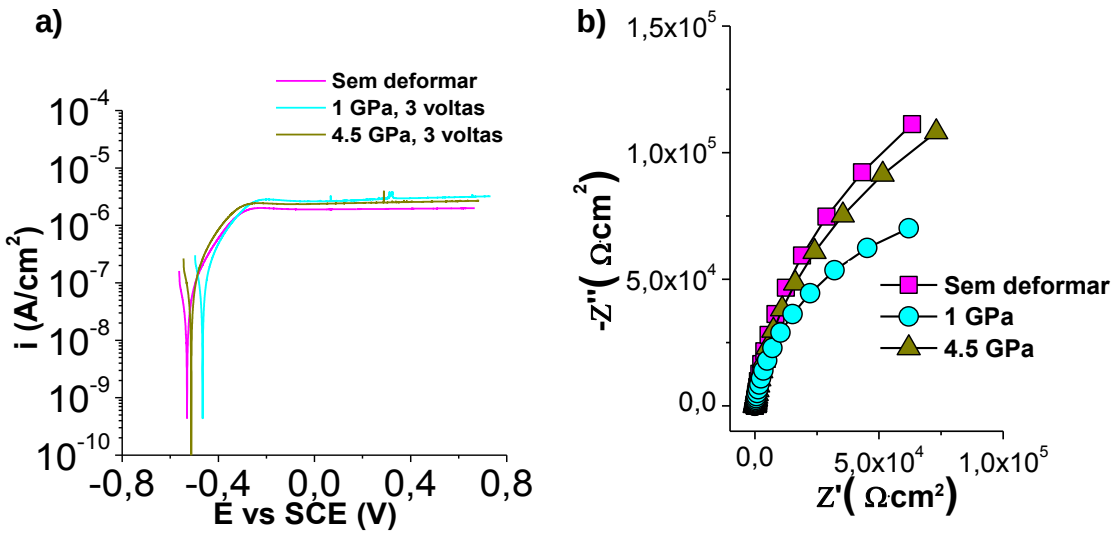

Figura 2: Curvas de polarização anódica (a) e diagramas de Nyquist (b) dos substratos polidos da liga Ti13Nb13Zr não processadas e processadas por HPT em meio fisiológico em uma solução de SBF a pH 7,4 a 37 ° C.

As densidades de corrente, representadas no eixo das ordenadas da Figura 2(a), foram calculadas dividindo-se a corrente medida pela área geométrica (0,283 cm²). Considera-se que a corrente medida na região do anodo se deve principalmente à reação de oxidação dos substratos ao TiO_2, o que contribui para o espessamento da camada passiva. Esta reação, que ocorre na interface de metal/óxido [30].

As correntes de passivação são semelhantes para as condições sem deformar como para as deformadas por HPT. Inicialmente para amostra sem

deformar, a corrente de passivação tem um valor aproximado de: 2,00 μA / cm^2. Para amostras com deformação plástica severa, as correntes de passivação são: 2,95 μA / cm^2, para a amostra com 1 GPa de deformação e 2,45 μA / cm^2 para a amostra com 4,5 GPa de deformação. Portanto, a deformação plástica severa não tem efeito significativo na corrente de passivação para as amostras deformadas comparando com o substrato sem deformação.

Para finalizar a caracterização eletroquímica das superfícies polidas, as amostras foram submetidas a medidas de espectroscopia de impedância eletroquímica. A Figura 2(b) mostra as medições da impedância por médio do diagrama de Nyquist. A observação dos diagramas de Nyquist revela que a forma do espectro de impedância para todos os substratos (arco) é típica de um sistema capacitivo-resistivo (associações de fenômenos capacitivos, isto é, acumulações de cargas e fenômenos resistivos, ou seja, transferências de carga ou resistência de uma camada).

Os espectros de impedância experimentais foram analisados ajustando-se a um circuito elétrico equivalente apropriado que descreve as propriedades do sistema sob investigação. Como modelo, foi considerado para amostras com bicamada composta de uma camada porosa externa e uma camada interna densa. A Figura 3 apresenta o modelo selecionado o qual é representado por um circuito equivalente $R_s + Q_a / (R_a + (Q_{dl} / R_{ct}))$. Onde R_s é a resistência da solução, R_a é a resistência da camada porosa externa, R_{ct} é a resistência à transferência de carga, Q_a é o elemento de fase constante para a camada porosa externa e Q_{dl} é o elemento de fase constante para a dupla camada elétrica na interface da camada interna densa -eletrólito.

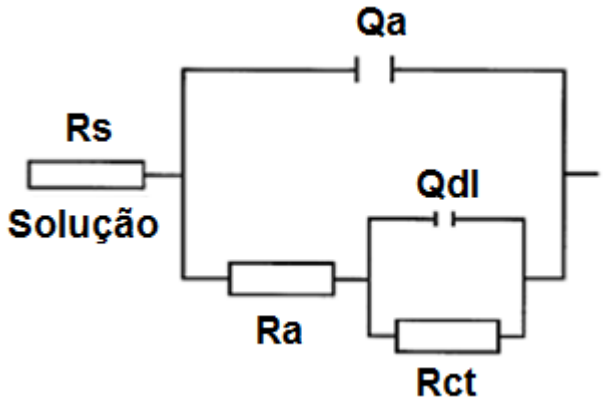

Figura 3: Circuito equivalente usado para modelar os resultados dos substratos polidos da liga Ti13Nb13Zr não processadas e processadas por HPT em meio fisiológico em uma solução de SBF a pH 7,4 a 37 ° C.

Os resultados do ajuste do modelo são apresentados na Tabela 2. Em geral, valores de resistência da solução entre 19 e 22 ($\Omega \cdot cm^2$) e também altos valores de resistência à transferência de carga entre $1{,}7x10^5$ e $3x10^5$ ($\Omega \cdot cm^2$) são observados, indicando uma alta resistência à corrosão. Além disso, as capacidades efetivas (C_{eff}) da camada externa porosa e da camada interna densa foram calculadas a partir dos parâmetros do elemento de fase constante usando a fórmula Brug [34]:

$$C_{eff}(Brug) = Q^{\frac{1}{\alpha}}(R_e^{-1} + R_t^{-1})^{\frac{\alpha-1}{\alpha}}$$

Esses valores de capacitância são dados na Tabela 2. Os valores de capacitância para a camada externa porosa ($C_{eff(a)}$) foram entre 7 e 16 $\mu F \cdot cm^{-2}$. Por outro lado, os resultados obtidos para a camada interna da barreira ($C_{eff(dl)}$) foram entre 17 a 20 $\mu F \cdot cm^{-2}$, que são típicos para uma capacitância de uma dupla camada elétrica.

Considerando a camada como um capacitor planar, a espessura do filme passivo δ (em nm) pode ser obtida a partir da equação:

$$\delta = \frac{\epsilon \cdot \epsilon_0}{C_{eff}}$$

onde ϵ0 é a permissividade do vácuo (8,8542 × 10^{-14} F/cm) e ϵ a constante dielétrica do material. O valor da constante dielétrica do TiO_2 está na faixa de 18,2 a 173 [35]. Aplicando um valor médio de constante dielétrica, ϵ = 100, valor selecionado por outros autores [36,37], obtemos espessuras dos filmes passivos protetores (associado com a camada interna densa) de 3,75, 4,53 e 3,80 nm para a liga Ti13Nb13Zr, nas condições não deformada (ND) e deformada por 1 GPa (HPT1GPa) e deformada por 4,5 GPa (HPT4.5GPa), respectivamente. Estes resultados mostram que os filmes passivos na liga de Ti13Nb13Zr deformada possuem maior espessura.

Resumindo, os resultados obtidos a partir do ajuste indicam que todos os substratos testados se comportaram de maneira muito semelhante.

Tabela 2: Valores dos parâmetros do ajuste do modelo da Figura 3 para amostras da liga Ti13Nb13Zr com superfície polida.

Condição	Rs $\Omega \cdot cm^2$	Qa $\mu F \cdot s^{(\alpha 2-1)}$	α_a	Ra $\Omega \cdot cm^2$	$C_{eff(a)}$ $\mu F/cm^2$	Qb $\mu F \cdot s^{(\alpha 3-1)}$	α_b	Rb $\Omega \cdot cm^2$	$C_{eff(b)}$ $\mu F/cm^2$
Sem deformar	22	7	0.94	57	16	9	0.94	3.0E+05	20
1 GPa	19	5	0.90	111	7	12	0.88	1.3E+05	17
4.5 GPa	21	6	0.90	124	9	11	0.91	1.7E+05	20

Amostras com nanotubos de TiO_2

As Figuras 4((a) e (b)) mostram as curvas de polarização anódicas e os diagramas de Nyquist respectivamente dos substratos com nanotubos de TiO_2 da liga Ti13Nb13Zr não processadas e processadas por HPT.

A observação geral da Figura 4(a) mostra que forma da porção anódica das curvas de polarização tem o comportamento característico de um estado passivo. Efetivamente, para todas as amostras, um patamar atual é estabelecido em uma ampla gama de potenciais, o que corresponde a uma limitação da corrente pelo transporte de massa através da camada de óxido.

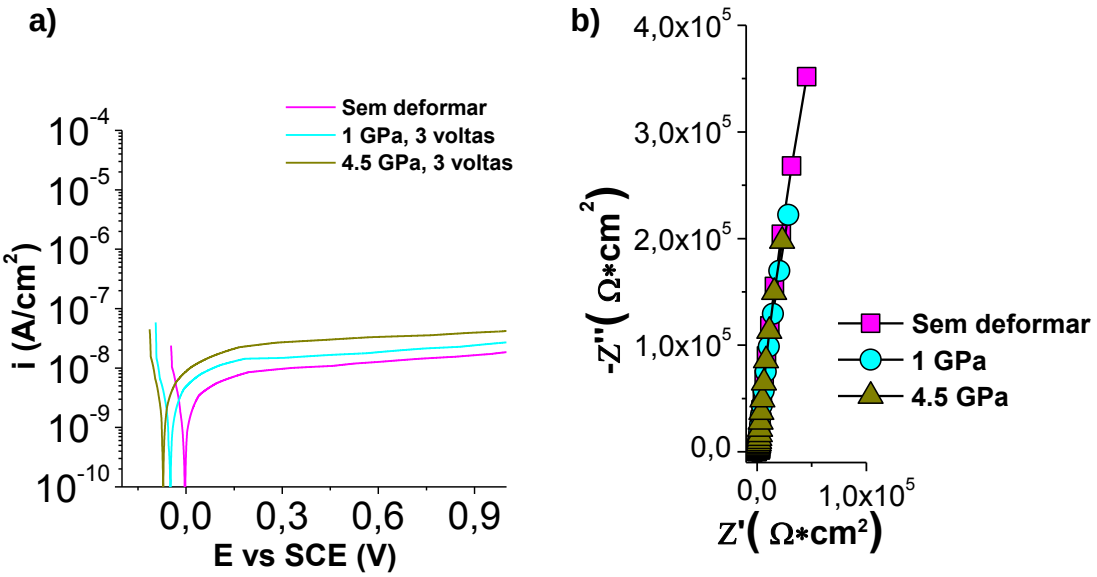

Figura 4: Curvas de polarização anódica (a) e diagramas de Nyquist (b) dos substratos com nanotubos de TiO_2 da liga Ti13Nb13Zr não processadas e processadas por HPT em meio fisiológico em uma solução de SBF a pH 7,4 a 37 ° C.

As correntes de passivação têm uma mudança drástica em comparação com substratos polidos. Inicialmente para amostra sem deformar, a corrente de passivação da liga Ti13Nb13Zr com TiO_2 e nanotubos recozidos tem aproximadamente o valor: 0,012 µA / cm^2. Para amostras com deformação plástica severa, as correntes de passivação são: 0,017 µA / cm^2, para a amostra com 1 GPa de deformação e 0,033 µA / cm^2 para a amostra com 4,5 GPa de deformação. Portanto, parece que a deformação plástica severa causa um ligeiro aumento na corrente de passivação em comparação com o substrato sem deformação.

A Figura 4(b) mostra as medições da impedância por médio do diagrama de Nyquist. A observação dos diagramas de Nyquist revela que a forma do espectro de impedância para todos os substratos é pseudo-capacitivo (inclinado em linha reta), isto é, que as trocas de elétrons e, portanto, as reações, são muito limitadas ou que a camada de óxido é muito resistiva.

Os espectros de impedância experimentais são analisados ajustando-se a um modelo desenvolvido de linha de transmissão para um eletrodo poroso, que descreve as propriedades do sistema sob investigação. A Figura 5 apresenta o modelo de linha de transmissão desenvolvido em este trabalho.

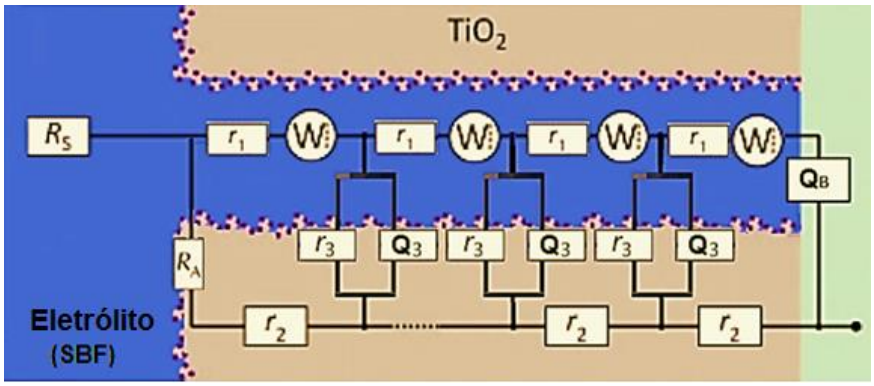

Figura 5: Modelo de linha de transmissão desenvolvido para os substratos com nanotubos de TiO_2 da liga Ti13Nb13Zr não processadas e processadas por HPT em meio fisiológico em uma solução de SBF a pH 7,4 a 37 ° C.

Os resultados do modelo são apresentados na Tabela 3. Os resultados do ajuste foram valores de resistência da solução de 20 ($\Omega \cdot cm^2$) e também uma alta resistência associada ao limite superior dos poros (R_A) entre $2x10^7$ e $3x10^7$ ($\Omega \cdot cm^2$) são observados, indicando uma alta resistência à corrosão, maior que os substratos com superfície polida. Além disso, as capacidades efetivas (C_{eff}) foram calculadas a partir dos parâmetros do elemento de fase constante usando a fórmula Hsu-Mansfeld [38]:

$$C_{eff}(H-M) = Q^{\frac{1}{\alpha}}(R_t)^{\frac{1-\alpha}{\alpha}}$$

Esses valores de capacitância são dados na Tabela 3. Os valores de capacitância foram entre 14 e 42 $\mu F \cdot cm^{-2}$ para C_{β}, que são típicos daqueles para uma capacitância de dupla camada. Além disso, os resultados obtidos para C_n, correspondente à capacitância do filme passivo, apresentaram valores entre 2 e 5 $\mu F \cdot cm^{-2}$.

A espessura do filme passivo δ (em nm) foi obtida a partir da capacitância do filme passivo. Os valores da espessura foram de 25,5, 39,6 e 17,6 nm para a liga Ti13Nb13Zr, nas condições ND, HPT1GPa e HPT4.5GPa, respectivamente.

Finalmente, foi observado que os substratos com maior comprimento de nanotubos de TiO_2 que são aqueles sem deformação apresentam maior resistência à corrosão.

Tabela 3: Valores dos parâmetros do ajuste do modelo da Figura 5 para amostras da liga

Condição	$\chi 1$	$\chi 2$	ξ				Z_A	Z_B			R_s
	R_1 (Ω)	R_2 (Ω)	R_3 (Ω)	Q_3 ($F^{\beta-1}$)	β	C_β μF/cm^2	R_A (Ω)	Q_B (F^{n-1})	n	C_n μF/cm^2	R_s (Ω)
Sem deformar	1	241	2.3E+15	1.4E-06	0.96	14	3.0E+07	1.4E-06	0.96	3	70.0
1 GPa	6	736	1.8E+15	1.2E-06	0.97	19	3.0E+07	1.0E-06	0.96	2	70.0
4.5 GPa	1	100	1.8E+15	2.4E-06	0.94	42	2.3E+07	2.0E-06	0.96	5	70.0

Ti13Nb13Zr com superfície com nanotubos de TiO_2.

Amostras com tratamento ácido por HCl e subsequentemente tratamento alcalino com NaOH.

As Figuras 6((a) e (b)) mostram as curvas de polarização anódicas e os diagramas de Nyquist respectivamente dos substratos com tratamento ácido por HCl e subsequentemente tratamento alcalino com NaOH da liga Ti13Nb13Zr não processadas e processadas por HPT.

Como uma observação geral da forma da porção anódica das curvas de polarização mostradas na Figura 6(a), revela que o comportamento das amostras em um ambiente fisiológico é característico de um estado passivo.

Observa-se variação nas correntes de passivação. Onde inicialmente as amostras sem deformar tem um valor aproximado de: 2,30 μA / cm^2. Para amostras com deformação plástica severa, as correntes de passivação são: 2,51 μA / cm^2, para a amostra com 1 GPa de deformação e 3,40 μA / cm^2 para a

amostra com 4,5 GPa de deformação. Deste modo, a deformação plástica severa causa um ligeiro aumento na corrente de passivação em comparação com o substrato sem deformação.

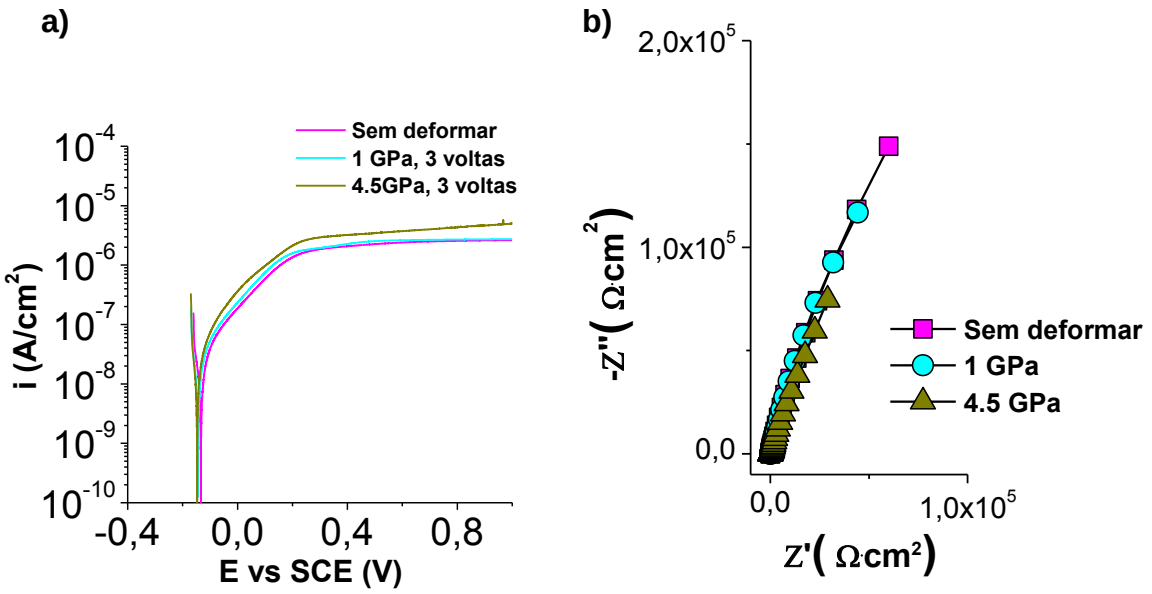

Figura 6: Curvas de polarização anódica (a) e diagramas de Nyquist (b) dos substratos com tratamento ácido por HCl e subsequentemente tratamento alcalino com NaOH da liga Ti13Nb13Zr não processadas e processadas por HPT em meio fisiológico em uma solução de SBF a pH 7,4 a 37 ° C.

A Figura 6(b) mostra as medições da impedância por médio do diagrama de Nyquist. A observação dos diagramas de Nyquist revela que a forma do espectro de impedância para todos os substratos (arco) é típica de um sistema capacitivo-resistivo.

Os espectros de impedância experimentais são analisados ajustando-se a um circuito elétrico equivalente apropriado que descreve as propriedades do sistema sob investigação. Os espectros foram ajustados usando o circuito R_s + (Q_b / R_b) + Q_a /(R_a+(Q_{dl} / R_{ct})), onde R_s representa a resistência da solução, R_b e Q_b representam a resistência e o elemento de fase constante para a camada porosa externa, R_a e Q_a representam a resistência e o elemento de fase constante para a camada porosa intermédia, R_{ct} e Q_{dl} representam a resistência à transferência de

carga e o elemento de fase constante para a dupla camada elétrica na interface camada interna densa- eletrólito. A Figura 7 apresenta o modelo selecionado.

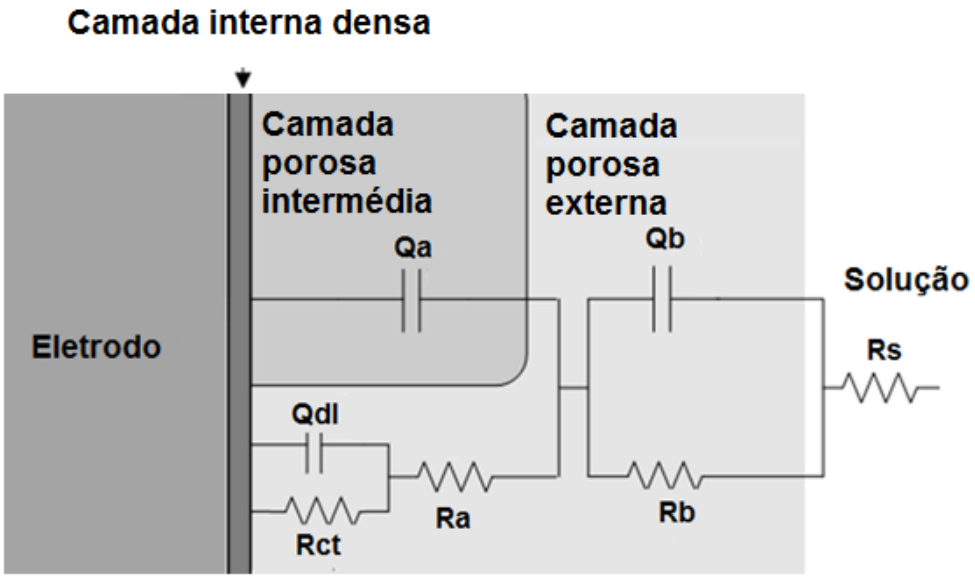

Figura 7: Circuito equivalente usado para modelar os resultados dos substratos com tratamento ácido por HCl e subsequentemente tratamento alcalino com NaOH da liga Ti13Nb13Zr não processadas e processadas por HPT em meio fisiológico em uma solução de SBF a pH 7,4 a 37 ° C.

Os resultados do ajuste do modelo e a capacitância efetiva associada ao CPE calculada com a equação de Brug são apresentados na Tabela 4. A partir do ajuste, obtemos valores de resistência da solução entre 20 e 22 ($\Omega \cdot cm^2$) e também altos valores de resistência à transferência de carga entre $6x10^5$ e $8x10^5$ ($\Omega \cdot cm^2$), indicando uma alta resistência à corrosão com valores levemente maiores que as amostras com superfície polidas.

Com relação às capacitâncias, os valores para a capacitância da dupla camada elétrica (Ceff ($_{dl}$)) foram entre 14 e 19 $\mu F \cdot cm^{-2}$. Os valores de capacitância para a camada externa porosa (Ceff($_b$)) e a camada porosa intermediária (Ceff($_a$)) foram menores que Ceff ($_{dl}$).

Além disso, a espessura do filme passivo δ (em nm) foi obtida a partir da capacitância da camada interna densa. Os valores da espessura foram de 4,05,

4,30 e 5,41 nm para a liga Ti13Nb13Zr, nas condições ND, HPT1GPa e HPT4.5GPa, respectivamente. Estes resultados mostram que os filmes passivos na liga de Ti13Nb13Zr deformada possuem maior espessura.

Tabela 4: Valores dos parâmetros do ajuste do modelo da Figura 7 para amostras da liga Ti13Nb13Zr submetidas ao tratamento ácido por HCl e subsequentemente tratamento alcalino com NaOH.

	Condição		
Elemento	**Sem deformar**	**1 GPa**	**4.5 GPa**
R_s ($\Omega \cdot cm^2$)	22	20	20
Q_b ($\mu F \cdot s^{(\alpha b-1)}$)	52	28	43
α_b	0.70	0.76	0.72
R_b ($\Omega \cdot cm^2$)	28	15	15
$C_{eff(b)}$ ($\mu F/ cm^2$)	2.2	2.0	2.0
Q_a ($\mu F \cdot s^{(\alpha a-1)}$)	19	11	55
α_a	0.70	0.75	0.70
R_a ($\Omega \cdot cm^2$)	7	2	10
$C_{eff(a)}$ ($\mu F/ cm^2$)	0.4	0.3	0.5
Q_{dl} ($\mu F \cdot s^{(\alpha dl-1)}$)	21	39	19
α_{dl}	0.98	0.90	0.96
R_{ct} ($\Omega \cdot cm^2$)	7.6E+05	6.8E+05	6.0E+05
$C_{eff(dl)}$ ($\mu F/cm^2$)	19	18	14

Amostras com tratamento ácido por H_3PO_4 e subsequentemente tratamento alcalino com NaOH.

As Figuras 8((a) e (b)) mostram as curvas de polarização anódicas e os diagramas de Nyquist respectivamente dos substratos com tratamento ácido por H_3PO_4 e subsequentemente tratamento alcalino com NaOH da liga Ti13Nb13Zr não processadas e processadas por HPT.

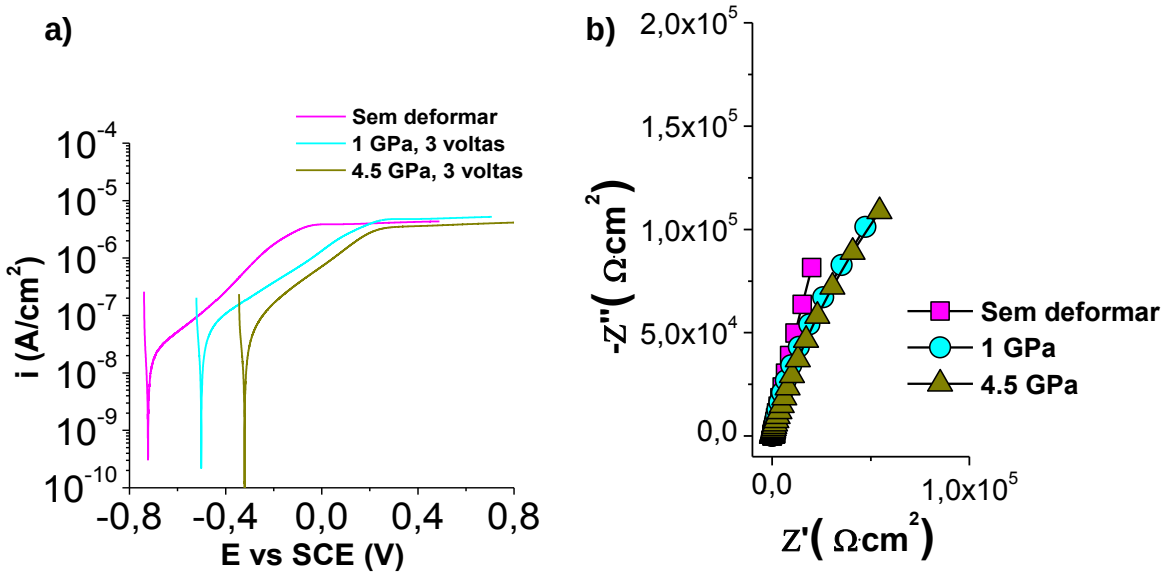

Figura 8: Curvas de polarização anódica (a) e diagramas de Nyquist (b) dos substratos com tratamento ácido por H_3PO_4 e subsequentemente tratamento alcalino com NaOH da liga Ti13Nb13Zr não processadas e processadas por HPT em meio fisiológico em uma solução de SBF a pH 7,4 a 37 ° C.

Observa-se o mesmo comportamento visto anteriormente para as outras curvas de polarização onde a porção anódica das curvas de polarização revela um comportamento passivo das amostras em SBF.

As correntes de passivação no estado sem deformar da liga Ti13Nb13Zr com ataque ácido-ácido por H_3PO_4 e subsequentemente tratamento alcalino por NaOH tem aproximadamente o valor de 4,05 µA / cm^2. Para amostras com deformação plástica severa, as correntes de passivação são: 5,13 µA / cm^2, para a amostra com 1 GPa de deformação e 4,21 µA / cm^2 para a amostra com 4,5 GPa de deformação. Portanto, parece que a deformação plástica severa não tem efeito para altas pressões na corrente de passivação quando comparamos com o substrato sem deformação.

A Figura 8(b) mostra as medições da impedância por médio do diagrama de Nyquist. A observação dos diagramas de Nyquist revela que a forma do espectro de impedância para todos os substratos é característica de um sistema capacitivo-

resistivo. Os espectros de impedância experimentais são analisados ajustando-se com o mesmo circuito elétrico equivalente utilizado para as amostras com ataque ácido por HCl (Ver Figura 7).

Os resultados do ajuste do modelo e a capacitância efetiva associada ao CPE calculada com a equação de Brug são apresentados na Tabela 5.

Tabela 5: Valores dos parâmetros do ajuste do modelo da Figura 7 para amostras da liga Ti13Nb13Zr submetidas ao tratamento ácido por H_3PO_4 e subsequentemente tratamento alcalino com NaOH.

	Condição		
Elemento	**Sem deformar**	**1 GPa**	**4.5 GPa**
R_s (Ω· cm^2)	20	20	20
Q_b (μF ·s(αb-1))	42	15	15
α_b	0.72	0.81	0.78
R_b (Ω· cm^2)	13	2	10
$C_{eff(b)}$ (μF/ cm^2)	1.9	1.3	1.2
Q_a (μF ·s(αa-1))	65	42	14
α_a	0.78	0.82	0.77
R_a (Ω· cm^2)	78	44	20
$C_{eff(a)}$ (μF/ cm^2)	9	8	1.0
Q_{dl} (μF ·s(αdl-1))	14	12	32
α_{dl}	0.96	0.98	0.91
R_{ct} (Ω· cm^2)	5.1E+05	4.5E+05	7.1E+05
$C_{eff(dl)}$ (μF/cm^2)	10	10	15

Em geral, valores de resistência da solução de 20 (Ω·cm^2) e também altos valores de resistência à transferência de carga entre 5x10^5 e 7x10^5 (Ω·cm^2) são observados, indicando uma alta resistência à corrosão com valores levemente maiores que as amostras com superfície polidas.

Com relação às capacitâncias, os valores para a capacitância da dupla camada elétrica (Ceff ($_{dl}$)) foram entre 10 e 15 μF·cm^{-2}. Os valores de capacitância

para a camada externa porosa (Ceff($_b$)) e a camada porosa intermediária (Ceff($_a$)) foram menores que Ceff ($_{dl}$).

A espessura do filme passivo ð (em nm) foi obtida a partir da capacitância da camada interna densa. Os valores da espessura foram de 7,62, 7,43 e 5,03 nm para a liga Ti13Nb13Zr, nas condições ND, HPT1GPa e HPT4.5GPa, respectivamente. Estes resultados mostram que o tratamento químico contribui com o aumento da espessura do filme passivo.

Testes de bioatividade da liga Ti13Nb13Zr

Testes de bioatividade, cujo princípio é avaliar a capacidade do material para formar espontaneamente apatita na superfície quando é imerso em SBF. Essa capacidade é um critério essencial para determinar a biocompatibilidade de um material. Neste estudo foram examinados depósitos de apatita após 1, 7 e 14 dias de imersão em SBF para as amostras da liga Ti13Nb13Zr com distintas modificação de superfície assim como os diferentes graus de deformação por HPT.

Amostras polidas

As observações de microscopia eletrônica de varrido (MEV) mostradas na Figura 9, indicam que mesmo após 14 dias de imersão na solução fisiológica, nenhuma formação de apatita é detectada nas superfícies dos substratos polidos (independentemente da deformação por HPT).

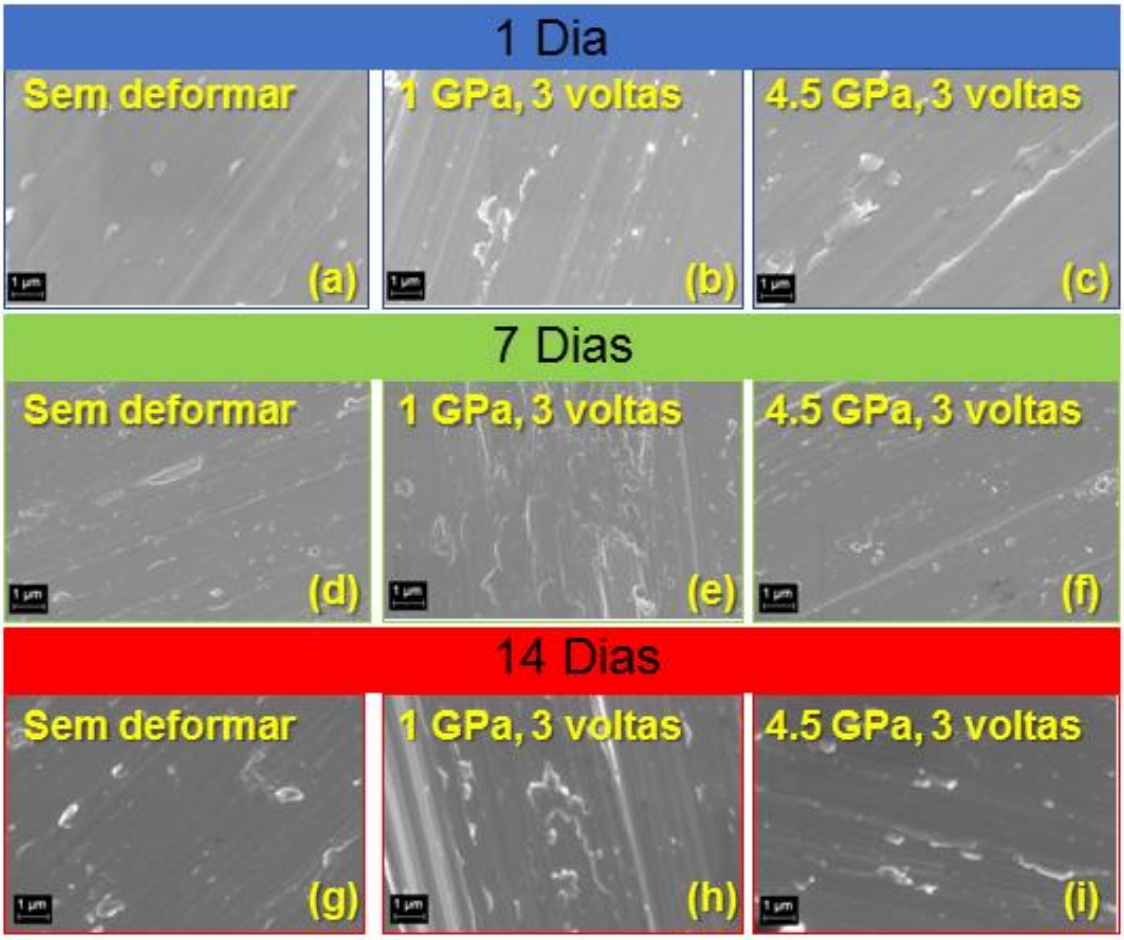

Figura 9: Observações por MEV das amostras com superfície polidas da liga Ti13Nb13Zr não processadas e processadas por HPT, submetidas a testes de bioatividade para tempos de 1, 7 e 14 dias em SBF.

Amostras com nanotubos de TiO_2

Desde o primeiro dia em imersão em SBF, a apatita é visível em pequenas áreas nos substratos da liga Ti13Nb13Zr deformados por HPT na condição de 4,5 GPa com nanotubos de TiO_2 recozidos como é observado na Figura 10(c). Depósitos homogêneos de apatita são observados em todas as condições nos períodos de 7 e 14 de imersão em SBF.

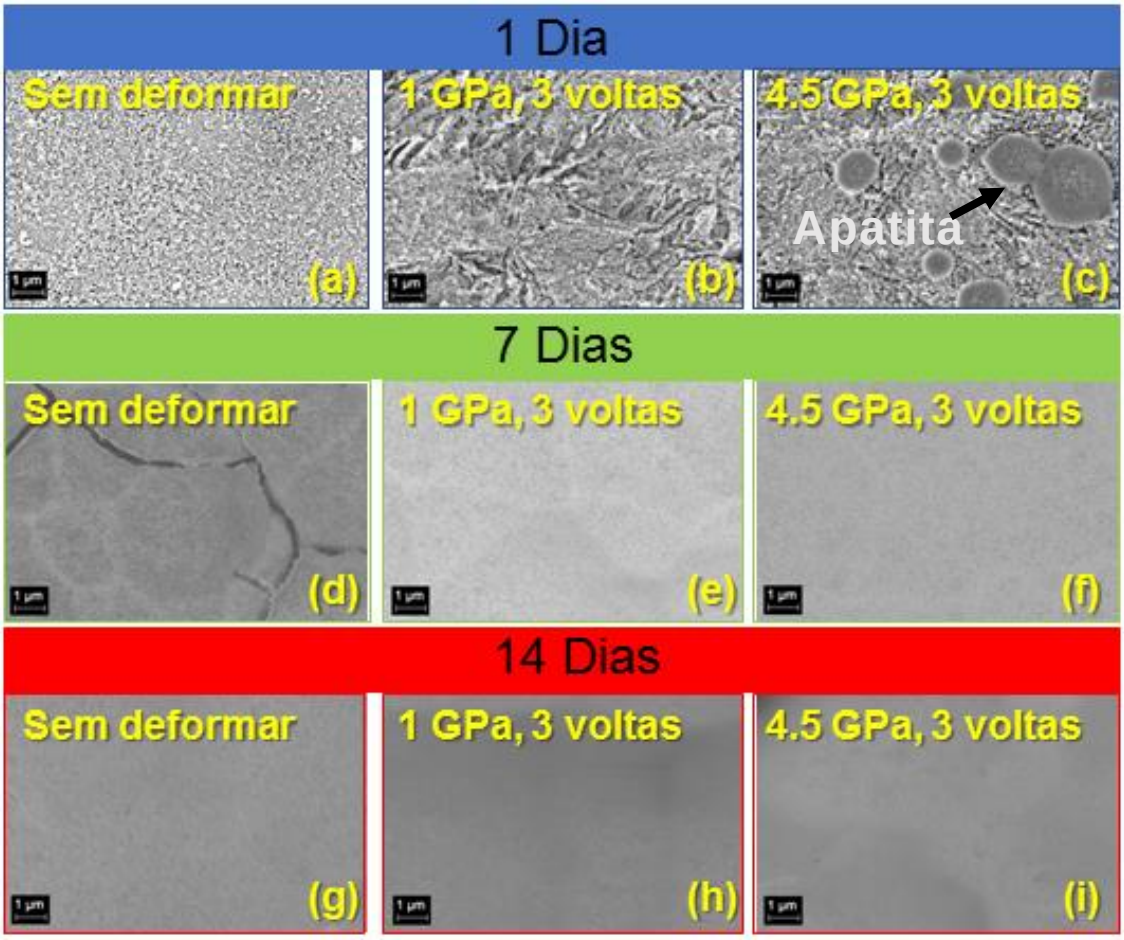

Figura 10: Observações por MEV das amostras com superfície com nanotubos de TiO_2 da liga de Ti13Nb13Zr não processadas e processadas por HPT, submetidas a testes de bioatividade para tempos de 1, 7 e 14 dias em SBF.

Amostras com tratamento ácido por HCl e subsequentemente tratamento alcalino com NaOH.

As observações por MEV mostradas na Figura 11 que, a partir do sétimo dia de imersão em SBF, depósitos de apatita são visíveis em substratos da liga Ti13Nb13Zr sob todas as condições de processamento.

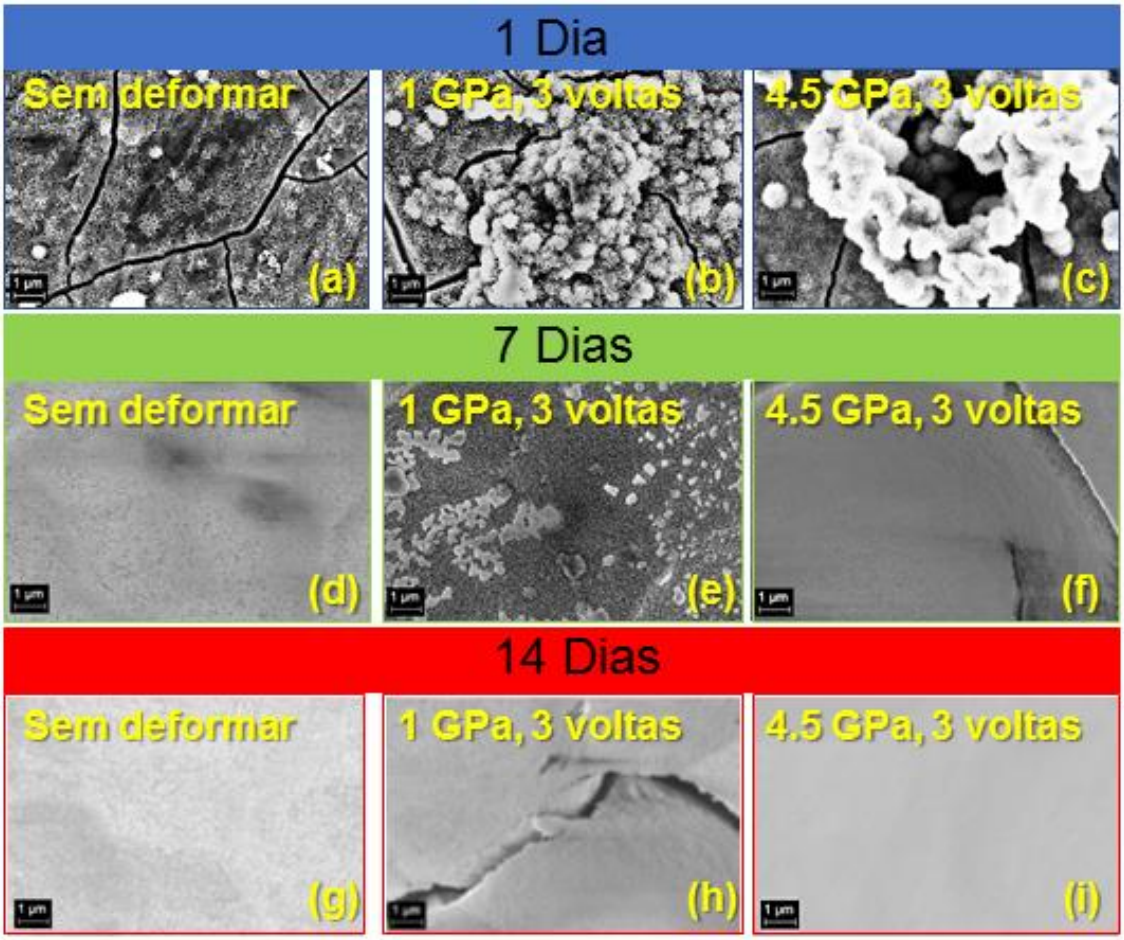

Figura 11: Observações por MEV das amostras com superfície com tratamento ácido por HCl e subsequentemente tratamento alcalino com NaOH da liga de Ti13Nb13Zr não processada e processada por HPT, submetidas a testes de bioatividade para tempos de 1, 7 e 14 dias em SBF.

Amostras com tratamento ácido por H_3PO_4 e subsequentemente tratamento alcalino com NaOH.

As observações por MEV mostradas na Figura 12, indicam que a partir do sétimo dia de imersão em SBF, depósitos de apatita são visíveis em substratos da liga Ti13Nb13Zr sob todas as condições de processamento.

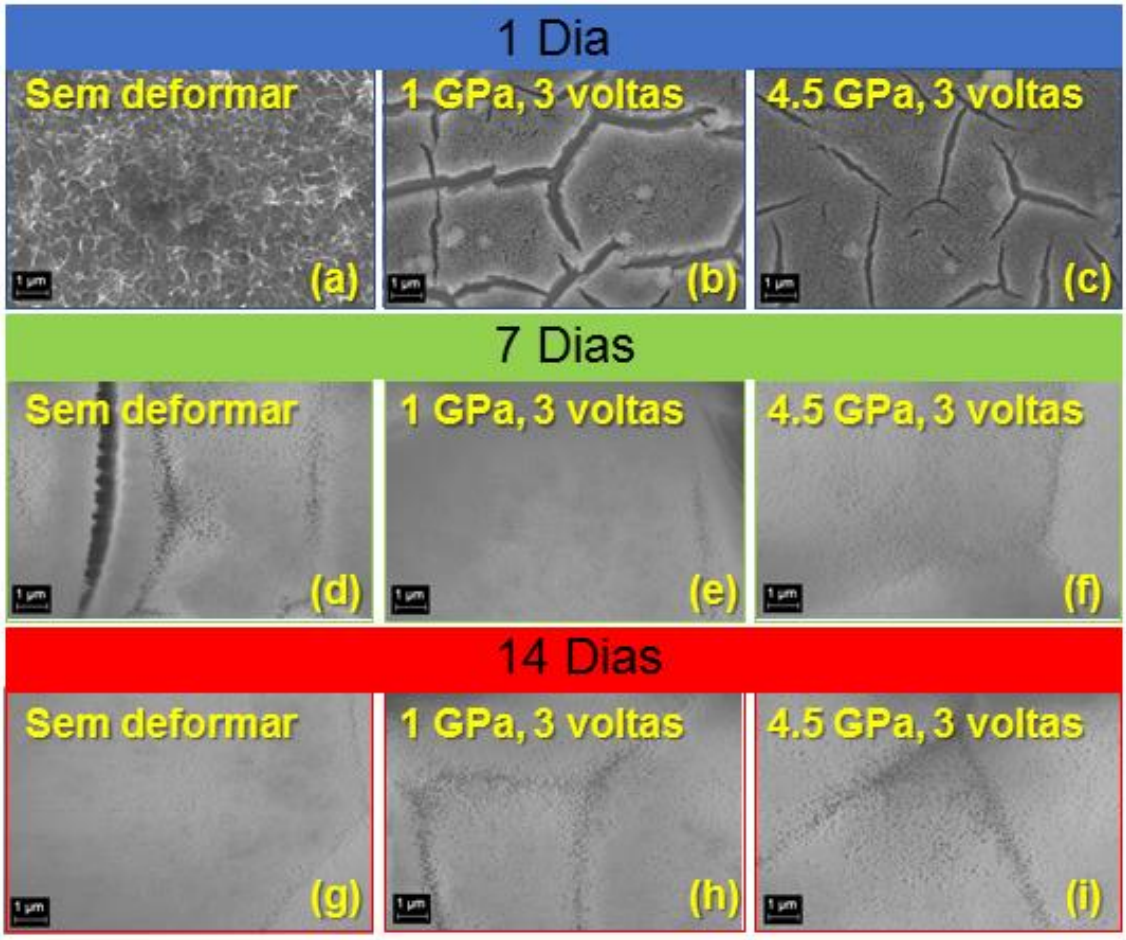

Figura 12: Observações por MEV das amostras com superfície com tratamento ácido por H_3PO_4 e subsequentemente tratamento alcalino com NaOH da liga de Ti13Nb13Zr não processada e processada por HPT, submetidas a testes de bioatividade para tempos de 1, 7 e 14 dias em SBF.

Caracterização inicial das amostras da liga Ti35Nb7Zr5Ta

Diferentes condições superfície são estudadas neste trabalho, a fim de resumir todas as superfícies modificadas com e sem deformação plástica severa. A Tabela 6 nos mostra de uma maneira geral todas as superfícies de trabalhos utilizadas nos testes de corrosão e bioatividade.

Tabela 6: Superfícies de trabalho iniciais da liga Ti35Nb7Zr5Ta com diferentes tratamentos de modificação de superfície, com e sem processamento por HPT.

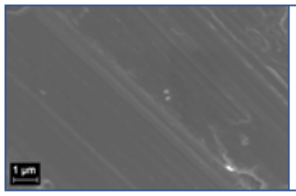	**Condição:** Sem deformar. **Tratamento de Superfície:** Polida. **Fases cristalinas :**β. **Tamanho de grão:** 240 µm.	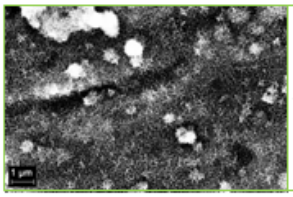	**Condição:** Sem deformar. **Tratamento de Superfície:** Ataque com HCl + NaOH . **Fases cristalinas :** Anatase, rutilo e titanato de sódio.
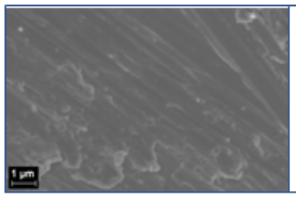	**Condição:** 1 GPa (HPT). **Tratamento de Superfície:** Polida. **Fases cristalinas :**β. **Tamanho de grão:** 89 µm.	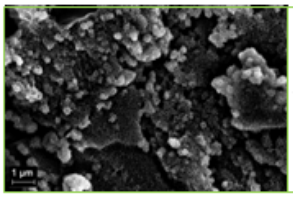	**Condição:** 1 GPa (HPT). **Tratamento de Superfície:** Ataque com HCl + NaOH . **Fases cristalinas:** Anatase, rutilo e titanato de sódio.
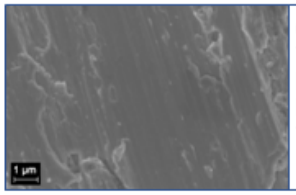	**Condição:** 4.5 GPa (HPT). **Tratamento de Superfície:** Polida. **Fases cristalinas :**β. **Tamanho de grão:** 112 nm.	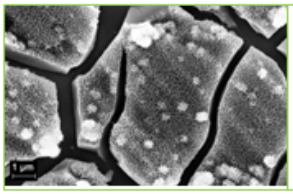	**Condição:** 4.5 GPa (HPT). **Tratamento de Superfície:** Ataque com HCl + NaOH . **Fases cristalinas :**Anatase, rutilo e titanato de sódio.
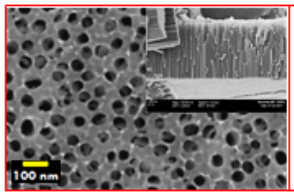	**Condição:** Sem deformar. **Tratamento de Superfície:** Nanotubos de TiO2. **Fases cristalinas :**α', α, β, anatase e rutilo. **Comprimento:** 2494 nm. **Diâmetro:** 82 nm.	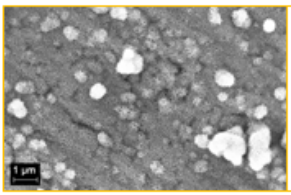	**Condição:** Sem deformar. **Tratamento de Superfície:** Ataque com H3PO4 + NaOH. **Fases cristalinas :** Anatase, rutilo e titanato de sódio.
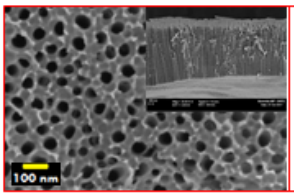	**Condição:** 1 GPa (HPT). **Tratamento de Superfície:** Nanotubos de TiO2. **Fases cristalinas :**α', α, β, anatase e rutilo. **Comprimento:** 2459 nm. **Diâmetro:** 81 nm.	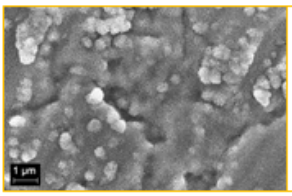	**Condição:** 1 GPa (HPT). **Tratamento de Superfície:** Ataque com H3PO4 + NaOH. **Fases cristalinas:** Anatase, rutilo e titanato de sódio.
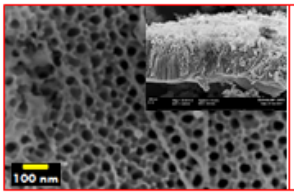	**Condição:** 4.5 GPa (HPT). **Tratamento de Superfície:** Nanotubos de TiO2. **Fases cristalinas :**α', α, β, anatase e rutilo. **Comprimento:** 1742 nm. **Diâmetro:** 69 nm.	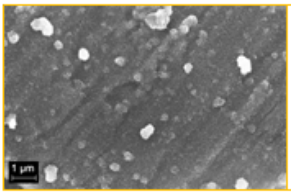	**Condição:** 4.5 GPa (HPT). **Tratamento de Superfície:** Ataque com H3PO4 + NaOH. **Fases cristalinas :**Anatase, rutilo e titanato de sódio.

Caracterização eletroquímica da Liga Ti35Nb7Zr5Ta

As medidas eletroquímicas apresentadas a seguir são, portanto, destinadas a avaliar o impacto do tratamento de modificação de superfície e a deformação plástica severa nas propriedades eletroquímicas em SBF para a liga Ti35Nb7Zr5Ta.

Amostras polidas

As Figuras 13((a) e (b)) mostram as curvas de polarização anódicas e os diagramas de Nyquist respectivamente dos substratos com superfície polida da liga Ti35Nb7Zr5Ta não processadas e processadas por HPT.

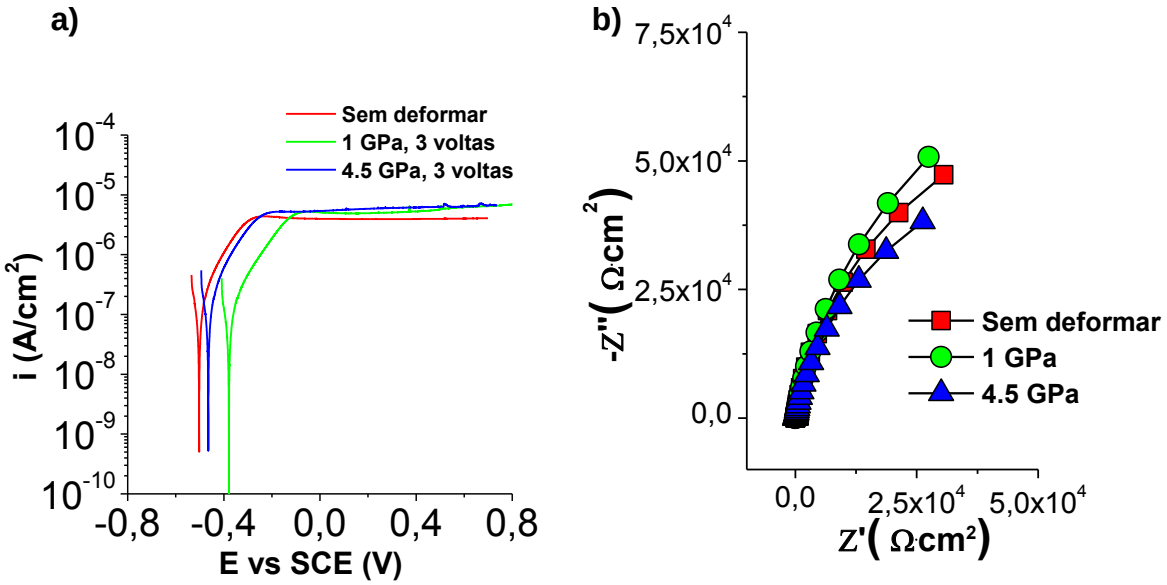

Figura 13: Curvas de polarização anódica (a) e diagramas de Nyquist (b) dos substratos polidos da liga Ti35Nb7Zr5Ta não processadas e processadas por HPT em meio fisiológico em uma solução de SBF a pH 7,4 a 37 ° C.

A corrente medida na região do ânodo é devida principalmente à reação de oxidação dos substratos ao TiO_2. Observa-se na porção anódica das curvas de polarização um comportamento passivo das amostras em SBF.

Nota-se na condição sem deformar uma corrente de passivação com um valor de: 3,52 μA / cm^2. Para amostras com deformação plástica severa, as correntes de passivação são: 5,18 μA / cm^2, para a amostra com 1 GPa de deformação e 6,03 μA / cm^2 para a amostra com 4,5 GPa de deformação. Portanto, parece que a deformação plástica severa causa um ligeiro aumento na corrente de passivação em comparação com o substrato sem deformação.

A Figura 13(b) mostra as medições da impedância por médio do diagrama de Nyquist. A observação dos diagramas de Nyquist revela que a forma do espectro de impedância para todos os substratos é característica de um sistema capacitivo-resistivo. Os espectros de impedância experimentais são analisados ajustando-se com o mesmo circuito elétrico equivalente utilizado para as amostras da liga Ti13Nb13Zr com superfície polida (Ver Figura 3).

Os resultados do ajuste do modelo e a capacitância efetiva associada ao CPE calculada com a equação de Brug são apresentados na Tabela 7. A partir do ajuste, obtemos valores de resistência da solução entre 21 e 22 ($\Omega \cdot cm^2$) e também altos valores de resistência à transferência de carga entre $1x10^5$ e $1.7x10^5$ ($\Omega \cdot cm^2$) são observados, indicando uma alta resistência à corrosão.

Por outro lado, os valores de capacitância para a camada porosa externa ($C_{eff(a)}$) foram entre 12 a 17 $\mu F \cdot cm^{-2}$. Além disso, os resultados obtidos para a dupla camada elétrica ($C_{eff(dl)}$) foram entre 40 a 49 $\mu F \cdot cm^{-2}$.

A espessura do filme passivo δ (em nm) foi obtida a partir da capacitância da camada interna densa. Os valores da espessura foram de 1,52, 1,90 e 1,70 nm para a liga Ti35Nb7Zr5Ta, nas condições ND, HPT1GPa e HPT4.5GPa, respectivamente. Estes resultados mostram que os filmes passivos na liga Ti35Nb7Zr5Ta deformada possuem maior espessura.

Tabela 7: Valores dos parâmetros do ajuste do modelo da Figura 3 para amostras da liga Ti35Nb7Zr5Ta com superfície polida.

Condição	Rs $\Omega \cdot cm^2$	Qa $\mu F \cdot s^{(\alpha 2-1)}$	α_a	Ra $\Omega \cdot cm^2$	$C_{eff(a)}$ $\mu F/cm^2$	Qb $\mu F \cdot s^{(\alpha 3-1)}$	α_b	Rb $\Omega \cdot cm^2$	$C_{eff(b)}$ $\mu F/cm^2$
Sem deformar	20	10	0.91	77	17	23	0.93	1.1E+05	49
1 GPa	21	10	0.89	129	15	22	0.91	1.7E+05	40
4.5 GPa	21	9	0.89	186	12	28	0.89	1.1E+05	44

Amostras com nanotubos de TiO_2

As Figuras 14((a) e (b)) mostram as curvas de polarização anódicas e os diagramas de Nyquist respectivamente dos substratos com nanotubos de TiO_2 da liga Ti35Nb7Zr5Ta não processadas e processadas por HPT.

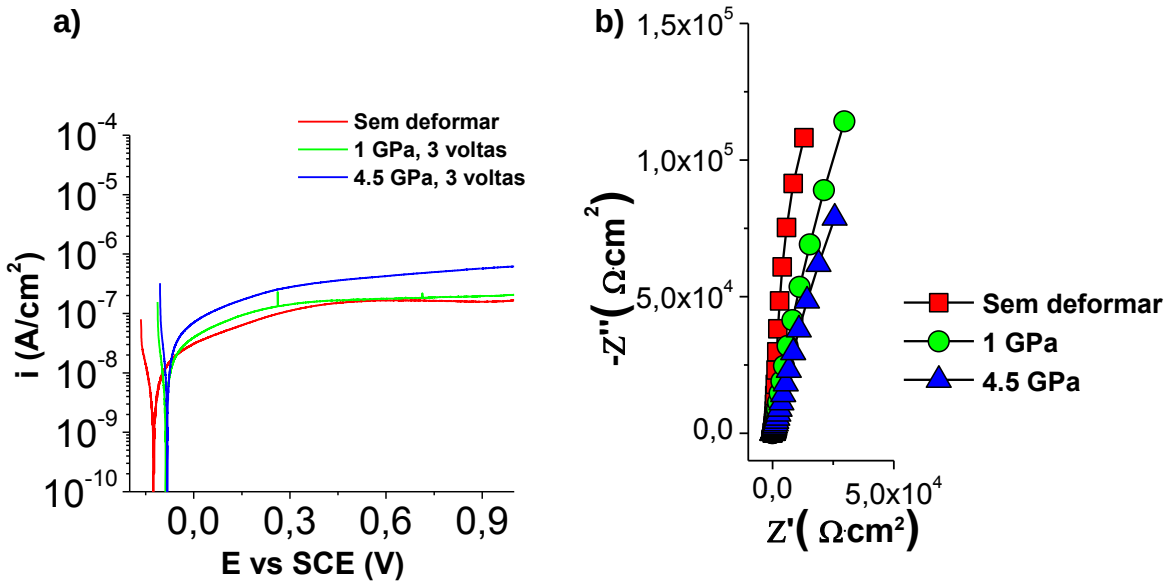

Figura 14: Curvas de polarização anódica (a) e diagramas de Nyquist (b) dos substratos com nanotubos de TiO_2 da liga Ti35Nb7Zr5Ta não processadas e processadas por HPT em meio fisiológico em uma solução de SBF a pH 7,4 a 37 ° C.

A forma da porção anódica das curvas de polarização mostrada na Figura 14(a) revela que o comportamento das amostras em um ambiente fisiológico é característico de um estado passivo.

Inicialmente, a corrente de passivação da liga Ti35Nb7Zr5Ta sem deformar tem um valor aproximado de: 0,16 μA / cm^2. Para amostras com deformação plástica severa, as correntes de passivação são: 0,19 μA / cm^2, para a amostra com 1 GPa de deformação e 0,52 μA / cm^2 para a amostra com 4,5 GPa de deformação. Portanto, parece que a deformação plástica severa causa um ligeiro aumento na corrente de passivação em comparação com o substrato sem deformação.

A Figura 14(b) mostra as medições da impedância por médio do diagrama de Nyquist. A observação dos diagramas de Nyquist revela que a forma do espectro de impedância para todos os substratos é pseudo-capacitivo (inclinado em linha reta), isto é, que as trocas de elétrons e, portanto, as reações, são muito limitadas ou que a camada de óxido é muito resistiva.

Os espectros de impedância experimentais são analisados ajustando-se ao mesmo modelo de linha de transmissão utilizado para a liga de Ti13Nb13Zr com nanotubos de TiO_2 (Ver Figura 5).

Os resultados do ajuste do modelo e a capacitância efetiva associada ao CPE calculada com a equação deHsu-Mansfeld são apresentados na Tabela 8. Em geral, valores de resistência da solução entre 20 e 21 ($\Omega \cdot cm^2$) e também uma alta resistência associada ao limite superior dos poros (R_A) entre $2x10^6$ e $8x10^6$ ($\Omega \cdot cm^2$) foram observados, indicando uma alta resistência à corrosão e este valor é maior em comparação com os substratos com superfície polida.

Os valores de capacitância foram entre 33 e 66 $\mu F \cdot cm^{-2}$ para C_β, que são típicos daqueles para uma capacitância de dupla camada. Além disso, os resultados obtidos para C_n, correspondente à capacitância do filme passivo, apresentaram valores entre 2 e 4 $\mu F \cdot cm^{-2}$.

A espessura do filme passivo δ (em nm) foi obtida a partir da capacitância do filme passivo. Os valores da espessura foram de 47,4, 34,3 e 22,3 nm para a liga Ti35Nb7Zr5Ta, nas condições ND, HPT1GPa e HPT4.5GPa, respectivamente.

Tabela 8: Valores dos parâmetros do ajuste do modelo da Figura 5 para amostras da liga

Condição	$\chi 1$	$\chi 2$	ξ				Z_A	Z_B			R_s
	R_1 (Ω)	R_2 (Ω)	R_3 (Ω)	Q_3 ($F^{\beta-1}$)	β	C_β μF/cm²	R_A (Ω)	Q_B (F^{n-1})	n	C_n μF/cm²	R_s (Ω)
Sem deformar	7	143	2.1E+15	2.0E-06	0.98	33	8.5E+06	1.2E-06	0.98	2	70.0
1 GPa	1	255	2.2E+15	1.9E-06	0.97	41	2.0E+06	1.0E-06	0.96	3	70.0
4.5 GPa	1	100	1.8E+15	3.1E-06	0.97	66	2.3E+06	1.6E-06	0.96	4	70.0

Ti35Nb7Zr5Ta com superfície com nanotubos de TiO_2.

Amostras com tratamento ácido por HCl e subsequentemente tratamento alcalino com NaOH.

As Figuras 15((a) e (b)) mostram as curvas de polarização anódicas e os diagramas de Nyquist respectivamente dos substratos com tratamento ácido por HCl e subsequentemente tratamento alcalino com NaOH da liga Ti35Nb7Zr5Ta não processadas e processadas por HPT.

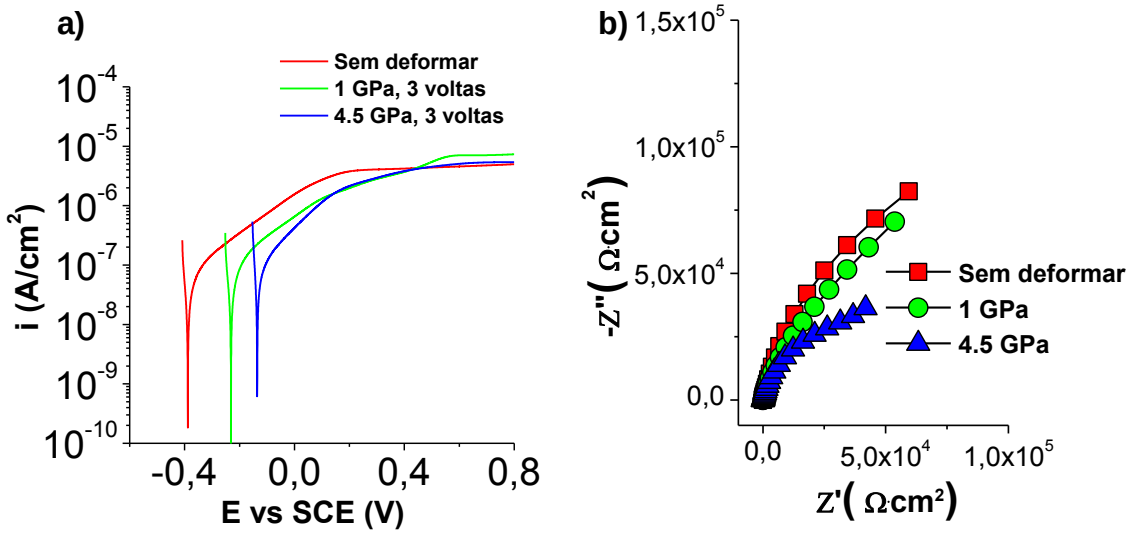

Figura 15: Curvas de polarização anódica (a) e diagramas de Nyquist (b) dos substratos com tratamento ácido por HCl e subsequentemente tratamento alcalino com NaOH da liga Ti35Nb7Zr5Ta não processadas e processadas por HPT em meio fisiológico em uma solução de SBF a pH 7,4 a 37 ° C.

As amostras exibem um comportamento passivo para uma amplia gama de potenciais. Inicialmente, a corrente de passivação para as amostras sem deformação tem aproximadamente um valor de: 4,58 μA / cm^2. Para amostras com deformação plástica severa, as correntes de passivação são: 7,20 μA / cm^2, para a amostra com 1 GPa de deformação e 5,21 μA / cm^2 para a amostra com 4,5 GPa de deformação. Portanto, parece que a deformação plástica severa causa um ligeiro aumento na corrente de passivação em comparação com o substrato sem deformação.

A Figura 15(b) mostra as medições da impedância por médio do diagrama de Nyquist. A observação dos diagramas de Nyquist revela que a forma do espectro de impedância para todos os substratos é característica de um sistema capacitivo-resistivo. Os espectros de impedância experimentais foram analisados ajustando-se com o mesmo circuito elétrico equivalente utilizado para as amostras da liga Ti13Nb13Zr com ataque ácido por HCl (Ver Figura 7).

Os resultados do ajuste do modelo e a capacitância efetiva associada ao CPE calculada com a equação de Brug são apresentados na Tabela 9. A partir do ajuste, obtemos valores de resistência da solução entre 20 e 21 ($\Omega \cdot cm^2$) e também são observados altos valores de resistência à transferência de carga entre $8,4x10^4$ e $3x10^5$ ($\Omega \cdot cm^2$), indicando uma alta resistência à corrosão com valores levemente maiores que as amostras com superfície polidas.

Com relação às capacitâncias, os valores para a capacitância da dupla camada elétrica (Ceff ($_{dl}$)) foram entre 10 e 18 $\mu F \cdot cm^{-2}$. Os valores de capacitância para a camada externa porosa (Ceff($_b$)) e a camada porosa intermediária (Ceff($_a$)) foram menores que Ceff ($_{dl}$).

Além disso, a espessura do filme δ (em nm) foi obtida a partir da capacitância da camada interna densa. Os valores da espessura foram de 4,07, 7,87 e 7,43 nm para a liga Ti35Nb7Zr5Ta, nas condições ND, HPT1GPa e HPT4.5GPa, respectivamente. Estes resultados mostram que os filmes passivos na liga de Ti35Nb7Zr5Ta deformada possuem maior espessura.

Tabela 9: Valores dos parâmetros do ajuste do modelo da Figura 7 para amostras da liga Ti35Nb7Zr5Ta submetidas ao tratamento ácido por HCl e subsequentemente tratamento alcalino com NaOH.

	Condição		
Elemento	**Sem deformar**	**1 GPa**	**4.5 GPa**
Rs ($\Omega \cdot cm^2$)	21	20	20
Qb ($\mu F \cdot s^{(\alpha b-1)}$)	42	40	40
α_b	0.72	0.72	0.72
Rb ($\Omega \cdot cm^2$)	10	9	3
$C_{eff(b)}$ ($\mu F/cm^2$)	1.8	1.6	1.1
Qa ($\mu F \cdot s^{(\alpha a-1)}$)	19	33	47
α_a	0.70	0.71	0.80
Ra ($\Omega \cdot cm^2$)	1	1	24
$C_{eff(a)}$ ($\mu F/cm^2$)	0.2	0.5	7.3
Qdl ($\mu F \cdot s^{(\alpha dl-1)}$)	32	17	12
α_{dl}	0.93	0.93	0.98
Rct ($\Omega \cdot cm^2$)	3.3E+05	2.7E+05	8.4E+04
$C_{eff(dl)}$ ($\mu F/cm^2$)	18	10	10

Amostras com tratamento ácido por H_3PO_4 e subsequentemente tratamento alcalino com NaOH.

As Figuras 16((a) e (b)) mostram as curvas de polarização anódicas e os diagramas de Nyquist respectivamente dos substratos com tratamento ácido por H_3PO_4 e subsequentemente tratamento alcalino com NaOH da liga Ti35Nb7Zr5Ta não processadas e processadas por HPT.

Como todas as amostras analisadas, observa-se um comportamento passivo para uma ampla gama de potenciais. Inicialmente, a corrente de passivação para as amostras sem deformar tem aproximadamente um valor de: 8,24 µA / cm^2. Para amostras com deformação plástica severa, as correntes de passivação são: 10,80 µA / cm^2, para a amostra com 1 GPa de deformação e

10,80 µA / cm^2 para a amostra com 4,5 GPa de deformação. Portanto, parece que a deformação plástica severa causa um ligeiro aumento na corrente de passivação em comparação com o substrato sem deformação.

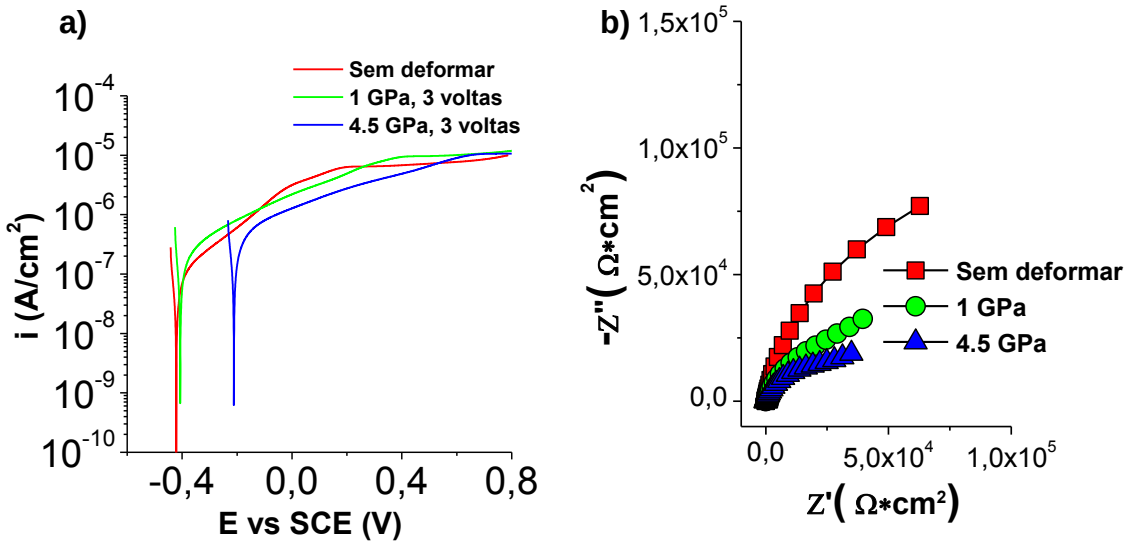

Figura 16: Curvas de polarização anódica (a) e diagramas de Nyquist (b) dos substratos com tratamento ácido por H_3PO_4 e subsequentemente tratamento alcalino com NaOH da liga Ti35Nb7Zr5Ta não processadas e processadas por HPT em meio fisiológico em uma solução de SBF a pH 7,4 a 37 ° C.

A Figura 16(b) mostra as medições da impedância por médio do diagrama de Nyquist. A observação dos diagramas de Nyquist revela que a forma do espectro de impedância para todos os substratos é característica de um sistema capacitivo-resistivo. Os espectros de impedância experimentais são analisados ajustando-se com o mesmo circuito elétrico equivalente utilizado para as amostras da liga Ti13Nb13Zr com ataque ácido por H_3PO_4 (Ver Figura 7).

Os resultados do ajuste do modelo são apresentados na Tabela 10. A partir do ajuste, obtemos valores de resistência da solução de 20 ($\Omega \cdot cm^2$) e também altos valores de resistência à transferência de carga entre $2x10^4$ e $2x10^5$ ($\Omega \cdot cm^2$), indicando uma alta resistência à corrosão.

Com relação às capacitâncias, os valores para a capacitância da dupla camada elétrica (Ceff ($_{dl}$)) foram entre 10 e 19 μF·cm^{-2}. Os valores de capacitância para a camada externa porosa (Ceff($_{b}$)) e a camada porosa intermediária (Ceff($_{a}$)) foram menores que Ceff ($_{dl}$).

A espessura do filme passivo δ (em nm) foi obtida a partir da capacitância da camada interna densa. Os valores da espessura foram 3,98, 7,62 e 7,69 nm para a liga Ti35Nb7Zr5Ta, nas condições ND, HPT1GPa e HPT4.5GPa, respectivamente. Estes resultados mostram que os filmes passivos na liga de Ti35Nb7Zr5Ta deformada possuem maior espessura.

Tabela 10: Valores dos parâmetros do ajuste do modelo da Figura 7 para amostras da liga Ti35Nb7Zr5Ta submetidas ao tratamento ácido por H_3PO_4 e subsequentemente tratamento alcalino com NaOH.

	Condição		
Elemento	**Sem deformar**	**1 GPa**	**4.5 GPa**
Rs (Ω·cm^2)	20	20	20
Qb (μF ·s$^{(αb-1)}$)	40	53	15
$α_b$	0.73	0.70	0.80
Rb (Ω·cm^2)	9	7	4
$C_{eff(b)}$ (μF/cm^2)	1.8	1.6	1.3
Qa (μF ·s$^{(αa-1)}$)	6	6	37
$α_a$	0.72	0.78	0.84
Ra (Ω·cm^2)	3	1	10
$C_{eff(a)}$ (μF/cm^2)	0.1	4.3	7.5
Qdl (μF ·s$^{(αdl-1)}$)	47	54	54
$α_{dl}$	0.88	0.80	0.80
Rct (Ω·cm^2)	2.2E+05	1.0E+05	2.5E+04
$C_{eff(dl)}$ (μF/cm^2)	19	10	10

Testes de bioatividade da liga Ti35Nb7Zr5Ta

Neste estudo foram examinados depósitos de apatita após 1, 7 e 14 dias de imersão em SBF para as amostras da liga Ti35Nb7Zr5Ta com distintas modificação de superfície assim como os diferentes graus de deformação por HPT.

Amostras polidas

As observações microscopia eletrônica de varrido (MEV) mostram na Figura 17 que, mesmo após 14 dias de imersão na solução fisiológica, nenhuma formação de apatita é detectada nas superfícies dos substratos polidos da liga Ti35Nb7Zr5Ta.

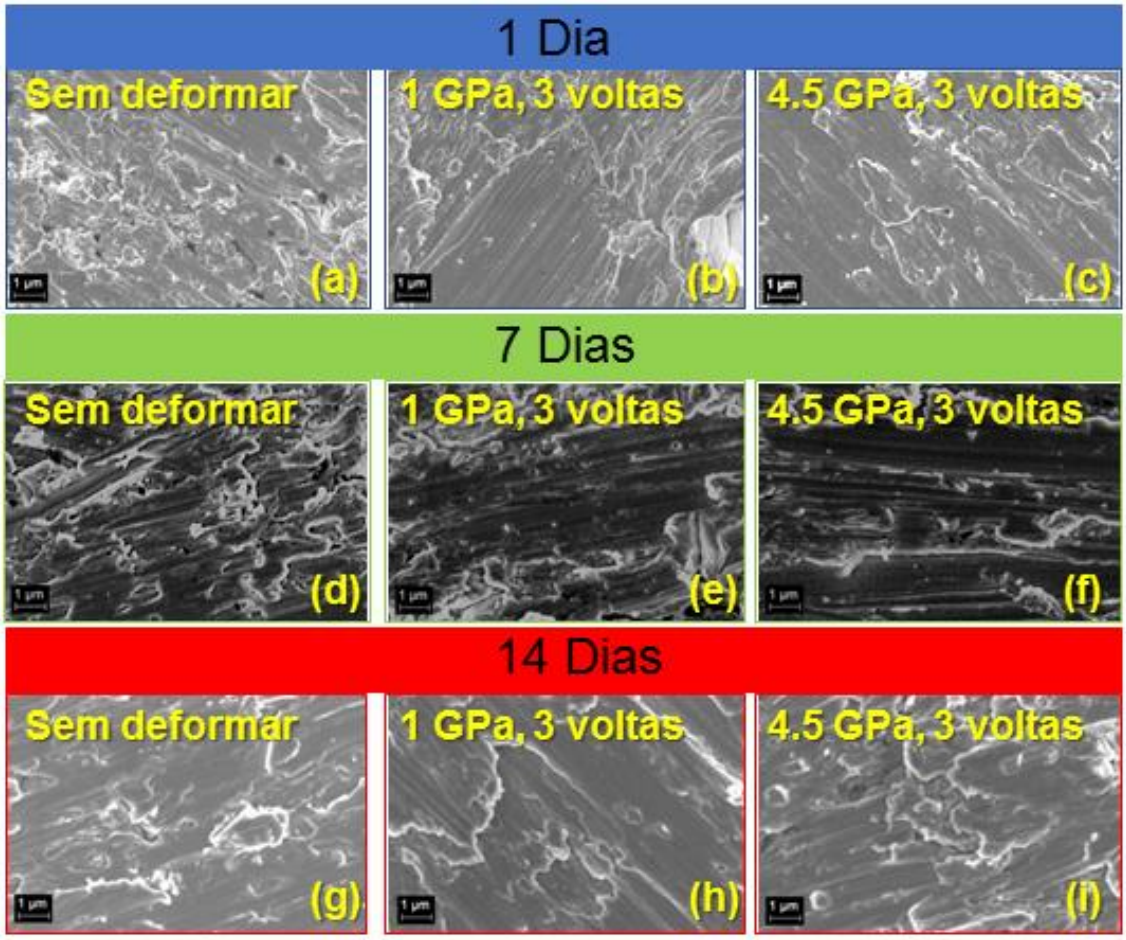

Figura 17: Observações por MEV das amostras com superfície polidas da liga de Ti35Nb7Zr5Ta não processadas e processadas por HPT, submetidas a testes de bioatividade para tempos de 1, 7 e 14 dias em SBF.

Amostras com nanotubos de TiO_2

A partir do décimo quarto dia na imersão em SBF, a apatita é visível em alguns substratos de Ti35Nb7Zr5Ta que são as amostras sem deformação e as amostras deformadas por HPT na condição de 4,5 GPa com nanotubos de TiO_2 recozidos. As Figuras 18((g) e (i)) são as condições mencionadas anteriormente que apresentam apatita na superfície dos substratos.

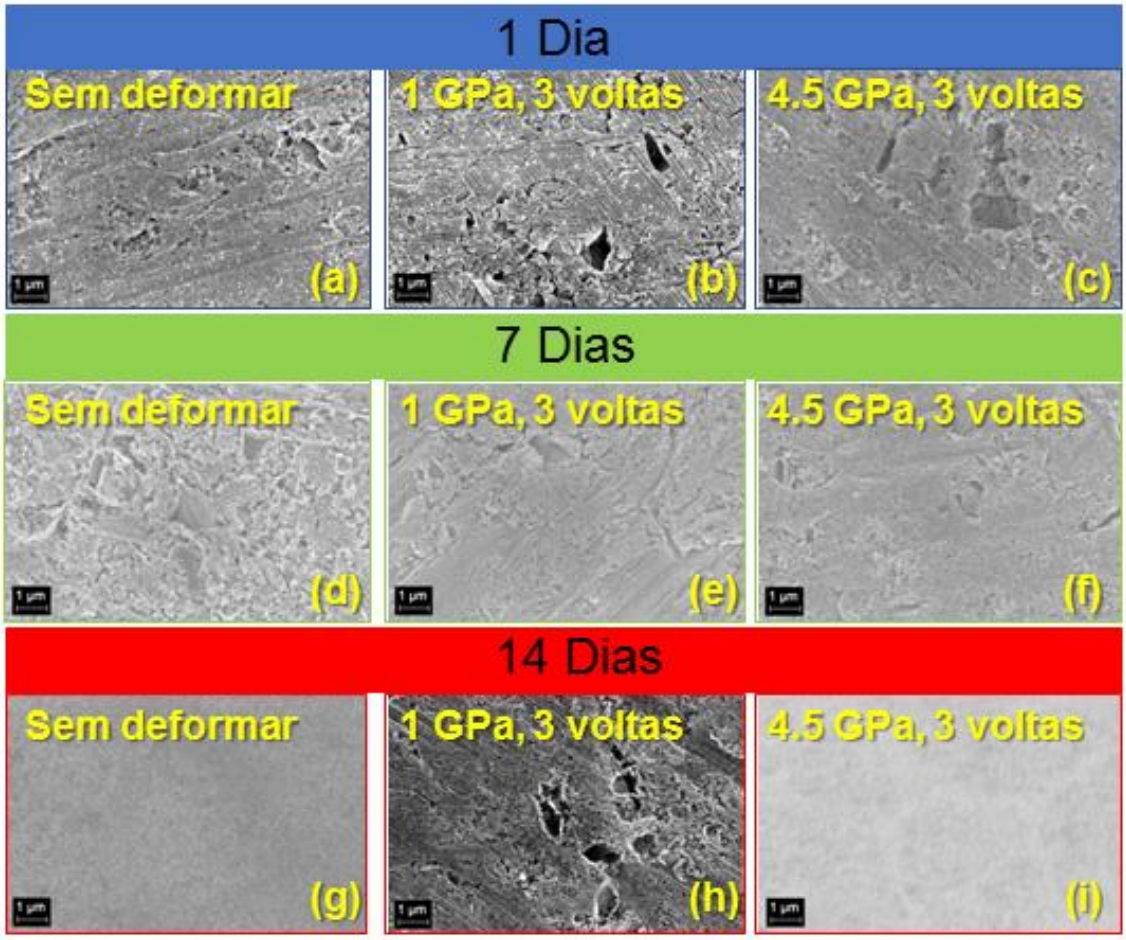

Figura 18: Observações por MEV das amostras com superfície com nanotubos de TiO_2 da liga de Ti35Nb7Zr5Ta não processadas e processadas por HPT, submetidas a testes de bioatividade para tempos de 1, 7 e 14 dias em SBF.

Amostras com tratamento ácido por HCl e subsequentemente tratamento alcalino com NaOH.

As observações microscopia eletrônica de varrido (MEV) mostram que a partir do décimo quarto dia na imersão em SBF, a apatita é visível em alguns substratos da liga Ti35Nb7Zr5Ta. Os substratos sem deformação e deformados por HPT na condição de 4,5 GPa são aqueles que formaram apatita na sua superfície e podem ser observados nas Figuras 19((g) e (i)).

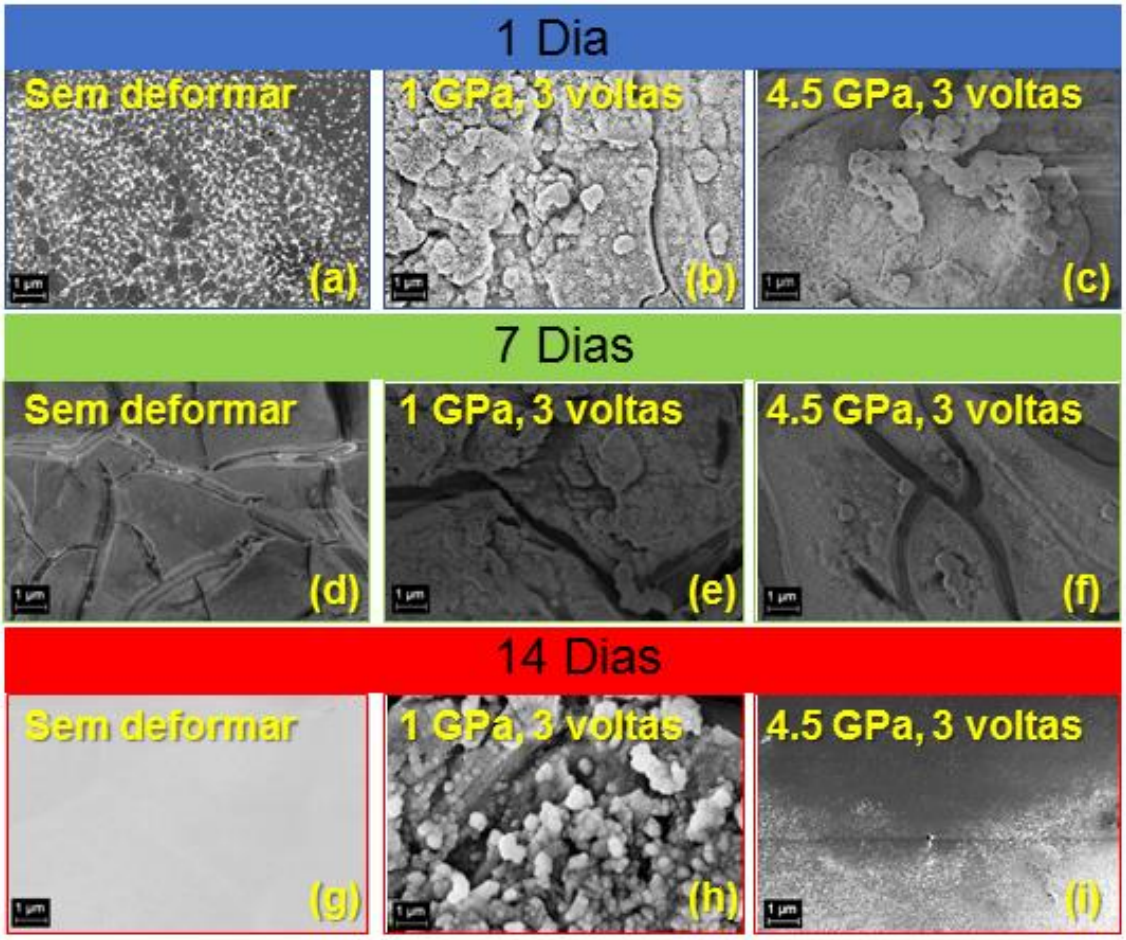

Figura 19: Observações por MEV das amostras com superfície com tratamento ácido por HCl e subsequentemente tratamento alcalino com NaOH da liga de Ti35Nb7Zr5Ta não processada e processada por HPT, submetidas a testes de bioatividade para tempos de 1, 7 e 14 dias em SBF.

Amostras com tratamento ácido por H_3PO_4 e subsequentemente tratamento alcalino com NaOH.

As observações microscopia eletrônica de varrido (MEV) mostram na Figura 20 que, mesmo após 14 dias de imersão na solução fisiológica, nenhuma formação de apatita é detectada nas superfícies dos substratos (independentemente da deformação por HPT).

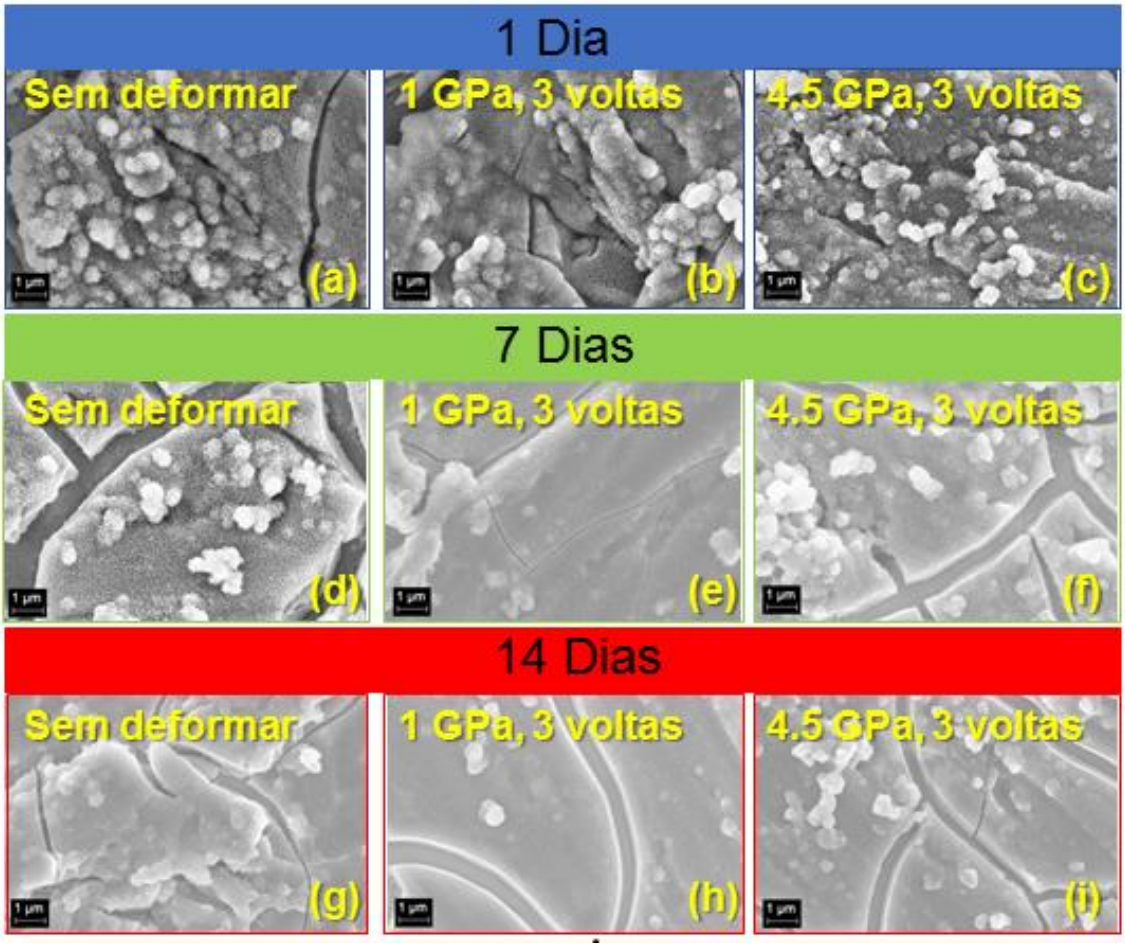

Figura 20: Observações por MEV das amostras com superfície com tratamento ácido por H_3PO_4 e subsequentemente tratamento alcalino com NaOH da liga de Ti35Nb7Zr5Ta não processada e processada por HPT, submetidas a testes de bioatividade para tempos de 1, 7 e 14 dias em SBF.

Recopilação

Ensaios de corrosão e testes de bioatividade foram desenvolvidos para as ligas de Ti13Nb13Zr e Ti35Nb7Zr5Ta com superfície modificadas e deformadas por HPT. A caracterização eletroquímica foi através de curvas de polarização e testes de impedância eletroquímica.

Em relação a correntes de passivação (I_{pass}) obtidas a partir das curvas de polarização, foi observado que as amostras com superfície polida e amostras tratadas quimicamente (HCl, H_3PO_4 + NaOH) tem valores de I_{pass} da mesma

ordem de grandeza (10^{-6} A $\cdot cm^{-2}$). Por outro lado, não foi observada uma grande diferença para as correntes de passivação entre amostras sem deformação e deformadas por HPT (exceto as amostras anodizadas).

Observou-se que a presença de nanoestruturas de TiO_2 possui o maior valor de resistência da camada porosa externa, o que significa que foi a condição com maior resistência à corrosão. Isto é melhor observado na liga Ti13Nb13Zr, onde os valores de resistência são apresentados na ordem de $3x10^7$ ($\Omega \cdot cm^2$). Por outro lado, os tratamentos químicos tendem a diminuir o valor da resistência da camada protetora de óxido, quando a pressão de deformação aumenta. Está redução de resistência à corrosão foi atribuída às microestruturas de não equilíbrio formadas durante o processamento de HPT. O acima mencionado faz com que a camada externa do filme de óxido seja mais suscetível à dissolução do que a camada interna, o que indica uma estrutura mais defeituosa da camada externa.

As micrografias de obtidas por MEV mostraram que para as ligas de Ti13Nb13Zr e Ti35Nb7Zr5Ta mesmo imersas em SBF durante 14 dias, nenhuma das amostras com superfícies polidas formou apatita na sua superfície, ou seja, não são bioativas. Isto confirma que a camada inicial inerte de TiO_2 criada na superfície dos substratos polidos não é suficiente para promover a formação de tecido entre o osso e o implante espontaneamente.

O comportamento observado pelos substratos polidos foi também observado para amostras de liga Ti35Nb7Zr5Ta tratada com H_3PO_4 e ativada com NaOH, indicando que, mesmo começando com fosfato na superfície, o referido material não adquire bioatividade utilizando tais tratamento de superfície. Por contraste, durante o mesmo tratamento de superfície, as superfícies das amostras da liga Ti13Nb13Zr mostraram bioatividade em períodos entre sete e quatorze dias em condições deformadas e não deformadas.

As superfícies com nanotubos de TiO_2 da liga Ti13Nb13Zr na condição não deformada começou a produzir uma camada de apatita entre sete e quatorze dias, enquanto as amostras deformadas formaram apatita a partir das primeiras 24

horas. No entanto, o mesmo tratamento de superfície provou não ser tão eficaz para as amostras da liga Ti35Nb7Zr5Ta. Neste caso, amostras (deformadas ou não) só começaram a produzir alguma camada de apatia aos quatorze dias.

Finalmente, este estudo mostrou que os tratamentos de modificação de superfície são benéficos para promover a osseointegração e também a deformação plástica severa promove a bioatividade, desta forma os substratos testados tem um grande potencial para aplicações biomédicas.

Referências

[1] G. Manivasagam, D. Dhinasekaran, A. Rajamanickam, Biomedical implants: Corrosion and its Prevention-A Review, Recent Patents Corros. Sci. 2 (2010) 40–54. doi:10.2174/1877610801002010040.

[2] M. Niinomi, Mechanical properties of biomedical titanium alloys, Mater. Sci. Eng. A. 243 (1998) 231–236. doi:10.1016/S0921-5093(97)00806-X.

[3] M. Niinomi, D. Kuroda, K. Fukunaga, M. Morinaga, Y. Kato, T. Yashiro, A. Suzuki, Corrosion wear fracture of new β type biomedical titanium alloys, Mater. Sci. Eng. A. 263 (1999) 193–199. doi:10.1016/S0921-5093(98)01167-8.

[4] A. Najdahmadi, A. Zarei-Hanzaki, E. Farghadani, Mechanical properties enhancement in Ti–29Nb–13Ta–4.6 Zr alloy via heat treatment with no detrimental effect on its biocompatibility, Mater. Des. 54 (2014) 786–791. doi:10.1016/j.matdes.2013.09.007.

[5] K.K. Wang, L.J. Gustavson, J.H. Dumbleton, Microstructure and properties of a new beta titanium alloy, Ti-12Mo-6Zr-2Fe, developed for surgical implants, in: Med. Appl. Titan. Its Alloy. Mater. Biol. Issues, ASTM International, 1996.

[6] P.L. Ferrandini, F.F. Cardoso, S.A. Souza, C.R. Afonso, R. Caram, Aging response of the Ti–35Nb–7Zr–5Ta and Ti–35Nb–7Ta alloys, J. Alloys Compd. 433 (2007) 207–210. doi:10.1016/j.jallcom.2006.06.094.

[7] H.J. Rack, J.I. Qazi, Titanium alloys for biomedical applications, 26 (2006) 1269–1277. doi:10.1016/j.msec.2005.08.032.

[8] S. Zherebtsov, G. Salishchev, R. Galeyev, K. Maekawa, Mechanical properties of Ti–6Al–4V titanium alloy with submicrocrystalline structure produced by severe plastic deformation, Mater. Trans. 46 (2005) 2020–2025. doi:10.2320/matertrans.46.2020.

[9] a. Azushima, R. Kopp, a. Korhonen, D.Y. Yang, F. Micari, G.D. Lahoti, P. Groche, J. Yanagimoto, N. Tsuji, a. Rosochowski, a. Yanagida, Severe plastic deformation (SPD) processes for metals, CIRP Ann. - Manuf. Technol. 57 (2008) 716–735. doi:10.1016/j.cirp.2008.09.005.

[10] Y.T. Zhu, T.G. Langdon, The fundamentals of nanostructured materials processed by severe plastic deformation, Jom. 56 (2004) 58–63. doi:10.1007/s11837-004-0294-0.

[11] D.A.G. Pérez, J. Junior, A. Moreira, C.S. Kiminami, C. Bolfarini, W.J. Botta, Ultrafine-Grained Ti-13Nb-13Zr Alloy Produced by Severe Plastic Deformation, Mater. Res. 20 (2017) 404–410. doi:10.1590/1980-5373-mr-2017-0037.

[12] K. Sharman, P. Bazarnik, T. Brynk, A. Gunay Bulutsuz, M. Lewandowska, Y. Huang, T.G. Langdon, Enhancement in mechanical properties of a β-titanium alloy by high-pressure torsion, J. Mater. Res. Technol. 4 (2015) 79–83. doi:10.1016/j.jmrt.2014.10.010.

[13] M. Kulkarni, A. Mazare, E. Gongadze, Š. Perutkova, V. Kralj-Iglič, I. Milošev, P. Schmuki, A. Iglič, M. Mozetič, Titanium nanostructures for biomedical

applications, Nanotechnology. 26 (2015) 62002. doi:10.1088/0957-4484/26/6/062002.

[14] R.Z. Valiev, I.P. Semenova, V. V. Latysh, H. Rack, T.C. Lowe, J. Petruzelka, L. Dluhos, D. Hrusak, J. Sochova, Nanostructured titanium for biomedical applications, Adv. Eng. Mater. 10 (2008) 15–17. doi:10.1002/adem.200800026.

[15] H. Miyamoto, Corrosion of Ultrafine Grained Materials by Severe Plastic Deformation, an Overview, Mater. Trans. 57 (2016) 559–572. doi:10.2320/matertrans.M2015452.

[16] J. Lu, Y. Zhang, W. Huo, W. Zhang, Y. Zhao, Y. Zhang, Electrochemical corrosion characteristics and biocompatibility of nanostructured titanium for implants, Appl. Surf. Sci. 434 (2018) 63–72. doi:10.1016/j.apsusc.2017.10.168.

[17] M. Takeuchi, Y. Abe, Y. Yoshida, Y. Nakayama, M. Okazaki, Y. Akagawa, Acid pretreatment of titanium implants, 24 (2003) 1821–1827. doi:10.1016/S0142-9612(02)00576-8.

[18] W.F. Oliveira, I.R.S. Arruda, G.M.M. Silva, G. Machado, L.C.B.B. Coelho, M.T.S. Correia, Functionalization of titanium dioxide nanotubes with biomolecules for biomedical applications, Mater. Sci. Eng. C. 81 (2017) 597–606. doi:10.1016/j.msec.2017.08.017.

[19] J.E.G. Hulshoff, K. Van Dijk, J.E. De Ruijter, F.J.R. Rietveld, L.A. Ginsel, J.A. Jansen, Interfacial phenomena: An in vitro study of the effect of calcium phosphate (Ca-P) ceramic on bone formation, J. Biomed. Mater. Res. 40 (1998) 464–474. doi:10.1002/(SICI)1097-4636(19980605)40:3<464::AID-JBM18>3.0.CO;2-J.

[20] S. Nishiguchi, T. Nakamura, M. Kobayashi, H.-M. Kim, F. Miyaji, T. Kokubo, The effect of heat treatment on bone-bonding ability of alkali-treated

titanium, Biomaterials. 20 (1999) 491–500. doi:10.1016/S0142-9612(98)90203-4.

[21] M.J. Filiaggi, N.A. Coombs, R.M. Pilliar, Characterization of the interface in the plasma-sprayed HA coating/Ti-6Al-4V implant system, J. Biomed. Mater. Res. 25 (1991) 1211–1229. doi:10.1002/jbm.820251004.

[22] K.S. Brammer, C.J. Frandsen, S. Jin, TiO_2 nanotubes for bone regeneration, Trends Biotechnol. 30 (2012) 315–322. doi:10.1016/j.tibtech.2012.02.005.

[23] A.P. Zhilyaev, T.G. Langdon, Using high-pressure torsion for metal processing: Fundamentals and applications, Prog. Mater. Sci. 53 (2008) 893–979. doi:10.1016/j.pmatsci.2008.03.002.

[24] X. Liu, P.K. Chu, C. Ding, Surface modification of titanium , titanium alloys , and related materials for biomedical applications, 47 (2005) 49–121. doi:10.1016/j.mser.2004.11.001.

[25] H. Tsuchiya, J.M. Macak, L. Müller, J. Kunze, F. Müller, P. Greil, S. Virtanen, P. Schmuki, Hydroxyapatite growth on anodic TiO_2 nanotubes, J. Biomed. Mater. Res. Part A. 77A (2006) 534–541. doi:10.1002/jbm.a.30677.

[26] V.P. Parkhutik, V.I. Shershulsky, Theoretical modelling of porous oxide growth on aluminium, J. Phys. D. Appl. Phys. 25 (1992) 1258. doi:10.1088/0022-3727/25/8/017.

[27] G.K. Grimes, Craig A., Mor, TiO_2 nanotube arrays: synthesis, properties, and applications, 2009. doi:10.1007/978-1-4419-0068-5.

[28] Y. Bai, I.S. Park, H.H. Park, M.H. Lee, T.S. Bae, W. Duncan, M. Swain, The effect of annealing temperatures on surface properties, hydroxyapatite growth and cell behaviors of TiO_2 nanotubes, Surf. Interface Anal. 43 (2011) 998–1005. doi:10.1002/sia.3683.

[29] P. Roy, S. Berger, P. Schmuki, TiO_2 nanotubes: synthesis and applications, Angew. Chemie. 50 (2011) 2904–2939. doi:10.1002/anie.201001374.

[30] F. Hilario, Synthèse et caractérisations de nanotubes de TiO_2 pour applications biomédicales: propriétés électrochimiques et bioactivité, (2017).

[31] L. Le Guéhennec, A. Soueidan, P. Layrolle, Y. Amouriq, Surface treatments of titanium dental implants for rapid osseointegration, Dent. Mater. 23 (2007) 844–854. doi:10.1016/j.dental.2006.06.02.

[32] H. Kim, F. Miyaji, T. Kokubo, T. Nakamura, Preparation of bioactive Ti and its alloys via simple chemical surface treatment, J. Biomed. Mater. Res. An Off. J. Soc. Biomater. Japanese Soc. Biomater. 32 (1996) 409–417. doi:10.1002/(sici)1097-4636(199611)32:3<409::aid-jbm14>3.0.co;2-.

[33] T. Kokubo, H. Takadama, How useful is SBF in predicting in vivo bone bioactivity?, Biomaterials. 27 (2006) 2907–2915. doi:10.1016/j.biomaterials.2006.01.017.

[34] B. Torres, A. Seyeux, S. Zanna, B. Tribollet, P. Marcus, I. Frateur, Influence of BSA adsorption on the oxide layers developed on 70Cu-30Ni alloy in static artificial seawater, Matériaux Tech. 101 (2013) 106.

[35] F. Hilario, V. Roche, A. Jorge Junior, R. Nogueira, Application of the transmission line model for porous electrodes to analyse the impedance response of TiO_2 nanotubes in physiological environment, 2017. doi:10.1016/j.electacta.2017.09.045.

[36] S.A.A. Yahia, L. Hamadou, A. Kadri, N. Benbrahim, E.M.M. Sutter, Effect of anodizing potential on the formation and EIS characteristics of TiO2 nanotube arrays, J. Electrochem. Soc. 159 (2012) K83–K92. doi:10.1149/2.077204jes.

[37] P. Pu, H. Cachet, E.M.M. Sutter, Electrochemical impedance spectroscopy to study photo-induced effects on self-organized TiO_2 nanotube arrays, Electrochim. Acta. 55 (2010) 5938–5946.

[38] B. Hirschorn, M.E. Orazem, B. Tribollet, V. Vivier, I. Frateur, M. Musiani, Determination of effective capacitance and film thickness from constant-phase-element parameters, Electrochim. Acta. 55 (2010) 6218–6227. doi:10.1016/j.electacta.2009.10.065.